



UNIVERSITY *of*
TASMANIA

Improving the understanding of H₂O-free aerosol
behaviour in the inductively-coupled plasma for
geochemical LA-ICP-MS applications: U-Pb dating
and trace element analysis in silicate minerals and
glasses

by

Jay Michael Thompson

MSc Geoscience

Department of Geoscience | University of Iowa

Submitted in fulfilment of the requirements for the degree of Doctor of Philosophy

University of Tasmania February, 2021

Declaration of originality

This thesis contains no material which has been accepted for a degree or diploma by the University or any other institution, except by way of background information and duly acknowledged in the thesis, and to the best of my knowledge and belief no material previously published or written by another person except where due acknowledgement is made in the text of the thesis, nor does the thesis contain any material that infringes copyright.

Signed

Date 22/2/2021

Statement of Authority of Access

This thesis may be made available for loan and limited copying and communication in accordance with the Copyright Act 1968.

Signed

Date 22/2/2021

Statement regarding published work

The publishers of the papers comprising Chapters 2 to 5 hold the copyright for that content and access to the material should be sought from the respective journals. The remaining nonpublished content of the thesis may be made available for loan and limited copying and communication in accordance with the Copyright Act 1968.

Signed

Date 22/2/2021

Statement of co-authorship

The following people and institutions contributed to the publication of work undertaken as part of this thesis:

| | |
|------------------|---|
| Candidate | Jay Thompson, Candidate (CODES Analytical Laboratories, University of Tasmania) |
| Author 1 | Leonid Danyushevsky (CODES Analytical Laboratories, University of Tasmania) |
| Author 2 | Sebastien Meffre (CODES, University of Tasmania) |
| Author 3 | Roland Maas (School of Earth Sciences, University of Melbourne) |
| Author 4 | R.S. Houk (Chemistry Department, Iowa State University) |
| Author 5 | Paul Olin (CODES, University of Tasmania) |
| Author 6 | Fred Fryer (Agilent Technologies) |
| Author 7 | Karsten Goemann (CSL, University of Tasmania) |
| Author 8 | Olga Borovinskaya (TOFWerk AG, Thun, Switzerland) |
| Author 9 | Martin Tanner (TOFWerk AG, Thun, Switzerland) |
| Author 10 | Vadim Kamenetsky (CODES, University of Tasmania) |
| Author 11 | Maya Kamenetsky (CODES, University of Tasmania) |
| Author 12 | Kathy Ehrig (BHP-Billiton, Olympic Dam, Australia) |

Author details and their roles

| | |
|------------------|--|
| Paper 1 | <i>The effects of H₂O, He, N₂ and H₂ on ion kinetic energies in inductively-coupled plasma mass spectrometry. Spectrochimica Acta Part B: Atomic Spectroscopy (2020), 169, 105870. Located in Chapter 2</i> |
| Candidate | (72.5%) was the primary author. |
| Author 1 | (10%) contributed to the idea, its formalisation and development |
| Author 4 | (10%) contributed to the interpretation of results and review of manuscript |

Author 5 (5%) contributed in data collection and review of manuscript
Author 6 (2.5%) contributed in the idea formalisation and development

Paper 2 *Matrix effects in Pb/U measurements during LAICP-MS analysis of the mineral apatite. Journal of Analytical Atomic Spectrometry (2016), 31(6), 1206-1215. Located in Chapter 3*

Candidate (80%) was the primary author
Author 2 (5%) contributed to the idea, its formalization and development
Author 10 (2.5%) contributed to the idea and provided samples for analysis
Author 1 (2.5%) contributed to the idea development
Author 3 (2.5%) provided analyses and review of the manuscript
Author 7 (2.5%) provided assistance with EMPA analysis and SEM imaging
Author 11 (2.5%) provided analyses to the manuscript
Author 12 (2.5%) contributed samples for analysis

Paper 3 *Impact of air, laser pulse width and fluence on U–Pb dating of zircons by LA-ICPMS. Journal of Analytical Atomic Spectrometry (2018), 33(2), 221-230. Located in Chapter 4*

Candidate (80%) was the primary author
Author 1 (10%) contributed to the idea, its formalization and development
Author 2 (10%) contributed to the idea, its formalization and development

Paper 4 *Time-of-flight ICP-MS laser ablation zircon geochronology: assessment and comparison against quadrupole ICP-MS. Accepted to Journal of Analytical Atomic Spectrometry in July 2020. Located in Chapter 5*

Candidate (82.5%) was the primary author
Author 1 (10%) contributed to the idea, its formalization and development
Author 8 (5%) contributed to the idea, its formalization and development
Author 9 (2.5%) assisted in use of instrumentation

We, the undersigned, endorse the above stated contribution of work undertaken for each of the published (or submitted) peer-reviewed manuscripts contributing to this thesis:

Signed:

Jay Thompson
Candidate
School of Natural Sciences
University of Tasmania

Leonid Danyushevsky
Primary Supervisor
School of Natural Sciences
University of Tasmania

Simon Ellingsen
Head of School
School of Natural Sciences
University of Tasmania

Date:

22/2/2021

4/8/2020

5/8/2020

Abstract

Laser ablation inductively-coupled plasma mass spectrometry (LA-ICP-MS) is an in-situ analytical technique for analysis of trace element and isotopic compositions in a wide range of materials. LA-ICP-MS has been utilized for more than 30 years in the geoscience community, but the technique still suffers from inaccuracies related to non-representative sampling of ablated material. This term has been broadly described as element fractionation and is thought to occur both at the site of ablation and in the plasma of the ICP-MS. Improvement of the LA-ICP-MS analytical technique by increased understanding of fundamental instrument processes and development of mineral standards can significantly improve geochemical and geochronological data capabilities and uses.

There are two main parts of this study, the first, is an investigation into the fundamental aspects of ionization and extraction of ions into the mass spectrometer using both laser ablation and nebulizing a solution of dilute nitric acid with ppb level solutes. The second is an investigation using nanosecond pulse width excimer lasers to analyse a variety of minerals and glasses for their trace element, U-Pb isotopic and Pb isotopic compositions and comparing the results to published values to assess sources of bias in the LA-ICP-MS analytical technique.

The use of ICP-MS for laser ablation was not initially considered during the design of ICP-MS instrumentation because most previous applications used a nebulizer and spray chamber to introduce liquid solutions. While early work showed that a laser ablation system could easily be coupled to an ICP-MS, with several advantages including lower polyatomic species from lack of H_2O ; little work has been done on understanding how the laser ablation aerosol (dry plasma) interacts with the plasma and ion extraction process compared to traditional solution nebulization (wet plasma). This study builds on previous work to demonstrate the differences in the electrical potential of the ICP between wet and dry plasma, as this has an effect on the distribution of ion energies that are sampled from the ICP. This distribution of ion energies is a function of plasma temperature, and temperatures calculated in this work suggest that dry plasma conditions are cooler than wet plasma conditions (2441 K vs. 3055 K). Ion energy distributions are also affected by perturbations in the ion beam such as space charge effects and

this work suggests there are likely differences in space charge, or spatial biasing light vs. heavy ions in the ion beam, between the wet and dry plasma ion beams.

Oxide and hydroxide polyatomic species are a common issue in ICP-MS, particularly for elements with high MO^+ bond energies (e.g. La). This study investigates the formation of oxide and hydroxide species between wet and dry plasma by investigating the parameters controlling formation, ways to suppress these interferences, and the interference's ion energy distributions. The interference's ion energy distributions can provide information about the location of formation within the plasma / ICP-MS, the knowledge of which aides in preventing and minimizing interferences. Oxide formation rates in dry plasma are significantly less than wet plasma (>10x lower) which is consistent with previous work. However, this study also demonstrates that a greater stopping potential is needed to attenuate the oxide signal relative to atomic ion signals for wet plasma compared to dry plasma (4 V vs. 1 V for wet and dry plasma respectively). This demonstrates there is a fundamental difference in the formation of oxide species between the two modes of ICP-MS operation; likely related to source of oxygen between wet and dry plasma. There is a similar effect on the hydroxide polyatomic species between wet and dry plasma, however the formation of hydroxide species and oxide species is not linked for dry plasma, suggesting a different mechanism of formation. Absorbed atmospheric air and water vapour can have a significant negative affect on accuracy of elements such as ^{57}Fe in high Ca matrixes, and this has implications for how samples are stored prior to analysis.

Addition of diatomic gases (N_2 and H_2) are common in LA-ICP-MS to improve sensitivity, however, the effect of these gases on the properties of the ion beam and ion energy distribution has not been previously explored. This study shows that the addition of H_2 has a significant impact on the ion energy distribution of the ICP-MS while N_2 has no effect on ion energy distribution despite similar ionization energies for both gases. N_2 and to a lesser extent H_2 can change how a plasma will digest particles during LA-ICP-MS by cooling the plasma and allowing for incomplete digestion of particles. Incomplete particle digestion is potential sources of element fractionation in ICP-MS and an improved understanding of these process will allow for better method development and improved accuracy of results.

U-Pb geochronology in zircon and apatite by LA-ICP-MS is commonplace in the geological community. However, despite this, there are situations where the precision is better than accuracy, leading to inaccurate age dating. This study contributes to the understanding of causes of this U-Pb inaccuracy by analysing a range of zircon and apatite reference materials with independent age constraints.

Optimization of laser parameters can improve the U-Pb dating method by reducing the amount of element fractionation during aerosol generation. Small variations in nanosecond pulse width (5 vs. 15) are shown to have a negligible impact on the accuracy of the technique and suggests the causes of intra-lab discrepancies are unlikely due to differences in source laser. However, lower ($< 2 \text{ J/cm}^2$) laser fluence will result in shallower laser craters and reduced element fractionation leading to more accurate results compared to analyses performed at higher fluence.

Differences in atmospheric air in the laser cell or system is an additional, previously unknown, source of inaccuracy of zircon U-Pb analysis. Because of the lack of H_2O species in the plasma, trace amounts of water vapour, O_2 or N_2 gas can significantly change the properties of the ICP or local conditions at the ablation site. Using a set of controlled degassed and un-degassed samples, up to a 4% difference in age throughout the laser cell is correlated to the amount of atmospheric air present.

The zircon matrix effect during U-Pb dating by LA-ICP-MS has been previously shown to correlate to the radiation dose a zircon has received. This effect on measured U-Pb ages as a function of radiation damage is reduced by using a lower laser fluence ($\sim 1.5\%$ difference in age for high radiation dose zircon). Additionally, a correction to the measured zircon U-Pb age based on the radiation dose has been developed using analysis of a wide range of zircon reference materials with varying radiation doses.

The addition of new matrix-matched reference materials will allow for U-Pb quantification and reduce the mineral-specific fractionation offsets possible in geochronology. Two new apatite reference materials for U-Pb dating: 401 apatite and the OD306 apatite have been developed and made available to the geochronological community. These two apatite materials are close to

concordant (1% to 10% discordant) and have isotope dilution ages, neither of which is true for most of the current apatite U-Pb reference materials available.

Quasi-simultaneous detection offered by time-of-flight (TOF) technology is compared to traditional sequentially-based measurements done by quadrupole mass filters. Use of math-based measurements are inherently disadvantageous for transient signals from LA-ICP-MS as the more elements in an analytical method, the more detail will be missed or mis-represented due to spectral skew. However, few studies have utilized the TOF technology for LA-ICP-MS. This study is the first to demonstrate a direct comparison of U-Pb dating of zircon using a split-stream arrangement between a quadrupole and a TOF-ICP-MS. The results of these experiments show that similar accuracy and precision can be obtained for each type of ICP-MS, despite the significantly lower (>10x) sensitivity of the TOF instrument. This study shows the potential of the TOF technology for wider application by the LA-ICP-MS community.

Acknowledgments

I would like to first acknowledge my primary supervisor Professor Leonid Danyushevsky for convincing me to undertake this work and keep me on track to finish. I have learned much from Leonid; both about science as well as life. He is constantly pushing me to think about things in greater depth than I would otherwise, and this has greatly helped me become the scientist I am today. I also really have to thank Leonid for taking the risk in hiring me back in June of 2011 to come and work at the CODES labs. I would also like to acknowledge my secondary supervisor Sebastien Meffre. Sebastien has been a pleasure to work with and I have learned much from his geochronology experience. It has been great bouncing ideas off Sebastien and hearing his when it comes to formulating paper ideas and his positive energy and enthusiasm has been greatly appreciated.

I cannot say enough about how much my wife Jen has been a help to me in this PhD. endeavour. She has constantly been at my side encouraging me and helping me through writing of the papers and edits. Jen has also helped with editing and formatting of the thesis and papers. Jen's help to me and my thesis is no small contribution as she was also working on a PhD. as well; all while raising our two sons, Zach and Ethan. I feel incredibly lucky to have met her and am very grateful for everything she does.

While I spent the last 4 years working on my PhD., I was also employed at the CODES Analytical Laboratories and this experience has greatly contributed to my thesis. It has been an honour to work with Leonid and everyone at the CODES Analytical Laboratories; there are few, if any, laser labs in the world that are developing the LA-ICP-MS technique to the level CODES is and doing it all through self-funding!

I would also like to acknowledge my co-workers at the CODES Analytical Labs over the past 8 years: Sarah Gilbert, Ian Little, Elena Lounejeva, Paul Olin, Sebastien Meffre, Ivan Belousov, Sasha Stepanov, Irina Zhukova, James Tolley, Katie McGoldrick, Sean Johnson, and Claire Rutherford. In particular, I would like to thank Claire Rutherford for being such a great friend, co-worker and office mate. It has been wonderful gleaning parenting advice from Claire to help cope with writing a thesis, working full time (and then some ;) and trying to raise two young children.

I would also like to thank Karsten Goemann, Sandrin Feig, Thomas Rodemann and Ashley Townsend at the CSL for all the help and advice on analysis and science in general they have provided to me over the years.

It has also been an honour to work with all of the different students and researchers at CODES over the last 8 years. While there are so many people to mention, I would really like to thank Peter Cornish, Ron Berry, Tony Crawford, Dima Kamenetsky, for all that I have learned from each of you.

Table of Contents

| | |
|---|-------------|
| Declaration of originality | ii |
| Statement of authority of access | ii |
| Author details and their roles..... | iii |
| Paper 1 The effects of H ₂ O, He, N ₂ and H ₂ on ion kinetic energies in inductively-coupled plasma mass spectrometry. Spectrochimica Acta Part B: Atomic Spectroscopy (2020), 169, 105870. Located in Chapter 2..... | iii |
| Paper 2 Matrix effects in Pb/U measurements during LAICP-MS analysis of the mineral apatite. Journal of Analytical Atomic Spectrometry (2016), 31(6), 1206-1215. Located in Chapter 3 | iv |
| Paper 3 Impact of air, laser pulse width and fluence on U–Pb dating of zircons by LA- ICPMS. Journal of Analytical Atomic Spectrometry (2018), 33(2), 221-230. Located in Chapter 4..... | iv |
| Paper 4 Time-of-flight ICP-MS laser ablation zircon geochronology: assessment and comparison against quadrupole ICP-MS. Accepted to Journal of Analytical Atomic Spectrometry in July 2020. Located in Chapter 5 | iv |
| Abstract | vi |
| Acknowledgments..... | x |
| Table of Contents | xii |
| List of Figures | xv |
| List of Tables | xx |
| List of Equations..... | xxii |
| Chapter 1 Introduction | 1 |
| 1.1 Laser ablation..... | 1 |
| 1.1.1 Overview of instrumentation..... | 1 |
| 1.1.2 LA-ICP-MS and element fractionation | 4 |
| 1.1.3 Calibration of LA-ICP-MS..... | 7 |
| 1.2 ICP-MS | 12 |
| 1.2.1 Inductively-coupled plasma ion source | 12 |
| 1.2.2 Interface region..... | 17 |
| 1.2.3 Mass filter and mass separation | 19 |
| 1.3 LA-ICP-MS applied to geochronology..... | 21 |
| 1.4 Purpose of this work..... | 26 |
| Chapter 2 Effects of H₂O, He, N₂ and H₂ on ion kinetic energies in inductively-coupled plasma mass spectrometry | 28 |
| Abstract..... | 28 |
| 2.1 Introduction | 28 |
| 2.1.1 Background to ICP-MS and LA-ICP-MS..... | 28 |
| 2.2 Experimental | 29 |
| 2.3 Measurements | 32 |
| 2.3.1 Measurements made under non-optimal setting..... | 33 |

| | | |
|------------------|--|-----------|
| 2.3.2 | Apparent T_{gas} from ion KEs. | 34 |
| 2.3.3 | Polyatomic ions | 34 |
| 2.4 | Results | 37 |
| 2.4.1 | Ion energy (KE) | 37 |
| 2.4.2 | Impact of torch shield | 39 |
| 2.4.3 | Effect of diatomic gases in carrier flow | 39 |
| 2.4.4 | Polyatomic species | 40 |
| 2.4.4.1 | ThO^+ | 40 |
| 2.4.4.2 | CaOH^+ | 40 |
| 2.4.5 | Ion lens tuning | 41 |
| 2.5 | Discussion | 44 |
| 2.5.1 | Ion KE for $m/z < 23$ | 44 |
| 2.5.2 | Ion KE for $m/z > 23$ | 44 |
| 2.5.3 | Impact of H_2O in the plasma | 47 |
| 2.5.4 | Ion KE with diatomic gas addition in dry plasma | 48 |
| 2.5.5 | Polyatomic ion formation in wet vs. dry plasma: | 49 |
| 2.5.6 | Differences in Omega lens settings for optimal tuning conditions between wet and dry plasma on Agilent 7900: | 54 |
| 2.6 | Conclusions: | 56 |
| 2.7 | Acknowledgements | 57 |
| Chapter 3 | Effects in Pb/U measurements during LA-ICP-MS analysis of the mineral apatite..... | 58 |
| | Abstract..... | 58 |
| 3.1 | Introduction | 58 |
| 3.2 | Samples and methods..... | 60 |
| 3.2.1 | Laser ablation ICP-MS | 60 |
| 3.2.2 | Isotope dilution MC-ICP-MS..... | 62 |
| 3.2.3 | Laser pit geometries and apatite compositions..... | 63 |
| 3.3 | Results | 63 |
| 3.4 | Discussion | 65 |
| 3.4.1 | Comparison of bulk vs. in-situ Pb/U ages: | 65 |
| 3.4.2 | Effects of common Pb and excess ^{206}Pb from ^{230}Th : | 68 |
| 3.4.3 | Effects of element substitutions in apatite crystal structure: | 69 |
| 3.4.4 | ICP-induced ‘matrix effects’: | 70 |
| 3.4.5 | Laser-induced element fractionation (LIEF) | 71 |
| 3.4.6 | Otter Lake apatite as primary standard: | 74 |
| 3.5 | Conclusions | 75 |
| Chapter 4 | Impact of air, laser pulse width and fluence on U-Pb dating of zircons by LA-ICP-MS | 77 |
| | Abstract..... | 77 |
| 4.1 | Introduction | 77 |
| 4.2 | Experiment setup | 79 |

| | | |
|-------------------------|---|------------|
| 4.3 | Results | 82 |
| 4.3.1 | Impact of atmospheric air on U-Pb fractionation | 82 |
| 4.3.2 | Matrix effects of LA-ICP-MS U-Pb ages in zircon | 84 |
| 4.3.3 | Impact of laser fluence on U-Pb fractionation and U-Pb matrix effects..... | 86 |
| 4.3.4 | Impact of laser pulse width on U-Pb fractionation and U-Pb matrix effects..... | 87 |
| 4.3.5 | Impact of annealing experiments on LA-ICP-MS matrix effects | 87 |
| 4.4 | Discussion | 88 |
| 4.4.1 | Atmospheric air: effect on U-Pb fractionation..... | 88 |
| 4.4.2 | Matrix effects seen in zircon reference materials | 90 |
| 4.4.3 | Laser fluence impact on U-Pb fractionation | 92 |
| 4.4.4 | Laser pulse width impact on U-Pb fractionation | 92 |
| 4.4.5 | Annealing vs. non-annealed zircon ages | 93 |
| 4.4.6 | U-Pb age uncertainties..... | 93 |
| 4.5 | Conclusions | 95 |
| 4.6 | Acknowledgements | 96 |
| Chapter 5 | Time-of-flight ICP-MS laser ablation zircon geochronology: assessment and comparison against quadrupole ICP-MS | 97 |
| Abstract..... | | 97 |
| 5.1 | Introduction | 97 |
| 5.2 | Methods..... | 101 |
| 5.3 | Results: | 107 |
| 5.3.1 | Experiment 1 | 107 |
| 5.3.2 | Experiment 2 | 111 |
| 5.4 | Discussion | 118 |
| 5.4.1 | Uncertainty budget | 118 |
| 5.4.2 | Ablation signal smoothing..... | 120 |
| 5.4.3 | Detector counting times | 120 |
| 5.4.4 | U-Pb and Pb-Pb age accuracy and precision..... | 122 |
| 5.4.5 | Trace element compositions measured by LA-ICP-MS | 125 |
| 5.5 | Conclusions | 128 |
| 5.6 | Acknowledgements | 129 |
| Chapter 6 | Conclusions and outlook | 130 |
| 6.1 | Optimization of ICP-MS for laser ablation | 130 |
| 6.2 | Use of U-Pb geochronology as a tool for understanding LA-ICP-MS | 130 |
| 6.3 | Time-of-Flight ICP-MS for laser ablation analyses..... | 132 |
| 6.4 | Summary of conclusions | 133 |
| 6.5 | Future research directions | 133 |
| References | | 136 |
| Appendices | | 147 |
| A.1 | List of additional publications | 147 |
| A.1.1 | Co-authored publications..... | 147 |

| | | |
|------------|---|------------|
| A.1.2 | First-authored conference abstracts..... | 150 |
| A.2 | Electronic appendices for Chapter 2 | 151 |
| A.3 | Electronic appendices for Chapter 3 | 151 |
| A3.1 | EMPA results for individual apatite analyses and isotope dilution results on the OD306 and 401 apatite samples. | 151 |
| A3.2 | EMPA instrument conditions and setup used to acquire major element compositions and halogen contents of the apatite in Chapter 3. | 151 |
| A.4 | Electronic appendices for Chapter 4 | 151 |
| A.4.1 | LA-ICP-MS instrumentation metadata including all instrument parameters and settings. | 151 |
| A.4.2 | Individual zircon results for all analyses and tests done in Chapter 4. | 151 |
| A.5 | Electronic appendices for Chapter 5 | 151 |

List of Figures

Figure 1.1. Model of gas flows through a single-volume ‘barrel’ laser cell showing heterogeneous gas flows modified from Bleiner & Koch, 2008 [32]. Dashed black circle is a 1” round sample mount. Locations A, B and C show representative laser ablation analyses performed on the mineral zircon to the three corresponding graphs on the right. Graphs on the right of the laser cell figure show the ^{238}U signal normalized to the maximum for chips of the same zircon sample mounted in different locations within the 1” round. In graph A the signal in the central gas channel has a relatively quick washout time, however those analyses done off the central gas channel (B and C) show a significantly longer washout and C shows significant residual aerosol from the previous analysis. 4

Figure 1.2. Figure showing particle / aerosol formation immediately after the laser pulse for an idealized sample and no gas flowing over sample. Time scales of particle / aerosol formation after Ullmann, Friedlander and Schmidt-Ott [43]. 5

Figure 1.3. Example of the concept of differences in yield due to differences in material properties between the enamel and dentine in a tooth sample. Figure reproduced from Alan Koenig (USGS) [60]. 9

Figure 1.4. A depiction of the plasma torch used to maintain the argon-based ICP. 13

Figure 1.5. Distribution of ion intensities from laser ablation mapped out in the ICP under various central channel gas flows and addition of H_2O vapour addition modified from Hu et al. [79]. Note the change in both the location (further downstream) and the length of the highest signal intensity (red) with the addition of H_2O vapour to the ICP-MS. Note the smaller offset between the peak intensity for $^{90}\text{Zr}^+$ (refractory) and $^{85}\text{Rb}^+$ (volatile) with the addition of H_2O vapour compared to dry plasma. Signal intensities in counts per second. 17

Figure 1.6. Diagram of ion sheath around sample cone and calculations for sheath thickness modified after Sakata et al., 2000 [85]. 19

Figure 1.7. Example of curve fit to primary zircon standard for $^{206}\text{Pb}/^{238}\text{U}$ used in this work. ... 25

Figure 2.1. A) Examples of stopping curves for wet plasma using the Agilent 7900 as an increasing stopping potential (QP bias) is applied. Signal normalized to QP bias at -4V. B) Expanded view of the lower region of the stopping curve for ^9Be where the signal crosses through the 1% value of the normalized signal. Equation from exponential fit line is used to calculate model voltage of QP bias at this 1% signal value and this voltage is utilized as the maximum ion KE value. 36

Figure 2.2. Measurements made on an Agilent 7900 by applying a stopping potential using the QP bias and using the voltage at 1% of normalized signal as shown in Figure 2.1. A: Ion KE distribution vs. ion mass for wet plasma with and without the shield present. B: Ion KE distribution vs. ion mass for dry plasma with and without the shield present. C and D: Corresponding ion yields for conditions in A and B respectively where wet plasma yield is in counts per second (cps) per ppb and in dry plasma are in cps per ppm. Wet plasma measurements performed in a 10 ppb solution while dry plasma measurements were performed using a line scan on the NIST612 glass..... 37

Figure 2.3. Plot of ion KE vs. ion mass for normal analytical conditions under wet and dry plasma for Agilent 7900 (3A) and Thermo X series 2 (3B). On the Agilent 7900, ions lighter than m/z 23 show different behaviour compared to ions greater than m/z 23, whereas this behaviour is not seen on the Thermo X series 2. Both ICP-MS instruments show a shallower slope for dry plasma conditions compared to wet plasma and for all tests the polyatomic $^{248}\text{ThO}^+$ has lower KE than adjacent ^{238}U 42

Figure 2.4. Ion KE measurements for U^+ at various conditions for dry plasma on Agilent 7700. A) Ablation performed in the atmosphere of pure He flowing at 350 ml/min. Changes in interface pressure (by changing sample position or Ar central channel gas flow rate) have a significant effect on ion KE for U^+ . Numbers next to symbols represent Ar flow rates in l/min. B) Ablation performed in the atmosphere of pure Ar, with He added to the carrier gas through a “T” junction after the aerosol exited the sample cell. Increasing the rate of He (blue circles) while keeping argon flow constant decreases ion KE, whereas increasing the He to Ar ratio (orange triangles) while maintaining a constant total flow rate, significantly increases ion KE. 43

Figure 2.5. Relationship between QP bias and U/Th ratio and ThO/Th ratio for wet and dry plasma on the Agilent 7900. U/Th ratio is from the NIST612 glass (dry plasma) and a 10 ppb solution (wet plasma), both of which have U/Th ratios nominally 1. ThO/Th is normalized to the ratio at a QP bias setting of -4V. Increasing QP bias decreases signal intensities for all masses, however masses corresponding to metal ions (e.g. U & Th) drop similarly such that the ratio does not change appreciably. Masses corresponding to oxide interference (ThO) drop preferentially relative to the metal ion species (^{232}Th) of similar mass..... 52

Figure 2.6. A) Relationship of changing QP bias vs. $^{43}/^{57}$ ratio (left axis) for wet and dry plasma on the Agilent 7900. ^{57}Fe quantified in BCR-2g using NIST612 (right axis) and in a prepared solution with similar Ca/Fe as BCR (‘BCR’ like solution) becomes more accurate as the $^{40}\text{Ca}^{16}\text{O}^1\text{H}$ interference is preferentially removed relative to the metal ion ^{57}Fe . Solid star indicates BCR-2g GeoReM preferred value for Fe (96,385 ppm) while trace star indicates Fe value from the

gravimetrically prepared solution (in ppb). B) Relationship of QP bias on mass 57 comparing wet and dry plasma conditions for two different Ca/Fe matrixes using the Agilent 7900. Note the steeper drop off with increasing QP bias voltage for the high Ca/Fe matrixes. 53

Figure 2.7. ^7Li and ^{238}U normalized signals plotted against varying Omega lens voltages for both dry and wet plasma on the Agilent 7900. Note the difference in signal maximums between wet and dry plasma..... 55

Figure 2.8. Plot of U^+/Th^+ vs $\text{ThO}^+/\text{Th}^+\%$ and $43^+/57^+$ production while ablating NIST612 in dry plasma conditions for the Agilent 7900. Changes in U^+/Th^+ are due to changing plasma conditions: presence /lack of shield on the torch, N_2 addition, H_2 addition, etc. Correlation of ThO^+/Th^+ with U^+/Th^+ present while none seen for 43/57 data. 55

Figure 3.1. Photographs of select apatite samples used in this study. 62

Figure 3.2. Optical profiler image of spots analysed in a grain of the McClure Mountain apatite. 63

Figure 3.3. Tera-Wasserburg concordia plots for the apatite samples analysed in this study. LA-ICP-MS analyses from this study are grey crosses. Two LA-ICP-MS ages reported are for data anchored to common Pb (using S-K Pb model curve [151]) or an un-anchored regression through the data. The preferred LA-ICP-MS age is in black while the other is grey. Where available, bulk digestion isotope dilution ages are plotted in red. All concordia intercept errors are given at 2-sigma level – see Table 3.2. 67

Figure 3.4. Select apatite REE patterns measured by LA-ICP-MS. Note the similar REE concentrations and patterns for Otter Lake and OD306 despite age discrepancies in LA-ICP-MS data. 68

Figure 3.5. Some minor and trace element compositions of the apatite samples studied. F is measured by EMPA while Ce, Th and U are measured by LA-ICP-MS. Radiation dose is given as decay events per milligram and is a function of U and Th contents and the age of the sample. Error bars for ages are at 2-sigma. 72

Figure 3.6. Normalized $^{206}\text{Pb}/^{238}\text{U}$ fractionation for apatite, zircon and NIST610 glass by stacking together >10 individual analyses from a single session. Data for each mineral / glass normalized to true $^{206}\text{Pb}/^{238}\text{U}$ value. Otter Lake apatite has been corrected for common Pb by applying a ^{207}Pb correction to the ^{206}Pb data – see Methods section for more details. 73

Figure 3.7. Backscatter electron image (BSE) of ablation crater in Durango apatite. Ejecta around crater is slightly brighter than surrounding apatite. Compositions from EDS spectrum indicate higher Ca (~20%) and lower P ~(30%) in brighter ejecta droplets. 74

Figure 4.1. (A) Photo of the S-155 large-format ablation cell. This is a two-volume cell with ablation occurring in a small, fixed funnel in the centre and a movable sample block. (B) Photo of the sample holder insert showing twenty samples of various zircon and glass RMs. 83

Figure 4.2. Atmospheric air in laser cell affecting measured U-Pb age. (A) Variable degassing in laser cell with poorly flushed conditions (residual atmospheric air). (B) Effect of variable mass 56

in the gas blank on measured U-Pb age introducing up to a 3% error in age. (C) Same as (B) but with samples kept under vacuum >48 hours. (D) Absence of variation in mass 56 produces more accurate U-Pb ages, 0.5% (2-sigma) on weighted average of all analyses in laser cell. 84

Figure 4.3. Plot of accuracy vs. radiation dose in alpha decays per gram for zircon reference materials used in this study. Uncertainty bars for age are 2-Sigma and include random sources of uncertainty from the LA-ICP-MS analyses as well as the uncertainty on published ID-TIMS ages. Vertical solid black lines represent $\pm 1\%$ of the ID-TIMS age. 85

Figure 4.4. Plot of LA-ICP-MS zircon U-Pb age accuracy compared to ablation crater depth, normalized to primary RM (91500 zircon) for multiple laser systems at the University of Tasmania. Uncertainty bars for age are 2-Sigma and include random sources of uncertainty from the LA-ICP-MS analyses as well as the error of ID-TIMS analysis. Uncertainty bars for crater depths are 1 standard deviation on the average depth (relative to 91500) for a zircon RM. Vertical solid black lines represent $\pm 1\%$ of the ID-TIMS age. 85

Figure 4.5. (A) Age of the zircon RMs measured against 91500 zircon at various laser fluences. Uncertainty bars for age are 2-sigma and include random sources of error (counting statistics) from the LA-ICP-MS analyses as well as the uncertainty on the ID-TIMS analysis. Colour coding same as in (B). (B) Impact of laser fluence on the U-Pb downhole fractionation trend. 86

Figure 4.6. U-Pb age results from annealing experiments. Uncertainty bars for age are 2-sigma and include random sources of uncertainty from the LA-ICP-MS analyses as well as the uncertainty on the ID-TIMS analysis. Symbols are colour coded to the radiation dose. Squares and triangles are for annealed and non-annealed zircons respectively. 88

Figure 4.7. Apparent radiation dose calculated using the known U and Th concentrations in zircon RMs vs. LA-ICP-MS age / ID-TIMS age. Black line is a log function which fits the data set with a R^2 value of ~ 0.86 . The equation presented would be used to calculate the zircon matrix effect correction factor based (and addition of associated uncertainty in the correction) on the apparent radiation dose of the unknown zircons. Error bars are 2-sigma. Penglai zircon excluded from calculation, but r^2 is ~ 0.84 if it is included in the correction. 95

Figure 5.1. Image of the Resolution S155 laser ablation system in split stream configuration with the Agilent 7900 on the right and TOFWERK “icpTOF R” on the left. The dashed red line outlines the tubing from the Y connector that goes into the Agilent 7900, while the dashed blue line outlines the tubing going to the TOFWERK “icpTOF R”. 101

Figure 5.2. Upper figure: TOF mass spectrum of total ion counts from one zircon analysis (91500 zircon). Isotope peaks are highly resolved despite the tailing effects from high intensity peaks. Lower figure is zoomed into isotopes of Zr showing how the baseline subtraction is done and the effects of high intensity Zr peaks on the detection of Nb in zircon. 107

Figure 5.3. Age plots for select zircon reference materials used in Experiment 1 (split stream analysis). Green circles represent individual analyses with 2-sigma error bars (Within-Run uncertainty). Yellow star indicates published age on reference material. Black line is the 1:1 line

between the TOFMS and the QMS. Individual ages are $^{206}\text{Pb}/^{238}\text{U}$ except for the OG-1 zircon which are $^{207}\text{Pb}/^{206}\text{Pb}$ ages. Note shift from 1:1 for Plesovice and Qing Hu – see text. 111

Figure 5.4. Average of 32 analyses for select trace elements measured in the 91500 zircon from Experiment 1 (split stream analyses) normalized to the GeoReM preferred values. Red bars: QMS results; blue bars: TOFMS results. A value of 1 represents the GeoReM preferred value. Black circle represents average of 32 analyses while the length of bars is the 1-sigma uncertainty and was propagated from the standard error of the average as well as the uncertainty from the GeoReM preferred values for the 91500 zircon. 111

Figure 5.5. Plot of U detector counts and the $^{238}\text{U}/^{235}\text{U}$ ratio. Natural $^{238}\text{U}/^{235}\text{U}$ ratio of 137.818 is represented by the grey dashed line. Figure A) shows results for Experiment 1 (split stream analysis) while Figure B) shows results from individual sessions (Experiment 2). $^{238}\text{U}/^{235}\text{U}$ values on graph represent the weighted average for each ICP-MS using the “Within-Run” uncertainty for the calculation in Isoplot. Error bars on graph are 1-sigma “Signal Precision” uncertainty shown on individual analyses for clarity. The expanded views on the right of A) and B) highlight the slight dependency of the U isotope ratio for the TOFMS data at higher detector counts. . 115

Figure 5.6. Age plots for select zircon reference materials used in Experiment 2, where analyses were performed under routine conditions and multiple sessions for each ICP-MS type. Green circles represent individual analyses with 2-sigma error bars (Within-Run uncertainty). Yellow star indicates published age on reference material. Black line is the 1:1 line between the TOFMS and the QMS. Individual ages are $^{206}\text{Pb}/^{238}\text{U}$ except for the OG-1 zircon which are $^{207}\text{Pb}/^{206}\text{Pb}$ ages. Since individual analyses were done on different days, there is no relationship in the data points between the TOFMS and QMS and as such analyses are simply plotted in order of analysis on the session day. 118

Figure 5.7. Relationship between detector counts and signal RSD for the TOF and quadrupole mass spectrometers in Experiment 1 (split-stream analysis). Data points are element to ^{238}U ratios for analysis 069 from the AusZ-2 zircon in Experiment 1. Black line represents the theoretical RSD based solely on counting statistics and ratio to ^{238}U at 2800 detector counts (the average of detector counts for the QMS and the TOFMS for this analysis. 127

Figure 5.8. Signal from ablation of Mud Tank zircon at analytical conditions used for Experiment 2 (normal analytical conditions) for ^{91}Zr using the QMS at various dwell times. A shows the raw Zr signal as the ablation drills into the zircon, causing the signal to drop in intensity. B shows the same signal that has been corrected for this signal drop off phenomenon and the RSD (1s) of the mean calculated on for the corrected signal for each dwell time with longer dwell times giving less signal variation and correspondingly lower RSD. Figure 5.8C shows the 1 standard deviation for the signal (solid bars) and for the theoretical standard deviation based on counting statistics for the number of detector counts (bars with cross pattern). Note the significantly higher standard deviations for the measured signal compared to the theoretical. 128

List of Tables

Table 2.1. Instrument settings for wet and dry plasma conditions for both ICP-MS instruments tested. 32

Table 2.2. Ion KE for $^{238}\text{U}^+$ under a variety of conditions measured on Agilent 7900. Note: sampling position for dry plasma was fixed at 4mm while for solution was fixed at 10mm. Tgas not reported for wet plasma without the shield due to unreliability of ion KE. *Solution analyses in cps/ppb. The lower intercept value in volts is the intersection of the line through masses ^{23}Na to ^{238}U at mass 0. Intercept value for wet plasma without the shield calculated using masses ^{23}Na to ^{238}U . Values in () for Tgas are the 95% confidence uncertainties in K. 39

Table 2.3. Ion KE for U^+ under a variety of conditions measured on Thermo X series 2. Note: sampling positions for both wet and dry plasma were fixed at a “Depth” value of 150. *Solution analyses in cps/ppb. The lower intercept value in volts is the intersection of the line through masses ^{25}Mg to ^{238}U at mass 0. Values in () for Tgas are the 95% confidence uncertainties in K. 39

Table 3.1. Instrument parameters used over a 3.5 year period 61

Table 3.2. Apatite results for Pb/U ages and select elemental compositions determined by LA-ICP-MS (Ce, Th & U) and EMPA (F, Cl). Isotope dilution ages for OD306, Kovdor, 401 apatite, and McClure Mountain were measured directly on apatite in the rock. Emerald Lake, Plesovice, and Temora are isotope dilution ages of zircon present in the same rock. The Otter Lake apatite age is from a step-leaching Pb isotopic MC-ICP-MS age – see Barfod et al.[135] for details. The Durango age is from ^{40}Ar - ^{39}Ar measurement on apatite from McDowell et al.[139] Numbers in parentheses are one standard deviation on the mean. *n.d. = not determined. All ages are reported at 2-sigma with the laser errors reported after the \pm symbol and are as follows: counting statistic errors / counting statistic errors + long term variance in secondary standards + error in common Pb composition / full analytical errors including counting statistics and all systematic errors..... 65

Table 4.1. LA-ICP-MS results on non-annealed zircon for both laser systems tested using a laser fluence of 2.0 J/cm². LA-ICP-MS uncertainties are 2-sigma: random + systematic uncertainties. *91500 zircon was primary standard for U-Pb ratios (self-normalized). All LA-ICP-MS ages are weighted averages from Isoplot using the $^{206}\text{Pb}/^{238}\text{U}$ age except the Monastery, Mud Tank, Penglai, SP07-05, and Qing Hu zircons which are concordia intercept ages anchoring on the Stacey & Kramer’s model common Pb at the age of the zircon. GJ-1 and Mud Tank ID-TIMS ages are from [161]. Radiation dose is calculated using ^{232}Th , ^{238}U , assumed ^{235}U ($^{238}\text{U}/^{235}\text{U} = 138.818$) and the ID-TIMS age of zircon. Ablation crater depths are as follows: 20 ns pulse width laser / 5 ns pulse width laser. NA = not available. 82

Table 4.2. LA-ICP-MS results on annealed zircon and non-annealed zircon, each calibrated on 91500 annealed and un-annealed grains respectively. Tests conducted on the 20 ns pulse width laser system. Uncertainties and radiation dose calculations are the same as in Table 4.1. LA-ICP-MS ages for 91500, OG-1, Plesovice and Temora are weighted averages from Isoplot using the

$^{206}\text{Pb}/^{238}\text{U}$ system and Mud Tank, TASDOL, and Qing Hu zircons are concordia intercept ages anchoring on the Stacey & Kramer's model common Pb at the age of the zircon. TASDOL age from Ivanov et al.[173] 87

Table 5.1. Weighted average results (using Isoplot) for Experiment 1, split stream analysis. All ages are weighted averages of $^{206}\text{Pb}/^{238}\text{U}$ except for the OG-1 and 91500 zircon, for which the $^{207}\text{Pb}/^{206}\text{Pb}$ age is reported. A common Pb correction is applied to analyses that were discordant with the $^{207}\text{Pb}/^{206}\text{Pb}$ age greater than the $^{206}\text{Pb}/^{238}\text{U}$ age. Uncertainties are 2s in Ma, except the “Within-Run” uncertainty column which also has the percentage error in brackets. “Measured / Accepted” column is the weighted average of the U-Pb age measured by LA-ICP-MS divided by the published age so that a perfectly accurate analysis has a value of 1. The 2s uncertainty on the “Measured / Accepted” ratio is the uncertainty of the LA-ICP-MS age / published age from the propagation of the uncertainties from the LA-ICP-MS analysis and from those from the published age. Underlined “Measured / Accepted” values are those which are outside the 2-sigma uncertainties of the published ages. 113

Table 5.2. Weighted average results (using Isoplot) for Experiment 2 where analyses were done over several individual analytical sessions. All ages are weighted averages of $^{206}\text{Pb}/^{238}\text{U}$ except for the OG-1 and 91500 zircon, for which the $^{207}\text{Pb}/^{206}\text{Pb}$ age is reported. Uncertainties are 2s in Ma, except the “within-run” uncertainty column which also has the percentage error in brackets. A common Pb correction is applied to analyses that were discordant with the $^{207}\text{Pb}/^{206}\text{Pb}$ age greater than the $^{206}\text{Pb}/^{238}\text{U}$ age. Measured / Accepted column is the weighted average of the U-Pb age measured by LA-ICP-MS divided by the published age so that a perfectly accurate analysis has a value of 1. The 2s uncertainty on the “Measured / Accepted” ratio is the uncertainty of the LA-ICP-MS age / published age from the propagation of the uncertainties from the LA-ICP-MS analysis and from those from the published age. Underlined “Measured / Accepted” values are those which are outside the 2-sigma uncertainties of the published ages..... 114

List of Equations

| | |
|---|-----|
| Equation 1.1. The Longerich et al.[58] equation for quantification of LA-ICP-MS results using a fixed internal standard element. The equation is solved for element of interest “PPM _{samp} ”. | 10 |
| Equation 1.2. Modified Saha equation reproduced from Hongsen & Houk [70] and based on Hayhurst et al. [71]. K_{ion} is the ionization constant for element “M”, E_{I_M} is the first ionisation energy for element M, Z is the partition function for M^+ or neutral M and T_{ion} is the ionisation temperature for element M. | 14 |
| Equation 2.1. Calculation of average ion kinetic energy where m = mass of ion, m_{Ar} = mass of Ar, k_B = Boltzmann constant, and V_p = plasma potential. | 34 |
| Equation 2.2. Calculation of maximum ion KE. Terms the same as in Equation 2.1. | 34 |
| Equation 5.1. LOD equation from Longerich et al. [58] where LOD is Limit of Detection, σ_{ind} is the standard deviation of the gas blank S is the Sensitivity calculated from the internal standard element sensitivity in the sample relative to the standards, n_b is the number of data points in the background and n_a is the number of data points for the ablation. See Longerich et al. [58] for more details. | 108 |

Chapter 1 Introduction

1.1 Laser ablation

Laser ablation inductively-coupled plasma mass spectrometry (LA-ICP-MS) is an in-situ analytical technique that involves a pulsed laser firing at a solid sample, creating an aerosol as a result of the ablation process, that is then sent into an ICP-MS for ionization and ion detection. The first publication that utilized laser ablation coupled to an ICP-MS was Gray, 1985 [1] who demonstrated the ability to sample solid geological materials, even though at the 1 mm scale, and achieved ng limits of detection. Prior to this, laser ablation was primarily performed on solid samples using resonance ionization spectrometry [2] or direct analysis of ablated material with time-of-flight mass spectrometry [3]. The LA-ICP-MS technique can measure elemental and isotopic compositions of samples with detection levels that can be sub-ppb (parts per billion) with minimal sample destruction (compared to bulk analytical methods). LA-ICP-MS also offers relatively rapid analysis with minimal sample preparation compared to other in-situ techniques such as electron microprobe or secondary ion mass spectrometry (SIMS), both of which require conductive coatings and well-polished surfaces. These features have allowed the LA-ICP-MS technique to be widely employed in the geoscience community for mineral chemistry [4-6], glass compositions of volcanic tephra [7], imaging of chemical zoning in minerals [8-10] and U-Pb dating of accessory phases [11-17]. This work will focus primarily on the geological application of LA-ICP-MS; however, the technique is widely used in biological and the medical sciences as well [18, 19].

1.1.1 Overview of instrumentation

Laser ablation involves photons, derived from a laser source (e.g. solid-state Nd-YAG crystal), that are focussed on to and remove or 'ablate' material from a sample surface. This laser source sends a pulsed beam through a set of mirrors, apertures and lenses to focus the laser beam on to a solid target. A microscope system is employed to visualize the location of the laser beam on the target sample as well as for alignment of the focal position of the laser beam. Typically, the laser beam is on the order of 0.5 cm or larger out of the laser source but is masked and focussed anywhere from ~3 microns up to >250 microns in size. Typically, circular laser spots are used, but other patterns such as square or rectangle have been utilized in specific applications [20].

There have been several types of laser sources used in LA-ICP-MS and past studies have shown the benefits to using shorter wavelengths [21, 22] and shorter pulse widths [23-25]. Most commercially available laser ablation systems have either a solid-state source that is typically a Nd-YAG crystal optically pumped with a flash lamp or use a gas excimer source where a high voltage is applied to a gas mixture to form coherent laser photons. The Nd-YAG source is relatively simple and does not require refreshing of a gas or high voltages, however the fundamental wavelength for the Nd-YAG source is 1064 nm and most solid materials are transparent to this wavelength [26]. So, by using beam splitting crystals, harmonics of this fundamental wavelength can be used [22] where the 4th (266 nm) and 5th (213 nm) are the most commonly used for geological materials. For excimer laser systems, a mixture of halogen (F or Cl) is mixed with noble gases (Ar, Kr, or Xe) to form a laser pulse with a specific wavelength. The ArF gas combination is by far the most common due to the shorter wavelength (193 nm), however some work has been done with KrF [27] operating at 248 nm. In both the excimer and Nd-YAG sources described so far, the pulse width of each laser pulse is generally between 5 ns and 25 ns. Shorter wavelengths have been shown to produce more representative sampling in metals [24, 28, 29] and the use of Ti-Sapphire femtosecond pulse width lasers have been utilized in many studies [28, 29, 30].

The interaction of the laser pulse with the sample is critical to obtain a representative sampling of the target material. How well a laser pulse interacts with a sample is dependent upon many variables including the degree a sample absorbs the wavelength of light [22], the pulse width of the source [22], the aspect ratio of the laser crater rim to the diameter [27], the depth of the ablation crater [26] and the gaseous medium in which the ablation takes place [31].

A critically important aspect of any laser ablation system is the vessel in which the ablation occurs, called the laser ablation cell. Requirements for the laser cell are that it be a sealed vessel, have a transparent window to allow viewing of the sample and entry of the laser pulse for ablation, and have homogenous gas flows to ensure similar uptake of sample throughout the laser cell such that there are no biases in the composition of the aerosol based on the location within the cell. Early designs of the laser cell featured a single-volume [32] where a jet or jets of inert gas (usually Ar or He) flowed over the sample surface and to an exit port on the other side (Fig 1.1). While these initial designs were suitable for the early

work done with laser ablation, it was quickly realized that the gas flows in such laser cells were not homogenous and produced heterogenous analytical results for reference materials [33] as well as poor sample washout from previous analyses (Fig. 1.1). This led to other laser cell designs such as the Jet Cell [34], and various small-volume cells to improve the sample washout [35-37]. However, it was the development of a two-volume laser cell which obtained a 'constant geometry' of gas flows in the laser cell, that was able to deliver a homogenous signal response across the laser cell [38]. Most commercially available laser ablation systems now contain some variant of the two-volume ablation cell where the samples are housed in the larger volume of the cell, while the ablation occurs within a smaller volume typically less than 1% of the larger cell volume. Sample movement is performed by either moving the small volume 'funnel' to desired locations within the cell, or by fixing the small funnel and moving the samples within the larger volume relative to the funnel.

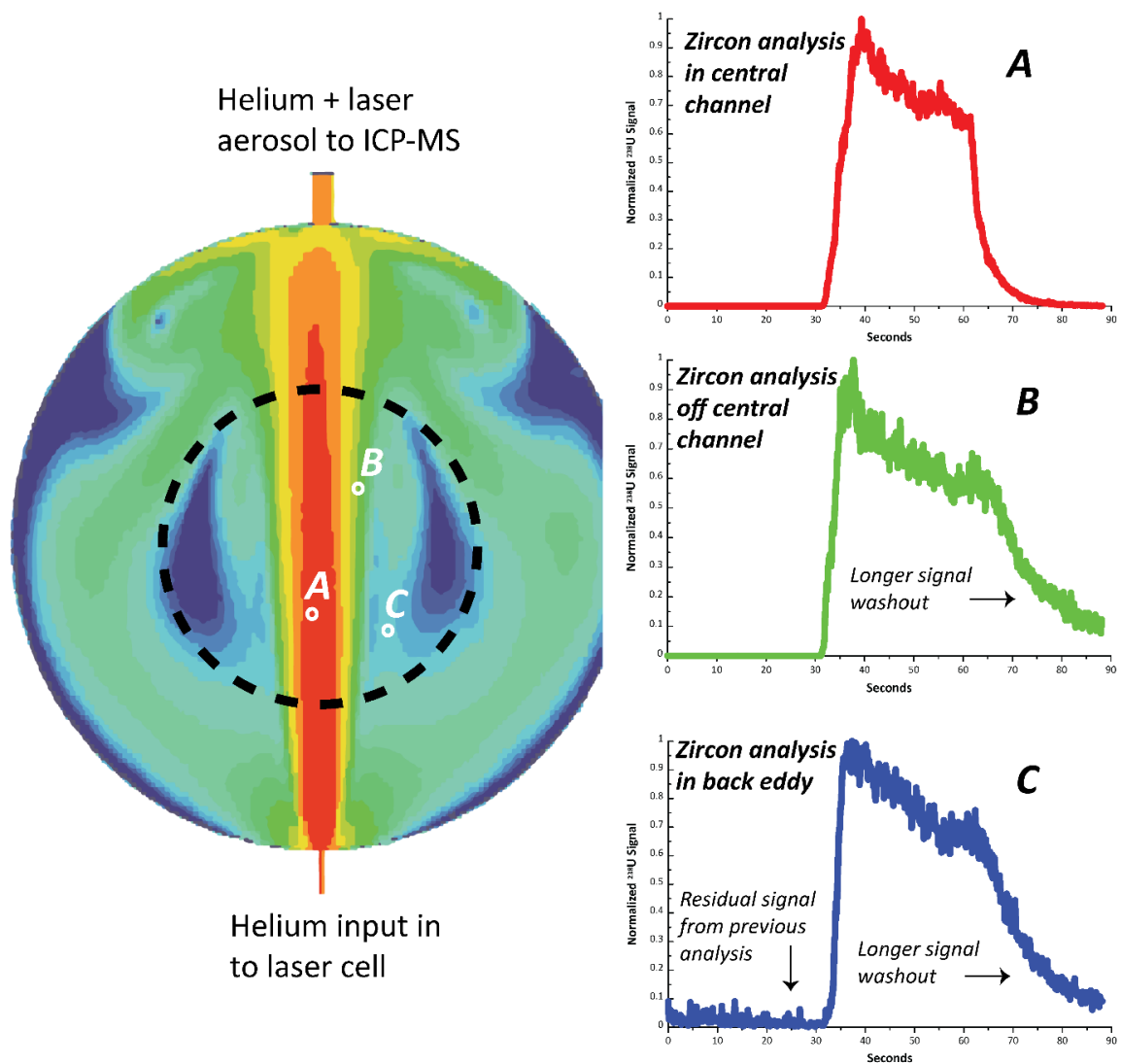


Figure 1.1. Model of gas flows through a single-volume 'barrel' laser cell showing heterogeneous gas flows modified from Bleiner & Koch, 2008 [32]. Dashed black circle is a 1" round sample mount. Locations A, B and C show representative laser ablation analyses performed on the mineral zircon to the three corresponding graphs on the right. Graphs on the right of the laser cell figure show the ^{238}U signal normalized to the maximum for chips of the same zircon sample mounted in different locations within the 1" round. In graph A the signal in the central gas channel has a relatively quick washout time, however those analyses done off the central gas channel (B and C) show a significantly longer washout and C shows significant residual aerosol from the previous analysis.

1.1.2 LA-ICP-MS and element fractionation

A laser pulse will interact with the sample surface and the transfer of the photon energy to the sample will produce a high temperature ($>10,000\text{ K}$ [39]) laser-induced plasma that is on the order of nanoseconds in duration. Since the duration of the plasma produced by the nanosecond laser pulse is relatively similar in comparison to the duration of the laser pulse itself, a phenomenon of plasma shielding [24, 40] occurs in nanosecond pulsed lasers where the laser induced plasma may interact with part of the incoming laser pulse and change how

this pulse interacts with the sample. Figure 1.2 shows a diagram of processes occurring after the absorption of the laser pulse by the solid sample. The laser-induced plasma is relatively short-lived in the time scale of this figure and is not shown to scale. Analysis of the laser-induced plasma is another field of analytical chemistry called Laser-Induced Breakdown Spectroscopy (LIBS). Details of this technique are beyond the scope of this work, but the reader is referred to reviews by Hahn & Omenetto [41, 42].

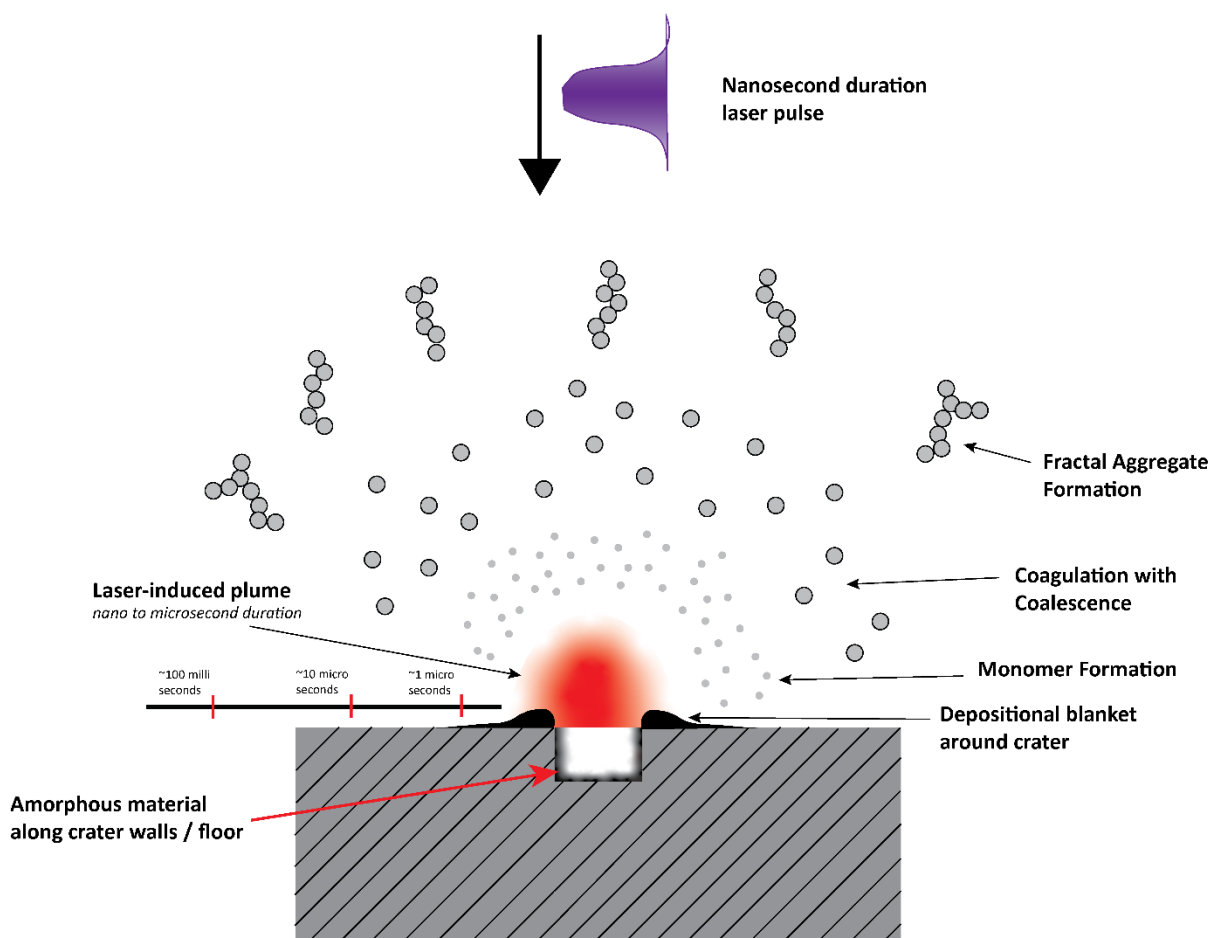


Figure 1.2. Figure showing particle / aerosol formation immediately after the laser pulse for an idealized sample and no gas flowing over sample. Time scales of particle / aerosol formation after Ullmann, Friedlander and Schmidt-Ott [43].

Upon cooling from the laser induced plasma, atoms will coalesce and form aggregates that can have a different composition from the original 'bulk' un-ablated material (i.e. elements can fractionate from each other [44, 45]). If these aggregates are unable to be completely transported to or digested within the ICP, a non-representative sampling of material will occur and cause a phenomenon called elemental fractionation. There are two

potential sources of element fractionation in LA-ICP-MS: at the ablation site and in the inductively-coupled plasma (ICP). Early work on the element fractionation problem showed a correlation between the length of the ablation time (i.e. depth of the ablation crater) and the degree of element fractionation [26]. Later work by Mank and Mason [27] showed that the amount of element fractionation on their system was significantly less if the aspect ratio (ratio of diameter to the depth) of the ablation crater was less than six. These studies suggested the primary location of element fractionation to be at the ablation crater, either in the crater walls or in the condensate blanket around the crater. Element fractionation at the ablation site was also observed in the mineral zircon when performing U-Pb analyses where Kosler et al.[46] showed decomposition of ZrSiO_4 to ZrO_2 at the ablation site. Using a SIMS to sample the ejecta blanket, enrichments in Th and U were seen relative to Pb for both zircon and the NIST61X series reference glasses commonly used in LA-ICP-MS as calibration materials [47]. This was later confirmed with a study by Kosler et al.[48] where the addition of O_2 gas at the ablation site helped facilitate the formation of ZrO_2 and increased the degree of element fractionation. Also, Hirata [49] showed use of trace additions of Freon gas at the ablation site substantially lowered the amount of element fractionation during U-Pb dating of zircon due to conversion of U to UF_6 , which is significantly more volatile than UO_x . If the element fractionation process occurs primarily at the ablation site, analysis of the fractionated aerosol / particles by ICP-MS will be biased. The phenomenon of element fractionation has been a source of inaccuracy in LA-ICP-MS [26] and is still a significant issue with nanosecond-based laser ablation systems and even femtosecond laser systems [24, 30].

The other potential source of element fractionation is in the ICP due to the incomplete breakdown of aerosol or particles delivered from the ablation site. This has been demonstrated by Guillong & Günther [44] where the authors used a filter to collect particulates from the ablation aerosol and a particle filter to preferentially remove larger particles during the ablation of the NIST610 reference glass [47]. By changing the size of the particles delivered to the ICP, the authors were able to significantly reduce (but not entirely eliminate) the observed element fractionation. The implications of this study [44] were two-fold: 1) the ICP is a potentially important source of element fractionation for the LA-ICP-MS technique by incomplete particle digestion, and 2) the larger particles that were filtered out and prevented from entering the ICP were not biased in composition relative to finer particles

such that the former's removal did not cause any element fractionation. Several subsequent studies have also demonstrated element fractionation due to incomplete particle digestion in the ICP [50, 51].

It is likely that both sources of element fractionation can affect the results of LA-ICP-MS and it is likely sample specific [44] as to which one of these will dominate. An important aspect of element fractionation is a material dependency on the presence and magnitude of fractionation. In particular, when reference materials used for calibration do not match the matrix of the target unknown it is likely there will be inaccuracies from the difference in element fractionation between the two materials. Several techniques have been employed to reduce the magnitude of element fractionation, including: shorter laser wavelengths [22], shorter laser pulse widths [24], ablation in helium rather than argon [31], minimizing the depth of ablated craters [27], decreasing the presence of oxygen impurities in the laser cell [48], increasing the sample residence time in the ICP to ensure particle digestion [52] (at the expense of instrument sensitivity) and addition of H₂O vapour to the ICP [53, 54] to change the properties of the ICP.

The application of femtosecond (fs) lasers in LA-ICP-MS has potential to solve many of the above problems that are ultimately related to nanosecond-pulsed ablation interaction with the laser-induced plasma and sample heating. However, while there can be a significant reduction in element fractionation, matrix-related ablation issues with silicates and some time-dependent element fractionation still occur in femtosecond laser ablation for static spot analyses [55, 56]. The use of femtosecond laser ablation in metals for isotopic analysis has been shown to have significant advantages over nanosecond laser ablation where there are: better yields, smaller particle sizes, less isotopic fractionation, and matrix independence for most materials [24, 30].

1.1.3 Calibration of LA-ICP-MS

One consequence of element fractionation is that quantification of results is more complex compared to traditional solution ICP-MS analysis. The detector response is linear in modern ICP-MS instruments, and the quantification of solution ICP-MS results involve using a calibration solution (solutions of known concentration) to quantify unknown sample solution compositions. A calibration factor or slope and intercept of the calibration line is calculated to quantify the signal intensity of the unknown based on the signal intensity per

unit concentration of the calibration. This works well if the matrix of the standards and unknowns are similar and there is negligible drift, a change in the ICP-MS signal response with time. Unfortunately, neither of these conditions are true in a practical sense and so the addition of several internal standard elements to unknown and standard solutions are used to correct for differences in matrix that affect ion yield, changes in instrument sensitivity, and mass bias with time. It is relatively easy to add internal standard elements to samples in solution and customize which elements to use based on their first ionization potentials and mass. In this case, solution ICP-MS analysis is a relatively mature technique and where many certified methods exist (e.g. USP<233>). Total analytical uncertainties for solution-based ICP-MS are typically on the order of 2% - 5% for most elements. Limitations on accuracy of quantification are from standards measured at different times than the unknowns, and internal standard elements, which do not behave identically to the target elements. Some problems can be overcome by isotope dilution wherein an enriched isotope spike is added to a sample. In this method, the standard (enriched spike, e.g. ^{233}U spike for ^{238}U quantification) and the sample are measured at the same time and using the same element. Isotope dilution is a far more accurate and precise method of quantification, but is time consuming, costly and only available to elements with multiple isotopes for which enriched spikes are available. However, results with accuracies and precision <1% are possible with the isotope dilution technique [57].

LA-ICP-MS calibration could in theory work in a similar way to solution-based ICP-MS however, early work [58] showed this was ineffective at accurate quantification due to differences in ablation yield (signal intensity for a given element concentration) between materials. The NIST61X reference glasses (610, 612, 614, 616, each with nominally 500, 50, 5 and 0.5 ppm of elements respectively) are widely used in LA-ICP-MS and are homogenous (for many elements), doped with most elements in the periodic table and are well-suited for quantification of LA-ICP-MS data. However, the matrix of these glasses is very different from most materials: ~70% SiO_2 , ~13% Na_2O , ~11% CaO , and ~2% Al_2O_3 so that the coupling of the laser beam between natural materials and the NIST61X glasses is variable. Several glasses based on natural compositions also exist for the calibration of LA-ICP-MS data, such as the USGS (United States Geological Survey) glasses BCR-2g, BHVO-2g, etc. However, these glasses do not contain as many elements as the NIST glasses, and concentrations for some can be too

low for calibration purposes. The USGS has also produced a series of synthetic glasses (e.g. GSD-1g [59]) doped with a wide range of trace elements, similar to the NIST61X glasses; however, the matrix elements are basaltic in composition and as such approximate the compositions of a wider range of geological materials. These USGS glasses have been widely adapted by the LA-ICP-MS community, however their replacement of the NIST61X glasses remains unlikely due to significantly less material availability and known heterogeneity issues for some elements (e.g. ^{232}Th in GSD-1g).

The ablation yield is defined here as the counts per second per ppm (cps/ppm) in a material and this yield is strongly controlled by the ablation rate of a material. Figure 1. 3 shows this visually with a laser image (laser rastered over the surface of a sample) with the dentine having an ~8x higher ablation yield than the enamel in a tooth sample.

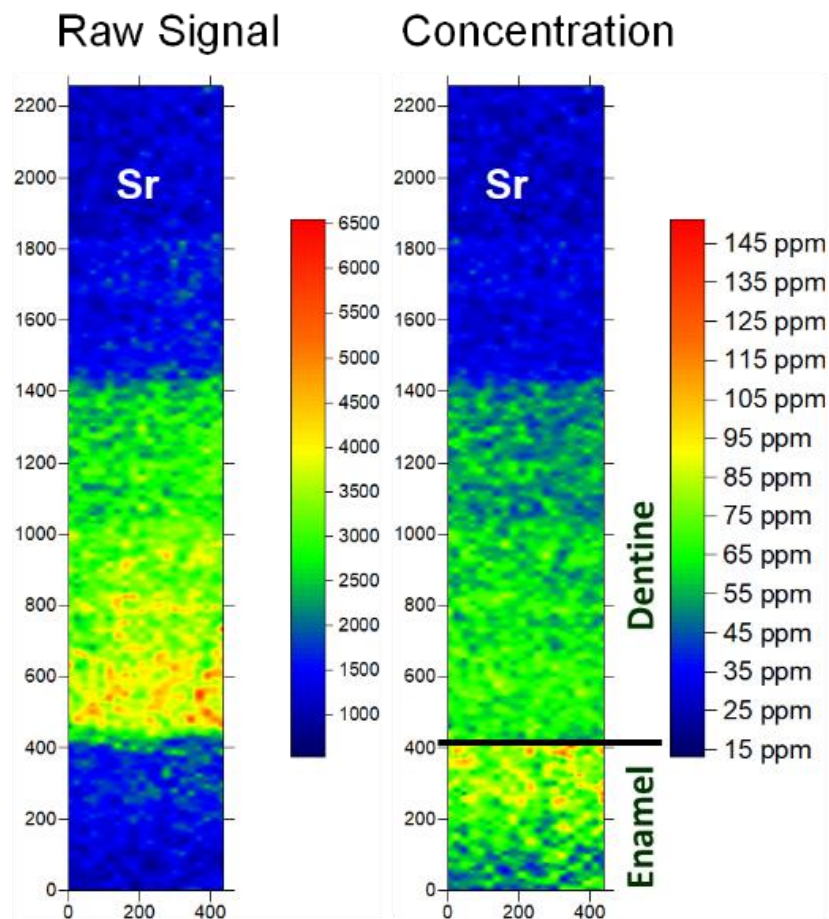


Figure 1.3. Example of the concept of differences in yield due to differences in material properties between the enamel and dentine in a tooth sample. Figure reproduced from Alan Koenig (USGS) [60].

Geological materials such as minerals and glasses have varying yields of 4x or more and the difference in yield is often laser system specific; depending on the laser wavelength, laser

pulse width, and possibly several other parameters. Longerich et al.[58] demonstrated a method of correcting differences in ablation yield, by the use of an internal standard element; similar to what is done for solution ICP-MS. The use of an internal standard (IS) element allows the quantification of a ratio of the element of interest to the IS, which should be constant with varying yields.

$$\frac{\left(\frac{CPS}{PPM}\right)_{STD}^{IS}}{\left(\frac{CPS}{PPM}\right)_{STD}^{EL}} = \frac{\left(\frac{CPS}{PPM}\right)_{SAMP}^{IS}}{\left(\frac{CPS}{PPM}\right)_{SAMP}^{EL}}$$

Equation 1.1. The Longerich et al.[58] equation for quantification of LA-ICP-MS results using a fixed internal standard element. The equation is solved for element of interest “PPM_{samp}”.

Equation 1.1 from Longerich et al.[58] requires a prior knowledge of the IS element concentration in the standard and the IS element concentration in the unknown material. The concentration of the IS in the unknown is typically obtained independently (e.g. electron microprobe analysis, EMPA), as a fixed value based on mineral stoichiometry (e.g. Si in quartz -SiO₂), or by summing the major cations with assumed or measured anions (e.g. oxygen) to a total (e.g. 100%) [61]. There are several drawbacks to this method of quantification compared to that used in solution ICP-MS, namely that the IS element is dictated by the composition of the target material so there may only be one potential candidate (e.g. Si in quartz, SiO₂). This means the IS can often only be one element and typically of low mass, making it difficult to correct for differences in mass bias and to match first ionization potential of the IS with the element. These aspects will lead to less accurate quantification of results for LA-ICP-MS data compared to solution ICP-MS with all other things being equal.

While the Longerich et al.[58] equation is still utilized today, there are some additional aspects of this equation that cause inaccuracies in LA-ICP-MS data. One of the biggest issues is element fractionation phenomenon described above. An assumption in the Longerich et al.[58] equation is that the standard material and the unknown either do not fractionate elements relative to the IS, or that they fractionate elements relative to the IS in a similar way. Unfortunately, this is often not true for many geological samples; Si is well known to fractionate from Zr during zircon spot analysis and this fractionation is not seen in the NIST61X glass reference material [62].

Historically the quantification of major elements in mineral phases and glass have seen restricted use by the LA-ICP-MS community due to known matrix effects or element fractionation, high signal intensities for mono-isotopic elements (e.g. ^{27}Al in feldspar), and interferences ($^{40}\text{Ar}+^{16}\text{O}$ on ^{56}Fe). This often led to analysing for one or two major elements in a given matrix while heavily relying on the determination of the internal standard element to be correct. While this works well for homogenous glasses and some minerals (e.g. quartz), materials that show significant element substitutions, zoning, or other heterogeneities from an ideal stoichiometry or from the location of the EMPA spot analysis, will give inaccurate results. This highlights one of the issues with use of the SEM (with EDS detector) or the EMPA for the estimation of the internal standard composition; the sampling volume of these electron beam techniques are often more than 10-100x smaller than the crater drilled by the laser.

These issues with LA-ICP-MS quantification can limit the total analytical precision and accuracy to 5-10% or worse, but this may not be an issue depending on the nature of the unknowns and the geological problems being addressed by the analyst (e.g. orders of magnitude zoning of trace elements in pyrite). However, for fully quantitative results, the issues described above need to be addressed and the uncertainties associated with any correction (e.g. correction for element fractionation) need to be fully propagated. The need for quantitative analysis has led to the analysis of all major cation constituents and for the summing of these metals with an anion (e.g. oxygen for silicates) to an analytical total (e.g. 100%) [61]. This can alleviate issues with zonation within the ablated volume when comparing with EMPA analysis. Verification of these methods to the accurate analysis of minerals can be done by comparing LA-ICP-MS results with those from EMPA or bulk solution ICP-MS; however Danyushevsky et al.[63] showed how the use of the mineral stoichiometry from LA-ICP-MS results normalized to 100% oxides can be an independent assessment of the LA-ICP-MS calibration accuracy. In Danyushevsky et al.[63] the use of plagioclase cations per formula unit from the LA-ICP-MS data was utilized (ideal formula is 5 cations per 8 oxygen) to show the use of some laser fluences produced better mineral stoichiometry (e.g. calibration) than others. This mineral stoichiometry verification of LA-ICP-MS results can be a useful tool in assessing the quality of the results with the assumption that the major elements being in the correct proportions will mean trace elements are similarly accurate. Some drawbacks to

this method are assumptions made about oxidation states of elements (e.g. Fe^{2+} vs. Fe^{3+}), mineral behaviour (ie. purely ionic manner and covalent bonding can make mineral stoichiometry calculations complex, such as in chalcopyrite), and species such as volatiles that are not able to be measured must be assumed when present (e.g. fluorine in apatite). Additionally, simple mineral formulas (e.g. FeTiO_3) may produce stoichiometric results but, have inaccurate concentrations.

1.2 ICP-MS

1.2.1 *Inductively-coupled plasma ion source*

The inductively-coupled plasma (ICP) as an excitation source has been utilized since the mid-1960s by the early pioneering work from Greenfield et al.[64] and Wendt & Fassel [65]. The ICP is an electrical discharge present in a stream of (partially) ionized gas, typically Ar. The ICP is maintained by a radiofrequency power generator that is coupled into the discharge using a water-cooled metal load coil. The ICP is housed within a quartz 'torch' that allows for Ar to enter the discharge in three ways, 1) through the main-volume of the torch to maintain the ICP discharge, 2) along the sides of the inner walls of the torch to prevent melting, and 3) through the central channel to introduce sample to the ICP (Fig. 1.4).

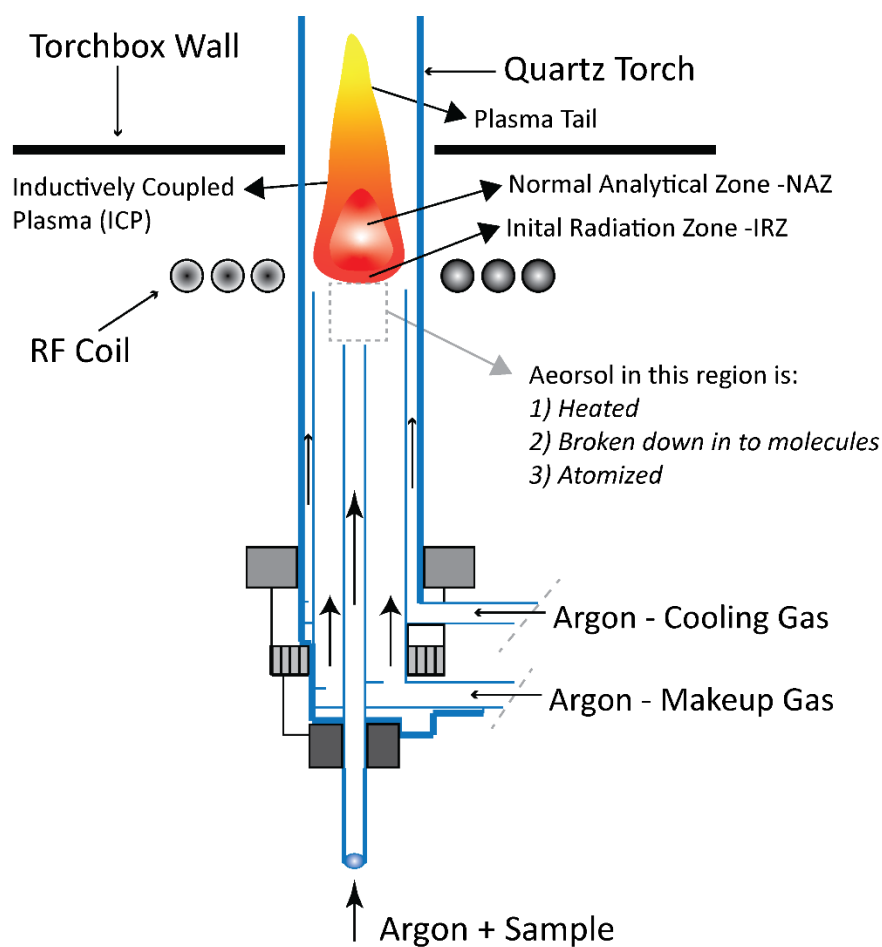


Figure 1.4. A depiction of the plasma torch used to maintain the argon-based ICP.

The first application of the ICP was as an atomic excitation source for optical emission spectroscopy (OES) leading to the ICP-OES technique for trace elements in solutions [66]. The ICP source is characterized by a high temperature ($>5,000\text{K}$ [64]) plasma discharge using argon gas that can excite (thermally) and ionize atoms either by electron impact [67] or by charge transfer [68]. Development by Houk et al. [69] led to the extraction of ions from the ICP source into a high-vacuum region for mass filtering (via quadrupole) and ion detection which is the design that modern ICP-MS instruments are based on.

The ionization of atoms by the ICP is a function of many parameters including the temperature of the plasma, electron density, the gas kinetic temperature (T_{gas}), and the ionization potential of the atom of interest. This has been summarized into the Saha-Eggert equation shown in Equation 1.2 for a given element “M”:

$$\log K_{\text{ion},M} = 1.5 \log T_{\text{ion}} - 5040(\text{IE}_M)/T_{\text{ion}} \\ + \log(Z_{M^+}/Z_M) + 15.684$$

Equation 1.2. Modified Saha equation reproduced from Hongsen & Houk [70] and based on Hayhurst et al. [71]. K_{ion} is the ionization constant for element “M”, IE_M is the first ionisation energy for element M, Z is the partition function for M^+ or neutral M and T_{ion} is the ionisation temperature for element M.

Using this equation for elements that are similar in mass but differ in first ionization potential, it is possible to estimate the temperature of the plasma that is extracted from the ICP [70]. Initially, samples were introduced to the ICP via a nebulized solution, which meant samples were digested in acid or other solvent and then delivered to the ICP and analysed. Given the amount of Ar and H_2O vapour that is introduced to an ICP and the constraints on ionization of these species above (Equation 1.2), the plasma dominantly consists of neutral species. Based on the equation above, some degree of doubly-charged species that have first ionization potentials less than that of Ar^+ will also be present in the plasma. These are typically the alkali earth metals and light rare earth elements (LREE), which have relatively low 2nd ionization potentials and can form interferences with target atomic analytes (e.g. ^{75}As interfered by mass 150 which is from ^{150}Sm and ^{150}Nd). However, even elements with higher 2nd ionization potentials can interfere with target species if the interferer is present at high concentrations (e.g. $^{45}\text{Sc}^+$ interfered by $^{90}\text{Zr}^{++}$ in the mineral zircon, ZrSiO_4).

During introduction of the sample via solution nebulization, only the finest (sub-nanometre) sized droplets enter into the ICP through the central axial channel. In this axial channel, the ICP will vaporize, atomize and finally ionize the sample. As a sample travels through the ICP, there are three main zones as defined by Koirtyohann et al.[72]: the initial radiation zone (IRZ), the normal analytical zone (NAZ) and the plasma tail (Figure 1.4). The IRZ is where the sample is vaporized and atomized, while the NAZ is where the highest abundance of ions are present and this is typically where ions are extracted from, and the plasma tail is predominately metal oxide species and atomic species due to the cooler temperature and the abundance of oxygen from either within the sample or from entrained atmospheric gas. The production of metal oxide species has been shown to be a function of the amount of oxygen in the ICP [73], the temperature of the ICP [73], as well as the degree of particle decomposition for laser ablation [74].

Tanner [75] showed that metal oxide species, characterized by lower ion kinetic energies, are formed in the cooler regions of the plasma and suggested that the plasma is temporally and spatially variable in temperature and potentially contains 'pockets' of cooler regions where these oxides species are preferentially formed. Oxide production rates in 'dry' plasma from laser ablation are typically 10x lower than those for 'wet' plasma with solution nebulization, as the amount of oxygen present in 'dry' plasma is significantly less [73]. Both oxide and doubly-charged species formation inhibit accurate results for ICP-MS and in particular for low-resolution instruments such as quadrupole mass filters.

The role of sample decomposition by the ICP is important for representative sampling, particularly for sampling aerosols associated with laser ablation. One source of element fractionation is when a sample introduced to an ICP is not representatively sampled. With solution nebulization, the sample is dissolved in H₂O and weak acid, which when nebulized, should have minimal or no element fractionation as the elements will be evenly dissolved in the solute. However, this is not always the case with laser ablation due to non-representative sampling at the ablation site [46].

The inability of an ICP to digest all particles has led to changes in methodology on how long a particle resides in the ICP by changing either the gas flow rates in the central channel or the sampling position of the ICP. For example, as a result of the Guillong et al.[44] who showed that Th was preferentially enriched in the larger size fraction of the laser aerosol relative to U, the U/Th ratio is commonly used as an indicator of the 'robustness' of the ICP. This is done by ablation of the NIST61X reference glasses that have equal proportions of U and Th so that any difference between the two element responses is likely due to incomplete particle digestion. The optimization of the ICP for digestion of aerosol derived from the NIST61X reference glasses may not be representative of the best conditions for unknown targets which may have different particle size distributions. However monitoring the U/Th ratio has made the community more aware of the issue of element fractionation in the ICP. A more recent study by Fietzke and Frische [52] suggested that optimization of gas flows into the ICP can be done by using the ratio of $^{38}\text{Ar}^+$ and $^{40}\text{Ar}_2^+$ in conditions where no sample is ablated. When the $^{38}\text{Ar}^+$ and $^{40}\text{Ar}_2^+$ is optimized, the authors show a reduction in oxide species, doubly-charged species and more consistent yields between ablated matrixes of differing compositions at the cost of instrument sensitivity.

While the ICP is Ar based, early work [76-79] showed that addition of small amounts (few ml/min or <0.05% of total gas flow into ICP central channel) of diatomic gases, particularly H₂ and N₂, allowed for a dramatic increase in instrument sensitivity and a lower rate of oxide species [73]. The increase in instrument sensitivity was highest for elements of higher first ionization potential and is thought to be related to a better energy or charge-transfer of the ICP [79]. Another advantage of N₂ addition shown by Hu et al.[79] is the location of ionization of atoms within the ICP, which becomes more uniform (Fig. 1.5). Figure 1.5 shows that without N₂ addition, the location of highest ion intensity in the ICP varies based on element, however these ion intensity distributions become more even with addition of N₂ gas to the central channel of the ICP. Of course, there are disadvantages to addition of these diatomic gases, namely interference produced either in the 'gas blank' part of the spectrum or as polyatomic species. N₂ interferences are found at various N combinations with N, O or Ar and include elevated background intensities at masses 28, 29, 31, 54, 55. However the production of polyatomic metal ions with nitrogen is very low compared to other polyatomic formation and typically is much less than 1x10⁻⁴ % and negligible for most applications [79]. H₂ addition also shows increase in backgrounds for some masses, 39 most notably, that can severely affect detection of potassium in samples. Metal hydride polyatomic formation is significantly higher ranging from 0.002% to 0.1% depending on the element [78]. Not all studies have shown an increase in sensitivity with specific diatomic gas addition. For example, Guillong and Heinrich [78] showed an increase in sensitivity using H₂ addition, but not with N₂ addition under the same analytical conditions. Reasons why some ICP-MS systems show differing behaviour during diatomic gas addition is still unclear, however there may be some impact from changes in the electrical properties of the ICP, in particular the ion energy distribution. This will be expanded upon in chapter 2.

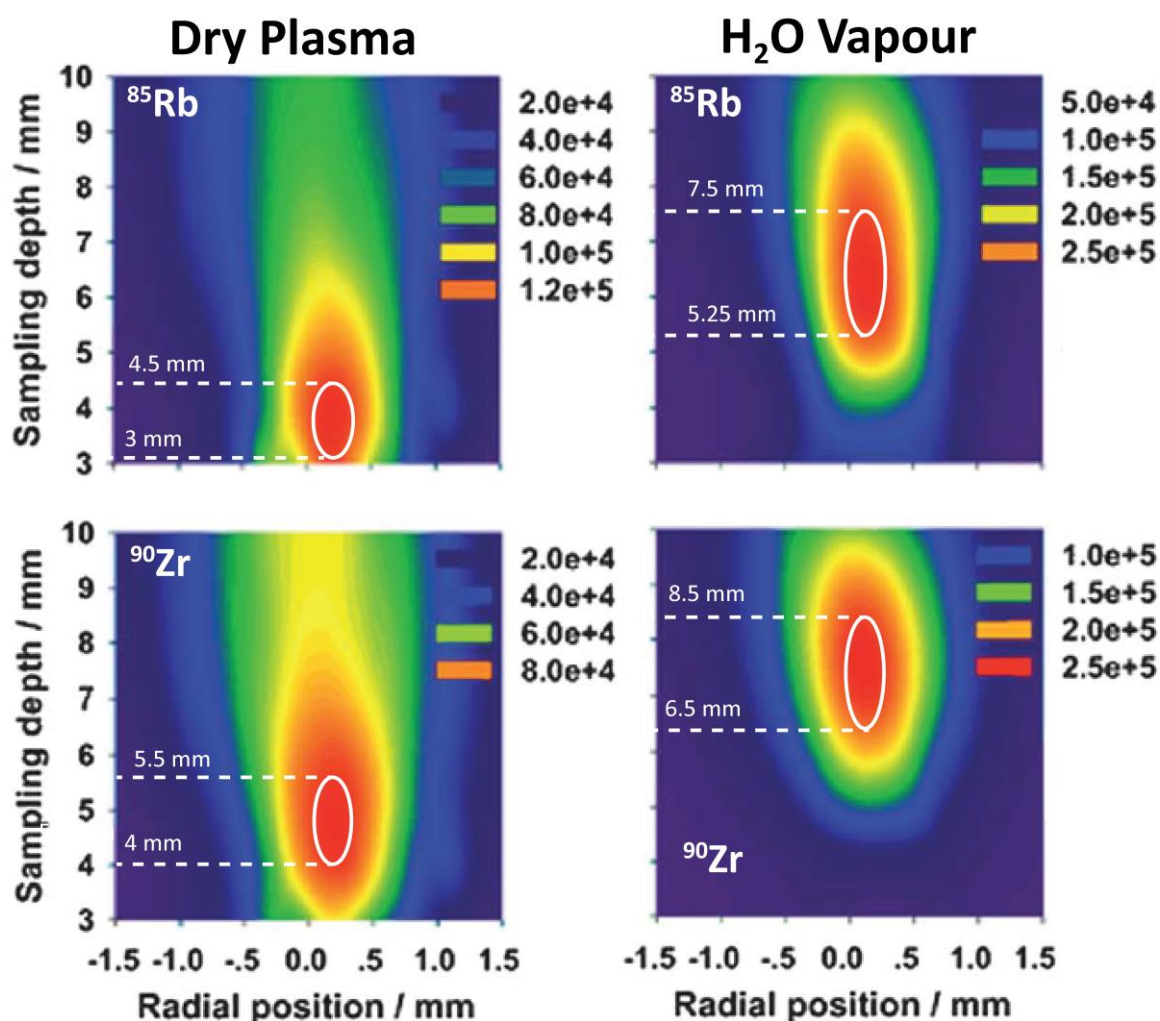


Figure 1.5. Distribution of ion intensities from laser ablation mapped out in the ICP under various central channel gas flows and addition of H_2O vapour addition modified from Hu et al. [79]. Note the change in both the location (further downstream) and the length of the highest signal intensity (red) with the addition of H_2O vapour to the ICP-MS. Note the smaller offset between the peak intensity for $^{90}\text{Zr}^+$ (refractory) and $^{85}\text{Rb}^+$ (volatile) with the addition of H_2O vapour compared to dry plasma. Signal intensities in counts per second.

1.2.2 Interface region

Atomic ions in an ICP-MS need to be focussed, mass filtered and detected, all of which is exceedingly difficult due to the poor ion transmission at atmospheric air conditions. To overcome these issues, the first ICP-MS [69] utilized a ‘cone’ to sample a small part in the middle of the ICP with the assumption that this sampling of the ICP is representative. This cone had a small orifice of 50 microns and behind the cone was a series of stages of increasing vacuum going from atmospheric pressure (760 Torr) down to 1×10^{-6} Torr. This initial design suffered issues with the cone needing frequent cleaning and replacing due to the small diameter clogging and damaging. Later work by Gray and Date [80] utilized two different

cones: an outer 'sampler' cone and an inner 'skimmer' cone such that there is an additional vacuum step in the system. This design allowed for several improvements in ion transmission and avoided the need to clean / change the cones as frequently as with the single cone design. The modern ICP-MS configuration utilizes the two-cone design for the interface between the ICP and the high vacuum components of the ICP-MS.

The interface region between the ICP and the extraction lens in the vacuum part of the instrument is a critical part of the ICP-MS and there are several complex interactions between the high temperature ICP and the metal cones, the base of which are water cooled. The cool region around the surface of the cones called the 'sheath' prevents the electron rich ICP from interacting with the cones (Fig. 1.6). This sheath is also responsible for some of the electrical properties of the ICP. For example, there is commonly a positive potential in the ICP, commonly referred to as a 'pinch' or 'secondary discharge' [70], where there is a capacitive coupling of the ICP to a gradient in the RF field due to the nature of the load coil. Using Langmuir probe measurements, Gray et al.[81] showed this discharge to be significantly higher when the ICP was not extracted to the higher vacuum region of the ICP-MS. This higher discharge voltage led the authors to conclude that the sheath around the cones is significantly larger when the plasma is not extracted into the vacuum region and this causes an increase in the secondary discharge. This secondary discharge has deleterious effects of significantly reducing the sensitivity of the ICP-MS as well as imparting a high electrical potential on the extracted ions, making mass filtering by quadrupole difficult [82]. This secondary discharge phenomenon was solved in two ways: 1) By placing a small metal band around (with a gap) the quartz torch that dissipates the secondary RF field that can be induced in the plasma. This is known as a shield torch [83]. 2) By changing the grounding of the RF coil so that the ground is in the middle of the coil, known as a centre-tapped coil [75, 84], Sciex ICP-MS instruments avoided the secondary discharge issue altogether. Both methods of mitigating the secondary discharge in the ICP are employed on modern ICP-MS instruments. It should be noted that the secondary discharge within dry plasma (laser ablation) is absent or highly diminished so that the presence of the shield has little effect on the performance of the ICP-MS and this will be expanded on in Chapter 2.

The location in which the ICP is 'sampled' by the cones is critically important for obtaining a robust plasma (i.e. complete particle digestion), minimal oxides, maximum atomic ions.

Typically, there are two controls on where the ICP is sampled, either changing the physical distance from the ICP to the sample cone or by changing the rate of flow of Ar gas in the central channel. Both will have similar effects on where the ICP is sampled.

Sheath Effect on Non-Shield Torch at the Skimmer Tip

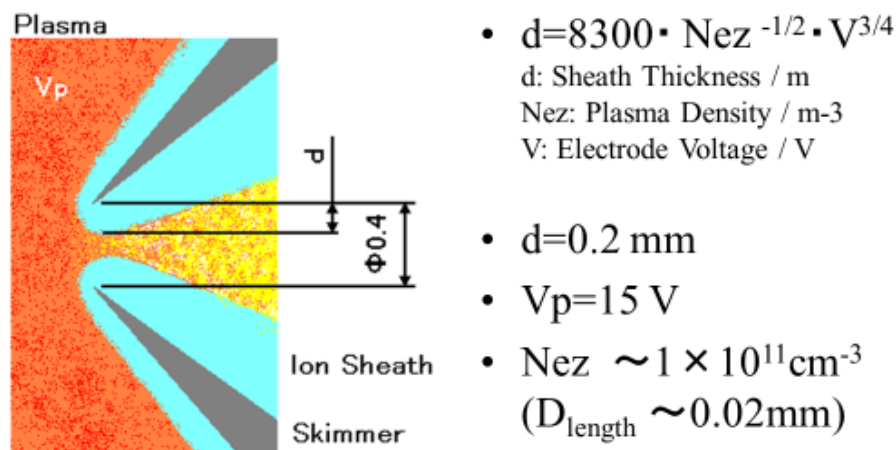


Figure 1.6. Diagram of ion sheath around sample cone and calculations for sheath thickness modified after Sakata et al., 2000 [85].

1.2.3 Mass filter and mass separation

Ion formation and extraction occurs within the ICP-MS interface, however once in the high vacuum region of the instrument, the ions need to be focussed, separated from each other and detected. While most ICP-MS instruments have broadly similar ICP sources and interface cone designs, there is a significant difference between different ICP-MS with respect to how ions are guided through, separated and detected. There are three general types of ICP-MS utilized in the geosciences for laser ablation today: quadrupole mass filter (QMS), magnetic sector with scanning field (SFMS) and time-of-flight (TOFMS). In each of these ions are detected based on their mass to charge (m/q) ratio.

Quadrupole instruments are the most widely used due to low cost and simplicity of use. These mass filters separate ions using four rods that change a DC and AC voltage to create stability fields for specific m/q . Quadrupole mass filters typically have a mass resolution ($r \approx 300$, where $r = m/\Delta m$ and m is the nominal atomic mass and Δm is the difference between

two resolved peaks) which is high enough to easily resolve all atomic ions, but not enough to resolve polyatomic interferences. An important aspect for laser ablation is that quadrupole mass filters are sequential, in that they can only detect one m/q at a time. However, the change in electrical fields on the quadrupole rods needed to isolate the next m/q in an analytical list is small, so that quadrupoles can 'scan' through a mass list relatively quickly (single to 10s of millisecond quadrupole 'jump' times). Once an ion is separated by the quadrupole mass filter, it is sent into an electron multiplier for ion detection.

Magnetic sector instruments require a significant potential and extraction voltage to obtain high enough ion kinetic energy (KE) to achieve m/q separation by a magnet field. Once ions have passed through the magnet and are separated based on their mass, typically a set of four rods (quadrupole) is used to energy filter the ions (doubly focussing), then they are detected by an ion multiplier or faraday cup. Magnetic sector instruments can be single collectors, in which they must scan (either electrically with the quadrupole rods or by 'magnet jumps') through the different m/q in an analytical list in a similar fashion to the quadrupole mass filter. However, because magnetic fields take longer to stabilize than electrical fields on the quadrupole rods, the scan time of single collector magnetic sector instruments is longer than for a quadrupole instrument scanning over the same analyte list (up to hundreds of milliseconds). Magnetic sector instruments can also be multi-collector instruments that have an array of various electron multipliers or faraday cups to simultaneously detect ions that have been separated by the magnet. The geometry of multi-collector instruments usually allows for m/q range of about 15% or less, meaning that these instruments are well suited for analysis of specific isotopic systems (e.g. Nd isotopes), but not at multi-element analysis where magnet jumps are required. Magnetic sector instruments can have variable resolution and typically operate in a low ($r \approx 300$), medium ($r \approx 4000$) and high ($r \approx 10,000$) resolution. Use of medium and high resolution is useful for resolving many, but not all, polyatomic interferences on atomic ions at the expense of instrument sensitivity. Also, in low resolution, magnetic sector instruments typically have much better ion transmission rates and often yield 10x better sensitivity than quadrupole instruments.

Time-of-Flight instruments utilize a pulse or 'packet' of ions that travel through an electrical field that accelerates the ions and as they travel, ions of different m/q will travel at different speeds and all ions will strike a multi-channel plate detector that records the precise

time (in microseconds) an ion struck the detector. So, ions are separated by their travel time or time of flight through the electrical field. This technology is not new, but the adaptation of it to laser ablation and geoscience is relatively recent due to technical challenges of the instrumentation. Time-of-flight instruments offer a significant advantage over sequential ICP-MS described above in that all elements are extracted from the ion beam simultaneously and detected quasi-simultaneously. Simultaneous detection of elements can avoid problems such as spectral skew that are problematic for transient techniques such as laser ablation. ICP-based TOFMS instruments offer mass resolution between 3,000 and 6,000 depending on the instrument and m/q and so can resolve many common interferences (e.g. doubly-charged species). However, TOFMS suffer from poor abundance sensitivity where one mass will ‘tail’ into another. Typical abundance sensitivities for TOFMS are on the order of 10^{-4} (counts at adjacent peaks due to nearby peak), however for QMS and SFMS are typically $<10^{-7}$ counts. The result of this is that there can be significant deconvolution of signal needed when there are high intensity peaks near target low intensity peaks. Time-of-Flight instruments will be discussed in greater detail in Chapter 5. Mattauch-Herzog geometry (MHMS) is another type of simultaneous detection mass spectrometer that utilizes a set of magnets to separate out ions that are then detected by photomultipliers or CCD arrays. However, use of MHMS has seen limited utilization in the geosciences with a few exceptions [86].

1.3 LA-ICP-MS applied to geochronology

One of the early applications of LA-ICP-MS to geological materials was to U-Pb or Pb-Pb dating of mineral phases [34, 87]. In U-Pb and Pb-Pb dating, the decay of the radioactive parent nuclides ^{238}U , ^{235}U and ^{232}Th to their respective daughter products, ^{206}Pb , ^{207}Pb and ^{208}Pb is utilized to assess the time in which the mineral phase became a ‘closed system’ with respect to U (Th) and Pb; allowing for the in-growth of radiogenic Pb. By measuring each of the nuclides in a mineral phase, and if there has been no disturbance to the systems (e.g. loss of Pb), no initial daughter products present (e.g. common Pb) and the decay constants of the parent nuclides are known, the isotopic composition of Pb and Pb to U and Th ratios will yield the age at which the mineral became a closed system (e.g. crystallized). When these three decay systems agree in age with each other, they are said to be in ‘concordance’. Historically

the $^{208}\text{Pb}/^{232}\text{Th}$ system has not been utilized as much as the U-Pb systems and this work will focus primarily on the U-Pb systems. The above assumptions needed to utilize the U-Pb system for accurate age determination in a sample, are often not valid, and these issues need to be assessed before an age can be calculated.

The mineral zircon was found to be an almost ideal mineral for determination of the U-Pb age due to its relatively high U contents, compatibility of Pb in its structure allowing for little or no initial daughter present, abundance in a wide range of silicic rocks, and its ability to stay a closed system during alteration and weathering. Other minerals such as apatite can often contain useful amounts of U, however these minerals often contain significant quantities of initial daughter product (Pb^{2+}) that can sit in the Ca^{2+} site in apatite due to the similar charge and ionic radius of Pb^{2+} and Ca^{2+} . In cases of significant initial daughter product, an estimate of the common Pb composition must be made either through linear regression of a two component (radiogenic vs. common Pb) mixture obtained via many analyses, or by analysis of a Pb rich phase (e.g potassium feldspar) assumed to be in isotopic equilibrium at the time of crystallization. Here the focus is on zircon as an example of U-Pb geochronology by LA-ICP-MS, but the technique could be applied to any number of other mineral geochronometers (e.g. monazite).

The ability of the LA-ICP-MS to sample domains that are 10s of microns within a crystal has a powerful advantage over traditional bulk methods of U-Pb measurement such as isotope dilution thermal ionization mass spectrometry (ID-TIMS) [88] that will have homogenized any potential age and compositional zoning. However, recent advances in chemical abrasion with ID-TIMS have allowed for a preferential sampling of less radiation damaged parts of grains as well as specific domains within a single grain [89]. Still LA-ICP-MS offers advantages over ID-TIMS and SHRIMP (Sensitive High-Resolution Ion Micro-Probe) because laser ablation is significantly cheaper, faster and requires less sample preparation. Many early publications showed analysis of Pb/U ratios by LA-ICP-MS hindered by the element fractionation phenomenon described above [34, 87]. The degree of Pb/U fractionation was mineral or material specific and had a significant effect on the accuracy of the measured age. While the calibration of LA-ICP-MS element results has been discussed above, the application of LA-ICP-MS to geochronology deserves more discussion here as more corrections are needed in reference to the Longerich et al.[58] equation.

The complexity of element fractionation during zircon U-Pb dating requires a detailed understanding of how an analysis is done and the aspects involved. A typical analysis will consist of ablation at a static location and drilling a hole into the sample. For U-Pb geochronology the length of time drilling at each location is usually kept relatively short (e.g. 30 seconds) with the goal of minimizing the depth of the ablated crater. A shallower crater will minimize the potential to drill through a mineral, drill into a different age zone, and will minimize the amount of element fractionation between Pb and U. As the laser drills deeper into a sample, Pb and U will fractionate from each other and this fractionation hinders both the accuracy and precision of the measurement. The cause of the element fractionation in the mineral zircon is thought to primarily be due to the formation of ZrO_2 on the crater walls and in the aerosol directly after a laser pulse [46, 48, 62]. These observations are consistent with the different element condensation temperatures for U, Th and Pb, where U and Th have significantly higher condensation temperatures than Pb (727 K vs. 1610 K 50% condensation temperatures for Pb and U respectively [90]) so that Pb will be enriched in the aerosol relative to refractory U as an ablation proceeds due to the deepening of the ablation crater [27]. Therefore, during ICP-MS data acquisition from an ablation of zircon, the apparent U-Pb age of the zircon will increase with time.

Guillong and Gunther [44] suggests the ICP is a significant source of element fractionation in LA-ICP-MS due to changes in particle size distributions during ablation and between minerals. While this mechanism of element fractionation is possible in LA-ICP-MS analysis of zircon, the particle size distributions of zircon are all sub-micron [44] and should easily be digested by the ICP. It is more likely the formation of ZrO_2 at the ablation site is the dominant cause of element fractionation in the mineral zircon. Other minerals such as apatite also show a time dependant increase in apparent U-Pb age within an analysis and Chapter 4 will address possible ablation site causes for element fractionation in this case.

While element fractionation occurs in most materials, it is rarely corrected for. Element fractionation can affect the accuracy of analytical results on the order of 5% to 10% which is similar to the uncertainties associated with LA-ICP-MS measurements; particularly if there is natural zoning within a material. Element fractionation in zircon during LA-ICP-MS analysis, by comparison, can be 30% or more change of Pb/U throughout an analysis. Another reason for the lack of correction for element fractionation during multi-element analysis also relates

to the geological questions or processes being address by multi-element analyses. These tend to be complex, multi-variable, and span concentrations of several orders of magnitude such that uncertainties of 10% can often prove adequate to address the research question. In geochronology however, the isotope ratios being measured are controlled by the decay of U and Th to their daughter isotopes so the amount of daughter Pb present, provided several of the above assumptions are true, is simply a function of the decay constants of U and Th. The decay constants for U and Th are well constrained to the ~0.1% (2s) level [91] so that the ability to interpret ages is often not limited by complex natural processes, but rather the ability to accurately and precisely measure the isotopic composition of Pb and the Pb/U ratio. The implication of this is that to obtain an accurate and precise age, a more robust correction for any element fractionation during LA-ICP-MS analyses is needed for U-Pb geochronology analyses.

Early work that recognized element fractionation in zircon [34, 87] noted the time-dependence of the element fractionation where the apparent U-Pb ‘age’ of the sample increased throughout an individual analysis due to drilling of laser into the sample. Several methods for correcting this time-dependent element fractionation have been attempted including an intercept method [34, 92] where a linear function is fit to the first 5 or 10 seconds of data, an average correction factor where the time intervals for samples and standards are short (<10 seconds) and fixed [93], and a model fractionation curve fitting the trend seen in the primary calibration material [94]. In all of these methods the calibration material must be ‘matrix matched’ to the unknowns, implying the use of a zircon of known and homogeneous U-Pb age must be analysed to accurately correct for element fractionation as the degree of element fractionation between zircon and NIST61X reference glasses has been shown to be significant [62]. Of the different methods for correcting U and Pb fractionation in zircon, the model curve fit of the primary standard trend used by Paton et al.[94] is commonly used and will be used in this work (Chapters 3, 4 and 5). In this method the individual analyses from the zircon calibration material are averaged on a sweep-by-sweep basis from the time that the laser is switched on to the end of an analysis. A curve is fit to the average of the fractionation factor (measured $^{206}\text{Pb}/^{238}\text{U}$ / published $^{206}\text{Pb}/^{238}\text{U}$) from the start to the finish of a single analysis. This model curve is then applied to each of the unknowns, correcting the analysis based on the time in which the laser starts ablating (Fig. 1.7). This method has the advantage

over other methods that the portion of the analysis used for quantification can be adjusted since all element fractionation is corrected for in the entirety of the analysis. This allows for selection of portions of analyses that are the most concordant or avoiding common Pb inclusions that would have otherwise been included in the analysis.

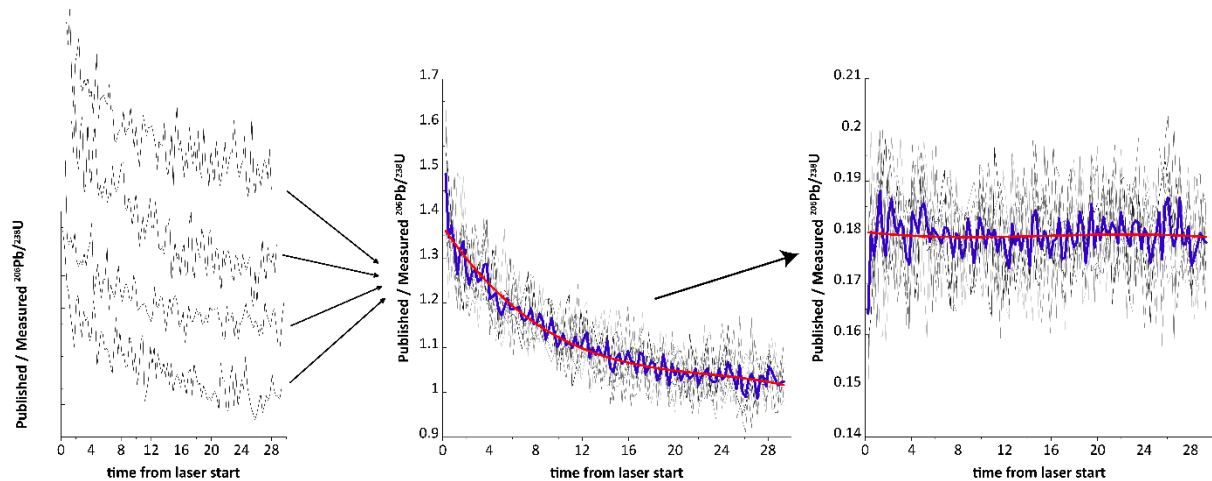


Figure 1.7. Example of curve fit to primary zircon standard for $^{206}\text{Pb}/^{238}\text{U}$ used in this work.

One important aspect of LA-ICP-MS U-Pb geochronology is the use of a single zircon reference material that corrects for both ICP-MS drift and time-dependent element fractionation. If there is a difference in ablation behaviour or element fractionation between different zircon samples, then inaccurate ages will result. This phenomenon was first documented by Allen and Campbell [95] and they termed it the zircon matrix effect. This offset in LA-ICP-MS U-Pb age correlated with the amount of radiogenic Pb in the zircon and led the authors to suggest that the radiation dose (from U and Th) a zircon has received will influence the ablation characteristics due to damage of the zircon crystalline structure. Allen and Campbell [95] mitigate this issue for high radiation dose zircon by annealing them at 850° C for 48 hours to repair this crystal damage from self-radiation. The unknown zircon would then have a more ‘similar’ matrix with respect to radiation damage to that of the calibration zircon standard and reduced offsets in the LA-ICP-MS U-Pb age were seen. Further work by Marillo-Sailer et al.[96, 97] showed that there was a correlation between the ablation rate and the accuracy of a zircon U-Pb analysis such that zircons of known age that measured too old by LA-ICP-MS had higher ablation rates than the primary calibration material and vice-versa for zircons that measured too young. Chapter 4 will expand on these issues and offer solutions to accuracy issues in zircon U-Pb dating by LA-ICP-MS.

1.4 Purpose of this work

To improve the understanding of the many processes involved in LA-ICP-MS analyses, a detailed investigation of important aspects of the whole system are needed. This work aims to better understand processes occurring at the ablation site and in the ICP, during extraction of ions from atmospheric pressure to a vacuum and ion mass filtering / detection. Understanding these processes better will improve the LA-ICP-MS technique, providing for more accurate and precise analyses and for a better estimation of the full uncertainty budget of an analysis.

Because of the natural variability in most minerals and glasses, this study will focus on investigation of the U-Pb dating of the minerals zircon and apatite as the ratio of these two elements is controlled by radioactive decay constants when the minerals have simple formation histories. Using U/Pb ratios, this work seeks to improve accuracy and assess limitations of accuracy for dating of minerals by LA-ICP-MS.

This contribution will address the following:

- Fundamental properties of the ICP by measuring the ion KE
- Use these ion KE measurements in both conventional 'wet' plasma with solution nebulization and in 'dry' plasma conditions (LA-ICP-MS). As part of this attention will be given to diatomic and helium gas addition to the ICP.
- Conditions of the ICP needed for accurate analysis (both interference reduction and 'robust' plasma)
- Investigation into matrix effects in the mineral apatite for U-Pb dating, which is complicated by poorly constrained ages and common Pb in reference materials.
- Investigation into matrix effects in the mineral zircon for U-Pb dating. A wide range of well characterized reference materials are used to investigate causes of systematic offsets in ages.
- Using knowledge gained from chapters 2 and chapters 4, an assessment of the time-of-flight (TOF) ICP-MS for U-Pb dating of zircon is done in Chapter 5.
- TOF technology is different from QMS and has some advantages / disadvantages for zircon U-Pb ages and these will be addressed in Chapter 5.

Chapter 2 will present and discuss ion energy (ion KE) measurements in the ICP for traditional 'wet' plasma and for laser ablation or 'dry' plasma. The differences in ion KE distribution between wet and dry plasma will be used to show that the current ICP-MS instrumentation can be improved for dry plasma analysis. Chapter 2 will also present results related to diatomic gas addition, common to LA-ICP-MS as well as interference production in the ICP-MS.

Chapter 3 will demonstrate the limitations of accuracy and precision in the U-Pb dating of apatite by LA-ICP-MS. Systematic offsets in ages of various apatite reference materials are observed and interpretations of these offsets are discussed. Two new apatite reference materials are presented to the geological community.

Chapter 4 will provide explanations for systematic offsets in zircon U-Pb ages by LA-ICP-MS relative to their ID-TIMS ages for a wide range of reference materials. A correction equation for age offset by LA-ICP-MS is presented and is based on the calculated radiation dose a zircon has received.

Chapter 5 will demonstrate the accuracy of zircon U-Pb dating using the TOF-ICP-MS and how this simultaneous detection technique can offer advantages for LA-ICP-MS compared to sequentially-based quadrupole instruments, while delivering similar accuracy and precision.

Chapter 2 Effects of H₂O, He, N₂ and H₂ on ion kinetic energies in inductively-coupled plasma mass spectrometry

As published in full: Thompson, J.M.; Houk, R.S.; Olin, P.H.; Fryer, F.; Danyushevsky, L.V. (2020) Spectrochimica Acta part B, V. 169, 105870.

Abstract

This study compares measurements of ion energy and the polyatomic species abundance in conventional solution inductively-coupled plasma mass spectrometry (ICP-MS) and laser ablation ICP-MS for multiple quadrupole instruments. Ion energy measurements in plasma sources have been used as a diagnostic tool for understanding processes occurring within the plasma during extraction of ions. Ion energy measurements have also allowed for determination of the nature of polyatomic species formation. In this study, ion energy measurements show that dry plasma conditions (laser ablation) result in a different ion energy distribution vs. mass compared to wet plasma (solution nebulization), suggesting a lower apparent temperature for dry plasma. The effect of helium and nitrogen or hydrogen additions to an argon plasma shows that helium is unlikely to ionize in the plasma or participate in charge transfer reactions, but primarily affects the interface pressure between the cones and the temperature of the plasma. Hydrogen addition to a dry plasma shows a slight increase in atomic ion energy, while nitrogen addition does not, and this suggests the two diatomic gases behave differently in the plasma. Investigation of ion energies with and without electrically shielding the torch shows no net benefit to using the shield for dry plasma. This behaviour, as well as differences in ion lens settings required for optimal ion beam properties, suggests different capacitive coupling between wet and dry plasma (un-shielded torch). This has implications for the optimal configurations of interface design of ICP-MS, which until now have been optimised primarily for wet plasma conditions.

2.1 Introduction

2.1.1 Background to ICP-MS and LA-ICP-MS

Laser ablation inductively-coupled plasma mass spectrometry (LA-ICP-MS) is a widely used tool for in-situ analysis of elemental and isotopic compositions in solid materials. Since the initial work by Gray [1] which demonstrated the possibilities for the technique, there have been significant improvements to the laser instruments, including shorter wavelengths (UV)

for better sample coupling [21, 22], better optical designs for smaller, more homogeneous beams[38], better laser ablation cells with homogenous signal response across the entire cell volume[38], and development of femtosecond lasers that can minimize matrix-dependent elemental fractionation, especially for metals and other samples with low melting points [24, 98].

ICP-MS design has also changed substantially over the last thirty years. Initial ICP-MS instruments [69], Gray & Date [80] demonstrated the possibilities and challenges of sampling an ICP for atomic ions. Improvements in design included use of a two stage vacuum interface with a sampler and skimmer cone [80, 82], use of off-axis ion beams to reduce detector noise [99], magnetic sector analysers [100], time-of-flight instruments [101], and introduction of collision cells [102] to reduce polyatomic species. These improvements have substantially increased ICP-MS sensitivities and reduced background noise, giving sub-ppt levels of detection for many isotopes.

Importantly, ICP-MS instrumentation has been designed and developed around use of a water-based sample solution introduced into the ICP via nebuliser and spray chamber, so-called ‘wet’ plasma conditions. In LA-ICP-MS, however, the sample is an aerosol formed by the ablation of a solid sample in a dry, helium (typically) atmosphere. Helium ablation gas is then mixed with argon gas and the combined gas stream and sample aerosol are sent directly into the ICP torch. Because there is no weakly acidified solution, relatively little O, H, or N are added to the plasma compared to solution ICP-MS. These are known as ‘dry’ plasma conditions, e.g., Witte & Houk [73]. In dry plasma even small additions of various gases (O₂, H₂, & N₂) can have significant changes to sensitivity [48, 76, 78, 79], often dependent on analyte first ionization potential.

Given these differences between wet and dry plasma ICP-MS, there is a need for a better understanding of 1) how processes such as ionization and ion extraction are different, and 2) whether ICP-MS instruments can be better optimized for dry plasma conditions. This paper addresses some of these issues.

2.2 Experimental

This study utilised two different models of quadrupole ICP-MS, an Agilent 7900 at CODES Analytical Laboratories, University of Tasmania, and a Thermo X series 2 at the University of

Iowa. Unless stated otherwise, the experiments were conducted under conditions summarised in Table 2.1 and described in detail below. These conditions correspond to the optimal instrument performance under both dry and wet plasma in term of sensitivity, plasma robustness and polyatomic interference production.

The Agilent 7900 was operated at a forward power of 1350 W with the load coil grounded at the downstream end. Sample introduction for solution analyses in wet plasma mode consisted of a Micro Mist nebulizer in a Scott-type double pass spray chamber cooled to 2° C with sample introduced through a 1 ml/min nebuliser with an Ar flow of 800 ml/min and 400 ml/min Ar flow of 'makeup gas' was added to the spray chamber. The Agilent 7900 was tuned while nebulizing a 1 ppb multi-element solution. The sampling position was adjusted to achieve oxide production on $^{140}\text{Ce}^{16}\text{O}^+ / ^{140}\text{Ce}^+$ signal ratio of $\approx 1\%$. Doubly charged species were 1.6% for $^{140}\text{Ce}^{2+} / ^{140}\text{Ce}^+$ while achieving 550 000 cps/ppb on $^{238}\text{U}^+$. Using the Omega lenses, a pair of ion lenses past the extraction lenses where there is 'bend' in the ion beam and a photon stop, were adjusted to achieve a mass bias for $^{238}\text{U}/^7\text{Li}$ to be ≈ 4 as further increases in light masses resulted in a significant drop in high mass sensitivity. Wet plasma analyses were conducted with the ion lenses in 'soft extraction' mode and with a shielded torch unless otherwise specified (Table 2.1).

In dry plasma mode, the Agilent 7900 operated at 1350 W and was coupled to an ASI RESolution S-155 laser ablation system which uses a Coherent ArF excimer laser with ≈ 20 ns pulse width, outputting a beam of 193 nm wavelength characterised by a flat energy profile. The laser was fired at 10 Hz using a fluence of 3.5 J/cm². Ablation was done in a helium atmosphere with a flow rate of 350 ml/min and mixed with Ar flowing at 1050 ml/min immediately after the laser cell. The Agilent 7900 was tuned for dry plasma while ablating NIST612 glass using a 43 μm -wide line rastered at 3 μs . Sampling position (Table 2.1) was adjusted to get signal ratios for $^{232}\text{Th}^{16}\text{O}^+ / ^{232}\text{Th}^+ < 0.2\%$ and $^{238}\text{U}^+ / ^{232}\text{Th}^+ \approx 1.05$ [44]. The very high Ca/Fe concentration ratio (1668) of NIST612 allows for using this RM to assess the extent of polyatomic interference production of CaOH^+ during tuning. Octopole bias lens voltages were optimized a $^{43}\text{Ca}^+ / ^{57}\text{Fe}^+$ ratio close to 100, indicating low OH^+ interference production rates [103], ≈ 8800 cps/ppm on $^{238}\text{U}^+$, and tuning ion lenses to achieve a mass bias for $^{238}\text{U}/^7\text{Li}$ to be ≈ 4 (using Omega lenses as above) and for low background (i.e., m/z 220 < 2 cps). Dry plasma analyses were conducted with the ion lenses in 'soft extraction' mode and with a

shielded torch unless otherwise specified (Table 2.1) without the shield present on the torch, unless otherwise specified.

For both wet and dry plasma tuning, the extract 1 lens was set in a position so that a small voltage in this lens would have minimal impact on the mass bias. While setting extract 1 in such a way can sacrifice some ICP-MS sensitivity, it can limit the amount of drift in the ICP-MS due to small changes in the effective voltage of extract 1 from sample introduction.

The Thermo X Series 2 was operated at 1420 W forward power with the load coil grounded at the downstream end. Sample introduction for wet plasma on the X Series 2 was with a MicroMist nebulizer (1ml/min) in an impact bead spray chamber cooled to 2 °C using an Ar flow of 880 ml/min. The instrument was tuned using a 10 ppb multi-element solution to achieve $^{140}\text{Ce}^{16}\text{O}^+ / ^{140}\text{Ce}^+$ of 1.5%, doubly charged species were 1.5% for $^{140}\text{Ce}^{2+} / ^{140}\text{Ce}^+$ while achieving 150 000 cps / ppb on $^{238}\text{U}^+$. On the X-Series 2, there is only a 'hard extraction' option for the extraction lens (-110V) and a shielded torch was used unless otherwise specified (Table 2.1).

In dry plasma mode the X Series 2 was coupled to a New Wave UP213 nm Nd:YAG system with a single-volume, barrel-shaped ablation cell. Ablation was conducted in a He atmosphere with a flow rate of 600 ml/min and mixed with Ar flowing at 780 ml/min in a "Y" junction after the ablation cell. NIST612 was ablated using a 40 μm -wide line traversing at 3 μs with a laser fluence of $\approx 12 \text{ J/cm}^2$ and firing at 10 Hz. Argon flow was adjusted to obtain signal ratios for $^{232}\text{Th}^{16}\text{O}^+ / ^{232}\text{Th}^+ < 0.3\%$ and $^{238}\text{U}^+ / ^{232}\text{Th}^+ \approx 1.55$. The hexapole bias was adjusted to achieve a maximum $^{43}\text{Ca}^+ / ^{57}\text{Fe}^+$ ratio ≈ 56 and less than 1 cps on background m/z 220. Under these conditions, sensitivity achieved was 2300 cps / ppm for $^{238}\text{U}^+$. Analyses were done using hard extraction (-110V on extraction lens) and without a shielded torch unless otherwise specified (Table 2.1). For both wet and dry plasma conditions, the X series 2 ion lenses had a minimal influence on the mass bias, so sensitivity was maximized for $^{238}\text{U}^+$.

To investigate the effect of analytical operating conditions on ion KE measurements for dry plasma, the Agilent 7900 and RESolution S-155 were also operated using different settings including: two different RF powers of 1350 W and 1550 W, sampling positions from 3 mm to 8 mm, carrier gas flows from 830 ml/min to 1230 ml/min, presence / absence of shield on torch (when present the shield is always grounded), He ablation gas flow from 0 ml/min to 815 ml/min, laser fluence of 3.5 J/cm^2 and 6.3 J/cm^2 , glass sample matrixes NIST610 and

STDGL-2b2 [104], type of diatomic gas addition (N₂ or H₂), and ion lens settings (hard and soft extraction modes and tuning for different mass bias).

| | Agilent 7900 | Thermo X series 2 |
|-----------------------------------|--|--|
| 1 st Extraction Lens V | 0 V for wet plasma +2 V for dry plasma | -130 V for both wet and dry plasma |
| 2 nd Extract Lens V | -120 V for wet plasma -100V for dry plasma | None |
| Ar Carrier gas flow | 800 ml/min through nebuliser 400 ml/min makeup for wet plasma 1050 ml/min for dry plasma | 880 ml/min for wet plasma 780 ml/min for dry plasma |
| He flow (for dry plasma) | 350 ml/min | 600 ml/min |
| RF Power | 1350W for both | 1400W for both |
| Sample position | 10 mm for wet plasma 3.5 mm for dry plasma | 145 mm for wet plasma 170 mm for dry plasma |
| Sample Cone | 1.1 mm diameter Pt cone | 1.0 mm diameter Ni cone |
| Skimmer Cone | 0.4 mm diameter Pt cone | 0.7 mm diameter Ni cone |

Table 2.1. Instrument settings for wet and dry plasma conditions for both ICP-MS instruments tested.

2.3 Measurements

To measure ion KE, a stopping potential was applied by increasing the bias offset voltage on the mass filter quadrupole rods (QP bias) as outlined by Olivares & Houk [105]. A maximum sensitivity plateau region is reached around -4 volts on the QP bias lens for both the Agilent and Thermo ICP-MS instruments. The QP bias voltages were then made more positive in one-volt increments. Signal intensities for ions at a range of m/z values were measured at each step until no signal was detected. Signal intensities were normalized to the maximum value and plotted against the corresponding QP bias voltages. An exponential function was fit to the curve at low signal values and a QP bias voltage at 1% of the original signal [81] at a QP bias voltage of -4V (normal operating conditions) was calculated from the exponential equation (Figure 2.1). Day to day reproducibility of these measurements is $\pm 0.3V$ for ions above m/z 40 and is $\pm 0.8V$ for ions less than m/z 40. Stopping potential measurements using $^{238}\text{U}^+$ were confirmed by using the octopole bias (Agilent 7900) or the hexapole bias (Thermo X Series 2) instead of the quadrupole bias to check that there was no distortion in the quadrupole RF and DC fields affecting the transmission of ions [106]. Using the octopole or hexapole bias, the ion KE derived varied by less than 0.3V from that measured by the QP bias. We also note that changes to ion lenses involved in ion beam offsets (i.e. photon stop) do not affect the measured stopping potentials.

Under optimal tuning conditions (Table 2.1), ion KE measurements were made in wet plasma mode nebulizing a 10 ppb multi element solution, and in dry plasma mode while ablating a 40µm line on the NIST612 glass at 10 Hz, 3.5 J/cm², and 3 µm/sec.

2.3.1 *Measurements made under non-optimal setting*

For ion KE measurements done with N₂ or H₂ addition, the diatomic gases were added after the ablation cell to minimize effects on the ablation process. The flow rates were controlled by a single mass flow controller that was normally plumbed with N₂, but was utilized for H₂ addition as well, with ample time allowed for all gas lines to purge between switching gas compositions. The flow rates for each gas (N₂ and H₂) were measured by external flow meter to be 5 ml/min. Ion KE measurements were measured with and without the shield on the torch for each diatomic gas tested.

Laser ablation is usually done in a He atmosphere [31], so He is a substantial component of the ICP-MS central channel gas in these experiments. Tests using the RESOLution S-155 and the Agilent 7900 ICP-MS were conducted to determine if He gas influences the ion KE. For this test ablation was done in an Ar atmosphere using a flow rate of 0.3 L/min. Additional Ar was added after the ablation cell to keep the sum of the gas flows similar to those used under normal analytical conditions. Helium was added using a “T” junction after the ablation cell. Ablation was done in Ar and He added after the ablation so that changes in He flow rates did not affect the ablation properties. Two experiments were conducted: the first in which the He flow rate was changed while keeping the argon flow rate constant; the second in which the ratio of He to Ar, was changed. Additionally, the sampling position and carrier gas flow rate were each changed systematically. These tests used only ²³⁸U⁺ to assess ion KE.

For each of the different plasma conditions described above, the signal intensities on either NIST612 (dry plasma) or a multi-element solution (wet plasma) were recorded to compare performance at each condition. The results are reported in the Electronic Appendix.

2.3.2 Apparent T_{gas} from ion KEs.

Apparent T_{gas} values were determined from plots of measured KE_{max} vs. m for various elements (Figure 2.2). The procedure is derived from that of Tanner [75] Tanner's study uses KE_{avg} = mean kinetic energy to derive apparent T_{gas} from the following Equation 2.1:

$$KE_{avg} = \frac{5}{2} k_B \left(\frac{m}{m_{Ar}} \right) T_{gas} + V_p$$

Equation 2.1. Calculation of average ion kinetic energy where m = mass of ion, m_{Ar} = mass of Ar, k_B = Boltzmann constant, and V_p = plasma potential.

where m = mass of ion, m_{Ar} = mass of Ar, k_B = Boltzmann constant, and V_p = plasma potential determined from intercept of plot with vertical axis. Thus, the plots of KE_{avg} vs m have slope = $5/(2 m_{Ar}) k_B T_{gas}$.

We actually measured KE_{max} instead of KE_{avg} . Long experience and inspection of many such plots indicate KE_{max} to be $\approx 2 * KE_{avg}$ [107]. Integration of the Boltzmann Distribution for various values of m and T_{gas} indicate the approximation $KE_{max} = 2.3 KE_{avg}$ (Equation 2.2) is accurate in the range of values likely in the present work [108].

$$KE_{max} = 2.3 KE_{avg} = \frac{11.5}{2} \left(\frac{m}{m_{Ar}} \right) T_{gas} k_B + V_p$$

Equation 2.2. Calculation of maximum ion KE. Terms the same as in Equation 2.1.

Thus, the slopes of our plots were interpreted to yield T_{gas} values in this modified way. In some cases, the measured ion KE for light ions fell far above the line through the points for other elements. These anomalously high ion KE values were ignored for purposes of calculating apparent T_{gas} . Hereafter we use abbreviation KE to indicate maximum ion kinetic energy, but for the purposes of apparent T_{gas} estimates we have converted KE_{max} to KE_{avg} . Uncertainties on the apparent T_{gas} estimates presented in Tables 2.2 and 2.3 are at the 95% confidence interval and calculated from the uncertainty in the slope of ion KE vs. mass

2.3.3 Polyatomic ions

Polyatomic interference production was assessed for both wet and dry plasma conditions by $^{232}\text{Th}^{16}\text{O}^+$ and $^{43}\text{Ca}^{16}\text{O}^+\text{H}^+$. ThO^+ has one of the strongest oxide bonds [74] (dissociation energy = 8.74 eV), making it the 'worst case scenario' under a given set of conditions. Also, no element exists at m/z 248, so the count rate there is solely attributed to $^{232}\text{Th}^{16}\text{O}^+$. The

NIST612 reference glass is commonly used in laser ablation and contains a large amount of Ca (>8 wt %) relative to Fe (51 µg/g). Because of this high Ca content, $^{57}\text{Fe}^+$ is subject to interference from $^{40}\text{Ca}^{16}\text{O}^1\text{H}^+$ in the NIST612 glass. This CaOH^+ interference will cause an inaccurate calibration for Fe in matrixes that have low Ca/Fe ratios (e.g. BCR-2g).

Two sets of dry plasma experiments were conducted on the Agilent 7900 ICP-MS to demonstrate the behaviour of polyatomic species vs. atomic species at the same mass. In the first experiment NIST612 and BCR-2g ($^{43}\text{Ca}^+ / ^{57}\text{Fe}^+ \approx 105$ and ≈ 0.03 , respectively, using GeoReM preferred values and natural isotopic abundances) were ablated using a 43-µm-wide line at 3 µm/sec, 10 Hz and 3.5 J/cm² fluence. The QP bias was increased from -6 V to +5V in 1 V increments and signal intensities recorded. In the second experiment using wet plasma, a solution containing Be, Sc, Y, In, Ba, Ce, Tl, Th, and U was spiked with Ca and Fe in two different ratios matching that of NIST612 and BCR-2g reference materials. As with the dry plasma tests, the QP bias was made increasingly positive while taking measurements at each step.

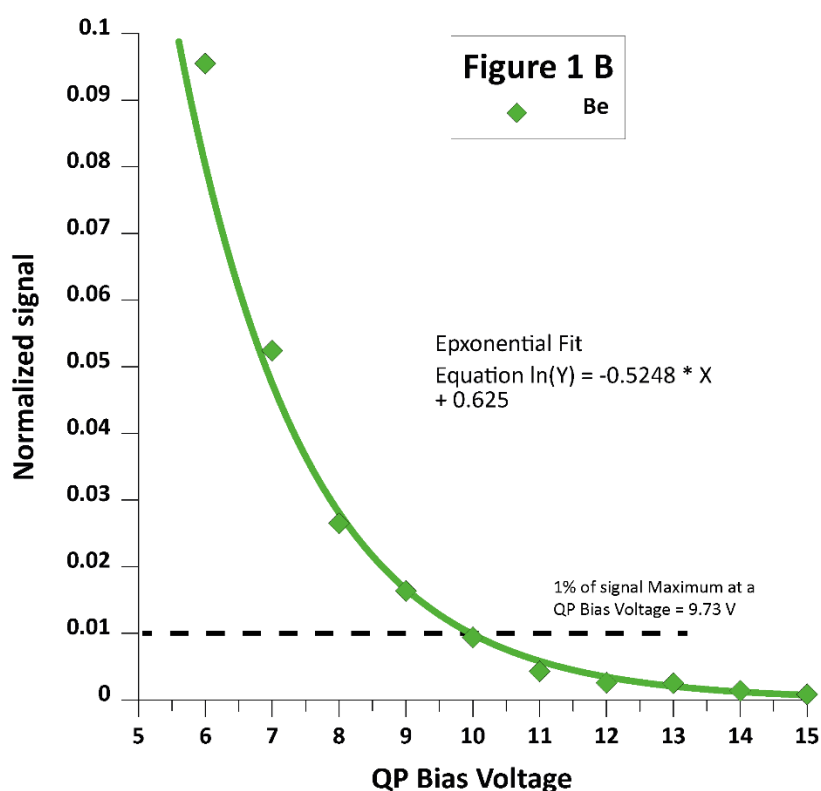
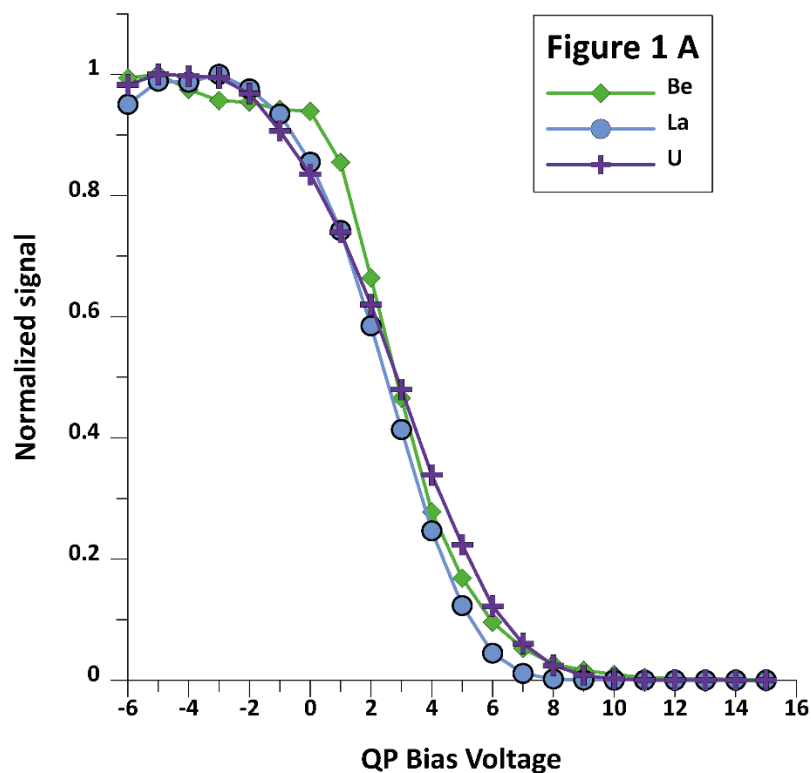


Figure 2.1. A) Examples of stopping curves for wet plasma using the Agilent 7900 as an increasing stopping potential (QP bias) is applied. Signal normalized to QP bias at -4V. B) Expanded view of the lower region of the stopping curve for ^9Be where the signal crosses through the 1% value of the normalized signal. Equation from exponential fit line is used to calculated model voltage of QP bias at this 1% signal value and this voltage is utilized as the maximum ion KE value.

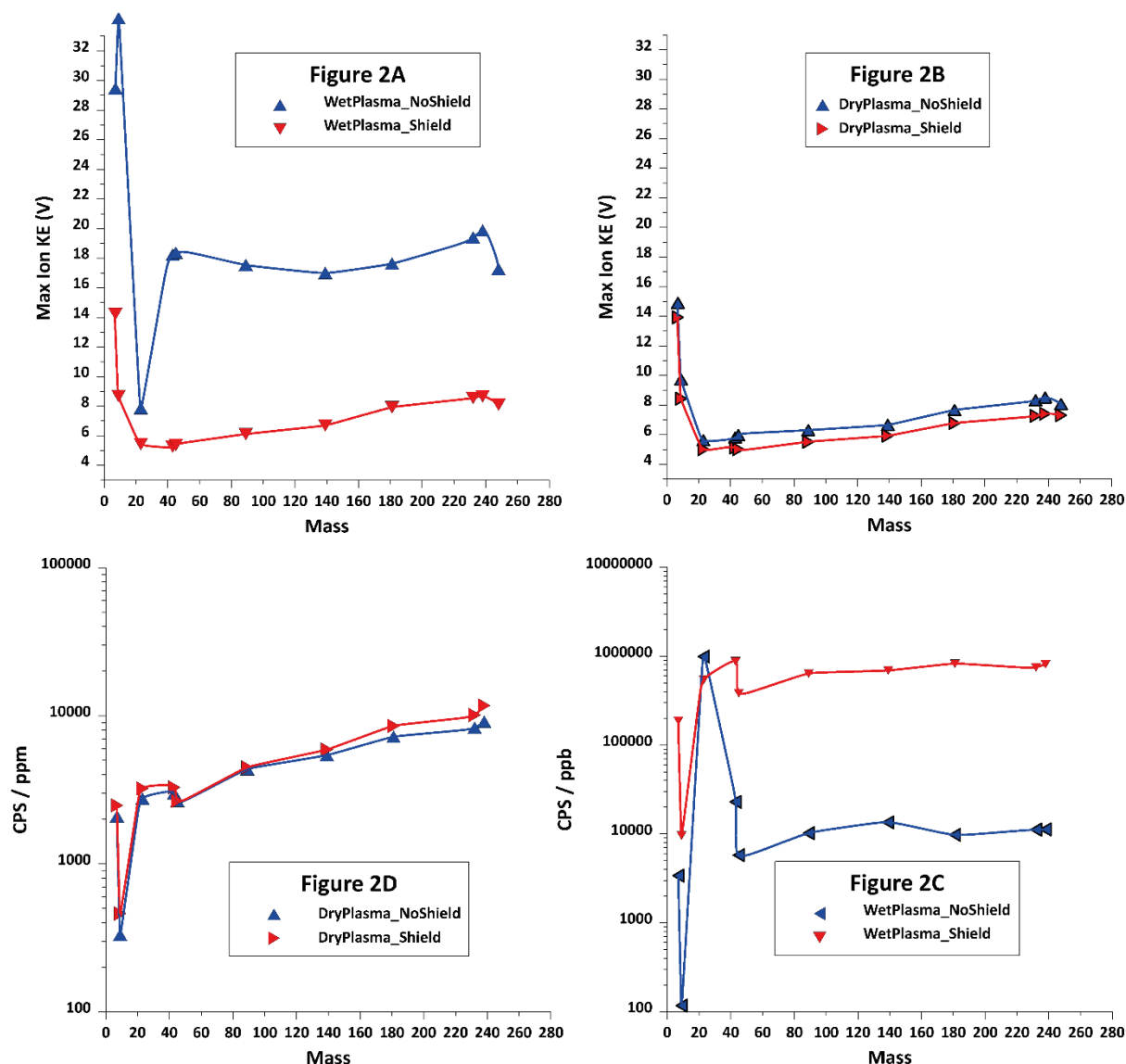


Figure 2.2. Measurements made on an Agilent 7900 by applying a stopping potential using the QP bias and using the voltage at 1% of normalized signal as shown in Figure 2.1. A: Ion KE distribution vs. ion mass for wet plasma with and without the shield present. B: Ion KE distribution vs. ion mass for dry plasma with and without the shield present. C and D: Corresponding ion yields for conditions in A and B respectively where wet plasma yield is in counts per second (cps) per ppb and in dry plasma are in cps per ppm. Wet plasma measurements performed in a 10 ppb solution while dry plasma measurements were performed using a line scan on the NIST612 glass.

2.4 Results

2.4.1 Ion energy (KE)

The measured ion KEs for both wet and dry plasma have similar patterns for ions greater than $^{23}\text{Na}^+$: ion KE increases with increasing mass (Figures 2.2 and 2.3), consistent with previous work [75, 105, 109]. For ions lighter than $^{23}\text{Na}^+$ the ion KEs generally increase with decreasing mass for both wet and dry plasma conditions for the Agilent 7900. $^7\text{Li}^+$ has the

highest measured KE of any ion, nearly double that of $^{238}\text{U}^+$. The phenomenon was not seen for the Thermo X Series 2 (Fig. 2.3B).

Comparisons of ion KEs for wet and dry plasma were done using the normal conditions for routine analysis (optimized as described above) initially. Further tests conducted measuring ion KEs while varying RF power, laser fluence, sample matrix and ion extraction lens settings (hard vs. soft extraction) did not significantly change (i.e. $<0.5\text{V}$ at mid to heavy masses) the measured ion KEs for dry plasma with the Agilent 7900 (data not shown). Importantly, changing the mass bias significantly, using the Omega lenses, did not cause a significant change in ion KE either. Other parameters including sampling position, carrier gas flow rate, the presence or absence of the shield, and He (ablation) gas flow rate had measurable impacts on the ion KE. There is a positive correlation between carrier gas flow rate and interface pressure, however, there is a negative correlation of these two parameters and ion KE (Figure 2.4A).

Tests conducted with ablation in argon with helium added to the carrier gas before the plasma are shown in Figure 2.4B. Addition of He while keeping Ar flow constant increases the interface pressure [84] causing a decrease in the $^{238}\text{U}^+$ ion KE, but much less so than for an equivalent decrease in Ar flow. Changing the ratio of He to Ar has a stronger effect on the $^{238}\text{U}^+$ ion KE than simply changing the He flow rate alone.

| Gas flow type and rates: | Plasma type | Shield on torch: | $^{238}\text{U}^+$ ion KE in V: | U/Th | $^{238}\text{U}^+$ cps / ppm* | Tgas K | Lower intercept (V) |
|--|-------------|------------------|---------------------------------|------|-------------------------------|------------|---------------------|
| 1050 ml/min Ar, 350 ml/min He | Dry | Shield | 7.42 | 1.10 | 11 725 | 2146 (760) | 4.6 |
| 1050 ml/min Ar, 350 ml/min He | Dry | No Shield | 8.51 | 1.06 | 9120 | 2441 (816) | 5.2 |
| 1050 ml/min Ar, 350 ml/min He, 5.0 ml/min N ₂ | Dry | Shield | 7.18 | 1.25 | 17 784 | 1791 (592) | 4.8 |
| 1050 ml/min Ar, 350 ml/min He, 5.0 ml/min N ₂ | Dry | No Shield | 8.28 | 1.19 | 15 590 | 1858 (297) | 5.8 |
| 1050 ml/min Ar, 350 ml/min He, 5.0 ml/min H ₂ | Dry | Shield | 8.09 | 1.16 | 15 240 | 1948 (579) | 5.5 |
| 1050 ml/min Ar, 350 ml/min He, 5.0 ml/min H ₂ | Dry | No Shield | 9.50 | 1.07 | 11 432 | 2127 (376) | 6.7 |
| 1200 ml/min Ar | Wet | Shield | 8.67 | 1.06 | 796 920 | 3055 (983) | 4.7 |

| | | | | | | | |
|----------------|-----|-----------|-------|------|--------|------|------|
| 1200 ml/min Ar | Wet | No Shield | 19.86 | 0.99 | 10 894 | n.d. | 17.4 |
|----------------|-----|-----------|-------|------|--------|------|------|

Table 2.2. Ion KE for $^{238}\text{U}^+$ under a variety of conditions measured on Agilent 7900. Note: sampling position for dry plasma was fixed at 4mm while for solution was fixed at 10mm. Tgas not reported for wet plasma without the shield due to unreliability of ion KE. *Solution analyses in cps/ppb. The lower intercept value in volts is the intersection of the line through masses ^{23}Na to ^{238}U at mass 0. Intercept value for wet plasma without the shield calculated using masses ^{23}Na to ^{238}U . Values in () for Tgas are the 95% confidence uncertainties in K.

| Gas flow type and rates: | Plasma type | Shield on torch: | $^{238}\text{U}^+$ ion KE in V: | U/Th | $^{238}\text{U}^+$ cps / ppm* | T _{gas} K | Lower intercept (V) |
|------------------------------|-------------|------------------|---------------------------------|------|-------------------------------|--------------------|---------------------|
| 780 ml/min Ar, 605 ml/min He | Dry | Shield | 7.67 | 1.18 | 1557 | 3629 (668) | 3.1 |
| 780 ml/min Ar, 605 ml/min He | Dry | No Shield | 7.47 | 1.24 | 1661 | 3164 (853) | 3.5 |
| 830 ml/min Ar, | Wet | Shield | 8.19 | 1.15 | 147 045 | 3905 (1168) | 3.4 |
| 830 ml/min Ar, | Wet | No Shield | 10.57 | 1.08 | 57 590 | n.d. | 5.8 |

Table 2.3. Ion KE for U^+ under a variety of conditions measured on Thermo X series 2. Note: sampling positions for both wet and dry plasma were fixed at a “Depth” value of 150. *Solution analyses in cps/ppb. The lower intercept value in volts is the intersection of the line through masses ^{25}Mg to ^{238}U at mass 0. Values in () for Tgas are the 95% confidence uncertainties in K.

2.4.2 Impact of torch shield

The results for shielding the torch under both wet and dry plasma conditions are shown in Table 2.2 and in Figure 2.2. As mentioned above, the shield was physically removed from the torch for the tests with no shield. An improvement in performance with use of the shield for wet plasma was seen, with >10V decrease in ion KE for $^{238}\text{U}^+$ and a >50x increase in sensitivity. For dry plasma conditions, however, there is a marginal decrease in ion KE of ≈ 1 V and a slight increase in sensitivity (up to 25%) compared to that obtained without the shield present. This small sensitivity gain for dry plasma with the shield is also associated with higher $^{238}\text{U}^+ / ^{232}\text{Th}^+$ signal ratios (≈ 1.14 vs. ≈ 1.08 without the shield).

It should be noted that there is a difference in mass bias between dry plasma and wet plasma conditions; the dry plasma has a higher mass bias (data not shown). Under dry plasma conditions the mass bias changes minimally under different conditions (i.e. with/without shield, with/without N_2 addition, etc.) and thus no correction for different mass bias had to be made when comparing these results.

2.4.3 Effect of diatomic gases in carrier flow

Ion KE and sensitivity were measured for dry plasma conditions on the Agilent 7900 with small amounts of diatomic gases N_2 and H_2 (5 ml/min for each gas, 0.36% of the total gas flow), while keeping all other gas flows, sampling position and other conditions constant.

These tests were done with and without the shield on the torch. With N₂ added, a slight drop (0.3 V) of the ion KE for ²³⁸U⁺ (Table 2.2) was observed with or without the shield present. Sensitivities increased ≈ 30% to 50% for elements with low first ionization potential with the shield present. Sensitivity increased ≈ 70% to ≈ 200% without the shield. The sensitivity gains with N₂ added are associated with an increase in ²³⁸U⁺/²³²Th⁺ ratios from 1.06 to 1.19 without the shield present, and from 1.10 to 1.25 with the shield present (Table 2.2).

Addition of H₂ increased ion KE by ≈ 1 to 1.5 V, depending on analyte ion mass; and with the shield present, the increase was ≈ 0.5 V to 1 V. Compared to no H₂ addition without the shield, addition of H₂ increased sensitivity by ≈ 30% to 50%, and increased sensitivity ≈ 20% to 30% with the shield. With H₂ addition, ²³⁸U⁺/²³²Th⁺ ratios are negligibly higher from 1.06 to 1.07 without the shield, and notably higher from 1.10 to 1.16 with the shield.

2.4.4 Polyatomic species

2.4.4.1 ThO⁺

For both wet and dry plasma conditions ²³²Th¹⁶O⁺ (hereafter denoted ThO⁺) has lower ion KE than its nearest atomic ion, U⁺ (Figure 2.3, the heaviest masses shown). The presence of the shield and diatomic gas addition increases ThO⁺ signal for dry plasma, while the presence of the shield decreases ThO⁺ production in wet plasma conditions. Increasing the stopping potential decreases signal for all m/z values, however, atomic ions (e.g. ²³²Th⁺) will decrease less at the same stopping potential as ThO⁺ (Figure 2.5), consistent with the lower ion energy measured for the polyatomic ion ThO⁺.

2.4.4.2 CaOH⁺

In NIST612 the concentration ratio [Ca]/[Fe] is high (1668), so even under dry plasma conditions the signal at m/z 57, corresponding to a minor isotope of Fe, has a large proportion of the polyatomic species ⁴⁰Ca¹⁶OH⁺ (hereafter called CaOH⁺). In BCR-2g the [Ca]/[Fe] concentration ratio is significantly lower (0.524), so that the signal at m/z 57 is largely atomic ⁵⁷Fe⁺, with a negligible contribution from CaOH⁺. With increasing stopping potential, the stopping curves for ions at m/z 57 for NIST612 (mostly CaOH⁺) show different behaviour than those for BCR-2g (almost purely ⁵⁷Fe⁺, Figure 2.6B). The stopping curves for m/z 57 in BCR-2g show a sharp decrease at QP bias values greater than 0 and relatively constant levels at lower QP bias values. However, the curve for m/z 57 for NIST612 (⁵⁷Fe⁺ & CaOH⁺) shows a

continuous decrease across the range of QP bias values. Consequently, the Fe concentration values for BCR-2g, calibrated using the NIST612 data and assuming that the entire signal at m/z 57 is composed of $^{57}\text{Fe}^+$ ions, become more accurate as the stopping potential increases (Figure 2.6A). Figure 2.6B shows that dry plasma has a greater discrepancy in the signal drop off for mass 57 between the two Ca/Fe matrixes than seen for wet plasma.

2.4.5 Ion lens tuning

Several tuning parameters had different optimum values for wet vs. dry plasma conditions. The sampling position for dry plasma conditions on the Agilent 7900 moved upstream substantially compared to wet plasma conditions to obtain optimum tune conditions (sensitivity, U/Th ratio, oxides, etc.). Extraction lens voltages required only minor adjustments between the two plasma conditions: extraction lens 1 was 0 V in wet plasma and 2 V in dry plasma, while extraction lens 2 was -120 V in wet plasma and -100 V in dry plasma. The behaviour of the omega lens in the Agilent 7900 was different between wet and dry plasma conditions (Figure 2.7) such that there is an offset ($\approx 6\text{V}$ for $^{238}\text{U}^+$) in the optimum omega lens value and a change in the relative effect this lens has on the sensitivity between wet and dry plasma conditions. The sensitivity for dry plasma is more affected than that for wet plasma for the same voltage change in the omega lens as seen in the broader shaped curves for the latter in Figure 2.7.

A similar set of tests were also done on the Thermo X series 2. When switching between wet and dry plasma, the sampling position remained essentially unchanged and very little or no change in any of the lens settings was needed for the optimum sensitivity, background, etc. (data not shown).

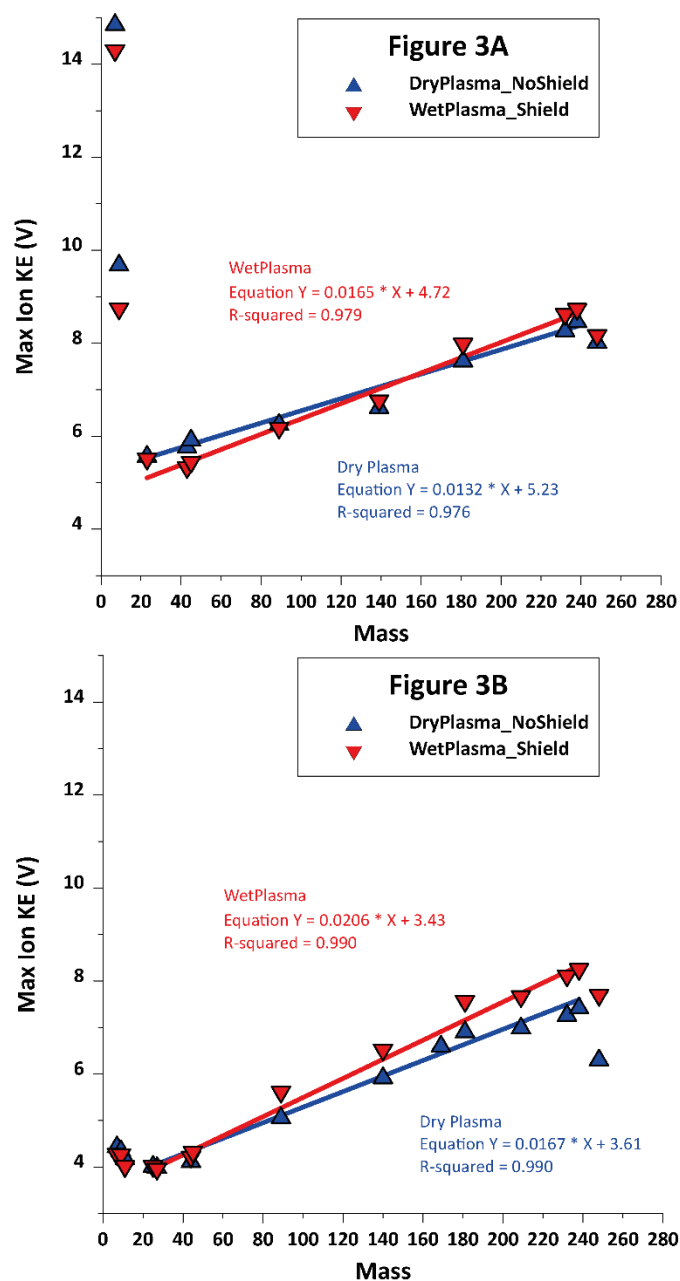


Figure 2.3. Plot of ion KE vs. ion mass for normal analytical conditions under wet and dry plasma for Agilent 7900 (3A) and Thermo X series 2 (3B). On the Agilent 7900, ions lighter than m/z 23 show different behaviour compared to ions greater than m/z 23, whereas this behaviour is not seen on the Thermo X series 2. Both ICP-MS instruments show a shallower slope for dry plasma conditions compared to wet plasma and for all tests the polyatomic $^{248}\text{ThO}^+$ has lower KE than adjacent ^{238}U .

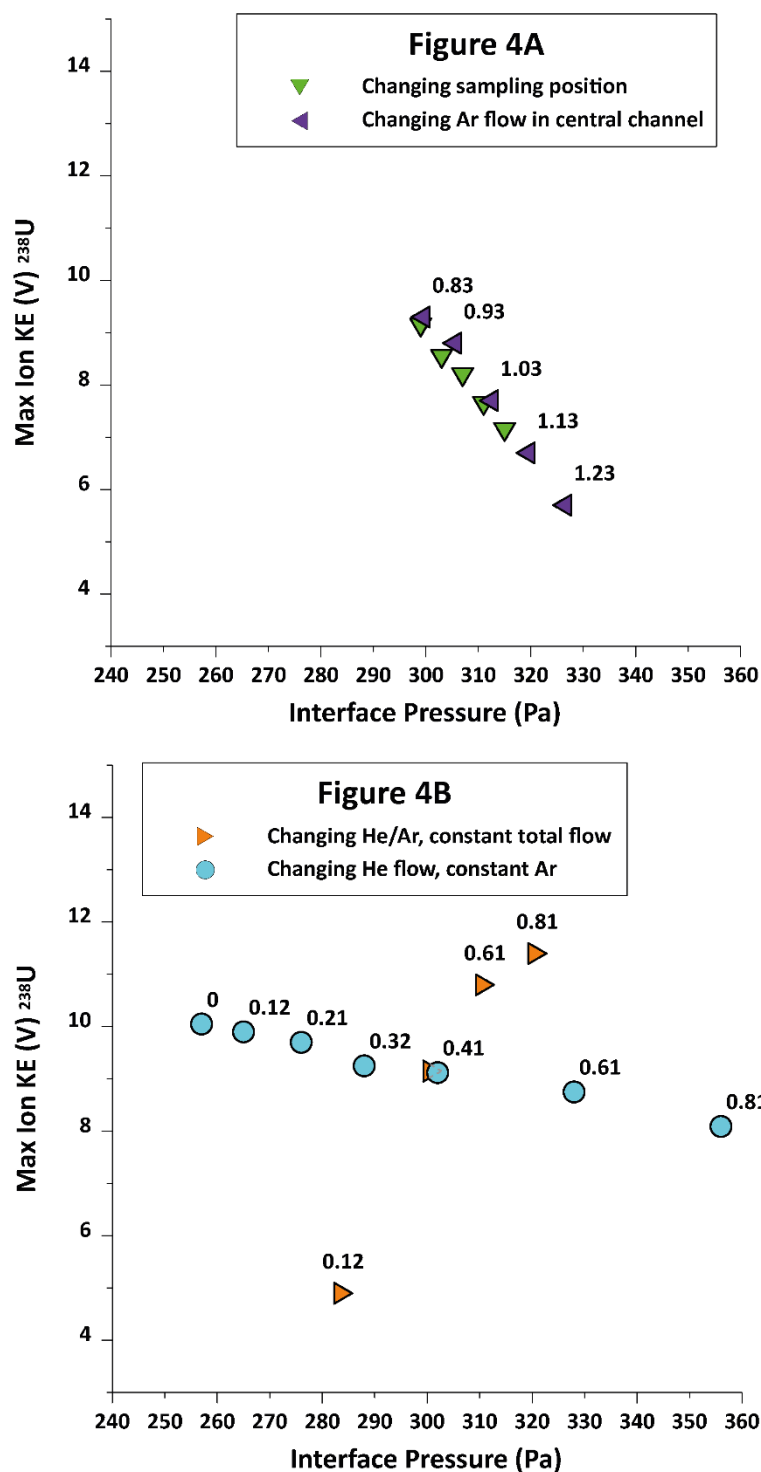


Figure 2.4. Ion KE measurements for U^+ at various conditions for dry plasma on Agilent 7700. A) Ablation performed in the atmosphere of pure He flowing at 350 ml/min. Changes in interface pressure (by changing sample position or Ar central channel gas flow rate) have a significant effect on ion KE for U^+ . Numbers next to symbols represent Ar flow rates in l/min. B) Ablation performed in the atmosphere of pure Ar, with He added to the carrier gas through a “T” junction after the aerosol exited the sample cell. Increasing the rate of He (blue circles) while keeping argon flow constant decreases ion KE, whereas increasing the He to Ar ratio (orange triangles) while maintaining a constant total flow rate, significantly increases ion KE.

2.5 Discussion

2.5.1 Ion KE for $m/z < 23$

The Agilent 7900 requires much more positive stopping voltages for ions lighter than Na^+ compared to the predictions extrapolated from the measured values for heavier elements (Fig. 2.3A) [75]. While this behaviour of light masses could be an artefact of using the quadrupole bias as the stopping potential, similar behaviour of ion KE of light masses was also observed by Chambers & Hieftje [106] using a retarding plate inserted into the mass spectrometer as the ion stopping mechanism. Alternatively, this behaviour could be due to some sort of space charge phenomenon [106, 109]. The Thermo X series 2 displays a different pattern under both wet and dry plasma conditions, characterised by little change in light masses stopping potential compared to m/z 23 (Fig. 2.3B). The cause of this difference in behaviour of light ions on some instruments remains unclear, therefore, the following interpretations are based on ion KE measured for ions above m/z 23.

2.5.2 Ion KE for $m/z > 23$

On both instruments under normal operating conditions, the ion KE measured in wet and dry plasma modes show behaviour consistent with the observations of Fulford and Douglas [109]. There is a minor, but consistent difference in the relationship between analyte ion mass and ion KE in dry plasma compared to wet plasma, with the latter showing a steeper slope (Fig. 2.3A & 2.3B; slopes calculated for m/z from 23 to 238).

The dependence of $^{238}\text{U}^+$ ion KE on the ICP operating conditions for dry plasma was investigated by changing the flow rate of Ar carrier gas and the sampling position (Fig. 2.4A). Changes in ion KE of $^{238}\text{U}^+$ were used to characterise changes of the slope as, in all measurements performed in this study, there was a strong correlation between these two parameters. As was previously shown for wet plasma [75, 105], increasing argon flow rate or moving sampling position downstream decreased $^{238}\text{U}^+$ KE for dry plasma at a given interface pressure (Fig. 2.4A). At lower pressure in the interface region, the gas dynamic expansion is faster, and the ions obtain higher KE [110]. The same behaviour is seen for the wet plasma (data not shown) and this behaviour is consistent with previous observations [75, 105]. The number of collisions and ion has with the background gas species in the ICP-MS interface has been given by Douglas and French [110] and these potentially have an impact on the

measured ion KE using stopping curves. However, previous studies [75, 105] have derived T_{gas} using ion stopping curves and give results consistent with spectroscopic measurements of the ICP temperature.

T_{gas} estimates calculated from the slope of mass vs. ion KE are presented in Table 2.2. Repeat measurements of ion KE on different days give a reproducibility of the calculated T_{gas} of ± 50 K (not shown), while the uncertainty on the slope (mass vs. ion KE) used for the T_{gas} estimate is ≈ 800 K. The intercept of this ion KE vs. mass line is between 4.6 and 5.2 volts for dry plasma with and without the shield, respectively (Table 2.2). The presence of the shield for wet plasma had the largest difference in the intercept of the KE vs. mass line; 4.7 and 17.4 volts with and without the shield respectively.

From equation (a) above, the intercept should represent any initial electrical potential present in the ICP, and since the intercept is lower with the shield present for both dry and wet plasma conditions, this suggests there is an electrical potential present in the plasma that the shield is able to mitigate. The presence of an electrical potential in the plasma is significant and implies that there can be some charge separation between negatively charged electrons and positively charged ions in the plasma before the extraction process. However, any charge separation for the ICP is very similar between wet and dry plasma when the shield is used.

Apparent T_{gas} calculated using the shield for wet plasma conditions are 3055 K and ≈ 3905 K for the Agilent 7900 and Thermo X series 2, respectively. For dry plasma conditions without the shield, apparent T_{gas} is 2441 K and 3164 K for Agilent 7900 and the Thermo X Series 2, respectively (Tables 2.2 and 2.3). Apparent T_{gas} estimates for wet plasma conditions without the shield are likely to be anomalous due to the high potentials present (Table 2.2), and no interpretations are made from these.

Apparent T_{gas} estimates in this study are consistent with measurements performed at similar ICP operating conditions [75] and are significantly lower than those obtained at lower carrier gas flow rates and at sampling positions further upstream [75, 105]. Interestingly, the apparent T_{gas} for dry plasma is consistently lower than those for wet plasma under normal analytical conditions on both the Agilent 7900 and the Thermo X series 2, in conflict with the term ‘hot plasma’ as it is often applied to dry plasma conditions lacking H_2O species. All apparent T_{gas} estimates here are significantly cooler than the typical ICP temperature (5000-7400K [111]) and these could be affected by the presence of ion optics, gas collisions in the

interface, use of the quadrupole as the ion stop. Previous unpublished work by Houk [107] using a similar Sciex instrument as Tanner [75] showed little difference between stopping curves produced with the quadrupole bias with ion optics present and those by the stopping grid without ion optics and are unlikely to affect results presented here. Gas collisions in the interface or due to the skimmer shock wave are more likely to affect the apparent T_{gas} values measured. For example, Taylor and Farnsworth [112] have shown that skimmer cone designs in modern ICP-MS have a shock formation behind the skimmer. It is possible that this shock is causing gas collisions that are impacting the free jet expansion properties and therefore our T_{gas} estimates. Previous work by Lim et al. [113] also showed that measurement of the temperatures in the Mach disk were significantly less than the ICP and are more consistent with the apparent T_{gas} results here so it is also possible that the apparent T_{gas} we record here is from the Mach disk. This study focusses on the differences in ion KE between wet and dry plasma rather than interpreting these apparent temperatures in further detail.

Given the negligible change in ion KE for dry plasma with parameters such as sample matrix or laser fluence (data not shown), it is likely that the nature of particles from the laser ablation process has little effect on ion KEs.

One important difference between dry and wet plasma is the use of He; in dry plasma He is $\approx 25\%$ of the total central channel gas entering the plasma. If He changes the temperature or electrical properties of the plasma [77], this would have an effect on the measured ion KEs. For example, Figure 2.4B shows that increasing He flow rate, while keeping the sampling position and the Ar flow rate constant, causes a decrease of $\approx 2\text{V}$ in the ion KE for $^{238}\text{U}^+$ despite a substantial increase in the interface pressure ($\sim 100\text{Pa}$). However, in Figure 2.4A there is 4V decrease in ion KE for $^{238}\text{U}^+$ with $<30\text{Pa}$ change in interface pressure when changing the Ar flow rate. Keeping the total gas flow rate constant but changing the ratio of He to Ar changes the $^{238}\text{U}^+$ ion KE by 6V for a 35Pa change interface pressure (Fig. 2.4B) and this change is consistent with the increasing Ar flow rate affect in Figure 2.4A. Taken together, the above observations suggest He has only a minor effect on ion KE, even when He comprises $\approx 50\%$ of the total gas flow into the plasma. This is surprising as the lighter He gas should accelerate to a higher velocity than Ar and therefore imparting higher ion KE. The relatively minor impact of the presence of He in the central gas channel on the ion KE may be because of He

preferentially diffusing out of the ion beam during sampling or possibly due to fewer background gas collisions due to the significantly smaller size of He to Ar.

Sesi et al. [77] showed that He can increase the T_{gas} of the plasma by up to 1500 °K with a 16.7% addition of He to the central channel, for a free-flowing ICP that is not being sampled for MS. The lower ion KE seen for increasing amounts of He addition to dry plasma in this study is inconsistent with the results from Sesi et al. [77] since the higher T_{gas} should have required higher stopping potentials (ion KE) especially for heavy ions. This discrepancy in the behaviour of He is likely due to the apparent T_{gas} measured here being influenced by the Mach disk.

2.5.3 *Impact of H₂O in the plasma*

The presence of H₂O in wet plasma applications causes a substantial increase in ion KE [81, 105, 114] compared to an Ar only plasma due to capacitive coupling of the metal cone interface and the plasma. It has been shown [70, 81] that the boundary layer between the plasma and the grounded interface (termed 'sheath') is likely to be responsible for the plasma attaining a positive potential, giving rise to ion KE greater than the calculations of Fulford and Douglas [109] based on supersonic jet expansion alone. In experiments where the plasma flows around the sampler cone, but is not extracted into it, Langmuir probe measurements show a significantly higher plasma potential than when the plasma is sampled into a low pressure interface [81]. The interpretation is that the sheath is thinner during normal plasma extraction than when the plasma is not extracted, and this allows preferential loss of electrons from the ICP, imparting the positive charge [81]. The nature (conductivity) of this sheath affects the degree of capacitive coupling and is substantially different between wet and dry plasma conditions. This could be one of the reasons why there is little benefit to use of the shield for dry plasma; there is very little capacitive coupling without H₂O species present.

The presence of H₂O in wet plasma has been shown to produce the substantial differences in electron density observed between wet and dry conditions [115] and could also be affecting the way the plasma interacts with the grounded interface via the sheath. In addition to affecting the ICP potential, H₂O addition to dry plasma has been shown to increase sensitivity with small amounts of water vapour addition (1 to 4% v/v) without the shield present ⁴³, suggesting that H₂O vapour may increase the electron density of the plasma, similar to the effect of N₂ addition [53, 116]. Liu et al. [53] showed a larger sensitivity increase

for dry plasma when adding small amounts of H₂O vapour when the shield was present, and the authors attributed this to a decrease in the ion KE in the plasma. Our results are consistent with this idea, however, there is a complex interplay between the plasma potential, charge transfer and heat transfer mechanisms of the ICP [70, 76], especially in dry plasma when trace amounts of H₂O are added. Any advantages in sensitivity and suppression of matrix effects [54] from addition of H₂O to dry plasma must be weighed against higher oxide interference rates, more complicated analytical setups and use of shield on torch.

Use of the shield on the torch for the Agilent 7900 is not advantageous for dry plasma due to the higher $^{238}\text{U}^+ / ^{232}\text{Th}^+$ and ThO^+ for the same operating conditions. The $^{238}\text{U}^+ / ^{232}\text{Th}^+$ ratio has been used as a measure of particle digestion [44] where $^{238}\text{U}^+ / ^{232}\text{Th}^+$ ratios higher than unity during ablation of NIST glass are interpreted as incomplete particle digestion in the ICP. Decreasing the Ar flow rate or moving the sampling position downstream to get $^{238}\text{U}^+ / ^{232}\text{Th}^+$ or ThO^+ production similar to values observed without the shield yields sensitivity identical to without shield conditions; negating any need or benefit of shielding the torch for dry plasma conditions. Use of the shielded torch for the Thermo X series 2 showed a different behaviour from the Agilent 7900 for dry plasma; a slight sensitivity increase, but with a similar $^{238}\text{U}^+ / ^{232}\text{Th}^+$ and ThO^+ abundances as without the shield. Causes for the different behaviour of the shield between the two ICP-MS instruments is related to their unique interface designs (e.g., cone orifice diameters) and is beyond the scope of this study.

2.5.4 Ion KE with diatomic gas addition in dry plasma

Small amounts of diatomic gases have been shown to increase sensitivity in dry plasma for either laser ablation or desolvated solution aerosols [76, 78, 79], but the impact of diatomic gas addition on ion KE for dry plasma remains unresolved. Our results show that the addition of N₂ at 5ml/min slightly decreases the heavy mass ion KE and slightly increases the plasma potential (intercept value in Table 2.2). Addition of H₂ significantly increases (>1 V) the ion KE for U⁺ as well as the plasma potential (Table 2.2). Addition of a diatomic gas at low levels ($\approx 0.3\%$ of total flow to the central channel) is unlikely to have significant effect on the gas dynamic expansion. The increase in ion KE with H₂ addition is, therefore, likely to be due to a change in the plasma potential (V_p term in equation (b)). We show that small additions of H₂ in dry plasma without a shield cause increase of ≈ 1.5 V of plasma potential relative to dry plasma without H₂ addition (intercept value in Table 2.2). This increase in plasma potential

is consistent with that of wet plasma without the shield where an increase in ion KE is seen relative to wet plasma without the shield present. However, in wet plasma there is significantly more H₂O causing an increase of ion KE by ≈ 12.7 compared to when the shield is present (Table 2.2). This suggests that the H⁺ species in the plasma may be partially responsible for the secondary discharge phenomenon seen in wet plasma. The lack of change of ion KE (with a slight decrease at heavy masses) caused by N₂ addition suggests that the two diatomic gases behave differently in the plasma. Both gases have high first ionization energies (13.6 eV for H⁺ and 14.5 eV for N⁺); however, calculation of the ionization efficiencies from the Saha-Eggert equation suggest there are $\approx 6X$ more H⁺ ions than N⁺ ions present in the plasma for the same amount of gas addition and a temperature of the ICP at 6000 K. The $\approx 7x$ greater thermal conductivity for H₂ compared to N₂ may also have an impact on the differential behaviour of the two gases in dry plasma conditions.

2.5.5 Polyatomic ion formation in wet vs. dry plasma:

One limitation to ICP-MS analyses is the formation of polyatomic species. Formation of these species, such as MO⁺ and MOH⁺, ions can potentially be different between wet and dry plasma conditions due to the substantial difference in abundances of O and H and presence of significant amounts of He [77] for dry plasma. This study utilized the ratio of mass 43 to 57 to assess the production of CaOH⁺ as ⁵⁷Fe is a commonly used isotope in LA-ICP-MS and its quantification in high Ca/Fe matrixes (e.g. calcite) can produce inaccurate results. Using the solution containing a Ca/Fe similar to the NIST612 for wet plasma and the NIST612 glass for dry plasma, Figure 2.6A shows there is greater than 10x difference between the measured 43/57 ratios between wet and dry plasma. The presence of H₂O species in wet plasma obviously affects the production of the CaOH⁺ interference. Increasing the stopping potential using the QP bias lens will preferentially remove the CaOH⁺ due to its lower ion KE, so that BCR-2g quantified on the NIST612 glass increases in accuracy with increasing stopping potential. At a QP bias setting of $\approx 2.5V$, the NIST612 has the correct 43/57 ratio (106) and BCR-2g quantified on the NIST612 glass is consistent with its GeoReM preferred values (Fig. 2.6A). Note however there is a significant decrease in signal intensities (Fig. 2.6B) for atomic masses as well for this level of stopping potential. The lower ion KE for CaOH⁺ suggests the polyatomic species is either being formed in a lower temperature environment than atomic ions [75, 117] or are preferentially attenuated from background gas collisions in the interface

or ion lenses relative to atomic ions. For wet plasma the significantly higher abundance of H₂O species means that applying a stopping potential using the QP bias only marginally improved the 43/57 ratio and that the quantification of ⁵⁷Fe in the 'BCR' like solution never achieved values consistent with the gravimetrically prepared calculated value when quantified on the 'NIST' like solution Fig. 2.6A). This suggests the mechanism of polyatomic formation (e.g. CaO & H⁺ vs. Ca⁺ & OH) or the primary location within the ICP of polyatomic formation may be different between wet and dry plasma.

Oxide polyatomic species can form interferences on atomic species for both wet and dry plasma. One advantage of wet plasma is the ability to prepare single element solutions for direct measurement of the oxide production rate for the session. For dry plasma, the nature of reference materials and minerals are such that most labs must measure ThO⁺ to estimate the rate of other species (e.g. CeO⁺) as most reference materials contain some of the target ion and the interferent (mass 57 example in NIST612 above). Preparation of synthetic glasses doped with specific elements for interference correction has been applied [118], however synthesis of these glasses requires specific equipment and can contaminate the system with other elements used in the glass flux (e.g. Li and B). This study utilizes ThO⁺ oxide species to understand the formation of other oxide species as the relationship of M⁺ and MO⁺ is dictated by the MO⁺ bond energy for a set of constant ICP conditions [74, 119].

The preferential decrease in ThO⁺ signal compared to those for both ²³²Th⁺ and ²³⁸U⁺ with increasing stopping potential (Fig. 2.5), suggests that the ion KE of the ThO⁺ species is lower than those of nearby atomic species; also seen in the ion KE plots in Figure 2.3A and 2.3B. Previously this phenomenon has been attributed to oxide species forming in a lower temperature parts of the plasma [75], however it is also possible that the oxide species preferentially collide with background gas molecules relative to atomic species, therefore imparting a lower ion KE for the oxide species. Given the significantly lower amount of oxygen species in dry plasma compared to wet plasma, a potentially important source of oxygen for oxide formation is from the matrix of the ablated material itself [74]. Witte & Houk [73] suggest oxygen from the ablated sample has little influence on the YO⁺/Y⁺ signal ratios observed while ablating Y metal and Y in SiO₂ and show that the gas kinetic temperatures in the plasma are similar while ablating the two matrices. During ablation of NIST glass used for this study, Th is likely to travel through the tubing attached to larger or more refractory

particles of the decomposed NIST glass due to very refractory nature of Th. Instead of being atomized in the ICP and ionized to $^{232}\text{Th}^+$ and finally combined with oxygen to form ThO^+ , ThO^+ may be directly ionized as ThO^+ . The positive correlation between the U/Th ratio, a measure of particle digestion, and ThO^+/Th^+ (Figure 2.8) could be evidence for such a mechanism of oxide ‘formation’, resulting from the partial decomposition of ThO^+ in the ICP, as suggested by Gilbert et al. [74]. The importance of this formation mechanism for ThO^+ is that even if the abundance of oxygen in the plasma was very low, ThO^+ would still form due to oxygen bound to thorium in the NIST glass. For dry plasma, oxides and U/Th are generally coupled as the latter is a proxy for particle digestion, which is related to temperature of the ICP. Since U/Th is correlated to temperature, there is a correlation between U/Th and ThO^+/Th in Figure 2.8 showing changing ICP conditions. In contrast to formation of oxide species, OH^+ species shows no correlation with U/Th (Figure 2.8) and this suggests that the conditions that form oxides are not the same as those where OH^+ species are formed. For dry plasma, there is less of a signal drop off for ThO^+ compared to wet plasma with increasing stopping potential (Fig. 2.5). This phenomenon is similar to that observed for mass 57 above for wet and dry plasma and again suggests that there is a difference the formation of oxide species between wet and dry plasma.

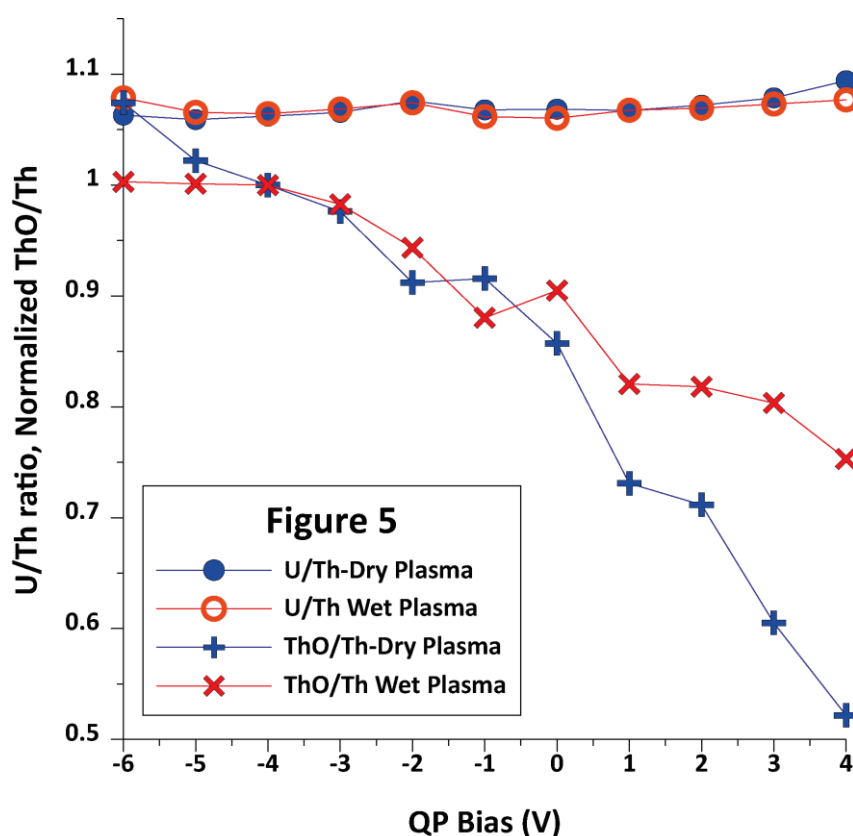


Figure 2.5. Relationship between QP bias and U/Th ratio and ThO/Th ratio for wet and dry plasma on the Agilent 7900. U/Th ratio is from the NIST612 glass (dry plasma) and a 10 ppb solution (wet plasma), both of which have U/Th ratios nominally 1. ThO/Th is normalized to the ratio at a QP bias setting of -4V. Increasing QP bias decreases signal intensities for all masses, however masses corresponding to metal ions (e.g. U & Th) drop similarly such that the ratio does not change appreciably. Masses corresponding to oxide interference (ThO) drop preferentially relative to the metal ion species (^{232}Th) of similar mass.

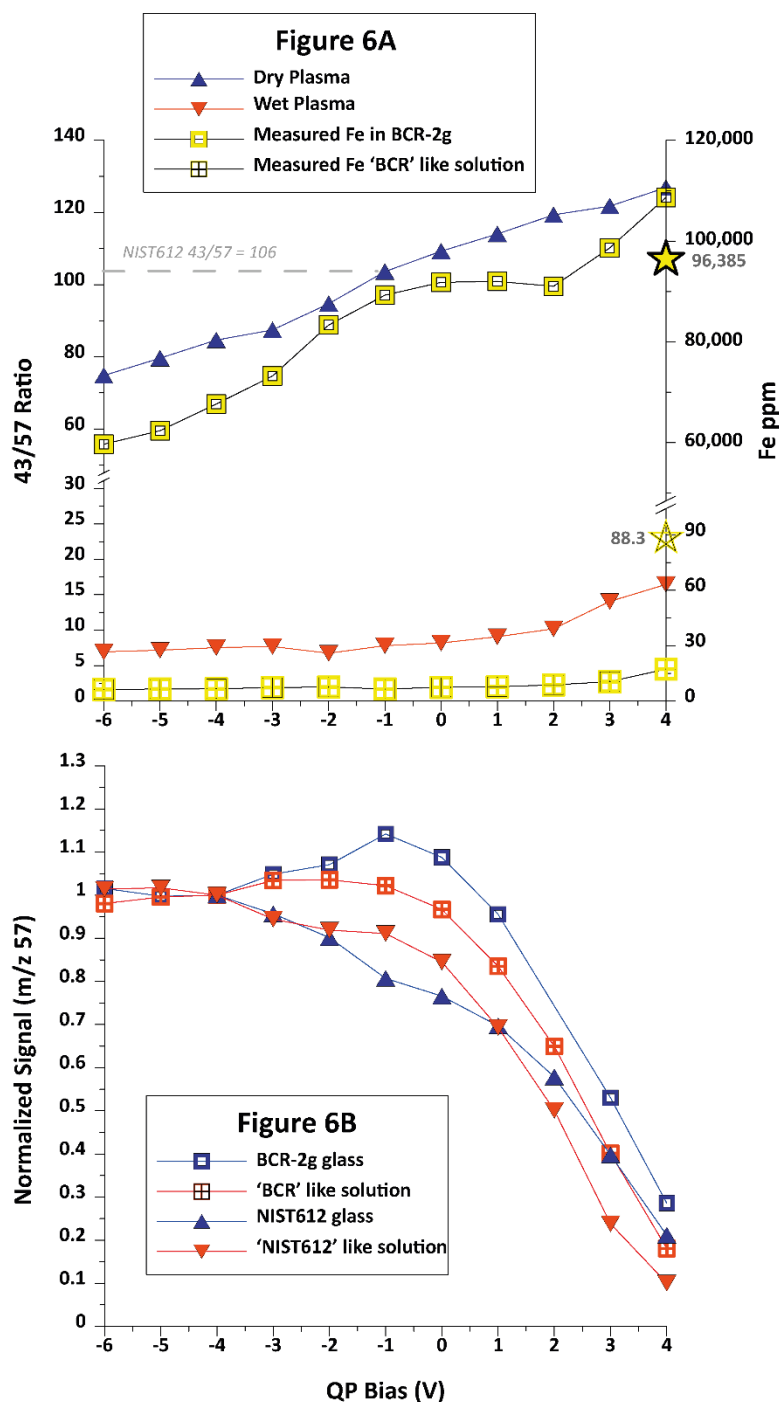


Figure 2.6. A) Relationship of changing QP bias vs. $43/57$ ratio (left axis) for wet and dry plasma on the Agilent 7900. ^{57}Fe quantified in BCR-2g using NIST612 (right axis) and in a prepared solution with similar Ca/Fe as BCR ('BCR' like solution) becomes more accurate as the $^{40}\text{Ca}^{16}\text{O}^1\text{H}$ interference is preferentially removed relative to the metal ion ^{57}Fe . Solid star indicates BCR-2g GeoReM preferred value for Fe (96,385 ppm) while trace star indicates Fe value from the gravimetrically prepared solution (in ppb). B) Relationship of QP bias on mass 57 comparing wet and dry plasma conditions for two different Ca/Fe matrixes using the Agilent 7900. Note the steeper drop off with increasing QP bias voltage for the high Ca/Fe matrixes.

2.5.6 Differences in Omega lens settings for optimal tuning conditions between wet and dry plasma on Agilent 7900:

One way to explain the smaller voltage change on the omega lens (Agilent 7900) needed to change mass bias in dry relative to wet plasma conditions (Fig. 2.7), is that the dry plasma ion beam has a lower charge. Since the omega lenses are one of the locations where the ion beam is deflected, the dry plasma ion beam should need less voltage to deflect the ion beam. Indeed, lower voltages are needed for optimum $^{238}\text{U}^+$ transmission for dry (≈ 9 V) relative to wet (≈ 15 V) plasma conditions (Fig. 2.7). The lower charge on the dry plasma ion beam could be due to the lower number of ions due to the lack H_2O species in the plasma compared to wet plasma, implying that the ablated particles (at these experimental conditions) are not adding as many charged species to the ion beam as the H_2O from wet plasma [120]. Simple calculations of the amount of H_2O loading at 2°C from Maessen et al. [121] shows the amount of H_2O entering the plasma to be $\approx 5\ \mu\text{mol}/\text{sec}$, and the volume of material from a line ablation on NIST612 at a $43\ \mu\text{m}$ spot diameter is $\approx 6 \times 10^{-5}\ \mu\text{mol}/\text{sec}$, or approximately four orders of magnitude less. Although Ar^+ makes up a large part of the charge in the ion beam, contributions from H_2O are significant given that the first ionization potentials of H and O are less than that of Ar. Additionally, there are only modest differences in the Ar^+ signal between wet and dry plasma ($\approx 30\%$) while there are >3 orders of magnitude greater signal intensities in wet plasma conditions for m/z such as 18 and 32 (H_2O^+ and $^{16}\text{O}^{16}\text{O}^+$). Interestingly, the Thermo X series 2 does not show such significant difference in optimum ion lens settings between wet and dry plasma and this could be due to the nature of the Omega lens function on the Agilent relative to the lenses on the Thermo of the fact that the Agilent was operated in 'soft' extraction while the Thermo was operated in 'hard' extraction modes. While differences in the design in lenses between the two instruments is beyond the scope of this study, we highlight the difference in ion lens setting between wet and dry plasma for the Agilent as an important aspect to consider for ICP-MS design.

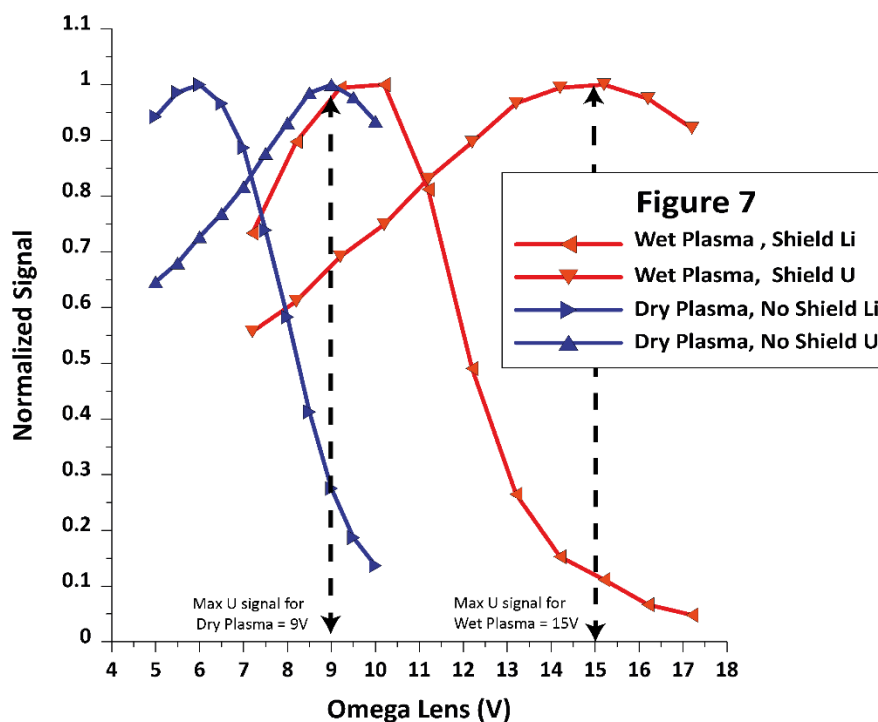


Figure 2.7. ^7Li and ^{238}U normalized signals plotted against varying Omega lens voltages for both dry and wet plasma on the Agilent 7900. Note the difference in signal maximums between wet and dry plasma.

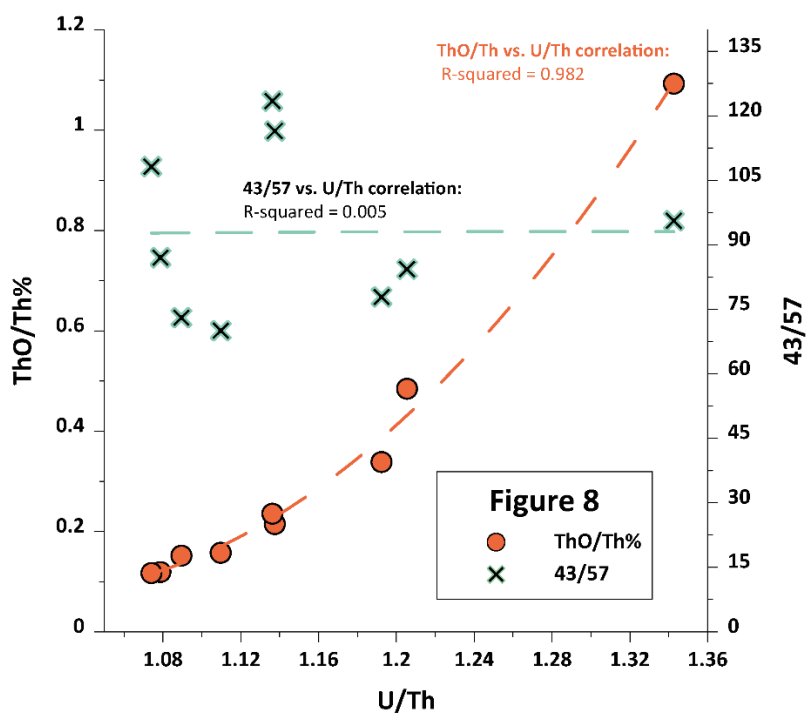


Figure 2.8. Plot of U^+/Th^+ vs ThO^+/Th^+ and $^{43}/^{57}$ production while ablating NIST612 in dry plasma conditions for the Agilent 7900. Changes in U^+/Th^+ are due to changing plasma conditions: presence /lack of shield on the torch, N_2 addition, H_2 addition, etc. Correlation of ThO^+/Th^+ with U^+/Th^+ present while none seen for $^{43}/^{57}$ data.

2.6 Conclusions:

We highlight some fundamental differences between conventional solution ICP-MS (wet plasma) and LA-ICP-MS (dry plasma) by presenting ion KE distributions for both plasma conditions. We show that there is a difference of ion KE distribution with mass between wet and dry plasma for both atomic and polyatomic species. Calculated T_{gas} for both dry plasma and wet plasma using the slope of the ion KE vs. mass line gives significantly lower temperature estimates than those found in the ICP and dry plasma consistently giving lower T_{gas} temperatures. These apparent temperatures are consistent with temperatures derived from the Mach disk [113]. The differences between wet and dry plasma cannot be simply explained by the presence of He in the carrier gas under dry plasma conditions and suggests the differences in H_2O species between wet and dry plasma has significant effects on the composition of the ICP and ion beam. The difference in ion KE distribution has implications for effects of ion lenses tuning between wet and dry plasma as seen in the omega lenses with Agilent instruments.

Electrically grounding the plasma through use of the shield torch in wet plasma is beneficial to analysis by lowering ion KE, effectively decreasing the spread in ion KE and substantially increasing instrument sensitivity ($\approx 50\times$ for Agilent). Electrically shielding the torch for dry plasma shows a $\approx 1\text{V}$ decrease in ion KE and a slight increase in sensitivity for the Agilent 7900, however, this is likely due to less power being coupled to the plasma with the presence of the shield on the torch, and leads to a cooler, less robust plasma.

Polyatomic species are interpreted to be forming due to various phenomenon with oxide species forming by different mechanisms from hydroxide species. Differences in ion KE for these polyatomic species suggest slightly different mechanisms or locations of formation between wet and dry plasma. Accuracy of elements in certain matrixes can be improved by increasing the stopping potential on the QP bias rods at a cost of ion sensitivity.

The presence of H_2O in wet plasma changes the electrical properties of the plasma and the sheath around interface region leading to higher plasma potentials. The addition of small amounts of H_2 to dry plasma make the plasma behave more like wet plasma in that the ion KE increases slightly and the shield on the torch has more of an effect. N_2 and H_2 addition to

dry plasma increases sensitivity, and for N₂ there is a marked increase in U/Th, suggesting cooler plasma than with H₂.

Different optimal lens settings and behaviour between wet and dry plasma as seen with the Agilent instruments highlights the implications for tuning in wet vs. dry plasma. Currently no ICP-MS manufacturer has an instrument designed specifically for dry plasma and results presented here suggest further development of the ICP-MS for LA-ICP-MS specific conditions may be useful to the community.

2.7 Acknowledgements

R. S. Houk was supported by Ames Laboratory, U. S. Department of Energy, Chemical and Biological Sciences Program, Contract No. DE-AC02-07CH11358, and by Iowa State University. The authors would like to thank Professor David W. Peate at the iTEA lab at the University of Iowa for use of the Thermo X series 2 and NWR 213 laser ablation system.

Chapter 3 Effects in Pb/U measurements during LA-ICP-MS analysis of the mineral apatite

As published in full: J. Thompson, S. Meffre, R. Maas, V. Kamenetsky, M. Kamenetsky, K. Goemann, K. Ehrig and L. Danyushevsky, (2016) *Journal of Analytical Atomic Spectrometry*, 31, 1206-1215.

Abstract

U-Pb ages of several apatite reference materials, acquired by LA-ICP-MS over a 3.5 year period using the Otter Lake apatite as primary standard, show systematic offsets (up to 3%) from reference ages obtained by isotope dilution mass spectrometry. The offsets are well outside known analytical errors from counting statistics, uncertainty in common Pb corrections or excess ^{206}Pb in high-Th/U materials. The age offsets also do not correlate strongly with concentrations of F, Cl, REE, Th and U, with accumulated radiation dose or with depth of ablation pits. We suggest that the observed age offsets are related to elemental fractionation at the ablation site, but their direction and magnitude cannot at present be predicted from compositional differences in different apatite samples. Our results further suggest that Otter Lake apatite is too heterogeneous for use as a calibration standard. Two other apatite samples, OD306 (1596.7 ± 7.1 Ma) and the 401 apatite (530.3 ± 1.5 Ma) are introduced as potential U-Pb standards.

3.1 Introduction

Laser Ablation Inductively-Coupled Plasma Mass Spectrometry (LA-ICP-MS) is widely used for in-situ solid sampling of materials. One example is the analysis of U-rich minerals for U-Pb geochronology. At present, LA-ICP-MS is widely used for U-Th-Pb dating of zircon [11, 122, 123], monazite [124], rutile [125], titanite [126], allanite [127] and apatite [14, 15]. While results can be acquired rapidly with minimal sample preparation, Pb/U ratios measured by LA-ICP-MS, like those obtained by SIMS methods, lack the precision of isotope dilution TIMS (MC-ICP-MS) techniques, and reasonable ($\pm 1\%$) age precisions can only be obtained by pooling of results from many ablations of the same age population. Because higher precision in isotope dilution U-Pb work comes with significantly greater analytical effort, sample consumption, loss of textural context, and higher costs; efforts are continuing to improve the quality of LA-ICP-MS U-Pb dating [128]. One area to look for such improvements is the

standardization of laser ablation U-Th-Pb isotope analyses. This is done using suitable 'matrix-matched' standards, in most cases gem-quality specimens of the same mineral, i.e. closely similar composition and ablation characteristics. However, U-rich minerals often show minor variations in composition and crystallinity which are impossible to match precisely with the available standard materials. It has been shown that small differences in composition between standard and unknown will adversely affect calculated Pb/U ratios and therefore ages [129].

Apatite, $\text{Ca}_5(\text{PO}_4)_3(\text{Cl}, \text{F}, \text{OH})$, is a common and widespread accessory mineral [130] and has the potential to offer further insight into the thermal history of a rock sample due to its lower U-Pb closure temperature compared to zircon [131-133]. Additionally, apatite can occur in geological environments where zircon is rare or where zircon age inheritance complicates the zircon age systematics. Finally, apatite is common in hydrothermal rocks and veins, and can be used to date ore deposits [134].

Apatite tends to be low in U and typically contains considerable and variable initial Pb compared to other commonly dated accessory mineral phases (e.g. zircon, monazite, baddeleyite, allanite), limiting the relative amount of in-grown radiogenic Pb. This places additional demands on data quality. The ability of LA-ICP-MS to rapidly accumulate data and the lack of age inheritance in most apatite suites allows pooling numerous spot analyses to offset counting statistics errors. This in turn makes systematic errors more noticeable. Such systematic errors are well documented for zircon [95, 122, 96] and have been attributed to 'matrix effects' related to inappropriate standard selection [122], radiation dose [95], and ablation rate [96]. Pb/U matrix effects limit the accuracy of zircon Pb/U ages acquired by LA-ICP-MS to 1-2%, even though pooling of numerous spot analyses can reduce the nominal internal precision to 0.5%. To date no equivalent effects have yet been described for the mineral apatite and this study demonstrates that such 'matrix effects' for Pb/U dating by LA-ICP-MS exist. Our observations are based on U-Pb data obtained in numerous LA-ICP-MS sessions over 3.5 years. Comparison with isotope dilution reference ages shows clear systematic age offsets in Pb/U ages (up to 3%) in some apatite samples but not in others. $^{207}\text{Pb}/^{206}\text{Pb}$ ages do not show any age offsets in the studied apatite samples due to large errors associated with common Pb corrections. We examine possible correlations of Pb/U age

offsets with apatite composition and ablation progress and discuss a number of other factors that could contribute to these offsets.

3.2 Samples and methods

The primary reference material used for this work was the Otter Lake apatite [14, 135] for which >400 spot analyses were accumulated. The secondary standard apatites used (and treated as unknowns) were McClure Mountain [136], Kovdor [137], Emerald Lake [138], Durango [139] and two in-house specimens: 401, several megacrysts from Iran weighing over 200 grams in total, and OD306 from the Acropolis Cu-Au prospect in South Australia [15] (Fig. 3.1). Slyudyanka apatite [14] was tested but is too heterogeneous in Pb/U for use in this study. Between 31 and 324 analyses of these secondary standards were included in this study. Apatite separated from the Temora gabbro [140] and Plesovice [141] granulite were also analysed in this study as the zircons in the respective rocks have ID-TIMS ages with the assumption that the apatite are the same age as the zircon.

3.2.1 Laser ablation ICP-MS

The LA-ICP-MS analyses were conducted at the University of Tasmania from April 2012 to December 2015 using the analytical conditions listed in Table 3.1. The laser ablation system was a Resonetics (now ASI) RESOLUTION S-155 with a two-volume ablation cell. The ICP-MS used was an Agilent quadrupole 7500cs ICP-MS, however in October 2014 the Agilent 7500cs ICP-MS was replaced by an Agilent 7900 ICP-MS resulting in a ~5x increase in sensitivity with a similar or lower background. At the start of each session, the instruments were tuned using the NIST612 glass scanned under the laser with a 43 μm laser spot (3 $\mu\text{m}/\text{sec}$, ~3.5 J/cm², the latter monitored on an external meter). The ICP-MS was sequentially tuned to yield U/Th ~1.05, ThO/Th <0.2 and low electrical noise (on the 7500cs ICP-MS only), and finally for sensitivity. N₂ added to the gas mix downstream of the ablation increased sensitivity [79] and decreased oxides [73]. Gas flow rates were kept constant to allow for better comparison of data on each ICP-MS. Masses analysed were ³¹P, ⁴³Ca, ⁵⁶Fe, ¹⁴⁰Ce, ²⁰²Hg, ²⁰⁴Pb, ²⁰⁶Pb, ²⁰⁷Pb, ²⁰⁸Pb, ²³²Th, and ²³⁸U.

For largely historical reasons the Otter Lake apatite [14, 135] was used as a primary standard, to correct for laser-induced fractionation, instrument mass bias, differences in element ionization and instrument drift. Because Otter Lake contains variable common Pb, a

^{207}Pb correction was applied to measured $^{206}\text{Pb}/^{238}\text{U}$ ratios on a sweep by sweep basis – see [142] for details. Each spot analysis was preceded by five shots of pre-ablation to clean the analytical site. NIST610 was analysed under the same conditions to monitor instrument mass bias in Pb isotope ratios [143]. The NIST610 standard [47] was also used to obtain trace element concentrations in the apatite samples, with ^{43}Ca as the internal standard isotope (Ca ~ 400,000 ppm in apatite). Line scan ablations were done with the same laser spot size and a scan speed of 3 $\mu\text{m}/\text{sec}$. Data were reduced using an excel-based spreadsheet, with error propagation following the recommendations from Horstwood et al.[144]. ^{204}Pb data were not used because corrections for ^{204}Hg interference caused the ^{204}Pb to be at or below the level of detection.

| Laser ablation parameters | | ICP-MS Parameters | |
|------------------------------------|--|---|--|
| System: | RESolution S-155 | Forward Power (W) | 1350W |
| Laser: | Coherent Compex Pro 110 | Reflected Power (W) | <2 |
| Wavelength (nm): | 193 | Carrier Gas flow (ml/min) | 1,050 |
| Pulse width (ns): | ~20 | Sample Depth | ~4mm |
| Laser Energy (J/cm ²): | 2.0 - unless otherwise noted | Additional Gas (N ₂ in ml/min) | 1.5 |
| Laser Rep. Rate (Hz) | 5 | Total sweep time (sec) | 0.18 |
| | | Detector | Ion Counting For Pb and U |
| Ablation time (sec): | 30 | Dwell Time (sec): | 0.03 for Pb, 0.01 for U and Th, 0.005 for others |
| Background time (sec): | 30 | Quad settling time (sec): | 0.0025 |
| Helium flow rate (ml/min): | 350 | Detector Dead Time (ns): | 37.1 |
| Laser spot size (microns): | 29-34 | | |
| Laser Cell: | Two-volume cell. Ablation in ~9 cm ³ funnel | | |

Table 3.1. Instrument parameters used over a 3.5 year period

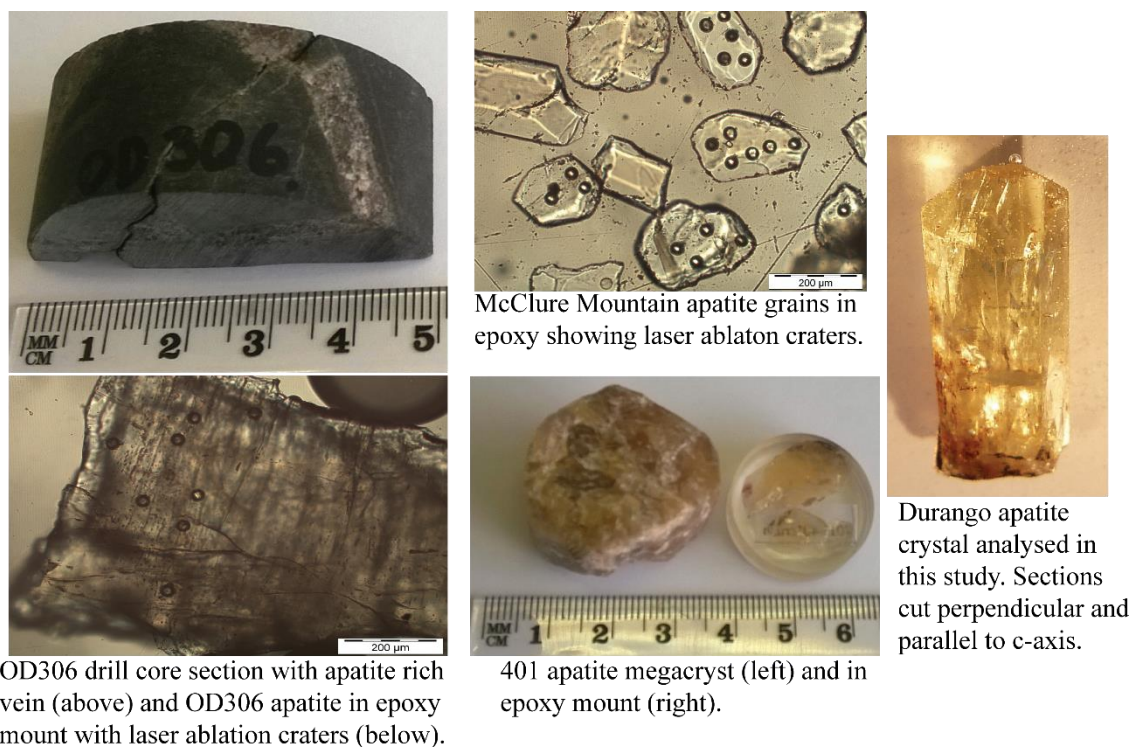


Figure 3.1. Photographs of select apatite samples used in this study.

3.2.2 Isotope dilution MC-ICP-MS

U-Pb reference ages for two in-house apatites (OD306 and 401 apatite) were produced by isotope dilution at the University of Melbourne, following methods adapted from Sniderman et al [145]. Apatite fragments weighing 1-5 mg were washed with hot distilled water, dissolved in 5M nitric acid and spiked with a ^{233}U - ^{205}Pb tracer checked against the EarthTime project synthetic zircon solutions. Pb and U were extracted using a single pass over a small anion resin column (0.15 ml of AG1-X8, 100-200 mesh [146]). Isotopic analyses were carried out on a Nu Plasma MC-ICP-MS equipped with $10^{-11}\Omega$ Faraday detectors and a CETAC Aridus desolvating system. Mass bias in Pb and U fractions was corrected using standard bracketing and internal normalization, respectively. Total Pb blanks are 20 ± 10 pg and total U blanks are 5 ± 2.5 pg. All data reduction was done using the EarthTime Microsoft Excel spreadsheet of Schoene and Schmitz [147]. U-Pb ages for the EarthTime synthetic 'zircon' solutions (provided by DJ Condon) acquired with the spike calibration and analytical protocol used here are identical within errors to their concordant 100, 500 and 2000 Ma nominal ages. Likewise, 3 fractions of low $^{206}\text{Pb}/^{204}\text{Pb}$ titanite from Mt Dromedary monzonite yield a lower

intercept age of 100.1 ± 1.9 Ma, within error of the $^{206}\text{Pb}/^{238}\text{U}$ zircon age of 99.12 ± 0.02 Ma age [89].

3.2.3 Laser pit geometries and apatite compositions

Laser ablation crater depths were measured relative to the surface of the apatite using a Wyko NT9100 optical profiler (20x objective). A false-colour image of ablation craters on McClure Mountain apatite is shown in Fig. 3.2. Major and minor element concentrations in apatite were measured on a Cameca SX100 electron microprobe at the Central Science Laboratory, Univ. of Tasmania, operated with a 15kV acceleration voltage and 30nA beam current. The electron beam diameter was defocussed to produce a 30 μm spot size to reduce migration of F and Na due to thermal interaction of the beam with the apatite target [148], and to better match the size of the laser ablation spots. The Probe for EPMA software (Probe Software Inc.) was used for acquisition and data reduction. A time-dependent intensity correction was applied to F, Na, Cl and Ca during the measurement. Spectral interference corrections were performed within the iterative quantification of the data. Settings and other information regarding EMPA are given in the ESI.

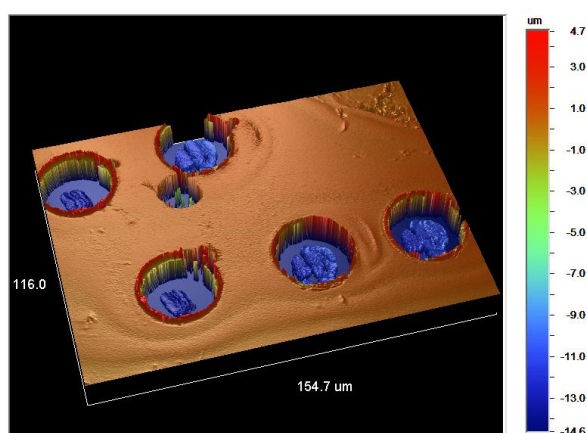


Figure 3.2. Optical profiler image of spots analysed in a grain of the McClure Mountain apatite.

3.3 Results

Average Pb/U ages for 8 apatites, all relative to Otter Lake, are given in Table 3.2 and reported at the 2-sigma level, together with available reference ages. Errors for laser ablation analysis are reported in three ways to the right of the age: error based on counting statistics and the excess uncertainty factor [94], error based on counting statistics and systematic errors related to uncertainty in common Pb composition and uncertainty in primary reference

material composition, and finally the total analytical uncertainty with all random and systematic errors included as per the recommendations of Horstwood et al.[144]. Results for each apatite sample are shown in the Tera-Wasserburg concordia diagrams (Fig. 3.3). LA-ICP-MS ages for several of these apatites show significant offsets from reference ages (Table 3.2): McClure Mountain, OD306 and 401 are younger (up to 3.5%), Emerald Lake is identical within error, and Kovdor is slightly older than, their respective reference age. MSWD values indicate a high degree of Pb/U homogeneity for most of the apatites. By contrast, Otter Lake (MSWD 2.0, n = 447, self-normalized) and OD306 large (MSWD 1.8, n = 324) are somewhat heterogeneous. Pb/U ages acquired from line ablations for some of the apatites are indistinguishable from the spot analyses and show the same age offsets relative to reference ages.

Trace element concentrations (REE and Y) are more homogeneous in large apatite crystals (e.g. Durango) than small crystals (e.g. McClure Mountain), but internal trace element variations are always smaller than the differences between different apatite samples. While absolute REE concentrations vary from apatite to apatite, the normalized REE patterns are broadly similar in all samples (Fig. 3.4). REE concentrations in the Durango apatite are better than 20% to values from Trotter & Eggins [149] solution ICP-MS analysis, despite natural variation between crystals.

Electron microprobe analysis of apatite in this study shows most are fluoroapatite in composition, however the Kovdor apatite has significantly less fluorine (0.9% vs. 3.1% to 3.8%) than the other samples and likely has a large OH component. F and Cl are measured in multiple oriented pieces of the Durango apatite. These crystals of Durango apatite are from the UTAS mineral collection and not the Smithsonian Durango apatite of Jarosewich [150], however the F contents are very similar to the expected values.

Laser crater depths (n = 5-20) measured each session varied by up to 1 μm averaged 13.7 μm (155 pulses) for all studied apatite samples (Table 3.2, Fig. 3.5). The line ablations had an average depth of 6.2 μm . Variability in ablation depth within single apatites over different sessions is as great as the variability between different apatite samples. Similar depth variations were observed for spot and line scans.

Inclusions of U-Th-rich minerals (e.g. zircon, monazite) can greatly affect laser ablation patterns in apatite. All ablation traces were examined for possible inclusions, but none were

found; consistent with the lack of such impurities in back-scattered electron images (BSE). Zircon and monazite are also unlikely to affect the bulk apatite solution-mode analyses because the dissolution procedure is too mild to dissolve such refractory minerals.

| Sample | LA-ICP-MS age (Ma) | Isotope dilution age (Ma) | # of analyses | Avg. Th $\mu\text{g/g}$ | Avg. U $\mu\text{g/g}$ | Avg. Ce $\mu\text{g/g}$ | Avg. F % | Avg. Cl $\mu\text{g/g}$ | Avg. crater / line depth (μm) |
|------------------|--------------------------------|---------------------------|---------------|-------------------------|------------------------|-------------------------|-------------|-------------------------|--|
| Otter Lake | Primary Ref. Mat. | 913 \pm 7 | 447 | 897 (96) | 113 (9) | 7339 (807) | 4.10 (0.08) | 353 (38) | 13.46 / 6.11 (0.78, 0.22) |
| OD306 | 1544.8 \pm 3.2 / 20.2 / 23.5 | 1596.7 \pm 7.1 | 324 | 71 (33) | 17 (4) | 7181 (2008) | 3.83 (0.09) | 1035 (86) | 13.84 / 6.27 (0.23 / 0.25) |
| Kovdor | 382.3 \pm 1.7 / 5.2 / 6.0 | 380.6 \pm 2.6 | 262 | 1733 (839) | 17 (10) | 5788 (2526) | 0.88 (0.02) | 140 (26) | 13.68 / 6.33 (0.86 / 0.20) |
| 401 apatite | 506.2 \pm 2.3 / 7.0 / 8.1 | 530.3 \pm 1.5 | 52 | 121 (20) | 15 (2) | 9550 (964) | 3.08 (0.14) | 7082 (40) | n.d. |
| McClure Mountain | 516.3 \pm 4.5 / 8.0 / 9.0 | 523.51 \pm 1.53 | 105 | 38 (16) | 13 (5) | 2754 (551) | 3.16 (0.12) | 203 (150) | 13.73 / 6.39 (0.56 / 0.22) |
| Emerald Lake | 92.9 \pm 1.7 / 2.1 / 2.2 | 92.2 \pm 0.9 | 77 | 106 (36) | 41 (12) | 2297 (554) | 3.82 (0.13) | 403 (91) | 13.93 / 6.19 (0.35 / 0.06) |
| Durango | 30.87 \pm 0.68 / 0.79 / 0.82 | 31.44 \pm 0.18 | 51 | 269 (40) | 12 (2) | 4450 (240) | 3.51 (0.07) | 4749 (371) | n.d. |
| Plesovice | 342 \pm 19 / 19.5 / 19.7 | 337.13 \pm 0.37 | 31 | 0.09 (0.17) | 6 (2) | 1431 (345) | n.d. | n.d. | n.d. |
| Temora | 419 \pm 12 / 13.2 / 13.6 | 416.8 \pm 1.1 | 33 | 18 (9) | 6 (2) | 1896 (359) | n.d. | n.d. | n.d. |

Table 3.2. Apatite results for Pb/U ages and select elemental compositions determined by LA-ICP-MS (Ce, Th & U) and EMPA (F, Cl). Isotope dilution ages for OD306, Kovdor, 401 apatite, and McClure Mountain were measured directly on apatite in the rock. Emerald Lake, Plesovice, and Temora are isotope dilution ages of zircon present in the same rock. The Otter Lake apatite age is from a step-leaching Pb isotopic MC-ICP-MS age – see Barfod et al.[135] for details. The Durango age is from ^{40}Ar - ^{39}Ar measurement on apatite from McDowell et al.[139] Numbers in parentheses are one standard deviation on the mean. *n.d. = not determined. All ages are reported at 2-sigma with the laser errors reported after the \pm symbol and are as follows: counting statistic errors / counting statistic errors + long term variance in secondary standards + error in common Pb composition / full analytical errors including counting statistics and all systematic errors.

3.4 Discussion

3.4.1 Comparison of bulk vs. in-situ Pb/U ages:

A laser-ablation U-Pb isotope analysis typically consumes 30 ng of target material. By comparison, isotope dilution studies consume between 1,000 and 1,000,000 ng. This enormous difference in sampling volumes could potentially produce some age differences in heterogeneous targets. However, we do not observe strong heterogeneity in Pb/U in the laser ablation data, other than those related to variable common Pb (Fig. 3.3). OD306, one of the apatites showing strong age offsets, appears to be somewhat heterogeneous (MSWD of 1.8), possibly due to small grain-scale open system behaviour. However, the excess scatter in OD306 (1.4% 2 standard deviations) is far less than the difference between the laser ablation

and reference age for this apatite (~3%). Further sources of this heterogeneity are discussed below. McClure Mountain and 401, the other two apatite showing strong negative age offsets, appear to be homogenous at the micrometer scale of the laser analysis and at the millimeter scale of the isotope dilution analyses. This suggests that comparison of spot analyses with bulk grain analyses is appropriate, and that the observed age offsets reflect matrix effects in the laser ablation analyses.

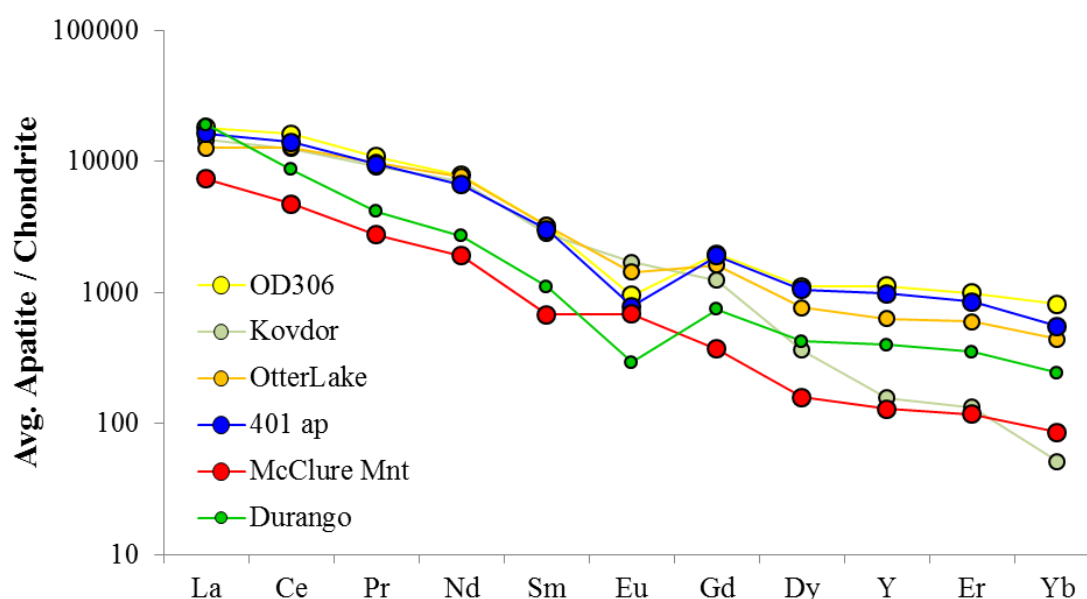


Figure 3.4. Select apatite REE patterns measured by LA-ICP-MS. Note the similar REE concentrations and patterns for Otter Lake and OD306 despite age discrepancies in LA-ICP-MS data.

3.4.2 Effects of common Pb and excess ^{206}Pb from ^{230}Th :

Apatite often contains significant and variable common Pb. Apatites also typically have high Th/U ratios; a potential source of excess ^{206}Pb (from excess ^{230}Th introduced with large amounts of ^{232}Th). The former can produce major but typically regular variations in $^{206}\text{Pb}/^{238}\text{U}$ while the latter may produce more random variation, depending on local Th/U. Correction for common Pb in apatite can be large (>10%). Several common Pb correction techniques are available (^{204}Pb , ^{208}Pb correction, ^{207}Pb correction). Here we use the 207-method implicit in the Tera-Wasserburg concordia diagram [14]. The common $^{207}\text{Pb}/^{206}\text{Pb}$ ‘anchor’ used in this correction method can be obtained by (i) selecting an age-appropriate common Pb composition from a Pb growth curve [151], from (ii) Pb isotope analysis of a co-existing low-U/Pb mineral such as feldspar, and (iii) from regression analysis of the usually linear dispersion of apatite U/Pb ratios on the Tera-Wasserburg diagram, provided the data show adequate variation in $\text{Pb}_{\text{rad}}/\text{Pb}_{\text{com}}$ (amount of radiogenic Pb to the common Pb). Micro-sampling with a 30 μm laser spot often resolves a wide range of $\text{Pb}_{\text{rad}}/\text{Pb}_{\text{com}}$ compared to bulk grain analyses where much small-scale variability is averaged. This gives the flexibility of using either a model common Pb composition for anchoring the data or a best fit isochron without an anchor. For the apatites studied here, use of an anchor $^{207}\text{Pb}/^{206}\text{Pb}$ derived from the Stacey-Kramers model Pb evolution curve [151] or regression of the data has very little effect on the obtained

lower intercept $^{238}\text{U}/^{206}\text{Pb}$ ages. Importantly, the two apatite samples with the largest age offset (OD306 and 401 apatite) contain the least common Pb, removing common Pb as a major factor in producing these offsets.

The apatite samples studied here have $\text{Th}/\text{U} > 2$ (except the apatite from the Plesovice granulite). Excess ^{230}Th incorporated during crystal growth will create an initial excess of ^{206}Pb , depending on the Th/U ratio of the mineral and the Th/U ratio of the parent melt [152]. This effect is strongest in young U-Pb systems with very high Th/U [152, 153]; but is much less important in older systems where ingrown ^{206}Pb tends to swamp any initial excess ^{206}Pb . The Kovdor apatite has a very high Th/U ratio (~ 100) and is the most likely of the apatite samples studied here to show significant excess ^{206}Pb effects, yet this has previously been shown to not be the case^{8, 18}. Excess ^{206}Pb is thus not considered to be a significant contributor to the age offsets observed in some of the apatite samples.

3.4.3 *Effects of element substitutions in apatite crystal structure:*

Apatite readily accommodates elemental substitution within its structure. The apatites studied here have high concentrations (>100 ppm) of Na, Mg, Si, V, Fe, As, Sr, REE, Th and U. Halogen (Cl, F) and hydroxyl (OH) contents vary at the % level. These substitutions are important as they could cause changes in colour, hardness and density of the apatites, which in turn could affect the ablation characteristics and produce the matrix effects observed here. The largest variations between the various apatites studied here are in their F, Cl and OH contents. Most are fluorapatite and thus have high F/Cl and F/OH; however, Kovdor apatite has low F/OH and Cl/OH. There is no obvious correlation between U-Pb age offset and halogen content (Fig. 3.5), nor does there appear to be any correlation between halogen content and ablation rate. This seems to eliminate variation in halogen contents as a matrix effect. Some trace elements show weak correlations with age offset, e.g. Th ($r^2 = 0.19$) and Ce ($r^2 = 0.21$, Fig. 3.5) but any effects would be marginal, consistent with the small variations in measured ablation rates between apatite of contrasting composition (Fig. 3.4).

Trace element substitution in apatite produces different levels of polyatomic interference during LA-ICP-MS analysis of U-Pb. Argides of the HREE are the most likely of these interfering species in the Pb mass range, and different levels of HREE would be expected to produce correlated levels of HREE argides. However, most of the apatite samples have broadly similar HREE abundances (Fig. 3.4). Also, Kovdor (slight positive age offset) and

McClure Mountain (negative age offset) both have relatively low HREE contents, precluding HREE argides as a source of differential matrix effects. We note that typical rates for argide production for transition metals are very low ($\sim 0.0005\%$ [103]). A typical Durango apatite ($\sim 50 \mu\text{g/g Er}$) would produce an Er signal of $\sim 65,000$ cps and ~ 30 cps Er-argide at mass 206. An interference of this size on Otter Lake apatite would amount to $<0.01\%$ of the total mass 206 signal, but it would account for 10% of the mass 206 signal for Durango. However, the LA-ICP-MS age for Durango is within 2% of the reference age. We conclude that HREE argides are not a major matrix effect.

3.4.4 ICP-induced 'matrix effects':

Elemental fractionation during laser ablation microsampling has been shown to be related particle size distribution effects occurring at the ablation site [44]. Elemental fractionation in the ICP has been shown to be correlated to how well particles released at the ablation site and transported to the ICP are digested in the plasma. Experiments with variably transparent NIST glasses showed that the more transparent glasses produce a broader range of particle sizes than less transparent and opaque glasses [44]. In that study, the U/Th ratio was used to assess the fate of the particles in the plasma. For this reason, gas flows on the ICP-MS instruments in the current study are tuned to generate a U/Th ratio around 1-1.05, using a line ablation on NIST612. Unfortunately, this cannot be done on apatite directly because U/Th is unlikely to be homogeneous enough in natural apatite. In other words, we can optimize the digestion of particles ablated from NIST glasses, but we do not know how well this works for minerals. Apatite is less transparent than NIST612 and should thus produce a smaller range of particle sizes during ablation, with smaller elemental fractionation. Variation in particle size distribution is thus an unlikely source of variable age offsets in apatite. A conclusive test of this assertion would require analysis of particle size distributions for each apatite. There can be a significant difference in the particle size distribution for spot vs. line analyses, with the scan speed of the lines being an important parameter [44]. It is possible that analysing lines instead of spots may produce size variable particle distributions and therefore, matrix effects within apatite. However, line scan ablations of some of the apatite samples show Pb/U ages that are the same as those of the respective spot analyses. Some apatite samples (Otter Lake, Kovdor and OD306) were analysed with a coil of narrow (2mm ID) Tygon tubing acting as a flow restrictor between ablation site and plasma. The

greater resistance to the gas flow should eliminate some of the larger particles and thus change the particle size distribution entering the plasma, yet no differences in relative Pb/U ages were observed with and without the flow restrictor. We speculate that particle size distribution is similar in all tested apatite samples, so that ICP-induced elemental fractionation is thus also unlikely to be variable between apatite samples. This eliminates the ICP source as the cause of the matrix effect on the U-Pb ages.

3.4.5 *Laser-induced element fractionation (LIEF)*

Another cause of matrix effects in LA-ICP-MS analysis is elemental fractionation at the ablation site, or laser-induced element fractionation (LIEF). Laser ablation matrix effects have been documented for zircon Pb/U ages [95, 96, 122] and the results of this study indicate similar effects could be occurring during apatite ablation. In zircon, the radiation dose (function of age and U + Th content) a mineral grain has received controls the degree of elemental fractionation [95, 154]. Zircon with high radiation doses produce ages too old relative to reference ages. However, there appears to be little correlation between radiation dose and the age matrix effect in apatite (Fig. 3.5). Radiation doses in apatite are low and the low annealing temperature (60°-110°C [133]) would tend to remove any radiation damage quickly.

Ablation rate is a control on elemental fraction (i.e. Pb/U age) in zircon [96]. As the crater deepens the measured Pb/U ratio in zircon changes substantially [94]. While ablation rates are variable in apatite, for both spot and line analyses, we did not observe a correlation with the age offsets. As shown in Fig. 3.6, there is less overall Pb/U fractionation for apatite than for zircon (same spot size, number of shots and laser energy) with ablation depth, and subtle changes in ablation rate in apatite are therefore unlikely to produce the type of age effects seen in zircon. Parameters such as crystal orientation, halogen content, colour, inclusions, etc. may influence the ablation rate in apatite, but this does not apparently produce strong differences in downhole Pb/U fractionation.

During ablation under a laser, zircon (ZrSiO_4) disintegrates to $\text{ZrO}_2 + \text{SiO}_2$ and this process has been shown to fractionate U from Pb [46]. This is the main reason for the strong downhole fractionation in zircon. During ablation of apatite, CaO deposited around the ablation site may trap the more refractory U (similar oxide boiling points: 2850°C for CaO, 2800°C for UO_2) while Pb (boiling point of PbO is 1535°C) remains mobile and may be transported to the plasma

preferentially, producing LIEF-type Pb/U fractionation. More detailed work is needed to examine this mechanism, but preliminary investigation by SEM shown in Figure 3.7 indicates that droplets around the ablation crater are depleted in P (~30%) and enriched in Ca (~20%) relative to the surrounding apatite. However, it is currently unknown why some apatite samples would have more or less of this CaO formation (or Pb/U fractionation more importantly) and it is possible there could still be other sources of Pb/U fractionation during LA-ICP-MS analysis of apatite. Figure 3.6 would suggest there is not a significant difference in the Pb/U fractionation between the Otter Lake apatite and the OD306 apatite as the laser drills down, but rather an offset that seems to be present from the onset of ablation.

Apatite Reference Materials Relative to OtterLake Apatite

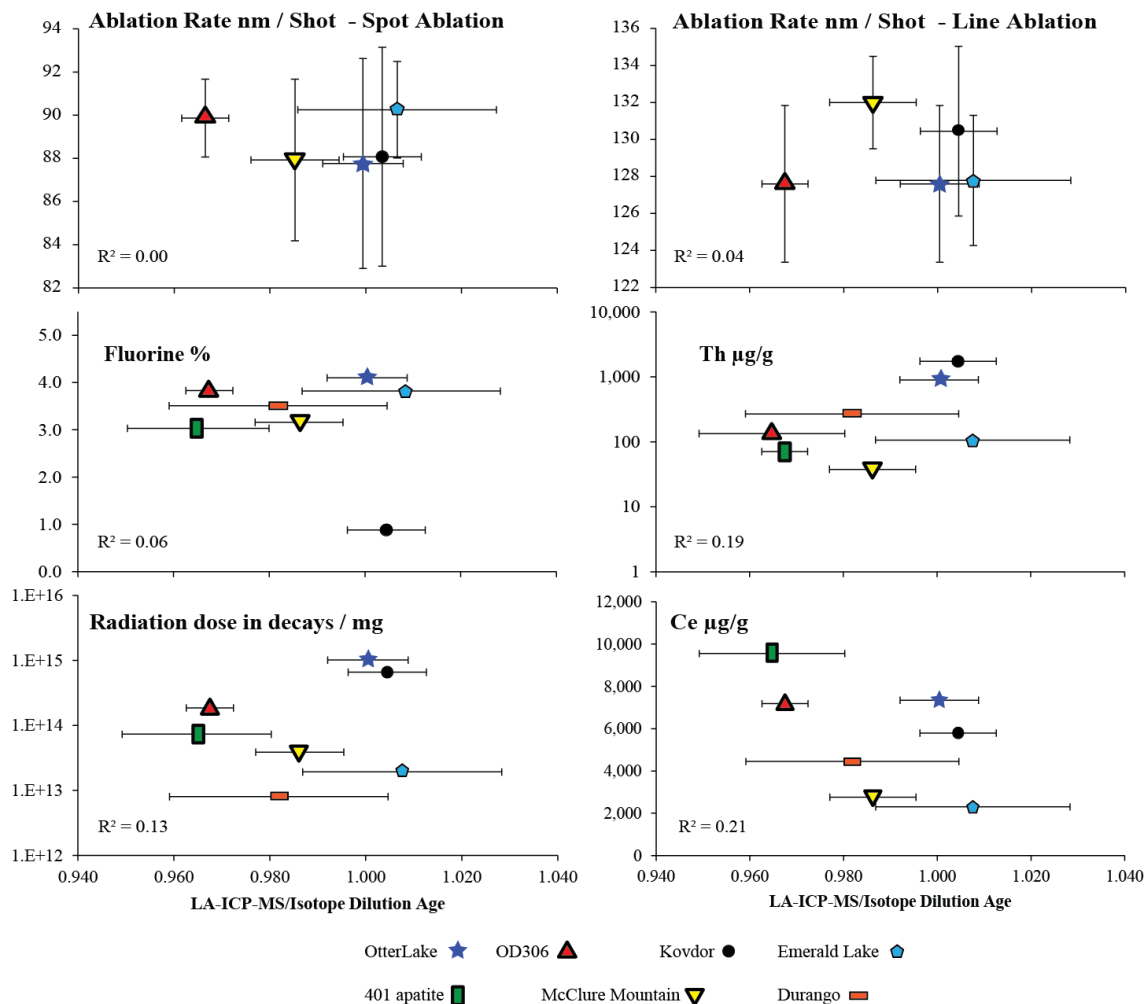


Figure 3.5. Some minor and trace element compositions of the apatite samples studied. F is measured by EMPA while Ce, Th and U are measured by LA-ICP-MS. Radiation dose is given as decay events per milligram and is a function of U and Th contents and the age of the sample. Error bars for ages are at 2-sigma.

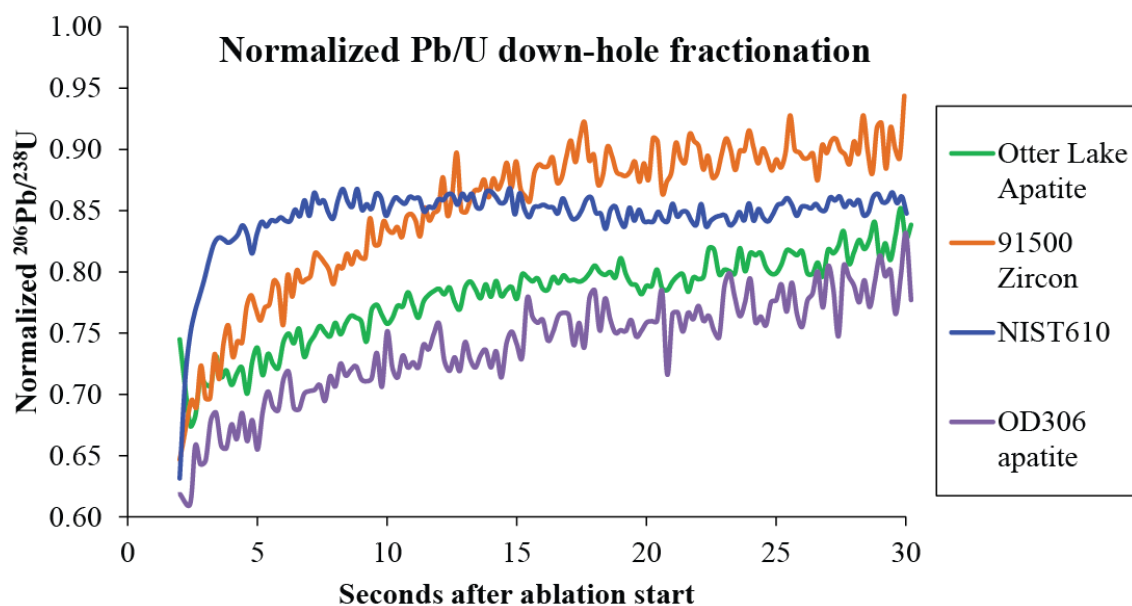


Figure 3.6. Normalized $^{206}\text{Pb}/^{238}\text{U}$ fractionation for apatite, zircon and NIST610 glass by stacking together >10 individual analyses from a single session. Data for each mineral / glass normalized to true $^{206}\text{Pb}/^{238}\text{U}$ value. Otter Lake apatite has been corrected for common Pb by applying a ^{207}Pb correction to the ^{206}Pb data – see Methods section for more details.

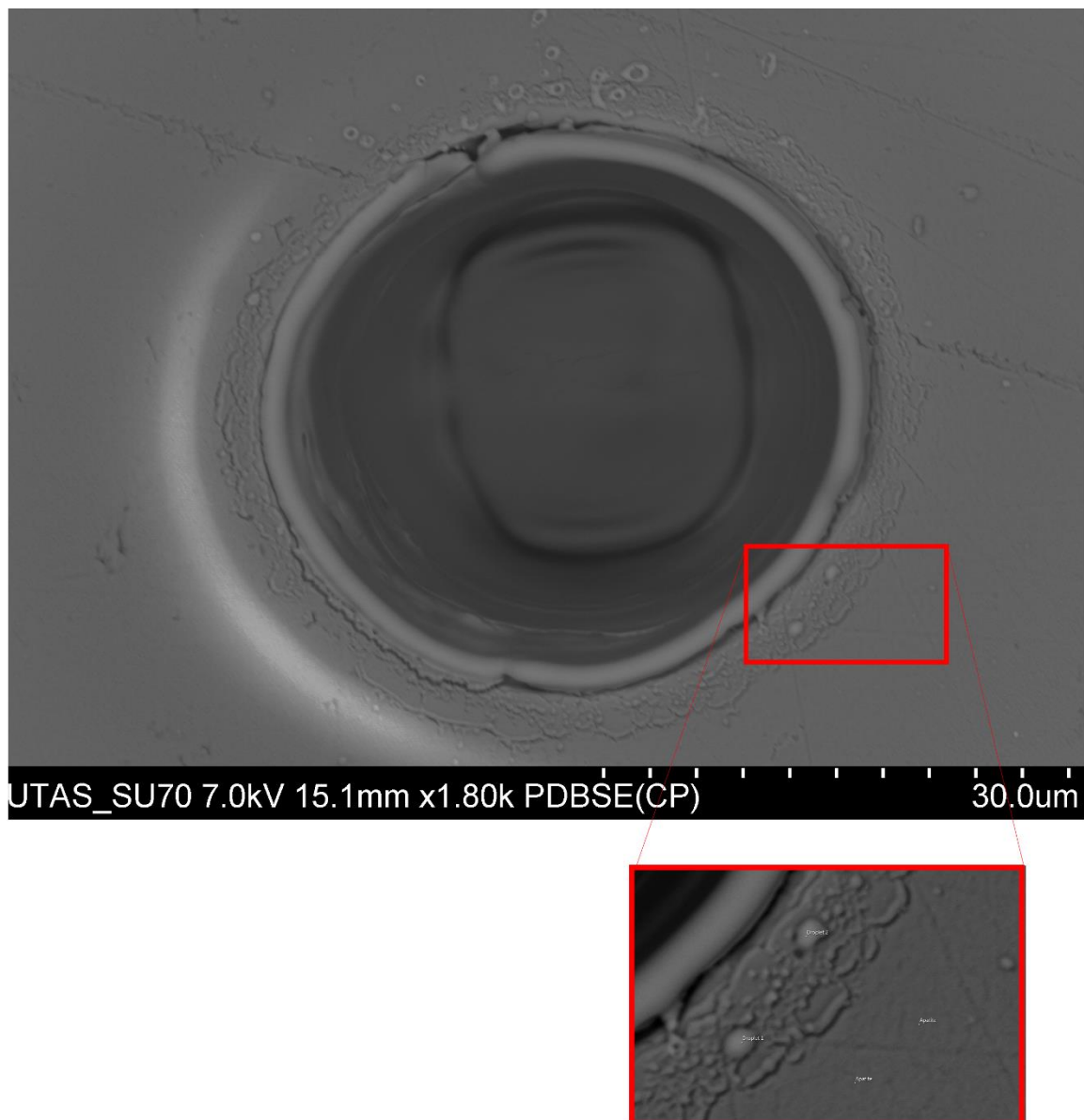


Figure 3.7. Backscatter electron image (BSE) of ablation crater in Durango apatite. Ejecta around crater is slightly brighter than surrounding apatite. Compositions from EDS spectrum indicate higher Ca (~20%) and lower P ~30% in brighter ejecta droplets.

3.4.6 Otter Lake apatite as primary standard:

Otter Lake apatite was used as primary standard in this work because it is old (913 Ma), has a high U content (110 ppm) and the parent crystal produced many mm-size fragments. However, Otter Lake is discordant due to the presence of common Pb and the reference age is based on Pb isotope step-leaching, a technique that is less reliable than isotope dilution U-Pb dating. Chew et al.[14] recommended using the Kovdor apatite as it has a high precision ID-TIMS reference age. However, Kovdor has a lower Pb_{rad}/Pb_{com} than Otter Lake, making it

more sensitive to common Pb correction. The self-normalized Otter Lake results (MSWD 2.0, $n = 447$) indicate that this apatite may not be homogenous for the Pb/U system at the scale of the laser sampling. It is conceivable that age offsets observed in this study are in part an artefact of inappropriate calibration, notably the demonstrated Pb/U heterogeneity and – perhaps – an inaccurate reference age for Otter Lake. However, this would be inconsistent with the lack of age offset for Kovdor and Emerald Lake apatite samples (Fig. 3.3).

While slightly heterogeneous, OD306 may be a better primary U-Pb standard for apatite than Otter Lake. It is even older (~ 1590 Ma) and contains very little common Pb, i.e. is almost concordant. Pb/U heterogeneity in OD306 may in fact reflect calibration with Otter Lake rather than being an intrinsic feature of OD306. Further work on OD306 characterization is in progress. The 401 apatite is also promising as a Pb/U age standard given its large size, low common Pb and homogeneity both at the bulk and laser sampling scale. However, this apatite is relatively low in U and radiogenic Pb so use as a calibration standard would be hindered by low counting statistics. It would be well suited for use as a secondary reference material for Pb/U age dating.

3.5 Conclusions

We report the first cases of significant age offsets (1-3%) between LA-ICP-MS ages and reference ages in apatite. Large numbers of analyses had to be combined to resolve these effects from counting statistic errors. This suggests that Pb/U ages for apatite obtained by LA-ICP-MS should carry a 3% error, even though other sources of errors (both random and systematic) may be smaller than this. Errors in laser ablation U-Pb dating of apatite are thus limited by matrix effects and not counting statistics, at least for apatites with well-preserved Pb/U systems for which good-quality isotopic analyses can be made. Our results fail to show significant correlation of age offsets with apatite composition, ablation rate and ablation type (spot, line). We speculate that the age offsets are related to a currently ill-defined laser ablation phenomenon. Further work is needed to improve the LA-ICP-MS technique for apatite U-Pb geochronology including resolving the matrix effects found in this work and possibly applying a correction for these. With this it might be possible to get accuracy of Pb/U results down to 1-2% (systematic errors), similar to what is seen in zircon.

The two new apatite reference materials presented here (401 apatite and OD306 apatite) are available to the community in small quantities upon request from the first author.

Chapter 4 Impact of air, laser pulse width and fluence on U-Pb dating of zircons by LA-ICP-MS

As published in full: J. M. Thompson, S. Meffre and L. Danyushevsky, *Journal of Analytical Atomic Spectrometry*, 2018, 33, 221-230.

Abstract

The accuracy of zircon U-Pb dating by LA-ICP-MS is limited by matrix effects related to differences in U-Pb fractionation between an unknown and the calibration standard. Zircon radiation dose has a strong influence on the ablation rate which in turn affects the amount of U-Pb fractionation and subsequent age calculations. Presented in this study is a previously unrecognized source of uncertainty in LA-ICP-MS U-Pb ages due to variations of atmospheric air absorbed on to the surfaces of samples. Laser properties such as fluence (J/cm^2) will change the laser ablation rate, and therefore the degree of U-Pb fractionation and this can change the amount of zircon matrix effect. To improve the accuracy of U-Pb dating by LA-ICP-MS, a systematic error component related to radiation dose needs to be included, or alternatively a correction to U-Pb dates can be applied as a function of radiation dose relative to the primary calibration standard. This study proposes a method to calculate a correction factor for the zircon matrix effect by measurement of several zircon reference materials with varying radiation dosages.

4.1 Introduction

U-Pb dating of zircon by laser ablation inductively-coupled plasma mass spectrometry (hereafter: LA-ICP-MS) is now widely used by the geochronology community [11, 92] due to its high spatial resolution, high throughput, and acceptable precision and accuracy for a wide range of applications. LA-ICP-MS U-Pb dating is a relative isotopic technique requiring a calibration reference material (RM) to quantify an age of the unknown. U-Pb dating is therefore highly dependent upon calibration standards and unknowns behaving the same during the laser ablation process and in the ICP-MS. Any difference in behaviour between reference materials and unknowns is commonly referred to as a matrix effect and can result in an inaccurate age. This is in contrast to isotope dilution thermal ionization mass spectrometry (ID-TIMS) which is an absolute technique relying on weights and isotopic ratios

of enriched spikes. ID-TIMS ages are considered by the geochronology community to be the benchmark for U-Pb ages determined in zircon and are referenced as being the 'true' age of all current zircon in-situ reference materials for LA-ICP-MS.

Use of widely available glass RMs (e.g. NIST glasses [47]) has been shown unsuitable for calibration of U-Pb ages in zircon [62]; prompting studies to characterize natural zircons of known ages for calibration of LA-ICP-MS U-Pb ages [11, 141, 155]. The need for matrix matched calibration in U-Pb ages by LA-ICP-MS is due to element fractionation occurring in two main locations: in the ICP [44] where larger particles, preferentially enriched in refractory elements, are not fully digested / ionized; and at the ablation site [46]. The latter appears to be the dominant cause of the observed U-Pb fractionation in zircon [46, 48].

Several types of mass spectrometers are commonly used in LA-ICP-MS applications. Quadrupole instruments have been widely adopted in LA-ICP-MS geochronology due to their fast mass scanning speed (typically between 0.1 and 0.5 seconds per quadrupole sweep) and relatively low cost. Magnetic sector instruments [93, 153, 156] are also used in LA-ICP-MS geochronology and offer higher sensitivity than quadrupole instruments. Multi-collector ICP-MS can eliminate random sources of noise from the laser and plasma flicker allowing for high precision isotope ratios. Diatomic gases addition has been utilized to increase sensitivity for LA-ICP-MS analyses [78, 79] and these innovations have led to increased precision and lower levels of detection on individual analyses, producing precision comparable to the ion probe [153, 157] and making analysis of very young (low radiogenic Pb) zircons by LA-ICP-MS possible [153, 158].

Improvements in laser ablation cell design have allowed for homogenous signal response across the laser cell, leading to significant improvements in accuracy and precision [38, 159]. These increases in precision reduce random sources of error and allow for investigations into other, systematic, sources of errors in the LA-ICP-MS dating technique. Many studies have shown inaccuracies outside of assigned errors for LA-ICP-MS zircon dating when compared to the corresponding ID-TIMS ages [95, 96, 122, 129, 160]. Sources of systematic errors can include uncertainties in the age of the RM used for calibration, long term excess variance of the validation materials [161], and any differences in ablation properties between standard and unknown zircons, (i.e. the zircon matrix effect [95, 96]). These systematic errors currently limit the accuracy of LA-ICP-MS zircon dating to >2% or worse depending on the

amount of zircon matrix effect between reference materials and unknowns. In particular the calculated alpha radiation dose a zircon has received, a function of age and the U and Th contents, has shown to be strongly correlated to inaccuracies in U-Pb ages [95]. Differences in ablation rates [96] between zircons, have also shown to be strongly correlated to inaccuracies in U-Pb ages.

Compounding these matrix effects is the absence of an accepted ‘best practice’ agreed upon by the LA-ICP-MS geochronology community. A wide range of analytical protocols are used for U-Pb zircon dating by LA-ICP-MS including, but not limited to: choice of calibration RM, laser wavelength, laser pulse width, laser repetition rate, laser fluence, laser cell design, type of tubing used in the interface to the ICP, ICP-MS design and gas flow rates. Several of these parameters are fixed on purchase of a specific laser / ICP-MS system (e.g. laser wavelength), however many of these parameters are variable (e.g. laser repetition rate, laser fluence, gas flow rates) and up to the discretion of a particular laboratory. For example there is a wide range of laser fluence (for the same laser wavelength & pulse width) reported in the literature ranging from $\sim 2 \text{ J/cm}^2$ [96] to 8 J/cm^2 [159]. The question remains what affect, if any, these parameters have on the accuracy of zircon U-Pb dating by LA-ICP-MS.

A wide range of zircon RMs with variable age, radiation dose, and trace element content, measured over several analytical sessions, are presented in this study. These U-Pb ages are used to investigate the effects of laser fluence, laser pulse width, radiation dose, annealing of zircon, and sample handling on the accuracy of U-Pb ages by LA-ICP-MS.

4.2 Experiment setup

Analyses were conducted using two RESolution systems (ASI), an HR model equipped with a Coherent Compex Pro 110 excimer laser, and an SE model equipped with an ATL (ATLEX 300) excimer laser. These two systems both use the S-155 large-format, constant geometry ablation cell, have similar optical path designs, and both operate at the same wavelength (193nm). Both systems use a sample exchange procedure developed at the University of Tasmania which involves 5 repeated steps of laser cell evacuation and backfilling with helium. The primary differences between the two systems is that the Compex Pro laser has a $\sim 20 \text{ ns}$ pulse width and was coupled to an Agilent 7900 ICP-MS, while the ATL laser has a $\sim 5 \text{ ns}$ pulse width and was coupled to an Agilent 7700 ICP-MS. Ablation in both systems was undertaken

in helium flowing at 0.35 l/min, which was mixed with argon flowing at ~1.05 l/min immediately after leaving the ablation cell. ~1.6 ml/min N₂ was added to the argon to increase sensitivity. ICP-MS tuning was performed using a ~50 micron diameter line scan at 3 µm/s on the NIST612 glass at ~3.5 J/cm² laser fluence. Both ICPMS are tuned for low oxides (ThO/Th <0.2%) maximising sensitivity for heavy masses (²³⁸U) and U/Th of ~1.05.

Zircons were analysed using a 30 micron laser beam fired at 5 Hz and a fluence of 2.0 J/cm², unless otherwise noted. Each analysis consisted of a 30 s gas blank followed by a 30 second ablation. Masses monitored were ⁴⁹Ti, ⁵⁶Fe, ⁹¹Zr, ¹⁷⁸Hf, ²⁰²Hg, ²⁰⁴Pb, ²⁰⁶Pb, ²⁰⁷Pb, ²⁰⁸Pb, ²³²Th, ²³⁵U and ²³⁸U, with a quadrupole sweep time of ~0.18 seconds. ²³⁵U was not used in calculations but was measured to ensure accurate analyses if ²³⁸U reached the analog counting mode (>4x10⁶ counts/s). When this happened, the ²³⁵U isotope was used and the present day ratio of ²³⁸U/²³⁵U = 137.818 [162] was assumed for calculation of the ²⁰⁶Pb/²³⁸U* system where ²³⁸U* is the ²³⁸U calculated from ²³⁵U. Using these analytical conditions, the typical sensitivity for zircon analysis is 2,200 cps / ppm for ²³⁸U in the 91500 zircon reference material, assuming ~80 ppm U. The 91500 zircon [155] was used as the calibration standard for the U-Pb ratios in zircons, while the NIST610 glass was used for quantification of Pb isotope compositions using Pb isotopic values from [143]. Trace elements were quantified using ⁹¹Zr as the internal standard; assuming stoichiometric proportions. Trace elements were quantified using the NIST610 glass with GeoReM preferred values [47].

All zircons were mounted in Struers© epoxy, cured >12 hours at 60° C, exposed with 1500 grit silica carbide paper, polished in 0.3 micron alumina polish, cleaned in DI water in an ultrasonic bath, and evacuated (<10 kPa) in a desiccator for at least 24 hours (unless otherwise noted). For annealing experiments zircons were put in a muffle furnace at 850°C for 48hours [95] in Pt foil vessels, then mounted as above. Data reduction was performed by 'stacking' the baseline subtracted U-Pb ratios from all analyses of 91500 on a given session as in Paton et al. [163]. A model of the downhole fractionation is created with the average U-Pb ratio for each individual sweep is divided by the true U-Pb ratio. Unknowns are corrected to this curve on a sweep by sweep basis, similar to Paton et al. [163] that simultaneously corrects for downhole U-Pb fractionation and ICP-MS mass bias. Drift in U-Pb values during the session is corrected by taking the average U-Pb for each 91500 analysis throughout the session and applying a correction with time to the raw U-Pb ratios of the unknowns. An assumption is

made that there is no change in the nature of U-Pb downhole fractionation, but that all changes in U-Pb ratios are due to ICP-MS drift. Uncertainties are calculated based on counting statistics of unknowns, uncertainty in drift correction, uncertainty in U-Pb calibration and uncertainty in the age of the calibration RM [163]. An excess uncertainty factor was added, as described in Halpin et al. [164] and based on Paton et al. [163]. The measured age and U and Th concentrations are used to calculate the alpha radiation dose in decays events / gram. Contribution of alpha radiation from decay of ^{147}Sm is considered negligible due to relatively low (<20 ppm) concentrations of Sm in most zircon and the long half live of ^{147}Sm (1.06×10^{11} years). Crater depths of ablated zircons are measured with a WykoNT9100 optical profiler (Veeco). Additional laser ablation and mass spectrometer information is summarised in the ESI metadata.

Well characterized zircon RMs were analysed over several sessions to assess accuracy of the LA-ICP-MS technique on the two laser ablation systems. The zircon RMs analysed were Plesovice [141], Temora [129], GJ1 [11], FC1 [165], OG-1 [166], AusZ-2 [167], AusZ-5 [167], Penglai [158], Monastery [168], Mud Tank [161, 169], Qing Hu [170], M257 [171] and two high U&Th Jurassic dolerite zircon samples SP07-05 [172] (Table 4.1) and TASDOL from Ivanov et al. [173]. These zircons vary in age from 4 to 3465 Ma and in U concentrations from ~5 to >1000 ppm and so have been subject to a wide range of natural radiation doses from 5×10^{16} to 4×10^{18} α events/g. The number of analyses acquired from each zircon reference material depended on the amount of material available and the amount of radiogenic Pb, so that zircon with low radiogenic Pb (e.g. Monastery) were analysed in greater numbers than higher radiogenic Pb (e.g. M257).

| Zircon | LA-ICP-MS age 20 ns pulse width laser (Ma) | LA-ICP-MS age 5 ns pulse width laser (Ma) | ID-TIMS age (Ma) | Average radiation dose in decays / g | Depth of ablation crater relative to 91500 zircon |
|-----------|--|---|----------------------|--------------------------------------|---|
| 91500* | $1062.5 \pm 2.6 / 11.1$ | $1062.3 \pm 3.7 / 11.3$ | 1062.4 ± 0.4 | 3.41×10^{17} | 1.00 / 1.00 |
| AusZ-2 | $38.44 \pm 0.27 / 0.47$ | $38.46 \pm 0.64 / 0.76$ | 38.8963 ± 0.0044 | 3.39×10^{16} | 0.970 / 0.963 |
| AusZ-5 | $38.29 \pm 0.25 / 0.46$ | $38.41 \pm 0.59 / 0.69$ | 38.9022 ± 0.0035 | 3.68×10^{16} | 0.972 / 0.954 |
| FC-1 | $1097.3 \pm 5.9 / 12.5$ | $1097.8 \pm 5.3 / 12.3$ | 1096.8 ± 0.3 | 1.54×10^{18} | NA / 0.990 |
| GJ-1 | $604.4 \pm 2.7 / 6.7$ | $605.9 \pm 3.8 / 7.2$ | 601.86 ± 0.37 | 7.42×10^{17} | NA / 0.996 |
| M257 | $566.8 \pm 3.9 / 6.9$ | $569.6 \pm 2.6 / 6.3$ | 561.3 ± 0.3 | 1.75×10^{18} | 1.059 / 1.007 |
| Monastery | $87.5 \pm 1.4 / 1.7$ | $88.3 \pm 4.1 / 4.2$ | 90.1 ± 0.5 | 3.70×10^{15} | 0.954 / 0.959 |
| Mud Tank | $715.1 \pm 5.9 / 9.3$ | $707 \pm 10 / 12$ | 731.65 ± 0.49 | 4.22×10^{16} | 0.967 / 0.960 |
| OG-1 | $3474 \pm 21 / 41$ | $3508 \pm 20 / 41$ | 3465.4 ± 0.6 | 3.20×10^{18} | 1.060 / 1.028 |

| | | | | | |
|-----------|--------------------------|------------------------|-------------------|-----------------------|-----------------|
| Penglai | $4.06 \pm 0.15 / 0.16$ | $4.18 \pm 0.51 / 0.51$ | 4.4 ± 0.1 | 9.68×10^{14} | $0.973 / 0.959$ |
| Plesovice | $339.4 \pm 1.1 / 3.6$ | $338.7 \pm 1.1 / 3.6$ | 337.13 ± 0.37 | 5.81×10^{17} | $0.943 / 0.944$ |
| Temora | $416.4 \pm 1.5 / 4.5$ | $419.0 \pm 3.4 / 5.5$ | 416.8 ± 1.1 | 1.88×10^{17} | $0.964 / 0.986$ |
| Qing Hu | $159.66 \pm 0.67 / 1.75$ | $159.9 \pm 1.2 / 2.0$ | 159.5 ± 0.2 | 5.63×10^{17} | NA / 1.002 |
| SP07-05 | $184.07 \pm 0.78 / 2.02$ | $185.5 \pm 1.1 / 2.2$ | 182.6 ± 0.3 | 1.01×10^{18} | $1.041 / 1.043$ |

Table 4.1. LA-ICP-MS results on non-annealed zircon for both laser systems tested using a laser fluence of 2.0 J/cm². LA-ICP-MS uncertainties are 2-sigma: random + systematic uncertainties. *91500 zircon was primary standard for U-Pb ratios (self-normalized). All LA-ICP-MS ages are weighted averages from Isoplot using the ²⁰⁶Pb/²³⁸U age except the Monastery, Mud Tank, Penglai, SP07-05, and Qing Hu zircons which are concordia intercept ages anchoring on the Stacey & Kramer's model common Pb at the age of the zircon. GJ-1 and Mud Tank ID-TIMS ages are from [161]. Radiation dose is calculated using ²³²Th, ²³⁸U, assumed ²³⁵U (²³⁸U/²³⁵U = 138.818) and the ID-TIMS age of zircon. Ablation crater depths are as follows: 20 ns pulse width laser / 5 ns pulse width laser. NA = not available.

4.3 Results

4.3.1 Impact of atmospheric air on U-Pb fractionation

To test the influence of atmospheric air on U-Pb fractionation, seven 25 mm diameter epoxy rounds containing the 91500 zircon were loaded into various positions in a 20 sample holder and placed into the laser ablation cell (Fig 4.1). Importantly, the epoxy rounds were not degassed under vacuum prior to loading into the laser cell and the routine sample exchange procedure was performed. The analyses were started after 1 hour of instrument warm-up. A mount containing the 91500 was placed in the centre of the cell and was used as the primary calibration RM while treating mounts in other positions as unknowns. The primary RM was measured in duplicate at the beginning and end of the analytical run as well as between each 91500 located in different positions throughout the cell to characterize any instrument drift. Atmospheric air within the laser cell was monitored using mass 56 (⁴⁰Ar+¹⁶O) from the 30 second gas blank collected prior to the laser firing for each analysis. During the analytical session, the abundance of atmospheric air in the laser cell decreased so that the intensity on ⁵⁶ArO⁺ also decreased. However, this decrease in ⁵⁶ArO⁺ was not uniform across the laser cell (Fig. 4.2A) and is correlated to the measured U-Pb age offset of 91500 zircon measured at each location. This effect is quantified by fitting a polynomial function to the trend in mass 56 on the primary standard (centre of laser cell). A deviation (%) from this trend is calculated for each of the 91500 throughout the ablation cell and compared to the offset of the measured U-Pb age (Fig. 4.2B). Those 91500 with higher amounts of ⁵⁶ArO⁺ in their 30

second background had older ages by up to 3% relative to the 91500 zircons used as the calibration RM.

A repeat of this test was conducted on a separate day where all parameters were kept identical except the epoxy mounts were placed in a desiccator and evacuated for more than 48 hours. Figure 4.2C shows $^{56}\text{ArO}^+$ measured in the 30 second backgrounds does not vary systematically throughout the analytical session and there is no difference between the primary RM mount in the centre and other positions in the cell. Figure 4.2D shows U-Pb ages of all 91500 analyses throughout the laser cell are well within uncertainty of each other (1063.2 ± 4.5 , MSWD 0.86, $n = 49$) with less than 0.5% 2-sigma variation.

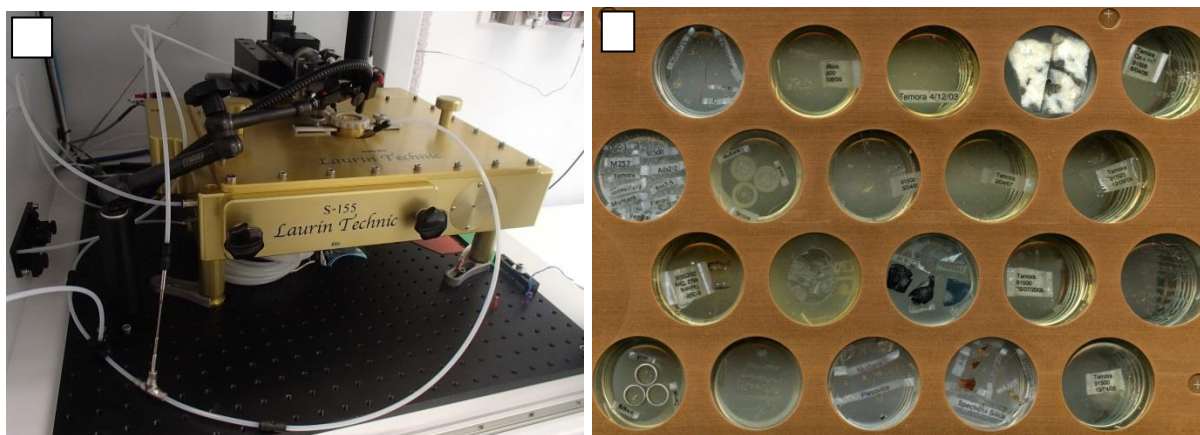


Figure 4.1. (A) Photo of the S-155 large-format ablation cell. This is a two-volume cell with ablation occurring in a small, fixed funnel in the centre and a movable sample block. (B) Photo of the sample holder insert showing twenty samples of various zircon and glass RMs.

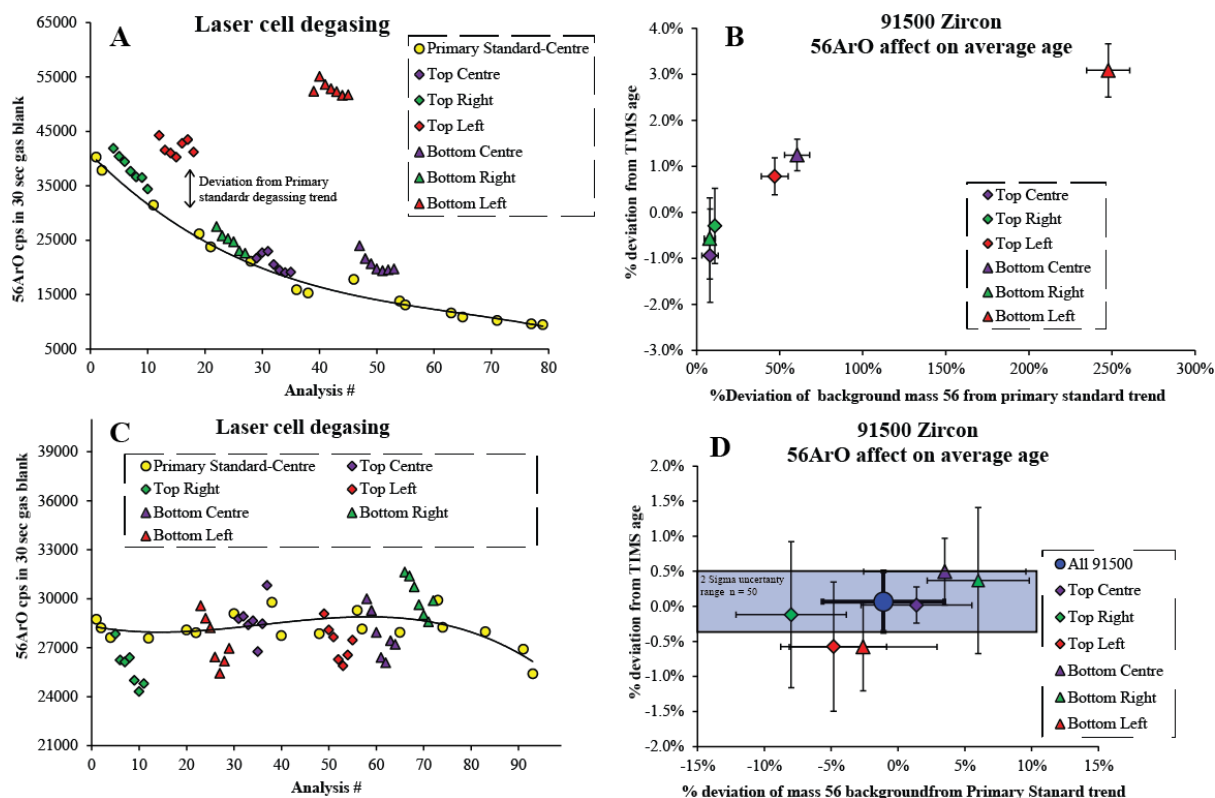


Figure 4.2. Atmospheric air in laser cell affecting measured U-Pb age. (A) Variable degassing in laser cell with poorly flushed conditions (residual atmospheric air). (B) Effect of variable mass 56 in the gas blank on measured U-Pb age introducing up to a 3% error in age. (C) Same as (B) but with samples kept under vacuum >48 hours. (D) Absence of variation in mass 56 produces more accurate U-Pb ages, 0.5% (2-sigma) on weighted average of all analyses in laser cell.

4.3.2 Matrix effects of LA-ICP-MS U-Pb ages in zircon

Weighted averages of the $^{206}\text{Pb}/^{238}\text{U}$ age for each of the zircon RMs are calculated using Isoplot [174] (Table 4.1). Ages for the Monastery, Mud Tank, Penglai, SP07-05, and Qing Hu zircons are Isoplot concordia intercept ages using a common Pb anchor based on Stacey & Kramer's [151] model common Pb at the age of the zircon. The term 'U-Pb age' will be used below to refer to both the $^{206}\text{Pb}/^{238}\text{U}$ age and the concordia intercept age. Offsets in LA-ICP-MS zircon RM ages relative to their ID-TIMS ages show a positive correlation with radiation dose as previously shown in [95] (Fig. 4.3). Zircon RMs with lower radiation dose compared to the 91500 zircon have too young U-Pb ages by up to 2.9% and higher radiation doses are too old by up to 1%. Zircons with similar radiation doses to the calibration RM (Temora, Qing Hu) no offset from their respective ID-TIMS ages.

Depth of ablation craters are 8 to 10 microns for zircon RMs analysed with 155 shots (30 second ablation at 5 Hz plus 5 shots of pre-ablation) and 2.0 J/cm^2 laser fluence, yielding an ablation rate of 52 to 65 nm per laser shot. Individual laser crater depths were matched to

corresponding U-Pb age results for each analysis. Crater depth measurements were measured on several analytical sessions and depths are normalized to the depth of the 91500 zircon. Offsets in zircon RM ages relative to their ID-TIMS ages results show a rough positive correlation with normalized ablation rate (Fig. 4.4) for RM with higher ablation rates. Zircon with lower ablation rates than the 91500 zircon show no correlation with LA-ICP-MS age offset from ID-TIMS and normalized ablation rate. These measurements were done on both laser systems used in this study.

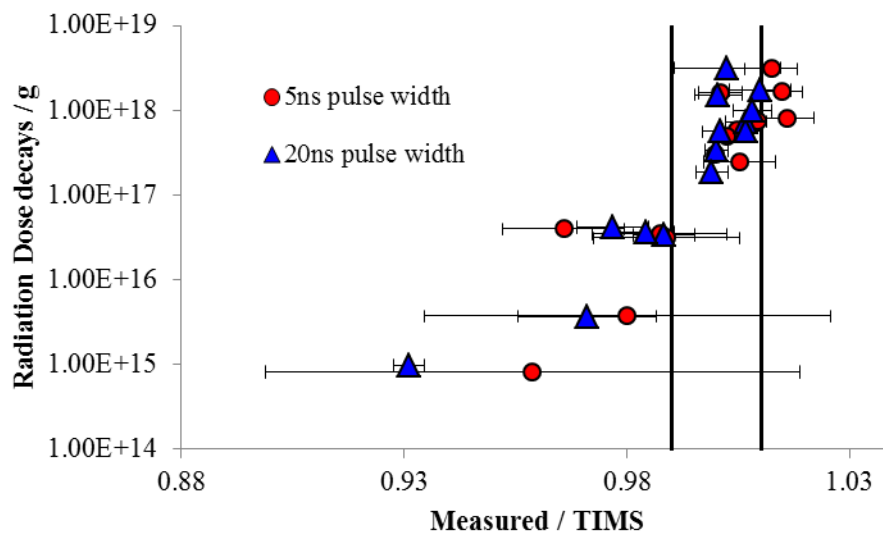


Figure 4.3. Plot of accuracy vs. radiation dose in alpha decays per gram for zircon reference materials used in this study. Uncertainty bars for age are 2-Sigma and include random sources of uncertainty from the LA-ICP-MS analyses as well as the uncertainty on published ID-TIMS ages. Vertical solid black lines represent $\pm 1\%$ of the ID-TIMS age.

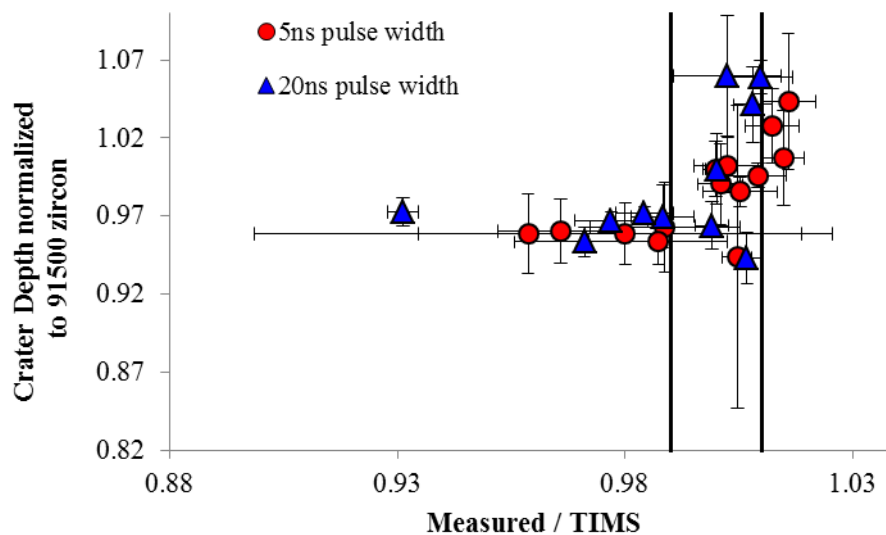


Figure 4.4. Plot of LA-ICP-MS zircon U-Pb age accuracy compared to ablation crater depth, normalized to primary RM (91500 zircon) for multiple laser systems at the University of Tasmania. Uncertainty bars for age are 2-Sigma and include random sources of uncertainty from the LA-ICP-MS analyses as well as the error of ID-TIMS analysis.

Uncertainty bars for crater depths are 1 standard deviation on the average depth (relative to 91500) for a zircon RM. Vertical solid black lines represent $\pm 1\%$ of the ID-TIMS age.

4.3.3 Impact of laser fluence on U-Pb fractionation and U-Pb matrix effects

To test the impact of laser fluence on the accuracy of U-Pb ages, the Plesovice, M257 and Mud Tank zircon were analysed at three different laser fluences of 1.2, 2.0, and 5.2 J/cm². Between 5 and 30 analyses for each RM at each laser fluence were calibrated against the 91500 zircon measured at the corresponding laser fluence. The number of analyses required for each RM was based on amount of radiogenic Pb so that uncertainties on the weighted averages were less than 1% and MSWD generally less than 1. To minimise any effects on the U-Pb age from natural compositional variation in each of the RMs, single large fragments of each RMs were used keeping all analysis spots in the same general area. The stacked downhole U-Pb curves for the 91500 zircon show both an increase and less linear U-Pb fractionation with increasing laser fluence (Fig. 4.5). The high U and radiogenic Pb zircons, Plesovice and M257, are within error of published ID-TIMS ages at lower laser fluence, but U-Pb age accuracy decreases at higher fluences (Fig. 4.5). The measured U-Pb age of Mud Tank was relatively unaffected by changes in laser fluence and was consistently younger than its ID-TIMS age. Detector linearity is assessed using the measured $^{238}\text{U}/^{235}\text{U}$ ratio in the various zircon RMs and this ratio was calibrated on the NIST610 assuming a $^{238}\text{U}/^{235}\text{U}$ of 420 (GeoReM value). The full data set is located in the ESI.

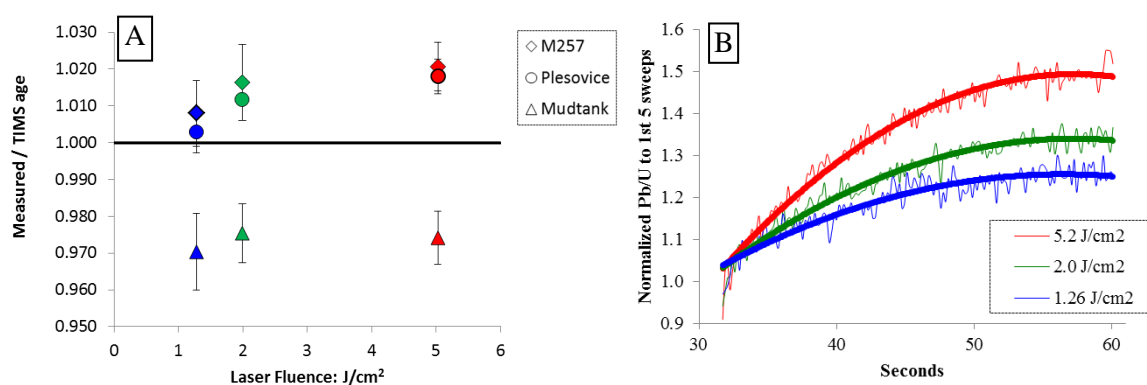


Figure 4.5. (A) Age of the zircon RMs measured against 91500 zircon at various laser fluences. Uncertainty bars for age are 2-sigma and include random sources of error (counting statistics) from the LA-ICP-MS analyses as well as the uncertainty on the ID-TIMS analysis. Colour coding same as in (B). (B) Impact of laser fluence on the U-Pb downhole fractionation trend.

4.3.4 Impact of laser pulse width on U-Pb fractionation and U-Pb matrix effects

To test the impact of laser pulse width on matrix effects in U-Pb ages, this study measured a wide range of zircon RMs using two laser systems with a ~20 ns and ~5 ns pulse width both operating at 193nm wavelength. To minimize variables from operating conditions, the same laser cell and gas flows were used in both laser systems. Also, both systems used Agilent ICP-MS and had similar mass bias and tuning to minimize any potential effects on the laser pulse width comparison. U-Pb ages from multiple zircons RMs are similar for the two different lasers sources (Fig. 4.4). There is no clear advantage of one laser pulse width (5 ns vs. 20 ns) with respect to zircon U-Pb age accuracy, however the 5 ns pulse width does have U-Pb ages outside 1% from the ID-TIMS age for the highest radiation dose zircon.

4.3.5 Impact of annealing experiments on LA-ICP-MS matrix effects

The 91500, Mud Tank, TASDOL, Qing Hu, OG-1, Temora, and Plesovice zircons were annealed at 850° C for 48 hours and analysed over several sessions using the same protocols and data reduction as for non-annealed zircons and results are presented in Table 4.2. Results for annealed Plesovice and TASDOL show an improvement in U-Pb age accuracy over the un-annealed grains (Fig. 4.6). Mud Tank and OG-1 zircons did not show any change in accuracy relative to the non-annealed grains. Temora, and Qing Hu annealed zircon U-Pb ages are slightly younger (~0.7%) than the ID-TIMS age. Zircon U-Pb ages for annealed grains, calibrated against annealed 91500 zircon, are within error of their non-annealed counterparts, calibrated on non-annealed 91500 zircon. Full data set is presented in the electronic appendix.

| Zircon | LA-ICP-MS age un-annealed zircon (Ma) | LA-ICP-MS age annealed zircon (Ma) | ID-TIMS age (Ma) | Average radiation dose in decays / g |
|-----------|---------------------------------------|------------------------------------|------------------|--------------------------------------|
| 91500* | 1062.5 ± 2.6 / 11.1 | 1062.4 ± 2.5 / 11 | 1062.4 ± 0.4 | 3.41x10 ¹⁷ |
| Mud Tank | 715.1 ± 5.9 / 9.3 | 715.1 ± 6.9 / 10 | 731.65 ± 0.49 | 4.22x10 ¹⁶ |
| OG-1 | 3474 ± 21 / 41 | 3475 ± 19 / 40 | 3465.4 ± 0.6 | 3.20x10 ¹⁸ |
| Plesovice | 339.4 ± 1.1 / 3.6 | 338.1 ± 1.2 / 3.6 | 337.13 ± 0.37 | 5.81x10 ¹⁷ |
| Temora | 416.4 ± 1.5 / 4.5 | 413.4 ± 2.6 / 4.94 | 416.8 ± 1.1 | 1.88x10 ¹⁷ |
| Qing Hu | 159.66 ± 0.67 / 1.75 | 158.5 ± 1.1 / 2.0 | 159.5 ± 0.2 | 5.63x10 ¹⁷ |
| TASDOL | 184.34 ± 0.78 / 2.2 | 183.03 ± 0.96 / 0.98 | 182.90 ± 0.21 | 4.06x10 ¹⁸ |

Table 4.2. LA-ICP-MS results on annealed zircon and non-annealed zircon, each calibrated on 91500 annealed and un-annealed grains respectively. Tests conducted on the 20 ns pulse width laser system. Uncertainties and radiation dose calculations are the same as in Table 4.1. LA-ICP-MS ages for 91500, OG-1, Plesovice and Temora are weighted averages from Isoplot using the ²⁰⁶Pb/²³⁸U system and Mud Tank, TASDOL, and Qing Hu zircons are

concordia intercept ages anchoring on the Stacey & Kramer's model common Pb at the age of the zircon. TASDOL age from Ivanov et al.[173]

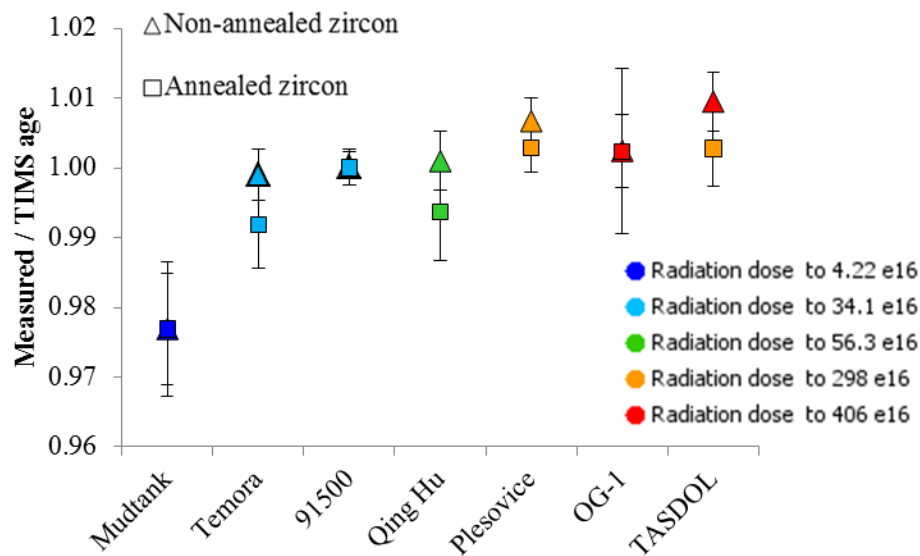


Figure 4.6. U-Pb age results from annealing experiments. Uncertainty bars for age are 2-sigma and include random sources of uncertainty from the LA-ICP-MS analyses as well as the uncertainty on the ID-TIMS analysis. Symbols are colour coded to the radiation dose. Squares and triangles are for annealed and non-annealed zircons respectively.

4.4 Discussion

4.4.1 Atmospheric air: effect on U-Pb fractionation

Mass 56 ($^{40}\text{Ar}+^{16}\text{O}$) is interpreted to be the result of argon combining atmospheric oxygen from a combination of sources including the laser ablation cell, interface tubing, impurities in the gas supply and entrainment of air at the ICP-MS sample cone [175]. Since most of the sources of atmospheric oxygen should be at a relatively steady state (e.g. impurities in gas supply should remain constant for a given batch or bottle), any changes in mass 56 are likely due to the degassing of atmospheric air from the laser cell. This can be seen in Figure 4.2 where different positions in the laser cell contain differing amounts of mass 56 in the 30 second gas blank before the ablation. This residual atmospheric air in the laser cell has a significant influence on the U-Pb age and can be potentially made worse if epoxy mounts with unknowns are, for example, cleaned or treated differently to the calibration standard mount before loading into the laser cell. Other potential sources of oxygen or atmospheric air are from unknown samples having relatively new epoxy compared to the calibration RM mount; or for in-situ zircons in rock samples with abundant clay minerals. However, if all mounts are placed under vacuum in a desiccator, most of the absorbed atmospheric air is removed and the U-Pb ages show no variation across the laser cell. Because of this phenomenon, the CODES lab

monitors mass 56 to assess any potential accuracy problems with LA-ICP-MS zircon ages. The absolute level of mass 56 can vary due to amount of absorbed air in the system / impurities in the argon supply, but also can vary due to tuning of the ICP-MS for light masses. Since the ICP-MS was tuned to maximize heavy masses, the light mass sensitivity can vary substantially from day to day and this is likely the cause for the higher mass 56 in the degased samples in Figure 4.2C vs. un-degased samples in Figure 4.2A.

There are two likely causes for atmospheric air affecting the U-Pb ages. First, atmospheric air is mostly N₂ and O₂ and small amounts of diatomic gas addition has been shown to affect the dynamics of the ICP [78, 79]. Tests involving the addition of N₂ on the Agilent instruments at CODES change the relative sensitivities of Pb and U. Small differences in the amount of N₂ in one part of the laser cell compared to another may have an effect on the ICP properties and potentially cause a difference in the U-Pb ratio due to differences in ionization between the two elements. Previous studies on the impact of diatomic gas addition to ICP-MS show variable sensitivity gains, so the effect of N₂ from atmospheric air may not be seen in all LA-ICP-MS labs depending on ICP-MS design [78].

Alternatively, the impact of atmospheric air on the accuracy of U-Pb ages may be due to some process at the ablation site. Kosler et al. [48] have demonstrated a positive correlation with the amount of O₂ addition (in helium line) to the ablation site and the formation of baddeleyite (ZrO₂) along the wall and rim of the laser ablation crater. This formation and deposition of baddeleyite along the crater walls and rim is thought to be a principle source of U-Pb fractionation in zircon [46, 48, 62]. In this scenario variable amounts of atmospheric air present locally will change the amount of baddeleyite formation and therefore the U-Pb age. Our results show that U-Pb fractionation (i.e. age) is increased in mounts with the highest concentrations of atmospheric air and this is consistent the results from Kosler et al. [48] showing more fractionation with higher oxygen additions. Thus, maintaining low and constant level of atmospheric air is critical for accurate U-Pb ages by LA-ICP-MS. Mounting zircon RMs in the same mount as unknowns would minimize the atmospheric air phenomenon; however, this practice is not always practical. It would require more time-consuming data reduction as each epoxy mount has to be reduced separately and would consume valuable RMs quickly. This is particularly important for RMs such as the 91500 zircon that is in limited supply.

A homogenous signal response in the laser cell, regardless of sample position [38] is required for accurate U-Pb ages. The S-155 ablation cell allows for accurate and precise LA-ICP-MS U-Pb dating with no systematic bias based on location in the cell provided atmospheric air has been removed from samples. Therefore, it is recommended that sample mounts be placed in a desiccator and evacuated prior to analysis. The practice of routinely imaging samples using cathodoluminescence on scanning electron microscopes will also mitigate this effect as long as the carbon coat is left intact and the samples are curated in a moisture free environment prior to analysis.

4.4.2 Matrix effects seen in zircon reference materials

Once atmospheric air is well removed from the system, this allows us to further investigate the zircon matrix effect. Results from our study confirm previous observations of a zircon matrix effect for U-Pb ages by LA-ICP-MS when unknown zircons have different calculated radiation doses from the primary RM [95] and confirm the idea that the radiation damage from alpha decay has a strong influence on the LA-ICP-MS accuracy. The radiation doses for these zircon RMs are only calculated however, and if there has been some natural annealing due to geological processes particular to a zircon RM's location, then the actual amount of crystal structural damage would be less than the calculated amount. Ideally the analyst would know or measure the fission track age of the zircon to calculate the accumulated radiation dose. However, given the variable effect of annealing experiments on accuracy of zircon LA-ICP-MS U-Pb ages [95, 96], it is possible that the amount of annealing need to reset zircon fission tracks might be different to the amount of annealing need to lessen the zircon matrix effect seen in LA-ICP-MS U-Pb ages.

A similar correlation of LA-ICP-MS zircon matrix effect is seen when comparing zircon ablation rates to that of the primary RM [96]. The rate at which a zircon ablates has been shown by Marillo-Sialer et al. [97] to be largely controlled by zircon crystallinity, which was assessed by Raman Spectroscopy [176]. Therefore, there should be a link between the calculated radiation dose a zircon has received, zircon crystallinity, zircon ablation rate and the zircon matrix effect. Marillo-Sialer et al. [97] showed a strong correlation between the ν_3 (SiO_4) Raman peak and ablation rate and suggest the crystallinity of the zircon has a strong influence on the accuracy of LA-ICP-MS ages. The width of the ν_3 (SiO_4) Raman peak has been shown by Nasdala et al. [177] to be a function of the radiation dose that a zircon has received,

but surprisingly Marillo-Sialer et al. [96] did not see any correlation with the radiation dose and zircon matrix effect. Our results suggest there is a stronger correlation of the zircon matrix effect with calculated radiation dose than with ablation rate for both of the laser systems used (Figs. 4.3 vs. 4.4).

While there are likely many factors controlling the nature of the zircon matrix effect [96], our results suggest that the radiation dose has a stronger influence than the ablation rate and this may indicate that there is a variable amounts of ZrO formation[46, 48] at the ablation site depending on the degree of crystallinity and this is broadly correlated with the ablation rate. If the ablation rate were the dominant source of the zircon matrix effect, it would be expected that analysing in line rasters would minimize this since the aspect ratio of the line scan would be substantially different to a spot ablation. The aspect ratio of an ablation crater has been shown to be an important parameter for element fractionation in LA-ICP-MS [27], however Klötzli et al. [122] showed similar zircon matrix effects while ablating lines. Results from our study suggest that both differences in radiation dose and differences in ablation rate contribute to the observed zircon matrix effect and that the two aspects are well correlated for zircon with higher radiation doses than the calibration zircon material. The zircon matrix effect is worse for lower radiation dose zircon, falling well outside 1% accuracy (Fig. 4.3), but these zircons have similar ablation rates to the calibration zircon (Fig. 4.4). This would suggest the ablation rate is only partially controlling the matrix effect seen in LA-ICP-MS and that there is likely some other 'crystallinity' component controlling the amount of Pb/U fractionation.

The choice of calibration RM is a critical factor for zircon LA-ICP-MS U-Pb age accuracy and if a high radiation dose zircon (e.g. FC-1) is used to calibrate a low radiation dose zircon (e.g. Mud Tank) this will exacerbate the zircon matrix effect. Thermal history of a zircon will control the use of calculated radiation damage [95, 97] and can partially or fully anneal damage. Use of Raman spectroscopy [97] may be the best option for assessing radiation dose / crystal damage and may prove as useful as CL imaging of zircon going forward.

As mentioned in Horstwood et al. [161] there are complications in comparing the LA-ICP-MS ages directly with the corresponding ID-TIMS ages since the former are usually done on the un-treated grains, while the latter are annealed and either mechanically or chemically abraded [88]. If there is a zone or portion of a zircon that has compromised crystal structure, it would have preferentially been dissolved away in the ID-TIMS analysis, while still being

available for sampling during LA-ICP-MS analysis. Recent work has shown the advantages of annealing or chemical abrasion for LA-ICP-MS zircon age accuracy [95, 178] and although time consuming (particularly chemical abrasion); implementing these tools should improve the agreement between LA-ICP-MS and ID-TIMS ages.

4.4.3 Laser fluence impact on U-Pb fractionation

Multiple zircon RMs analysed using different laser fluences showed a decrease in accuracy of the LA-ICP-MS ages with increasing fluence. This suggests that the zircon matrix effect becomes worse at higher laser fluence. Increase of laser fluence will cause an increase in the ablation rate [96] and drilling deeper can cause more element fractionation due to increased aspect ratio of the ablation crater [27].

These results provide an explanation of the difference between Plesovice and 91500 RM results in our study (0.7% difference in U-Pb age using a laser fluence of 2.0 J/cm²) and the previous study by Allen & Campbell [95] (~1.6% in the U-Pb age using a laser fluence of 4-5 J/cm² for Plesovice vs. 91500 zircon). When using a laser fluence of 5.2 J/cm² our study shows a similar 1.8% offset in the U-Pb age between Plesovice and 91500 as Allen & Campbell [95]. The trade-off of using lower laser fluence is lower sensitivities (2.7 times lower sensitivity at ²³⁸U using 1.2 J/cm² compared to 5.2 J/cm²); however, we suggest that it is preferable to have higher random errors (counting statistics) with lower systematic errors (zircon matrix effect) as the former can be reduced by increasing the number of analyses.

4.4.4 Laser pulse width impact on U-Pb fractionation

To investigate effects on LA-ICP-MS analyses from laser pulse width, two nanosecond lasers with different pulse widths (20 ns vs. 5 ns) are compared. The ICP-MS models are different (Agilent 7700 vs. 7900), but tuning parameters, and in particular the U/Th ratio [44] were kept the same between the two ICP-MS instruments, suggesting that each had similar properties. Data were collected over several months to ensure that results were reproducible for each laser system. Results in Figure 4.3 show no statistical difference at the 2-sigma level for these two laser systems for any of the zircon RMs. This is not surprising as the relative difference in pulse width between the two lasers is relatively minor compared to the pulse width difference between nanosecond and femtosecond lasers where much less down-hole U-Pb element fractionation occurs [55]. The similar results obtained on the two different

instrument setups suggests that much of the variation in inter-laboratory studies [160] could be due to user parameters such as: laser fluence, sample preparation, and particularly the choice of primary RM.

4.4.5 Annealing vs. non-annealed zircon ages

Several studies have shown the benefit of annealing zircon prior to LA-ICP-MS analysis [95, 154], however Marillo-Sialer et al. [96] showed no benefit. Our study shows variable accuracy improvements in U-Pb ages with annealing and it is likely that the higher laser fluences used in Allen & Campbell [95] and Solari et al. [154] likely caused the zircon matrix effect to be worse for the non-annealed grains so that annealing the zircon was more beneficial to the accuracy. Therefore, use of low laser fluence may reduce the need for annealing zircon for LA-ICP-MS U-Pb dating for high radiation dose zircons. For low radiation dose zircon it is less clear. For example, the Mud Tank zircon is consistently >2% too young relative to its ID-TIMS age for both annealed and non-annealed grains. Annealing should repair some of the radiation damage and this is seen in Marillo-Sialer et al. [97] where the Raman peak widths lessen with annealing. Therefore, some improvement in the accuracy would be expected for the Mud Tank zircon, however our annealed Mud Tank are identical in age to the non-annealed grains and suggest there is no improvement in the zircon matrix effect when annealing, at least for low radiation dose grains. Three previous studies that have done zircon annealing for LA-ICP-MS U-Pb ages [95, 96, 154], have mentioned little about the low radiation dose zircons (e.g. Mud Tank, Monastery, etc.). We note specifically the Mud Tank zircon is significantly too young (~3.5%) for its radiation dose before and after annealing, especially compared to the two Eocene zircons of similar radiation dose (AusZ-2 and AusZ-5) from Kennedy et al. [167], and future ID-TIMS work on the Mud Tank grain may help understand the cause of this.

4.4.6 U-Pb age uncertainties

Published guidelines for random (e.g. counting statistics) and systematic errors for U-Pb geochronology in zircon by LA-ICP-MS have been presented by Horstwood et al. [161]. For the purposes of this study we ignore systematic errors that are identical for all tests conducted such as uncertainty in decay constants and uncertainty in 91500 U-Pb composition. Uncertainties related to random sources of (e.g. counting statistics) are below 1% on the

weighted mean U-Pb age of multiple zircon RMs was ensured by using between 10 and 30 analyses in the age calculation. The long term variance of validation material (ϵ') of Horstwood et al [161] is not included in the uncertainties for investigation of the zircon matrix effect as there is no excess variance of our validation material from session to session outside analytical uncertainty (2-sigma); see electronic appendix. Also our average uncertainty on Temora is equivalent to the relative standard deviation of the mean U-Pb ages, suggesting our estimate of uncertainty is accurate [179] assuming the Temora zircon is homogenous for Pb/U ratios. The number of analyses used depended on the amount of RM available to the lab as well as the concentration of radiogenic Pb. The relatively large number of analyses was used to minimize random counting statistic errors and while this can produce artificially low uncertainties [161], the reduction of counting statistic errors can allow investigation into non-random, systematic bias such as the zircon matrix effect which is currently not accounted for. We confirm the results of previous studies showing a systematic bias for U-Pb ages by LA-ICP-MS in some zircon RMs relative to their ID-TIMS age correlated to the zircon radiation dose. In addition to the systematic error calculations in the Horstwood et al. [161] study, there should be a term for the zircon matrix effect as a function of the zircon apparent radiation dose or other estimate of zircon crystallinity such as Raman spectroscopy. Because of differences in operating conditions (e.g. laser fluence), laser systems and calibration materials, this systematic uncertainty should be characterized for each laboratory setup by analysing a range of zircon reference materials. Calculation of U and Th concentrations using the widely available NIST glasses would allow for a relatively accurate estimate of the apparent radiation dose. As an example, the correlation in Figure 4.7 between the LA-ICP-MS age relative to ID-TIMS and apparent radiation dose shows how this zircon matrix effect systematic error term can be calculated. Using an equation fit to the data in Figure 4.7, zircons with lower or higher radiation dose compared to the primary standard could then be accurately corrected for the zircon matrix effect, thus improving the accuracy of the LA-ICP-MS technique.

This correction factor would be applied to the weighted average of LA-ICP-MS U-Pb ages based on apparent radiation dose. To assess the accuracy of any such correction; several zircon RM of varying radiation dose, preferably not used in the correction factor equation, should be analysed on a session. The accuracy of the radiation dose estimate could be

checked on unknowns by using Raman spectroscopy and using the ν_3 (SiO_4) width or shift and comparing with RMs for cases where the apparent radiation dose and the true radiation dose are significantly different. The uncertainty in this correction factor should be calculated on the mismatch between the equation used in Figure 4.7 and the zircon RM data points and should be propagated after taking the weighted average of a sample.

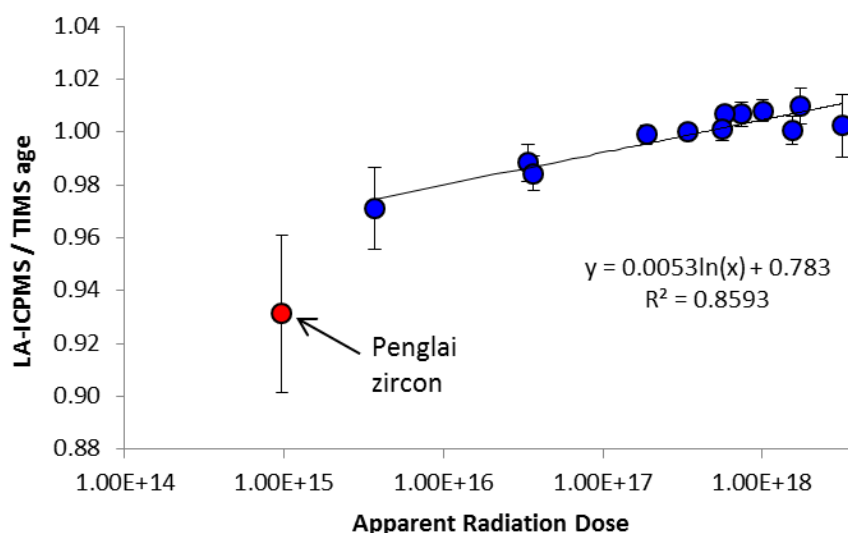


Figure 4.7. Apparent radiation dose calculated using the known U and Th concentrations in zircon RMs vs. LA-ICP-MS age / ID-TIMS age. Black line is a log function which fits the data set with a R^2 value of ~ 0.86 . The equation presented would be used to calculate the zircon matrix effect correction factor based (and addition of associated uncertainty in the correction) on the apparent radiation dose of the unknown zircons. Error bars are 2-sigma. Penglai zircon excluded from calculation, but r^2 is ~ 0.84 if it is included in the correction.

4.5 Conclusions

We demonstrate the accuracy of the LA-ICP-MS technique to around 1% (2-sigma) for zircon with radiation doses significantly higher than the primary standard and around 2% (2-sigma) for zircon with radiation doses significantly lower than the primary standard. There is a clear need for controlled and optimized operating conditions for LA-ICP-MS as well as sufficient sample preparation to ensure accurate and precise U-Pb ages. The abundance and distribution of atmospheric air in the laser cell can be assessed by measuring mass 56 during U-Pb data collection, and this can be used to assess data quality. Lower laser fluence ($< 2 \text{ J/cm}^2$ for the 193nm wavelength and nanosecond pulse widths) can reduce the zircon U-Pb matrix effect, precluding the need to anneal zircon before analysis. No differences in the zircon matrix effect are seen between the 20 ns pulse width laser and the 5 ns pulse width laser system.

We suggest a correction for the zircon matrix effect be applied to the weighted average age of a sample based on the apparent radiation dose, including the addition of a systematic error term for this correction factor.

Variables in instrumentation and operating conditions can have important influences on the accuracy of the LA-ICP-MS technique and this hinders inter-laboratory comparisons. While annealing and chemical abrasion may help improve the accuracy, understanding and optimizing instrumentation is also required to improve the quality of LA-ICP-MS U-Pb ages in zircon.

4.6 Acknowledgements

The authors would like to thank Karsten Goemann and Sandrin Feig for help with CL imaging of the zircon. Additionally, the authors would like to thank the following for contributing reference materials used in this study: Dima Kamenetsky for samples of Monastery and TASDOL zircon, Henrik Svensen & Fernando Corfu for SP07-05 Karoo dolerite zircon, Jiri Slama for the Plesovice zircon, Natalie Kositsin at Geoscience Australia for the Temora and OG-1 zircon samples, Sam Bowring for the FC-1 zircon sample, and Allen Kennedy for the AusZ-2 and AusZ-5 samples. We would also like to thank Matt Horstwood and an anonymous reviewer for constructive comments on the manuscript.

Chapter 5 Time-of-flight ICP-MS laser ablation zircon geochronology: assessment and comparison against quadrupole ICP-MS

As accepted to the Journal of Analytical Atomic Spectroscopy, July 2020. J. M. Thompson, L.V. Danyushevsky, O. Borovinskaya, M. Tanner

Abstract

This study presents U-Pb isotopic results from the mineral zircon measured by nanosecond laser ablation coupled to either a time-of-flight inductively-coupled plasma mass spectrometer (ICP-MS), a quadrupole ICP-MS or both via a split stream arrangement. Results show both ICP-MS types produce similar levels of precision and accuracy for most U-Pb ages in the mineral zircon. The time-of-flight ICP-MS however shows slight non-linearity at high detector counts ($>7,000$ for ^{238}U) producing a bias in zircon U-Pb ages from published values outside analytical uncertainty. Use of ^{235}U instead of ^{238}U is shown to resolve the inaccuracy in the U-Pb age at the expense of analytical precision due to lower abundance of ^{235}U . Trace element concentrations also measured along with U-Pb isotope data in zircon show the time-of-flight ICP-MS to provide similar accuracy and precision as the quadrupole ICP-MS, except for isotopes in regions around high intensity major element peaks (e.g. Zr) where accuracy and levels of detection of the time-of-flight ICP-MS are matrix dependent relative to the quadrupole ICP-MS. A comparison is made between the analytical capabilities of the time-of-flight ICP-MS and the quadrupole ICP-MS highlighting some advantages and disadvantages of the time-of-flight technology for zircon U-Pb geochronology.

5.1 Introduction

Inductively-coupled plasma mass spectrometry (ICP-MS) is widely used for chemical and isotopic analysis due to the ability of the ICP to ionize most elements in the periodic table and due to the relatively simple mass spectra the technique generates. Laser ablation (LA) of a wide range of matrices is a common sample introduction method for *in-situ* microanalysis by ICP-MS. This type of analysis commonly requires time-resolved data acquisition on the MS detector to adequately characterise the transient nature of the LA signal which may involve rapid variations in intensity due to sample inhomogeneity or other factors. In U-Pb dating of zircon and other mineral phases by LA-ICP-MS, there is a need for high precision and accuracy

measurements of two elements of differing behaviours during ablation [26] and in the ICP [44]. This effect is known as 'element fractionation' and leads to the observed effect of changing of element ratios during analysis. [26] To address this effect, a time dependent correction needs to be applied to the Pb/U signal ratios. This is typically done using a model curve [163], line intercept [11], or projection back to the initial ratio at the start of ablation [93]. In either case, it is important to have rapid and ideally simultaneous readouts for U-Pb dating to best characterize this element fractionation phenomenon since it is a limiting factor to accuracy and precision of the technique.

Commonly used ICP-MS are quadrupole (QMS), magnetic sector with scanning fields (SFMS), Mattauch-Herzog geometry (MHMS), magnetic sector with multiple detectors (MCMS), and time-of-flight (TOFMS). QMS and scanning SFMS are mass filters and sequential in nature; detecting the target ions of interest sequentially and then repeating the analyte list. Each readout of a sequential mass filter will constitute one 'sweep' or 'cycle'. The time length of each 'sweep' on a quadrupole system is dictated by the number of isotopes of interest, the counting time on each isotope, the quadrupole jump time between settings required for different isotopes and the quadrupole settling time (the time waiting after a quadrupole 'jump' in m/q before the detector measures, to allow electronics to stabilize). Scanning SFMS instruments operate in a similar sequential fashion with magnetic- and electric field 'scans' and 'jumps'. When using an MS with a sequential mass filter, there is thus a trade-off between the number of measured isotopes and the time resolution of the instrument readout. Additionally, sequential acquisition is not ideal for isotope ratio measurements or trace element concentration analysis based on transient signals produced by LA sampling technique due to continuous variations in the laser ablation signal caused by either laser pulse induced spectral skew [180], sample heterogeneity (e.g. inclusions of other phases or chemical zoning) or plasma flicker; all affecting the measurement precision and the ability to accurately characterise a sample. MCMS instruments do offer simultaneous isotope detection but only for a fixed set of isotopes and not for multi-element analysis. Two other MS that allow for simultaneous detection of a wide range of isotopes are the TOFMS and MHMS.

For analyses with transient signals, such as those from laser ablation (LA), the ability of TOFMS to collect full mass spectra with rapid instrument readout is a significant advantage over sequentially based mass filters. The full mass spectra recorded by the TOFMS, in

combination with the rapid instrument readouts, allows for better characterization of transient LA signals, leading to more confident identification of inhomogeneities within the target phase.

With time-of-flight as the detection unit for ICP-MS, ions from the ICP source are extracted through grounded sampler and skimmer cones to the high vacuum chamber of the instrument. After separation from background gas the ion beam is focused and guided to the TOFMS for analysis. In the TOFMS, packages of the ion beam are accelerated to bring all ions to the same kinetic energy so that they will travel at different velocities based on their mass to charge ratio (m/q). The fixed ion flight path means that the difference in velocity of ions will produce different arrival times at the detector. Mass calibration is applied to transform the initial time-dependent spectrum into a mass spectrum.

TOFMS technology has been used with ICP-MS for more than 25 years [181] with the concept of the technology dating back to the 1940s. Despite this history, it has not seen wide usage in LA-ICP-MS applications compared to that of QMS. Previous studies using TOFMS have demonstrated two main issues relative to other types of ICP-MS, low sensitivity [51] and a lower dynamic range of linear detection response [182]. Another issue with TOFMS due to the hyperspectral nature of the instrument output is the need for an additional data processing step to obtain results that are in a similar format (isotope intensity vs. time) as other ICP-MS types. The most important part of this additional processing step for TOFMS is the baseline subtraction for tailing from adjacent peaks. However, the simultaneous nature and rapid data collection of the TOFMS ion detection should theoretically allow for more representative sampling of transient signals generated by LA. MHMS is also capable of providing for simultaneous, multi-elemental detection [183] with potentially superior linear dynamic range and higher isotope ratio precision [184] that what is currently achievable via TOFMS. However, with a few exceptions [86, 183] this technology has yet to achieve widespread usage in the Earth Science community.

A laser ablation instrument typically consists of a laser source, a set of optics to focus the laser beam, a sealed sample cell [38] (typically flushed with helium [31]) in which ablation of the samples takes place, and interface tubing to transport aerosol to the mass spectrometer. Use of relatively small laser beam sizes (≈ 1 to > 100 μm) allow for *in-situ* analysis of specific zones within the sample and/or micro-inclusions that would have otherwise been

homogenized in bulk analytical techniques. This is particularly true for the mineral zircon and its use as a U-Pb geochronometer, as zircon can often record multiple growth events that can be significantly different in age (e.g. 100s of Ma). While other techniques, such as the secondary ion mass spectrometry (SIMS), can also obtain accurate and precise in-situ isotopic information on minerals, LA-ICP-MS has advantages in higher throughput and relatively simple sample preparation (e.g. no conductive coating needed). However, one significant trade-off is that LA-ICP-MS is a more destructive technique, sampling $\approx 10\times$ more material than SIMS.

Zircons have been analysed by LA-ICP-MS to determine ages by U-Pb and Pb isotopic compositions since the early 1990s [185] using a variety of different ICP-MS types: QMS [11, 159], scanning SFMS [128] and MCMS [93]. Many analytical issues complicate accurate U-Pb ratios via laser ablation; mostly due to non-representative sampling of the zircon during the LA process [46] as well as incomplete digestion in the ICP [44]. These two phenomena are collectively known as 'element fractionation' [31] and hinder accurate U-Pb isotopic ages without a matrix matched (e.g. zircon) calibration material [62]. Typically, in LA-ICP-MS zircon U-Pb dating, there is a single zircon of known age or U-Pb isotopic composition that is used to correct for element fractionation, mass bias and instrument drift. However, it has been shown that not all zircon matrices are the same with respect to the LA-ICP-MS technique [95] and this has limited the accuracy of dating of zircon to between ≈ 1 and 2% [122], depending on the analytical conditions and zircon materials used in a particular study. The Pb/U element fractionation becomes more distinct as the laser drills down into a zircon crystal [186] and minimizing the depth of the analysis was shown to provide best accuracy and precision. This can be done by analysing line scans across zircons [122] or by limiting the number of laser pulses fired at the zircon [93].

Although the type of MS has relatively small importance for the above matrix and element fractionation effects, the rapid duty cycle and full mass spectrum data collection of the TOFMS, should allow for an improvement in measurement precision and sample characterization by LA-ICP-MS compared to sequential QMS, if all other parameters are equal. To assess the potential benefits of TOFMS, this study compared the accuracy and precision of a QMS and a TOFMS for ablation of various zircon reference materials (RMs) for

U-Pb isotopic ages using methodology previously used for and optimized for QMS [164, 186]. Multiple analytical sessions on both instrument types as well as analyses in split stream arrangement are presented, along with a discussion of the main sources of signal uncertainty for the two ICP-MS types.

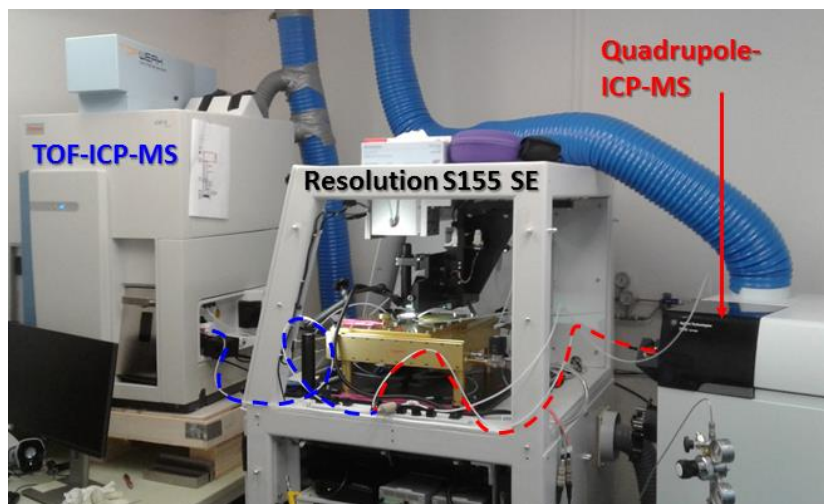


Figure 5.1. Image of the Resolution S155 laser ablation system in split stream configuration with the Agilent 7900 on the right and TOFWERK “icpTOF R” on the left. The dashed red line outlines the tubing from the Y connector that goes into the Agilent 7900, while the dashed blue line outlines the tubing going to the TOFWERK “icpTOF R”.

5.2 Methods

Measurements were conducted at the CODES Analytical Laboratories at the University of Tasmania. All laser ablation analyses were carried out using an ASI RESOLution S-155 instrument equipped with an ATL-X ArF excimer laser with a laser pulse at a 193nm wavelength and ≈ 5 ns duration. Laser fluence was kept at 2.1 J/cm^2 while firing the laser at 5 Hz and using a $30 \mu\text{m}$ beam size. All ablations were performed in a pure helium atmosphere flowing at 0.35 l/min. Immediately after the ablation, helium was mixed with argon flowing at 1.0 l/min. Tuning of the ICP-MS instruments was performed using line ablations on the NIST612 glass. The sampling position of the plasma was optimised for sensitivity and robustness, while keeping the $^{238}\text{U}^+/^{232}\text{Th}^+$ ratio ≈ 1.05 . Other ICP-MS lenses were optimized for highest sensitivity on heavy masses.

Two experiments were conducted for this study. Analyses in Experiment 1 were performed in a split stream configuration where the laser ablation aerosol was divided equally between two different ICP-MS instruments: An Agilent 7900 quadrupole ICP-MS and a TOFWERK icpTOF R. The icpTOF R is based on an ICP-QMS, ThermoFisher Scientific iCAP Q

where the analyser quadrupole and detector are replaced by a notch filter and a TOFMS. Further details of the icpTOF R can be found in Hendriks et al. [187]. A “T” junction was added after the ablation cell with supplementary argon to give optimum gas flows into each ICP-MS. After the “squid” smoothing device [38] a “Y” junction was added ≈ 2 cm downstream and two different 1.5-metre-long nylon tubes went from the “Y” junction to the two ICP-MS instruments (Fig. 5.1). The helium gas flows in the laser cell were as above to avoid any change in ablation characteristics; however, the supplementary argon gas flow was increased to achieve U/Th ratios of 1.05 for both ICP-MS instruments under tuning conditions described above. The gas flows were measured with an external flow meter at each end of each of the tubing from the “Y” junction just before the ICP torches on both instruments and flows were found to vary by less than 2 ml/min between the two ends. The positions of the nylon tubing into each ICP-MS was in a similar geometry (1 loop) and position of the tubing in the quartz injectors was at a constant distance to the tip of the injector since the ends of the respective torches had slightly different lengths.

Using the routine zircon geochronology methodology from the CODES Analytical Laboratories [186], the Agilent 7900 recorded data for the following masses ^{31}P , ^{49}Ti , ^{56}Fe , ^{89}Y , ^{91}Zr , ^{93}Nb , ^{139}La , ^{140}Ce , ^{141}Pr , ^{146}Nd , ^{147}Sm , ^{153}Eu , ^{157}Gd , ^{159}Tb , ^{163}Dy , ^{165}Ho , ^{166}Er , ^{169}Tm , ^{172}Yb , ^{175}Lu , ^{178}Hf , ^{181}Ta , ^{202}Hg , ^{204}Pb , ^{206}Pb , ^{207}Pb , ^{208}Pb , ^{232}Th , ^{235}U and ^{238}U with the quad sweep time of 0.25 seconds. Dwell times were 25 ms for ^{206}Pb and ^{207}Pb , 20 ms for ^{204}Pb and ^{235}U , 15 ms for ^{238}U , 10 ms for ^{49}Ti , ^{202}Hg , ^{208}Pb and ^{232}Th , 5 ms for ^{31}P , ^{139}La and ^{141}Pr , and 2 ms for all other masses. This data collection methodology is optimized for the best analytical precision on U-Pb and Pb isotopes while also collecting compositional information about zircons and inclusions within. ^{238}U was not used above 3.2 Mcps to safely avoid the pulse to analog transition of the detector.

The icpTOF R samples the ion beam by extracting discrete pulses at a rate of 33,000 Hz which corresponds to 30 μs , the flight time of the heaviest expected ion in the ion beam: uranium isotopes and their oxides species. The icpTOF R uses a micro-channel plate (MCP) detector with a chevron configuration to resolve the short time dependent signals from ions of individual m/q. The time-dependent signal is sampled and digitized with 0.625 ns intervals leading to about 40,000 datapoints per mass spectrum. Signals of 9000 TOF extraction pulses were averaged, corresponding to 0.278 seconds, to correspond to the sweep time of the QMS

system for a more direct comparison with QMS data. The resolving power of the TOFMS was tuned to $R = 2900$ at the start of each session ($R = m/\Delta m$, where m is the centre and Δm the full width of the mass peak at half maximum – FWHM). The ThO production rate ($^{248}\text{ThO}^+ / ^{232}\text{Th}^+$) was 0.7% and 0.2% for the TOFMS and QMS respectively. Each analysis consisted of a 30 second ‘gas blank’ followed by a 30 second ablation. The split stream setup up for Experiment 1 is shown in Figure 5.1.

For Experiment 2 the laser ablation system was coupled to the TOFMS for two different analytical sessions and the QMS for another two analytical sessions. All analyses were performed using the ‘squid’ signal smoothing device [38]. The TOFMS had an averaging of 6170 ion extraction pulses, corresponding to an instrument readout of 0.187 seconds. The resolving power was tuned to $R = 2900$ at the start of each session. Under these conditions, the ThO production ($^{248}\text{ThO}^+ / ^{232}\text{Th}^+$) rate was 0.6-0.8% for the TOFMS, whereas the QMS rate was $\approx 0.15\%$. Each analysis consisted of a 30 second ‘gas blank’ followed by a 30 second ablation.

The zircon analyses performed on an QMS recorded the following masses for both sessions: ^{49}Ti , ^{56}Fe , ^{91}Zr , ^{202}Hg , ^{204}Pb , ^{206}Pb , ^{207}Pb , ^{208}Pb , ^{232}Th , ^{235}U , and ^{238}U with the quad sweep time of 0.188 seconds. Dwell times for individual masses were kept the same as during Experiment 1, however there were a much smaller number of other elements measured so as to improve analytical precision with more instrument readouts over the same analysis time and methodology is similar to Halpin et al. [164].

Because the TOFMS samples the entire atomic mass spectrum, it is subject to high intensity m/q regions from plasma generated background ions such as O and Ar isotopes. During the ablation of zircon, Zr isotopes have high intensity as well. The icpTOF R utilises a notch filter between the collision cell and the entrance to the TOFMS. The notch filter allows for up to 4 masses to be attenuated by a voltage that causes an unstable trajectory of the notching mass. The notch filter is not able to isolate exact masses but rather a region of masses - a few m/q on either side of the target mass are affected by the attenuation. Notching of high intensity peaks is important to keep the detected ion signal of individual m/q below 200mV, and the total ion current below about 35 Mcps to avoid oversaturation of the detector [187]. Notched m/q in this study were: 18, 36, 40 and 90.

To facilitate comparisons between the uncertainties of the measured signals and isotope ratios obtained from the two instruments, the results are plotted in the form of counts recorded on the MS detectors during measurements, rather than in 'counts per second' which reflect the overall sensitivity of the instrumentation rather than the number of counts measured during analyses.

A range of zircon RMs were ablated to assess the accuracy and precision for a range of different ages and U contents. Analysed zircons included: 91500 [155], FC-1 [165], AusZ-2 [167], BB16 [188], OG-1 [166], Plesovice [141], Qing Hu [170], Temora [140] and Mud Tank [189]. These zircons ranged in age from ≈ 38 Ma to ≈ 3465 Ma and U contents from ≈ 10 ppm to $\approx 5,000$ ppm. Each of these different zircon reference materials have previously published ID-TIMS or TIMS ages and have been shown to be homogenous at the scale of the laser ablation sampling. Most of the zircon ages reported in this study are U-Pb ages, except for the OG-1 zircon and the 91500 zircon for which the $^{207}\text{Pb}/^{206}\text{Pb}$ ages are reported due to lack of ID-TIMS age on OG-1 and because the 91500 was used as the calibration material for the U-Pb system so by definition it would give an accurate U-Pb age.

Data collected by the TOFMS consists of the mass spectrum from 2 to 260 m/q (Th) divided into 44,000 channels. These channels are plotted as a sum of ion counts for a single analysis to be used for assessing the mass spectra (Fig. 5.2). Tofware (v 3.1.1, <https://www.tofwerk.com/software/tofware/>, running in Igor Pro 7) was used to process data. First, a time-dependant mass calibration was applied to each analysis using ^{27}Al , ^{51}V , ^{115}In , ^{141}Pr , ^{169}Tm , ^{208}Pb and ^{238}U as measured in the NIST610 glass. These elements span a range of masses, mostly monoisotopic and are free of interferences to provide an accurate mass calibration. This calibration corrected for any slight variance of the atomic mass peak position over the course of the experiments. Drifts in mass calibration were extrapolated between blocks of duplicate NIST610 analyses measured throughout each analytical session and the mass calibration was not found to vary between different matrixes.

While TOFMS instruments have significantly higher mass resolving power compared to QMS, they also have relatively poor abundance sensitivity compared to other MS. Because of this, a baseline subtraction is required based on m/q regions on low and high-mass side of each peak of interest (Fig. 5.2) due to tailing from adjacent, intense peaks. A baseline fit equation was defined using the 'integrated peaks' option and a set of parameters available

under the 'peak list' option for the baseline function in Tofware. Since the baseline shapes of mass spectra vary depending on the elemental abundances in the analysed materials (zircon is shown as example on Figure 5.2, with clear baseline maxima at masses 90 and 180 corresponding to Zr and Hf, respectively), a standard of similar matrix is required for accurate baseline subtraction of unknowns. The baseline fit algorithm can be adjusted to mass spectra of specific sample matrix to provide best accurate integration and baseline subtraction, e.g. for small peaks in the vicinity of intense peaks. The baseline fit for the 91500 zircon analysis was applied to all zircon analyses as the Zr and Hf isotopic peaks are the dominant peaks for zircon, while a separate baseline subtraction fit was done for the NIST610 glass analyses. Using these settings and the sum of all the mass spectra for a 91500 zircon and a NIST610 analysis, a function was fit to the baseline regions between isotopes. In each analysis, the baseline fit function was applied to each TOFMS readout to account for time dependent changes in the baseline. Widths of the integration regions (Fig. 5.2, lower figure) for the isotopes of interest are determined from a calculated mass calibration using an $r = 2900$ and vary systematically with mass. Purple regions in Figure 5.2 are the region the baseline curve is fit to and their widths are a function of the adjacent peak intensity, where a higher intensity peak will produced a smaller purple region.

Time-resolved peak data were exported in a comma separated value (csv) format to be used by the laser ablation data reduction software, LADR [190] <https://norsci.com/?p=ladr>; with care taken to ensure all intervals selection, gas blank subtractions and calibrations were done consistently between the different data sets. LADR can evaluate different levels of uncertainty and the two levels utilized in this study are: the "Signal Precision" which consists of the measurement uncertainty on the ratio of two elements (e.g. $^{206}\text{Pb}/^{238}\text{U}$), and the "Within-Run Uncertainty" which consists of the "Signal Precision" added quadratically to the uncertainty on the calibration for the ratio of the same two elements. The "Within-Run" uncertainty does not include systematic uncertainties, such as uncertainty in known age of the primary reference materials, and thus any comparison made between the published ages and those measured in this study have added the systematic uncertainty component to the weighted average of the U-Pb and Pb-Pb ages, using the protocol in Horstwood et al. [189].

The 91500 reference zircon was used for calibration of the U-Pb ratios while the NIST610 reference glass was used for the $^{207}\text{Pb}/^{206}\text{Pb}$ ratios using values of Baker et al. [143]. Trace

elements in zircon were quantified using the NIST610 glass and GeoReM preferred values with ^{91}Zr as the internal standard element and normalizing measured cations to a stoichiometric Zr site total. Limit of Detection (LOD) calculations were similar to that in Longerich et al. [58] where the 'gas blank' was used in the estimate of the LOD. Data reduction was similar to that of Thompson et al. [186], however the data reduction software "LADR" was used to process all results instead of an in-house macro-based Excel workbook. Age results were plotted and calculated in Microsoft Excel using Isoplot 4.15 [174]. Individual analyses were corrected for common Pb when present, using the ^{207}Pb correction method [14] anchoring on the composition of common Pb using Stacey and Kramers [151] model Pb at the age of the zircon. Uncertainties in U-Pb and Pb-Pb dates were propagated according to Thompson et al. [186] and Horstwood et al. [189].

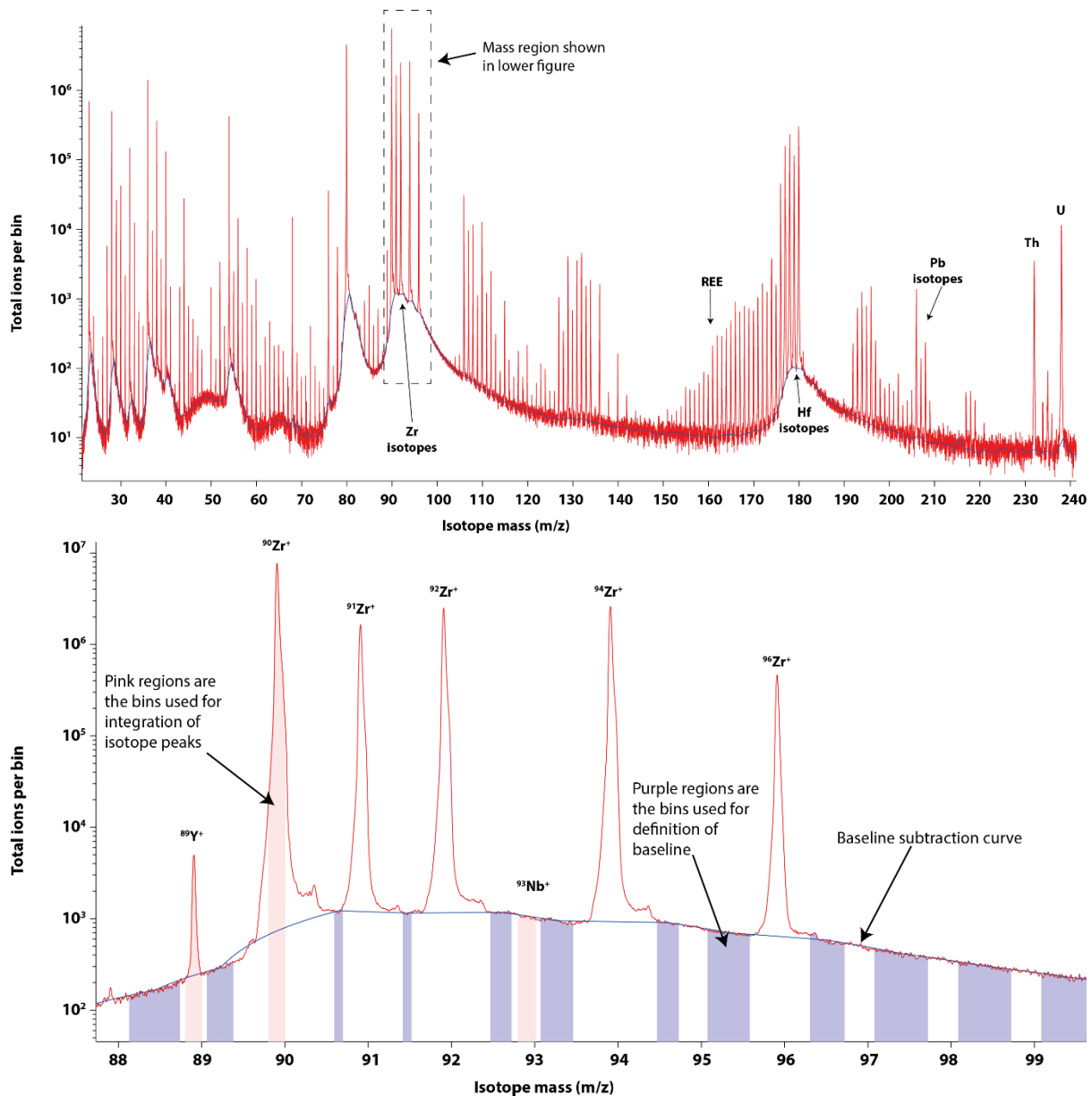


Figure 5.2. Upper figure: TOF mass spectrum of total ion counts from one zircon analysis (91500 zircon). Isotope peaks are highly resolved despite the tailing effects from high intensity peaks. Lower figure is zoomed into isotopes of Zr showing how the baseline subtraction is done and the effects of high intensity Zr peaks on the detection of Nb in zircon.

5.3 Results:

5.3.1 Experiment 1

Experiment 1 involved the split-stream setup described above and was completed in a single analytical session. Each individual analysis had a corresponding instrument readout from the ICP-TOFMS and the QMS, allowing for a direct comparison of a single ablation. Since the aerosol was split between the two instruments, the sensitivity was $\approx \frac{1}{2}$ of what could be achieved with the normal configuration when the entire aerosol goes into a single mass

spectrometer. Ages calculated from individual analyses are shown in Figure 5.3 and the weighted averages for each zircon are presented in Table 1. The laser ablation zircon U-Pb and $^{207}\text{Pb}/^{206}\text{Pb}$ ages calculated on the basis of weighted averages were within uncertainty of published results for each instrument, except for the Mud Tank zircon (both ICP-MS instruments) and the Qing Hu zircon that is 0.3 Ma too young outside the uncertainty for the TOFMS.

For the individual analyses of the Plesovice and QingHu zircon which are characterised by higher U contents, there was a systematic shift to younger dates with the TOFMS compared to the QMS results, although all analyses were within the 2-sigma within-run uncertainties on both instruments (Fig. 5.3).

The within-run analytical uncertainties for $^{206}\text{Pb}/^{238}\text{U}$ ratios on individual analyses were between 0.93% and 5.11% for the TOFMS and between 0.60% and 2.03% for the QMS. The within-run analytical uncertainties on individual analyses for the $^{207}\text{Pb}/^{206}\text{Pb}$ ratio was 0.82% to 16.3% on the TOFMS and 0.55% to 11.7% on the QMS.

Trace element data collected along with the U-Pb isotopic data are presented in the Electronic Appendix and Figure 5.4 shows results for the 91500 zircon for both ICP-MS types. The 91500 zircon is a well-characterized reference material and relatively homogenous for many trace elements. The lower abundance elements like P, Ti, Nb, La and Pr were generally not above limit of detection and are not discussed further for this Experiment. There is a good agreement between the two mass spectrometers for most elements with the exceptions of Nd, Sm and Ta.

Since the laser aerosol is divided in two, the LOD of an individual isotope, as calculated by Longerich [58] (Equation 5.1), for both mass spectrometer types was significantly worse than the typical setup (Experiment 2).

$$LOD = \frac{3\sigma_{ind}}{s} \sqrt{\frac{1}{n_b} + \frac{1}{n_a}}$$

Equation 5.1. LOD equation from Longerich et al. [58] where LOD is Limit of Detection, σ_{ind} is the standard deviation of the gas blank S is the Sensitivity calculated from the internal standard element sensitivity in the sample relative to the standards, n_b is the number of data points in the background and n_a is the number of data points for the ablation. See Longerich et al. [58] for more details.

The LOD based on the signal noise of the gas blank were also different between the two ICP-MS types. For both instruments, the LODs generally varied with mass where the lighter

masses had higher LODs, particularly on the TOFMS. The QMS generally had lower LODs by a factor of ≈ 10 although some elements on the TOFMS, such as ^{93}Nb , had higher LODs due to notching at Zr peaks. Pb isotopes and ^{56}Fe were an exception with similar LOD for both ICP-MS types due to a relatively high gas blank signal.

The mass bias and instrument performance were assessed using the $^{238}\text{U}/^{235}\text{U}$ ratio in the zircon reference materials. The TOFMS gave a weighted average of 138.7 ± 1.6 (2s), while the QMS gave a weighted average of 137.93 ± 0.95 (2s); both using within-run uncertainty inputs for the weighted average calculation and both within uncertainty of the expected natural ratio. In both sets the ratio was calibrated on the $^{238}\text{U}/^{235}\text{U}$ in the 91500 zircons using a value of 137.818 [162]. There is a slight dependence of the $^{238}\text{U}/^{235}\text{U}$ ratio on ^{238}U signal above $\approx 6,000$ counts for the TOFMS data (Fig. 5.5A) where the $^{238}\text{U}/^{235}\text{U}$ increases with increasing ^{238}U signal. The observed trend at high ^{238}U count rates has not caused excess scatter in the weighted average of the entire dataset when using the signal precision uncertainty, with an MSWD of 1.3 that is identical to the QMS results. However, when only the high signals are considered (6,000 counts; see insert on Fig. 5.5), the MSWD is 3.0, indicating variability beyond the uncertainty of counting statistics for the TOFMS.

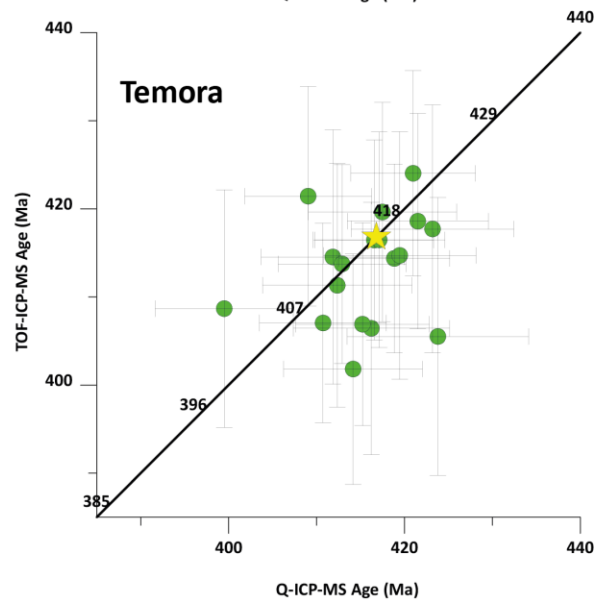
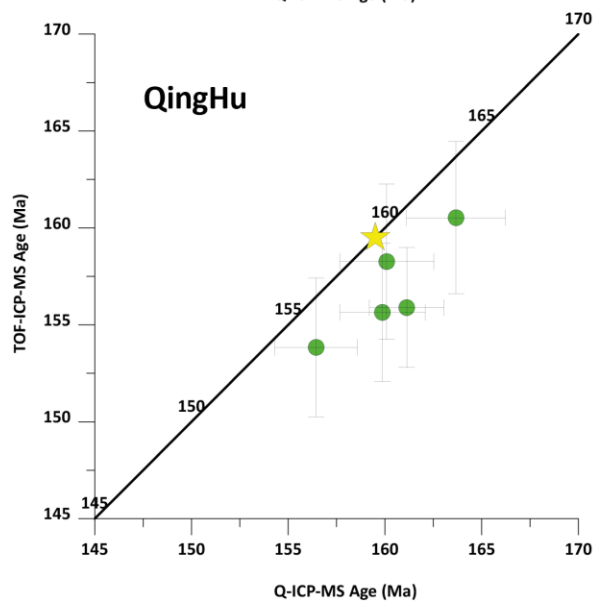
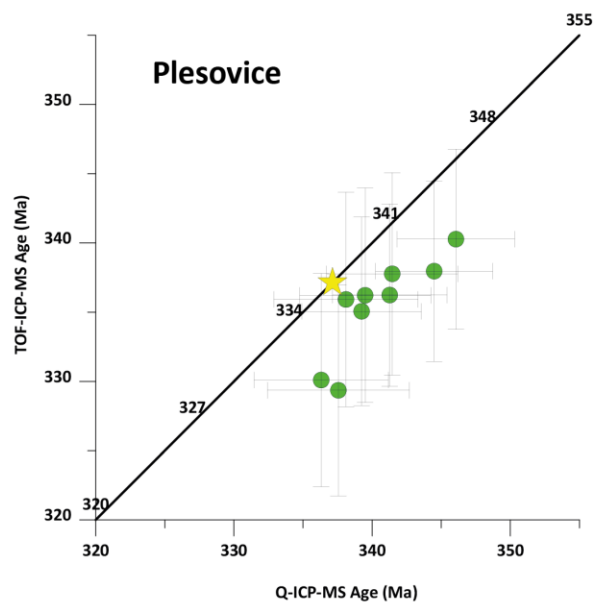
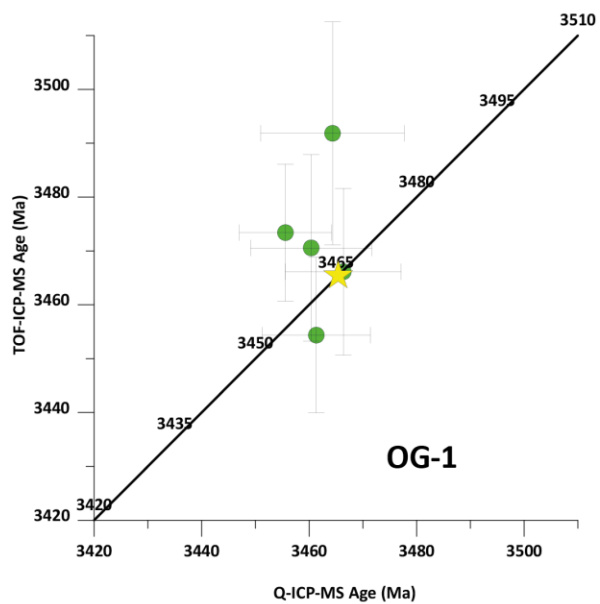
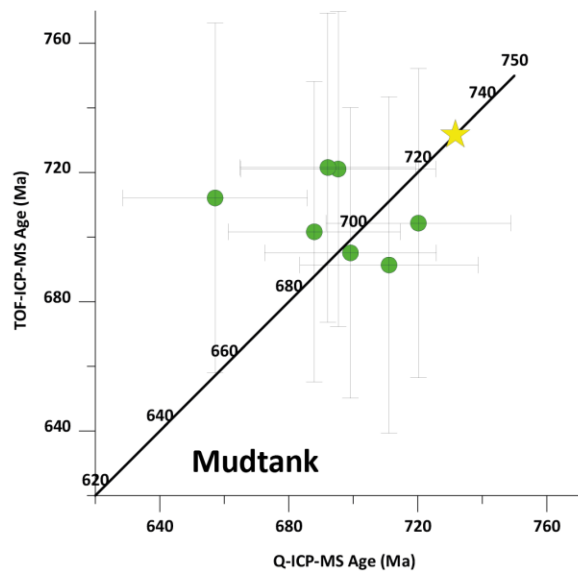
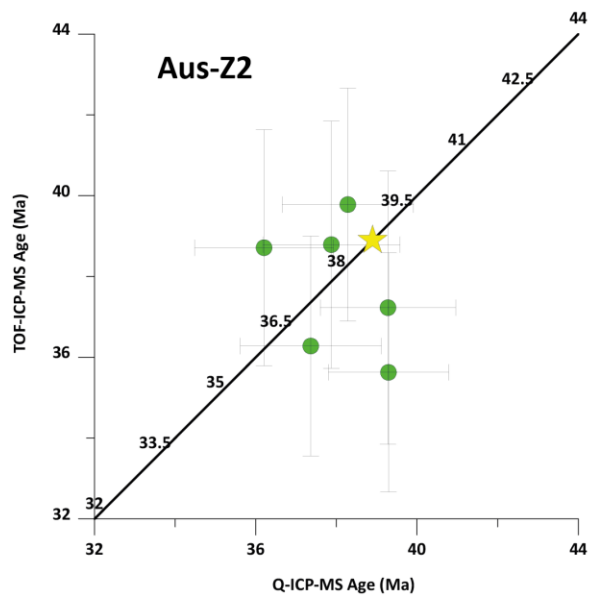


Figure 5.3. Age plots for select zircon reference materials used in Experiment 1 (split stream analysis). Green circles represent individual analyses with 2-sigma error bars (Within-Run uncertainty). Yellow star indicates published age on reference material. Black line is the 1:1 line between the TOFMS and the QMS. Individual ages are $^{206}\text{Pb}/^{238}\text{U}$ except for the OG-1 zircon which are $^{207}\text{Pb}/^{206}\text{Pb}$ ages. Note shift from 1:1 for Plesovice and Qing Hu – see text.

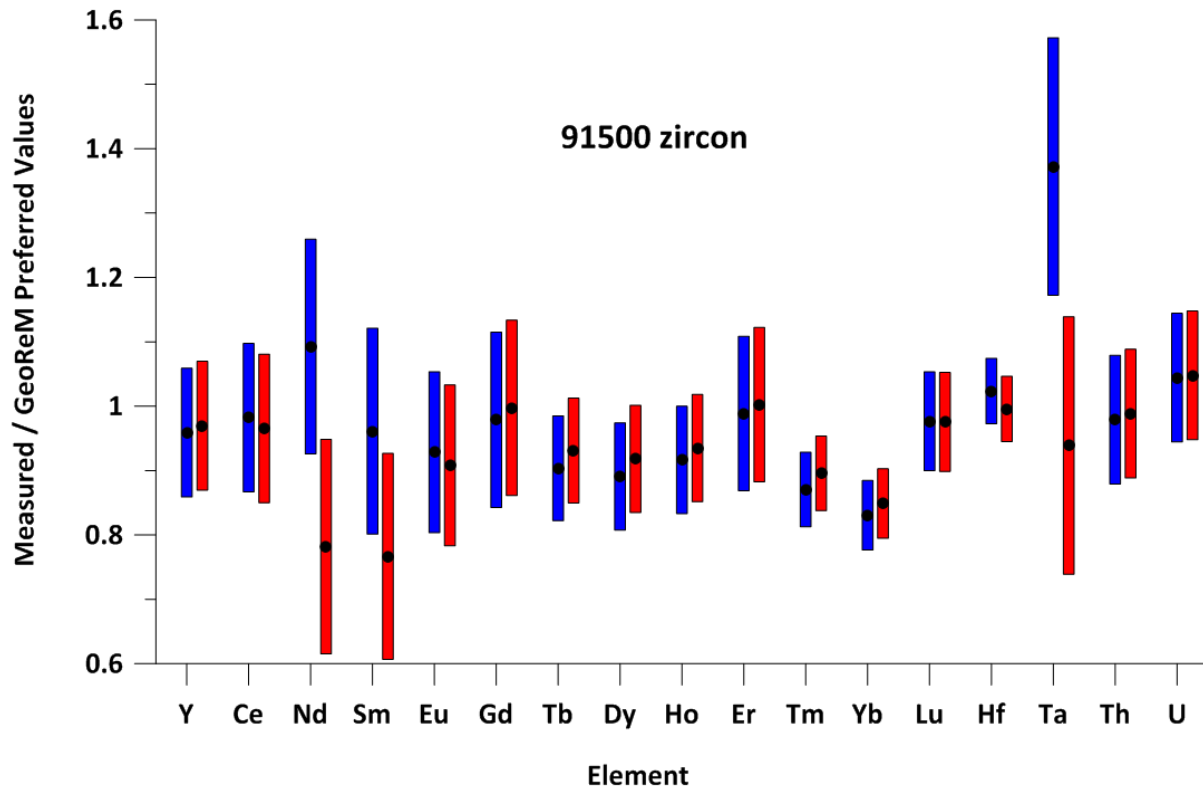


Figure 5.4. Average of 32 analyses for select trace elements measured in the 91500 zircon from Experiment 1 (split stream analyses) normalized to the GeoReM preferred values. Red bars: QMS results; blue bars: TOFMS results. A value of 1 represents the GeoReM preferred value. Black circle represents average of 32 analyses while the length of bars is the 1-sigma uncertainty and was propagated from the standard error of the average as well as the uncertainty from the GeoReM preferred values for the 91500 zircon.

5.3.2 Experiment 2

Due to the lower instrument sensitivities associated with the split stream analysis in Experiment 1, a second set of tests was performed to compare the TOFMS results relative to the QMS under more typical analytical conditions. Between 4 and 12 analyses were performed on each of the zircon RMs using the TOFMS and the QMS. The Temora and Plesovice zircon reference materials were analysed on two different sessions, while the other zircon reference materials were analysed on a single session. These results mostly show no bias in U-Pb or $^{207}\text{Pb}/^{206}\text{Pb}$ ages relative to published values (Table 2) for both ICP-MS types. The exceptions were the Mud Tank zircon, which was systematically too young for both ICP-MS types, and the Qing Hu zircon for the TOFMS which was systematically too young by 3.8%

and outside the uncertainty on the weighted average of the 7 analyses. The $^{206}\text{Pb}/^{238}\text{U}$ within-run uncertainties on individual analyses were between 0.58% and 15.5% for the TOFMS and 0.79% to 15.0% for the QMS depending on the amount of radiogenic Pb. Figure 5.6 shows the results for select zircon reference materials for each ICP-MS type demonstrating the levels of accuracy and precision for each. The U-Pb age results in Figure 5.6 have been randomized since there is no correlation between individual analyses done on different analytical sessions.

As with Experiment 1, the mass bias and instrument performance were assessed using the $^{238}\text{U}/^{235}\text{U}$ ratio in the zircon reference materials. The TOFMS gave a weighted average of 136.88 ± 0.99 (2s), while the QMS gave a weighted average of 137.6 ± 1.3 (2s); both using within-run uncertainty inputs for the weighted average calculation and both within uncertainty of the expected natural ratio. In both sets the ratio was calibrated on the $^{238}\text{U}/^{235}\text{U}$ in the 91500 zircons using a value of 137.818 [162]. There is a slight dependence of the $^{238}\text{U}/^{235}\text{U}$ ratio on ^{238}U signal above $\approx 7,000$ counts for the TOFMS data and possibly above 12,000 counts for the QMS (Fig. 5.5B), where the $^{238}\text{U}/^{235}\text{U}$ increases with increasing ^{238}U signal. In the case of QMS this is likely due to an offset in the detector dead-time. The MSWD on the weighted average using the within-run precision is not greatly affected by this dependence of ratio on the signal intensity where the QMS gives an MSWD of 0.47 and the TOFMS gives an MSWD of 1.00. Calculating the MSWD using the signal precision, the QMS gives an MSWD of 1.07 while the TOFMS gives a significantly higher MSWD of 5.0 due to the dependence of the $^{238}\text{U}/^{235}\text{U}$ ratio on ^{238}U count rates and indicates variability beyond counting statistics for the TOFMS.

| Sample | Age (Ma) | $\pm 2s$ within-run | $\pm 2s$ full analytical | MSWD | Probability of Fit | # of analyses | Measured / Accepted | $2s$ uncertainty | Published age (Ma) |
|--------------|----------|---------------------|--------------------------|------|--------------------|---------------|---------------------|------------------|--------------------|
| TOF: | | | | | | | | | |
| 91500 | 1056.5 | 24.4 (2.31%) | 25.0 | 1.21 | 0.17 | 44 | 0.991 | 0.024 | 1066.01 |
| AusZ-2 | 38.0 | 1.2 (3.19%) | 1.3 | 0.62 | 0.68 | 6 | 0.976 | 0.034 | 38.90 |
| Mud Tank | 695.6 | 18.4 (2.64%) | 20.4 | 0.60 | 0.73 | 7 | <u>0.951</u> | <u>0.028</u> | 731.65 |
| OG-1 | 3469.2 | 13.9 (0.40%) | 23.0 | 0.60 | 0.66 | 5 | 1.001 | 0.007 | 3465.4 |
| Plesovice | 335.7 | 2.4 (0.71%) | 4.9 | 0.97 | 0.46 | 9 | 0.996 | 0.015 | 337.13 |
| QingHu | 156.6 | 1.6 (1.02%) | 2.6 | 1.90 | 0.11 | 5 | <u>0.982</u> | <u>0.016</u> | 159.50 |
| Temora | 413.6 | 3.0 (0.72%) | 6.0 | 0.94 | 0.53 | 18 | 0.992 | 0.015 | 416.80 |
| | | | | | | | | | |
| Quad: | | | | | | | | | |
| 91500 | 1068.7 | 15.3 (1.43%) | 16.3 | 1.04 | 0.40 | 44 | 1.003 | 0.015 | 1066.01 |
| AusZ-2 | 37.7 | 1.7 (4.63%) | 1.8 | 4.04 | 0.00 | 6 | 0.969 | 0.047 | 38.90 |
| Mud Tank | 706.3 | 10.5 (1.49%) | 13.8 | 0.73 | 0.62 | 7 | <u>0.965</u> | <u>0.019</u> | 731.65 |
| OG-1 | 3460.8 | 9.4 (0.27%) | 20.6 | 0.18 | 0.95 | 5 | 0.999 | 0.006 | 3465.4 |
| Plesovice | 340.8 | 2.5 (0.73%) | 5.0 | 2.02 | 0.04 | 9 | 1.011 | 0.015 | 337.13 |
| QingHu | 160.1 | 3.1 (1.96%) | 3.7 | 5.16 | 0.00 | 5 | 1.004 | 0.023 | 159.50 |
| Temora | 415.3 | 2.8 (0.68%) | 6.0 | 2.12 | 0.00 | 18 | 0.996 | 0.015 | 416.80 |

Table 5.1. Weighted average results (using Isoplot) for Experiment 1, split stream analysis. All ages are weighted averages of $^{206}\text{Pb}/^{238}\text{U}$ except for the OG-1 and 91500 zircon, for which the $^{207}\text{Pb}/^{206}\text{Pb}$ age is reported. A common Pb correction is applied to analyses that were discordant with the $^{207}\text{Pb}/^{206}\text{Pb}$ age greater than the $^{206}\text{Pb}/^{238}\text{U}$ age. Uncertainties are $2s$ in Ma, except the “Within-Run” uncertainty column which also has the percentage error in brackets. “Measured / Accepted” column is the weighted average of the U-Pb age measured by LA-ICP-MS divided by the published age so that a perfectly accurate analysis has a value of 1. The $2s$ uncertainty on the “Measured / Accepted” ratio is the uncertainty of the LA-ICP-MS age / published age from the propagation of the uncertainties from the LA-ICP-MS analysis and from those from the published age. Underlined “Measured / Accepted” values are those which are outside the 2-sigma uncertainties of the published ages.

| Sample | Age (Ma) | $\pm 2\sigma$ within-run | $\pm 2\sigma$ full analytical | MSWD | Probability of Fit | # of analyses | Measured / Accepted | 2σ uncertainty | Published age (Ma) |
|---------------|----------|--------------------------|-------------------------------|------|--------------------|---------------|---------------------|-----------------------|--------------------|
| TOFMS: | | | | | | | | | |
| 91500 | 1061.5 | 22.3 (2.10%) | 23.0 | 0.60 | 0.91 | 20 | 0.996 | 0.022 | 1066.01 |
| AusZ-2 | 38.5 | 0.7 (1.90%) | 0.9 | 1.41 | 0.22 | 6 | 0.991 | 0.023 | 38.90 |
| BB16zircon | 561.4 | 3.7 (0.66%) | 8.1 | 1.11 | 0.35 | 5 | 1.002 | 0.017 | 560 |
| FC-1 | 1101.9 | 17.0 (1.54%) | 22.0 | 3.36 | 0.00 | 7 | 1.005 | 0.020 | 1096.8 |
| Mud Tank | 713.1 | 10.0 (1.40%) | 13.5 | 1.08 | 0.37 | 10 | <u>0.975</u> | <u>0.018</u> | 731.65 |
| OG-1 | 3459.0 | 9.3 (0.27%) | 20.5 | 1.91 | 0.13 | 4 | 0.998 | 0.006 | 3465.40 |
| Penglai | 4.2 | 0.9 (20.6%) | 0.9 | 3.12 | 0.00 | 7 | 1.000 | 0.210 | 4.22 |
| Plesovice | 338.7 | 1.6 (0.48%) | 4.6 | 1.09 | 0.36 | 12 | 1.005 | 0.014 | 337.13 |
| QingHu | 153.4 | 2.4 (1.58%) | 3.1 | 2.77 | 0.01 | 7 | <u>0.962</u> | <u>0.020</u> | 159.50 |
| Temora | 415.2 | 2.7 (0.65%) | 5.9 | 0.73 | 0.71 | 12 | 0.996 | 0.014 | 416.80 |
| QMS: | | | | | | | | | |
| 91500* | 1050.7 | 26.9 (2.56%) | 27.4 | 1.58 | 0.05 | 20 | 0.986 | 0.026 | 1066.01 |
| AusZ-2 | 38.9 | 0.7 (1.90%) | 0.9 | 0.46 | 0.80 | 6 | 0.999 | 0.023 | 38.90 |
| BB16zircon | 559.9 | 4.6 (0.83%) | 8.5 | 0.53 | 0.71 | 5 | 1.000 | 0.018 | 560 |
| FC-1 | 1095.2 | 6.6 (0.60%) | 15.4 | 0.67 | 0.67 | 7 | 0.999 | 0.014 | 1096.8 |
| Mud Tank | 702.7 | 8.9 (1.26%) | 12.6 | 1.40 | 0.18 | 10 | <u>0.960</u> | <u>0.017</u> | 731.65 |
| OG-1* | 3465.4 | 9.9 (0.29%) | 20.8 | 0.09 | 0.97 | 4 | 1.000 | 0.006 | 3465.40 |
| Penglai | 4.5 | 0.5 (10.1%) | 0.5 | 1.07 | 0.38 | 7 | 1.068 | 0.117 | 4.22 |
| Plesovice | 339.1 | 1.9 (0.55%) | 4.7 | 0.93 | 0.51 | 12 | 1.006 | 0.014 | 337.13 |
| QingHu | 160.0 | 1.1 (0.69%) | 2.3 | 1.08 | 0.37 | 7 | 1.003 | 0.015 | 159.50 |
| Temora | 417.8 | 3.0 (0.72%) | 6.1 | 1.38 | 0.18 | 12 | 1.003 | 0.015 | 416.80 |

Table 5.2. Weighted average results (using Isoplot) for Experiment 2 where analyses were done over several individual analytical sessions. All ages are weighted averages of $^{206}\text{Pb}/^{238}\text{U}$ except for the OG-1 and 91500 zircon,

for which the $^{207}\text{Pb}/^{206}\text{Pb}$ age is reported. Uncertainties are 2s in Ma, except the “within-run” uncertainty column which also has the percentage error in brackets. A common Pb correction is applied to analyses that were discordant with the $^{207}\text{Pb}/^{206}\text{Pb}$ age greater than the $^{206}\text{Pb}/^{238}\text{U}$ age. Measured / Accepted column is the weighted average of the U-Pb age measured by LA-ICP-MS divided by the published age so that a perfectly accurate analysis has a value of 1. The 2s uncertainty on the “Measured / Accepted” ratio is the uncertainty of the LA-ICP-MS age / published age from the propagation of the uncertainties from the LA-ICP-MS analysis and from those from the published age. Underlined “Measured / Accepted” values are those which are outside the 2-sigma uncertainties of the published ages.

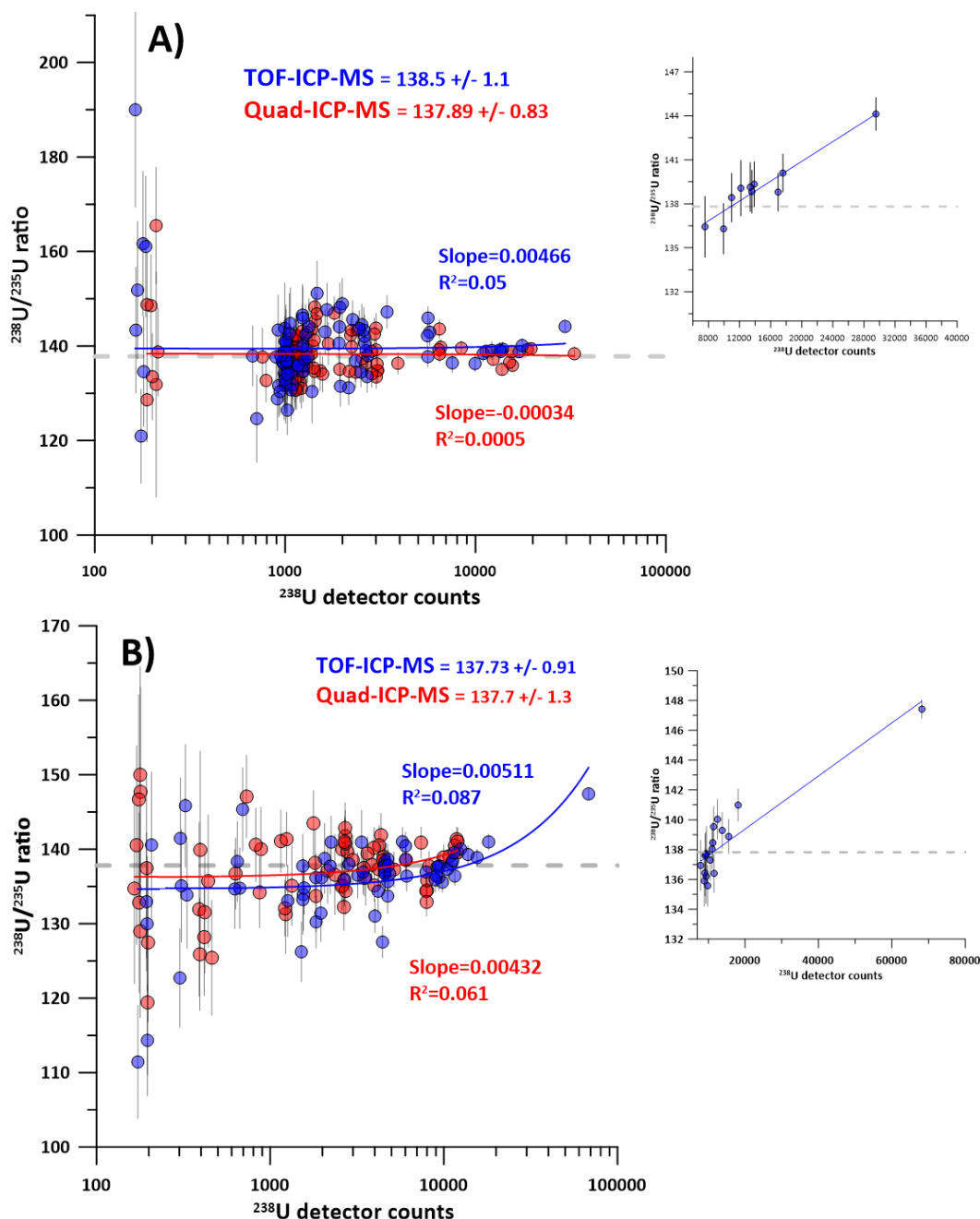


Figure 5.5. Plot of U detector counts and the $^{238}\text{U}/^{235}\text{U}$ ratio. Natural $^{238}\text{U}/^{235}\text{U}$ ratio of 137.818 is represented by the grey dashed line. Figure A) shows results for Experiment 1 (split stream analysis) while Figure B) shows results from individual sessions (Experiment 2). $^{238}\text{U}/^{235}\text{U}$ values on graph represent the weighted average for each ICP-MS using the “Within-Run” uncertainty for the calculation in Isoplot. Error bars on graph are 1-sigma “Signal Precision” uncertainty shown on individual analyses for clarity. The expanded views on the right of A) and B) highlight the slight dependency of the U isotope ratio for the TOFMS data at higher detector counts.

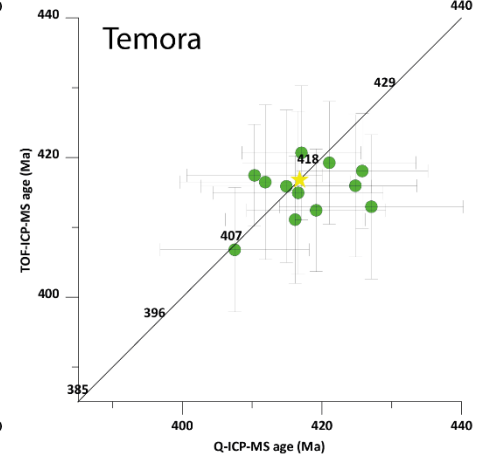
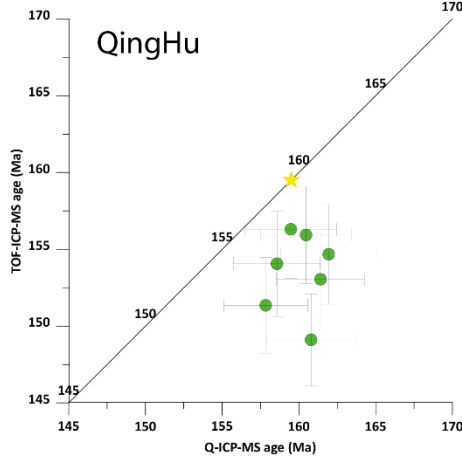
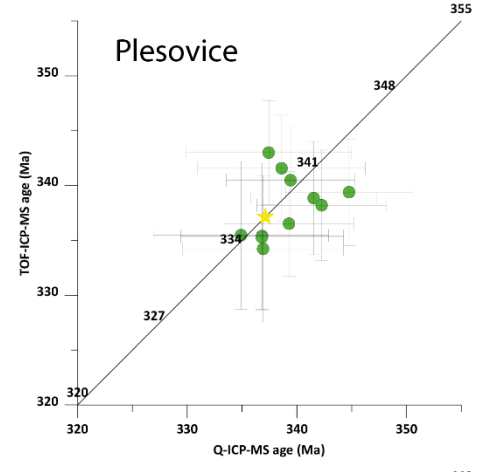
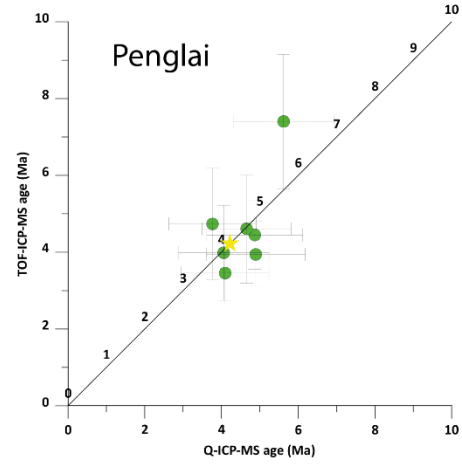
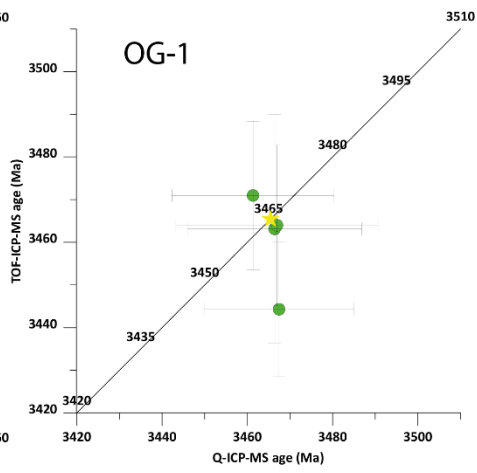
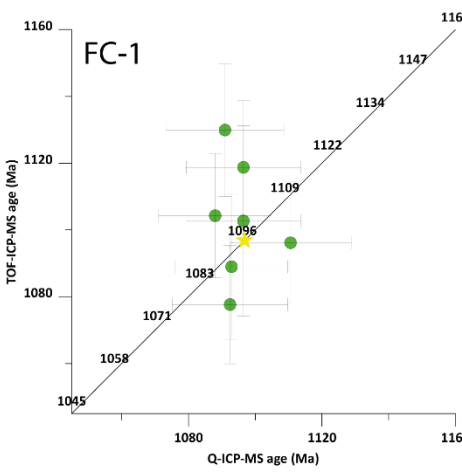
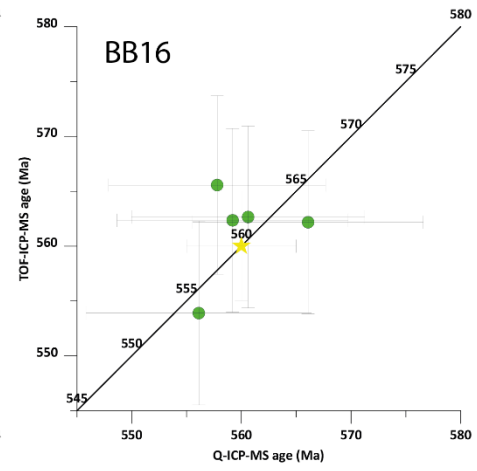
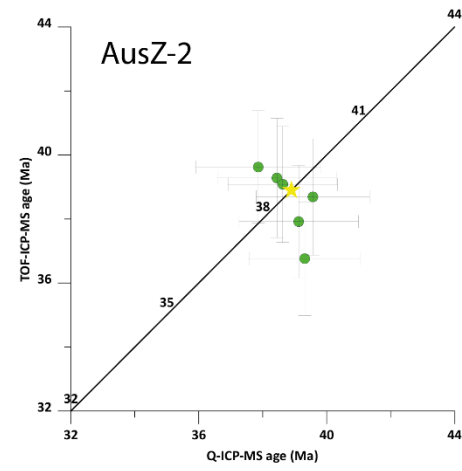


Figure 5.6. Age plots for select zircon reference materials used in Experiment 2, where analyses were performed under routine conditions and multiple sessions for each ICP-MS type. Green circles represent individual analyses with 2-sigma error bars (Within-Run uncertainty). Yellow star indicates published age on reference material. Black line is the 1:1 line between the TOFMS and the QMS. Individual ages are $^{206}\text{Pb}/^{238}\text{U}$ except for the OG-1 zircon which are $^{207}\text{Pb}/^{206}\text{Pb}$ ages. Since individual analyses were done on different days, there is no relationship in the data points between the TOFMS and QMS and as such analyses are simply plotted in order of analysis on the session day.

5.4 Discussion

5.4.1 Uncertainty budget

This study aims to compare the analytical performance of two different ICP-MS types: quadrupole and time-of-flight. To adequately compare these two ICP-MS types, an understanding of the sources of uncertainty in the results for each instrument is required. Sources of uncertainty include counting statistic noise, uncertainty in calibration and instrument drift corrections, and uncertainty from any common Pb corrections. In the case of the U-Pb and $^{207}\text{Pb}/^{206}\text{Pb}$ analyses in this study, much of the uncertainty budget for the zircon reference materials analyses is dominated by the noise related to counting statistics. This counting statistic noise is controlled by the detector counts on an isotope and thus for the same ion beam for a given isotope, the longer the detector counting time, the lower the uncertainty. There is thus an apparent advantage to longer detector counting times for isotopic analysis requiring high precision. However, the longer counting times mean fewer instrument readouts and more time between measurement of isotopes, which for transient signals found in laser ablation will lead to increased spectral skew and higher uncertainties. Additionally, longer sweep times can mask heterogeneous sample compositions (age or chemistry) and the presence of inclusions. For these reasons, relatively short (<0.3 sec) instrument readouts are chosen for both ICP-MS to provide a relatively high time resolution of an analysis to better detect the nature of any compositional or age zoning and inclusions.

The uncertainty related to the calibration of U-Pb and $^{207}\text{Pb}/^{206}\text{Pb}$ ages also contributes to the total uncertainty budget. During static spot ablation of zircon, the signal intensities of all elements will drop by $\approx 40\%$ from beginning of ablation to the end over 150 laser shots. However, Pb and U will change relative intensities to each other in what is referred to as element fractionation [26, 27]. This element fractionation has been an issue with nanosecond pulsed lasers in that there is a bias of the Pb/U ratios relative to the true ratios, and this bias changes as the ablation drills deeper into the zircon [62]. This time-dependent element

fractionation has been corrected in a variety of ways [11, 163] and an important aspect of this correction is that a matrix matched standard is needed as zircon fractionates Pb and U differently from glasses [62] that are commonly used as reference materials in LA-ICP-MS. The results from this study were corrected using a polynomial (3rd order) fit to the 91500 zircon $^{206}\text{Pb}/^{238}\text{U}$ ratio from the start of ablation to the end. The fit is averaged over all the 91500 analyses throughout the whole session (drift corrected) as done by Paton et al. [163], and this downhole correction model is then applied to the unknowns along with the ICP-MS time-dependent drift correction for the $^{206}\text{Pb}/^{238}\text{U}$ ratio. The $^{207}\text{Pb}/^{206}\text{Pb}$ ratio is calibrated on the NIST610 and as Pb isotopes are not observed to fractionate from each other during ablation, a calibration was applied via a correction factor calculated relative to the NIST610 Pb isotopic composition of Baker et al. [143] and the measured value on the LA-ICP-MS session, taking into account any correction for ICP-MS time-dependent drift in $^{207}\text{Pb}/^{206}\text{Pb}$ values during the session. The uncertainty from each of the components of the calibration are propagated through the corrections including: any misfit from the down-hole Pb/U correction model, misfit in drift correction, measurement uncertainties in calibration materials, etc. An example of the impact of the uncertainty from the calibration from the Temora zircon analysis (#65) from the split stream (Experiment 1, TOFMS results) shows the ‘signal precision’ (uncertainty of measurement) of the $^{206}\text{Pb}/^{238}\text{U}$ to be 1.072% while the ‘within-run precision’ (combination of measurement and calibration uncertainties) is 1.361%. This uncertainty is important to include in interpretations of data sets collected on different instruments or different days and all the weighted averages calculated in this study use uncertainties that include the calibration uncertainty component.

Since the zircon reference materials used in this study are relatively concordant, the amount of uncertainty related to corrections for common Pb is minimal since only a few analyses required correction with the amount of common Pb being <0.5% of the total measured Pb in all analyses. So, for the experimental conditions used in this study, the two main sources of uncertainty on the U-Pb and $^{207}\text{Pb}/^{206}\text{Pb}$ ages is the individual measurement uncertainty (‘Signal Precision’) and the calibration uncertainty (included in the ‘Within-Run Precision’).

5.4.2 Ablation signal smoothing

It is important to note that the experiment configuration in this study was that which is normally utilized for the QMS, namely that there is significant signal smoothing being done by the “squid”. If the squid were removed from the experiments in this study and a single tube went from the laser to the ICP-MS, there would be significant impact of spectral skew in the QMS results due to the low (5 Hz) repetition rates relative to the laser cell washout time (≈ 1.5 second to 0.1% without the squid) [35, 38]. Therefore, signal smoothing was necessary to provide precise results for the QMS and to more directly compare with TOFMS. This signal smoothing from the “squid” negates some of the advantages of the TOFMS described above, such as the high temporal resolution to allow for better investigation of mineral chemistry zonation and inclusion composition [191]. The high temporal resolution of the TOFMS coupled with its ability to capture the entire mass range can allow for a more detailed study of mineral chemical and isotopic chemistry than what is possible with sequential based ICP-MS.

5.4.3 Detector counting times

For U-Pb dating, it is important to integrate the largest possible number of Pb and U analyte ions as often as possible to obtain the highest precision on the age; so ideally, sequentially based ICP-MS would only measure these isotopes to maximise the integrated analyte signals and to minimize imprecision related to spectral skew from longer instrument readouts. However, having other elements in the method allows for target phase confirmation (e.g. Was the mineral zircon?), better identification of inclusions, identification of compositional zoning and more geological context for interpreting zircon ages; Ti geothermometry in zircon [192] or Ce and Eu anomalies for oxidation level and differentiation history [193, 194]. This study balances the need for multi-element analysis and the need for minimal spectral skew in QMS by having very short counting times on the major and trace elements in zircon, as the LODs and precision required for geological interpretation of these elements is much less than for U-Pb. The difference in analytical precision for the QMS between a ‘short’ method with Pb, Th and U isotopes only, compared to the method used in Experiment 1 (with 30 masses) is typically around $\approx 0.2\%$ 2s on an individual analysis. However, the difference in analytical precision for the QMS between Experiments 1 and 2 is 0.6% and this is primarily due to the split-stream arrangement in Experiment 1 lowering

sensitivity by $\approx 1/2$. Thus, although the addition of more masses to sequential ICP-MS instruments does negatively impact the precision on time-resolved analyses, the small magnitude of this effect (0.2%) can be overcome by analysing more laser spots for the weighted average calculation for a sample.

The impact of the short counting times on the non-geochronology elements can be seen in Figure 5.7 where the relationship of counting statistic uncertainty, as RSD of the ratio of an element to ^{238}U , and detector dwell time (in milliseconds) is shown for an analysis from Experiment 1 (split stream analysis). The black line is the signal RSD predicted by counting statistics of the detector signal (integrated counts). Both instruments detected about $\approx 70,000$ counts of ^{91}Zr , the TOFMS during 271 ms integration time (while partially notching the Zr isotopes) and the QMS dwell time of 2 ms. ^{206}Pb for both ICP-MS types plot close to or on the theoretical line of counting statistics, whereas ^{89}Y for the QMS displays significantly higher RSD than ^{89}Y for the TOFMS, with the latter matching the theoretical line. Since the dataset in Figure 5.7 is from the Experiment 1 (split stream analysis), the QMS results for ^{89}Y indicates a significantly less precise measurement compared to the TOFMS despite the similar detector counts for ^{89}Y on both instruments. The same is true for Hf and Zr which have also been measured at 2 ms dwell time on QMS, whereas U measured on QMS with 15 ms dwell time plots on the theoretical curve for both instruments. The relatively poor RSD of the masses measured on QMS with a very short dwell time of 2 ms suggest that there exists an additional factor, in addition to the counting statistics, which affects LA-ICP-MS results on quadrupole instruments when using a very short dwell time. This additional factor is likely to be variations of the LA-ICP-MS aerosol density or particle size distributions on very short time scales, which have not been smoothed by the 'squid'. Also, shorter dwell times can produce higher analytical uncertainties as a larger proportion of the sweep time is taken by the quadrupole 'jump' and settling time between masses. These additional variations seem to decrease substantially at dwell times $\Rightarrow 15$ ms and are thus not seen in TOFMS results. This interpretation is supported by Figure 5.8 where ^{91}Zr counts collected on the QMS at different detector counting times are compared. Here there is significantly higher signal RSD than predicted by counting statistics, however this signal RSD gets lower with increasing the counting time for ^{91}Zr (Fig 5.8C). The detector counting time is also what likely controls the lower "floor" around 5,000 detector counts for the TOFMS in Figure 5.7 where increasing the

detector counts has no decrease in the signal RSD with the lower limit around 1.5%. (Fig. 5.7). Increasing the detector counting time would produce a lower RSD, but at the expense of less instrument readouts per analysis and thus decreasing time resolution to identify zoning and inclusions. Longer integration would at the same time not improve the standard error ($SE = SD/\sqrt{n}$) of an experiment of equal total duration due to the lower number of readouts. However, longer integration time for TOFMS would reduce the uncertainty of the background to be subtracted for each integration period and could improve accuracy for low abundant isotopes or trace elements (see Discussion below).

Because the QMS geochronology method in Experiment 1 has been optimized for U-Pb and Pb isotopic analysis while still being able to see inclusions and sharp compositional zonation, a short counting time on ^{89}Y and other non-geochronology elements is used to keep the sweep time relatively short. This trade-off with short detector dwell times for the sequential ICP-MS is not required with the full mass spectral TOF and highlights an important advantage of the latter.

5.4.4 U-Pb and Pb-Pb age accuracy and precision

There is a significant (5x to 15x) differences in instrument sensitivity between QMS (in single ion mode) and TOFMS which is largely due to the difference in mass analyser and ion detection designs as the Thermo iCAP Q running in quadrupole mode has similar instrument sensitivity and performance to the Agilent 7900. Note however that the recorded counts on the detector are similar on both instrument (Figs. 5.5 and 5.7) due to significantly longer integration times per analyte on TOFMS for the same readout frequency. Both ICP-MS show that in most cases accurate zircon U-Pb ages can be obtained by QMS and TOFMS. There is substantial literature on quadrupole-based LA-ICP-MS zircon U-Pb dating of which the results are consistent with the ones of this study; however, accurate zircon geochronology has yet to be demonstrated for the TOFMS. For most of the zircon reference materials the TOFMS produced accurate results under the optimal laser ablation conditions.

Two exceptions were the Mud Tank zircon and the QingHu zircon, which were both systematically too young relative to their published ages. The Mud Tank zircon U-Pb ages were systematically lower on both the TOFMS and QMS and this is consistent with what has been noted in previous data [186]. The U-Pb ages for QingHu zircon using the TOFMS were systematically lower ($\approx 1.8\%$) than both the quadrupole ICP-MS results as well as the

published ID-TIMS data, while the U-Pb ages for the Plesovice zircon were systematically lower for the TOFMS relative to the QMS. In Experiment 2 where the full laser aerosol was directed into the TOFMS, the QingHu zircon age was $\approx 3.8\%$ too young from the ID-TIMS age of the zircon and well outside the uncertainty of $\approx 1.5\%$ (2s). Since this offset in age is not seen for the QMS, this phenomenon is likely related to the way the TOFMS data are acquired or processed. Given that QingHu zircon has very high U contents, the observed difference may be due to issues with background subtraction or changing detector performance at higher signal intensities.

To test the impact of different baseline subtraction functions on the measured age, two different baseline function equations were applied to the QingHu zircon results, one using the fit based on the 91500 (as described in the Methods section) and the other using a fit based on one of the QingHu zircons. The results of different baseline equations applied to the same data set were at most a 0.25% (2s) change in the age and so are unlikely to be the source of the systematic offset. This small difference in the impact of the baseline subtraction is due to two main aspects: 1) the difference in baseline settings between the 91500 and QingHu zircon (and all other zircon analysed here) were relatively minor, 2) the importance of the baseline subtraction was small relative to the signal intensities for ^{206}Pb (>2 orders of magnitude over baseline) in the QingHu zircon.

The Plesovice zircon analysed on the TOFMS was also systematically younger in U-Pb age than on the QMS in Experiment 1. Results from Experiment 1 for Plesovice are consistent with the Qing Hu zircon and the interpretation that the high U contents in Plesovice are likely responsible for the slightly younger TOFMS age is likely. The QMS U-Pb age is slightly higher than the published ID-TIMS ages and this is likely related to the zircon 'matrix effect' [95, 96, 186].

Previous literature [182, 195, 196] has shown that there can be a concentration dependence on isotope ratio measurements and there is a slight dependence of the $^{238}\text{U}/^{235}\text{U}$ ratio on concentrations (Fig. 5.5), particularly at higher count rates, with the TOFMS, which merits further investigation. The U contents of the QingHu were generally much higher than other zircons analysed in this study, although there is significant variance in the U contents (650 to 2300 ppm). Given the previous literature and the high U nature of QingHu zircon, it is likely that the age offset for the QingHu zircon is due to the impact of high U count rates on

the TOFMS detector. This is consistent with the behaviour seen in Figure 5.5B where the slight dependence of the $^{238}\text{U}/^{235}\text{U}$ produces anomalously high ^{238}U with increasing count rates – which should produce younger $^{206}\text{Pb}/^{238}\text{U}$ ages. While there is scatter in the $^{238}\text{U}/^{235}\text{U}$ on Figure 5.5B, most of this is related to counting statistic noise since the error bars are all within the accepted value. However, at signal intensities above $\approx 7,000$ counts ^{238}U , there is a slight offset in the TOFMS measured $^{238}\text{U}/^{235}\text{U}$ ratio that is outside uncertainty, and this is not seen in the QMS results. The age offset in QingHu is less for the split-stream analysis due to the lower overall ^{238}U signal for the same U concentration; however, this can be complicated by the relatively large (50%) variations in U content in the QingHu zircon, making direct comparisons of Experiments 1 and 2 difficult. To confirm the offset in QingHu age on TOFMS is related to artificially high ^{238}U counts at high count rates, LADR software's option to calculate ^{238}U using ^{235}U above a user-specified count rate threshold was utilized. Setting a threshold of ^{238}U above 50,000 cps to be calculated using ^{235}U instead, the QingHu zircon weighted average was 158.8 ± 3.7 Ma for the $^{206}\text{Pb}/^{238}\text{U}^*$ age, in agreement with the ID-TIMS age of 159.5 Ma and thus confirming that at high rates the TOFMS detector introduces a measurable bias on high precision isotope ratios. It is also important to note that this behaviour of the TOFMS detector is easier seen in the Pb-U ages compared the U isotope ratios due to the latter having significantly worse counting statistics due to low abundance of ^{235}U compared to ^{206}Pb for most zircon (all but the Eocene AusZ-2). For the QingHu zircon weighted average age calculated on ^{238}U only, the uncertainty is 2.4 Ma or 1.6%, while using ^{235}U the uncertainty on the weighted average age is 3.7 Ma or 2.3% so that there is a notable decrease in precision when utilizing ^{235}U as expected from counting statistics.

Future zircon U-Pb dating that utilizes small-volume, low aerosol dispersion ablation cells [197] for rapid analysis and higher signal to noise ratio [197], may be affected by the above performance of the TOFMS detector more than the analyses done under in this study, as the signal intensities will be even higher. Future improvement of either the signal notching or the detector performance will need to be addressed for accurate analysis with these higher signal intensities, however the option in LADR for calculating ^{235}U from ^{238}U is a relatively simple short-term fix and the option was originally put in place to deal with a similar issue with QMS: increased uncertainty introduced by the pulse to analog detection mode transition for ^{238}U signal.

5.4.5 Trace element compositions measured by LA-ICP-MS

One advantage of the TOFMS is to collect multi-element data while also collecting U-Pb isotopic data, without compromising the number or frequency of instrument readouts. Various trace / minor elements measured in Experiment 1 were investigated further as the data collected in Experiment 2 suffer from significant natural variation in zircon chemistry, making direct comparisons of accuracy and precision of the two different ICP-MS difficult. There are only a few well characterized and naturally homogenous zircon crystals available for analysis with compositional data derived from independent techniques (e.g. isotope dilution), which can be used to assess the accuracy of the trace element results for both mass spectrometers. The 91500 zircon is one such natural sample and results from Experiment 1 were compared to GeoReM preferred values. While the exact values for the 91500 are difficult to constrain due to some natural heterogeneity [155, 198] what is more important for this study is any biases in trace element results between the QMS and TOFMS. Figure 5.4 shows that for Experiment 1, most elements show excellent agreement in trace element concentrations between the TOFMS and the QMS and additionally, most elements agree with the GeoReM preferred values. However, there are clear differences in the measured concentrations of Nd, Sm and Ta between the two ICP-MS types, with Ta being significantly (outside 1s uncertainty) different in the TOFMS data relative to the QMS. Since the aerosol and calibration procedures are identical between the datasets, it is likely there is some other effect causing the discrepancy for these elements. The average gas blank subtracted signal intensities for ^{181}Ta in 91500 on TOFMS is ≈ 25 cps. While this is significantly above the average gas blank of ≈ 1 cps, the Ta peak is right next to the high abundance Hf peak during ablation of the zircon. This highlights an important issue with calculating the LOD based on the 'gas blank' (e.g. the Longerich et al. [58] method in Equation 5.1) for TOFMS data. While the gas blank might be very low for an element such as ^{181}Ta , there is a relatively large TOFMS baseline subtraction needed from the adjacent Hf peaks. If the LOD is calculated based on the standard deviation of the TOFMS baseline on either side of the ^{181}Ta peak (similar to the highlighted ^{93}Nb peak situation in Figure 5.2), the ^{181}Ta peak becomes less than the LOD. This is also the case for Nd and Sm where the TOFMS baseline subtraction results in less than LOD. Therefore, methodology for the LOD calculation needs to be modified when using the TOFMS. Limits of detection need to be calculated on both the gas blank and that on the baseline subtraction

from the TOF peak interrogation in Tofware as there will be cases where the gas blank will be significant relative to the baseline subtraction and vice-versa. This makes the TOFMS relatively matrix sensitive compared to the QMS instrument, as Nb and Ta in zircon are negatively impacted by high Zr and Hf peak tails while other materials, such as the NIST610 are un-affected by this phenomenon due to similar abundances of these elements. The abundance sensitivity of modern QMS instruments would be subject to very minimal peak tailing from Zr and Hf (10^{-6} to 10^{-7}). With the relatively poor abundance sensitivity of the TOFMS, it is important to have an accurate baseline subtraction for accurate results (e.g. mineral-matched).

The attenuation of high intensity peaks by the notch filter also will affect the detection of nearby the notched peak causing a deterioration of the LODs. For zircon this will be seen in higher LODs for ^{93}Nb and ^{89}Y compared to LREE due to notching at ^{90}Zr . The analyst needs to investigate the nature of the matrix elements in the target mineral, how these might affect isotopes of interest and which reference material is best suited for the quantification of results.

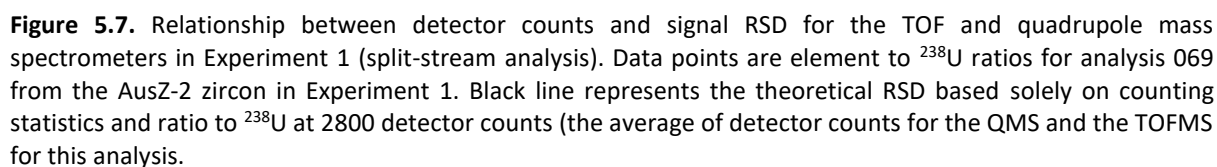


Figure 5.8. Signal from ablation of Mud Tank zircon at analytical conditions used for Experiment 2 (normal analytical conditions) for ^{91}Zr using the QMS at various dwell times. A shows the raw Zr signal as the ablation drills into the zircon, causing the signal to drop in intensity. B shows the same signal that has been corrected for this signal drop off phenomenon and the RSD (1s) of the mean calculated on for the corrected signal for each dwell time with longer dwell times giving less signal variation and correspondingly lower RSD. Figure 5.8C shows the 1 standard deviation for the signal (solid bars) and for the theoretical standard deviation based on counting statistics for the number of detector counts (bars with cross pattern). Note the significantly higher standard deviations for the measured signal compared to the theoretical.

5.5 Conclusions

For time-resolved multi-element LA-ICP-MS applications with a given readout rate, the lower sensitivity of TOFMS compared to QMS is compensated by longer integration times on TOFMS per analyte compared to the relatively short dwell times of individual isotopes on QMS. The sequential nature of QMS limits both the number of elements and the counting time on each to achieve the optimum readout rate. In contrast, the simultaneous detection of the TOFMS allows for significantly longer integration times without compromising the range of analysed elements. This advantage of TOFMS is particularly important for minimising uncertainties of signals recorded with very short dwell times (2 ms) on QMS, a necessary compromise to achieve time resolution for inclusion and zonation identification, as signals recorded with such short dwell times are prone to additional noise outside what is expected from counting statistics.

This study demonstrates for typical analytical conditions the counted ions for most elements are similar for both instruments. As a result, there is no impact on accuracy and similar levels of analytical precision in zircon U-Pb and $^{207}\text{Pb}/^{206}\text{Pb}$ ages obtained by TOFMS using laser ablation compared to QMS. Similar levels of accuracy for the TOFMS relative to QMS is also seen for trace elements in zircon when above the LOD. The full mass spectrum provided by TOFMS allows for more geological context for interpretation of the U-Pb isotopic ages and better identification of mineral inclusions that would be missed in a short element list.

This study demonstrates that the smaller linear dynamic range of the TOFMS compared to the QMS in pulse counting mode may affect the U-Pb ages determined on high U signals (over 7,000 counts). In relation to this we note that the use of low aerosol dispersion ablation cells which amplify the advantages of TOFMS by significantly improving the LOD of single laser shot integrations by increasing the signal to noise ratio, may cause accuracy issues due to the

limited linear dynamic range of the TOFMS detector at higher count rates. We demonstrate that use of ^{235}U instead of ^{238}U for high U signals can mitigate this issue for U-Pb dating applications at the expense of some analytical precision.

Future work with TOFMS analysis of zircon is promising as it can give similar analytical performance but access to a wide range of elements and with significantly higher data collection rates relative to sequentially based ICP-MS.

5.6 Acknowledgements

The authors would like to thank both reviewers for their help improving the manuscript. The authors would also like to acknowledge Martin Rittner, Yannick Bussweiler, and Mike Cubison at Tofwerk for help with testing of zircon reference materials and with Tofware software development. The authors would also like to thank the following for contribution of zircon reference materials to this study: Jiri Slama for the Plesovice zircon, Natalie Kositcin at Geoscience Australia for the Temora and OG-1 zircon samples, Bradley McDonald and Noreen Evans for the FC-1 zircon sample, and Allen Kennedy for the AusZ-2 samples.

Chapter 6 Conclusions and outlook

6.1 Optimization of ICP-MS for laser ablation

This study demonstrated several important differences between ‘wet’ and ‘dry’ plasma conditions for inductively-coupled plasma (ICP). While modern ICP-MS instruments have greatly improved in performance over first-generation models, to date no instrument manufacturer has an ICP-MS system dedicated to “dry” plasma or laser ablation sample introduction. Chapter 2 demonstrated that small additions of gases such as H₂, N₂ or H₂O can have significant impact on the sensitivity and particle digestion properties of dry plasma. This has important implications for sample storage and cleaning prior to analysis, as adsorbed H₂O vapour can have a significant impact on the analyses. This is especially true if introduced H₂O vapour is not homogeneously distributed in the laser system. Adsorbed atmospheric air on sample surfaces in the laser cell cause significant (up to 4%) shifts in the analysed U-Pb age as demonstrated in Chapter 4.

While the addition of H₂, N₂ and H₂O appear to improve the ICP’s ability to digest particles[53], the addition of these gases also will significantly increase the background intensities and polyatomic interferences for several low atomic number elements. These increased backgrounds and polyatomic interferences potentially leading to increased inaccuracies for some elements. While there are some significant advantages for addition of gases such as H₂, N₂ and H₂O for geochronology methods involving U-Pb dating, use of these gases during multi-element analyses is inhibited by polyatomic interferences. Chapter 2 demonstrated that under a certain set of analytical conditions, interferences in the ICP-MS spectrum can be minimized during LA-ICP-MS and this is important for trace and minor element analysis of geological materials.

6.2 Use of U-Pb geochronology as a tool for understanding LA-ICP-MS

Analytical improvements and remaining challenges of the LA-ICP-MS technique when high accuracy (<3%) is required was demonstrated in Chapters 3 and 4. Using U and Pb, the amount of element fractionation and inaccuracies in the LA-ICP-MS method were evaluated and found to be strongly linked to processes occurring at the ablation site. Use of the mineral zircon and apatite for investigation into complexities in the LA-ICP-MS process were ideal as

the ratio of U-Pb is fixed by radioactive decay. Uranium and Pb are two elements that have different behaviour during laser ablation and in the ICP, mostly due to their contrasting volatilities. The effects of laser fluence on the behaviour of U and Pb in the mineral zircon, the degree of element fractionation, and the degree of matrix effects was demonstrated in Chapter 4. While the laser fluence can change the particle size distributions and therefore the digestion of particles in the ICP[44], this work, in conjunction with previous studies[46, 48, 62], suggested that the change in laser fluence has a control on the formation of ZrO₂ at the ablation site and highlights the need for understanding and testing the best operating conditions for LA-ICP-MS analysis.

A correlation exists between the accuracy of a U-Pb analyses by LA-ICP-MS and the calculated zircon radiation dose (Chapter 4). While others[95-97] have confirmed this observation, this study has demonstrated this for two laser systems of varying pulse widths (20 ns vs. 5 ns). Contrary to Marillo-Sialer[96, 97], Chapter 4 showed a poor correlation with zircon accuracy and ablation rate or depth. Instead, the calculated radiation dose is much better correlated with the accuracy in the zircon U-Pb age result by LA-ICP-MS. This suggests element fractionation is associated with variable ablation rates, and a change in laser coupling with zircon based on radiation damage. Preliminary Raman Spectroscopy work on zircon suggests that the degree of crystallization is well correlated to the calculated radiation dose for these zircon and that future analyses would benefit from prior Raman spectroscopy characterization, similar to traditional CL analysis. *A priori* knowledge of the crystal structure of the zircon (via Raman imaging) could help in analysis location selection and in correction for the LA-ICP-MS matrix effect. Future work is needed to assess the Raman technique for this task.

Chapter 3 demonstrated limitations of accuracy of U-Pb dating in apatite. Unlike zircon, apatite is complicated by incorporation of common Pb. Presently available apatite primary reference materials have some degree of common Pb in their structure [14], however, it can be corrected [142]. Several of the currently available U-Pb apatite reference materials had LA-ICP-MS results inconsistent with published values, despite robust correction for common Pb (Chapter 3). These inconsistencies may be due to a matrix effect, possibly correlated with Th content. However, the most likely cause is inconsistencies in the standard age determination. High quality ID-TIMS ages are not always available and other dating methods

such as Pb-Pb step leaching or assumptions of zircon dated in the same rock as hosts apatite to be the same age are utilized. Chapter 3 presented two new apatite reference materials containing high quality isotope dilution (MC-ICP-MS) ages: 401 apatite and OD306 apatite. Both of these have minor common Pb contents, are close to Concordia, and have modest radiogenic Pb contents (1 to 4 ppm) for use as a primary calibration or a secondary check standard. Since publication in 2016, more than 10 of each of these reference materials have been distributed to the geochronology community.

6.3 Time-of-Flight ICP-MS for laser ablation analyses

The TOFMS technology offers a significant advantage over traditional quadrupole and sequential magnetic sector ICP-MS analyses by removing spectral skew and increasing data collection rates. The rapid data collection rates (up to 33 kHz) potentially allow for a much more detailed sampling of the aerosol during ablation. While the TOFMS technology has been available for more than 20 years, it has had limited usage in the Earth Sciences. The work in Chapter 5 demonstrated the use of TOFMS technology on geological samples for high precision and accuracy zircon U-Pb dating work. Demonstration of accurate and precise analyses will help encourage the implementation of this technology. The wider implementation of TOFMS will aid in the understanding of both LA-ICP-MS and Earth Science as the simultaneous detection of the whole mass spectrum allows for interpretation of analyses on a scale that previously was not possible with sequential based ICP-MS.

Building on the aspects of optimum plasma conditions from Chapter 2, U-Pb matrix effects in geochronology from Chapters 3 and 4, results from a split stream analysis (quad and TOFMS) in Chapter 5 showed that, despite significantly lower count rates for the TOFMS relative to the quadrupole ICP-MS, the accuracy and precision of the two instruments are similar. The TOFMS suffered from non-linearity and has a significantly reduced linearity range for high precision isotope ratios compared to the quadrupole ICP-MS. By using ^{235}U instead of ^{238}U the non-linearity issue for U-Pb ages can be eliminated until the detector technology improves. An advantage of the TOF instrument highlighted in Chapter 5, is higher precision during trace element analyses relative to the quad ICP-MS, where the latter requires short (<10ms) dwell times) and was subject to additional analytical uncertainties.

6.4 Summary of conclusions

- First measurement of ion KE distributions for dry plasma and for dry plasma with H₂ and N₂ gas addition.
- First evidence of matrix effects in the mineral apatite during LA-ICP-MS U-Pb dating
- Two new apatite reference materials for U-Pb dating: 401 apatite and OD306
- Confirmation of zircon matrix effect during LA-ICP-MS U-Pb dating for two different excimer laser systems of different pulse width and that this matrix effect is correlated to radiation dose experienced by a zircon sample.
- Introduction of a correction factor based on the radiation dose for improving the accuracy of zircon U-Pb analysis by LA-ICP-MS.
- Link of laser fluence to degree of element fractionation and accuracy in zircon U-Pb dating.
- Demonstration of the influence of atmospheric air in the laser cell leading to position dependent inaccuracies for zircon U-Pb ages.
- First comprehensive assessment of the TOFMS for U-Pb geochronology of zircon by laser ablation.
- First direct comparison of the TOFMS with a quadrupole ICP-MS by use of a split stream arrangement.

6.5 Future research directions

Laser ablation ICP-MS has been utilized for more than 30 years in the geoscience community. While the technique has seen significant utilization in determining in-situ trace element and isotopic compositions in minerals and glasses, issues remain obtaining accurate results for some elements and some matrixes. One significant source of these accuracy issues is related to the use of non-matrix matched calibration standards for the unknown matrixes. In the past, the requirements of LA-ICP-MS accuracy and precision were enough to provide insights to geological questions; however, future requirements of the LA-ICP-MS technique will include accurate analyses, particularly as laser cells and mass spectrometers are likely to evolve towards optimal designs. Future research into LA-ICP-MS will benefit from

understanding which major element constituents can be accurately determined in a given matrix using widely available glass standards. If inaccuracies persist, then use of matrix matched standards for calibration of specific elements may be necessary. Currently, use of multiple calibration materials in LA-ICP-MS is not widely applied, but this may be the best way of obtaining accurate major element analysis for mineral chemistry. Obtaining accurate major element chemistry of minerals can save time and money in avoiding traditional electron microprobe analyses.

Though not tested in this work, trace H₂O vapour stored within geological materials, such as fluid inclusions, may be present in high enough abundances to impact the performance of the ICP and ion extraction process. Because these H₂O is not present in commonly used reference glasses (NIST61X and USGS), this could lead to a systematic offset in the chemical and or isotopic results from the analysis. More work is needed to assess the importance of this phenomenon.

Another significant issue to the quality of LA-ICP-MS data is the lack of understanding in the community about the importance of many aspects of the technique (i.e. gas flow geometry, laser cell design, tuning of ICP-MS, optical path design, etc.). While much work in this area has been done, currently there is no standard practice or set instrumentation design in LA-ICP-MS leading to significantly different inter-laboratory results, even when the same materials are analysed under similar analytical conditions. Even within a single laboratory, the external reproducibility of the LA-ICP-MS technique is significantly worse than other microbeam techniques (e.g. EMPA) and more research is needed to understand the causes of this.

Finally, the recent developments in TOF ion detection technology have the potential to significantly improve the LA-ICP-MS technique. The ability of the TOF technology to obtain rapid, simultaneous ion detection for all masses cannot be understated. TOF technology coupled to fast washout laser cells in particular, offers the ability for the analyst to quantify compositional variations with a depth resolution that is on the order of 100nm. Investigation of mineral chemistry variability at the sub-micron scale using LA-ICP-MS could potentially open up a wider range of applications for LA-ICP-MS and provide new insight to outstanding geological and other scientific questions. Future work with fast washout laser cells with the TOFMS will also require an improvement in the current TOF technology including wider range

of detector linearity, better deconvolution of TOFMS spectrums in software and an improvement in baseline subtraction for individual TOF spectrum outputs.

References

1. Gray, A., *Solid Sample Introduction by Laser Ablation for Inductively Coupled Plasma Source Mass Spectrometry*. Analyst, 1985. **110**.
2. Mayo, S., T.B. Lucatorto, and G.G. Luther, *Laser ablation and resonance ionization spectrometry for trace analysis of solids*. Analytical Chemistry, 1982. **54**(3): p. 553-556.
3. Maksimov, G.A. and N.V. Larin, *Mass-spectrometric Analysis of Solids Using Laser Ion Sources*. Russian Chemical Reviews, 1976. **45**(12): p. 1091-1100.
4. Wilkinson, J.J., et al., *The chlorite proximator: A new tool for detecting porphyry ore deposits*. Journal of Geochemical Exploration, 2015. **152**: p. 10-26.
5. Hong, W., et al., *Cathodoluminescence features, trace elements, and oxygen isotopes of quartz in unidirectional solidification textures from the Sn-mineralized Heemskirk Granite, western Tasmania*, in *American Mineralogist*. 2019. p. 100.
6. Hong, W., et al., *Tourmaline-rich features in the Heemskirk and Pieman Heads granites from western Tasmania, Australia: Characteristics, origins, and implications for tin mineralization*. American Mineralogist, 2017. **102**(4): p. 876-899.
7. Ukstins Peate, I., et al., *Extreme geochemical heterogeneity in Afro-Arabian Oligocene tephras: Preserving fractional crystallization and mafic recharge processes in silicic magma chambers*. Lithos, 2008. **102**(1): p. 260-278.
8. Steadman, J.A., et al., *Paragenesis and composition of ore minerals in the Randalls BIF-hosted gold deposits, Yilgarn Craton, Western Australia: Implications for the timing of deposit formation and constraints on gold sources*. Precambrian Research, 2014. **243**: p. 110-132.
9. Large, R.R., et al., *Gold and Trace Element Zonation in Pyrite Using a Laser Imaging Technique: Implications for the Timing of Gold in Orogenic and Carlin-Style Sediment-Hosted Deposits*. Economic Geology, 2009. **104**(5): p. 635-668.
10. Raimondo, T., et al., *Trace element mapping by LA-ICP-MS: assessing geochemical mobility in garnet*. Contributions to Mineralogy and Petrology, 2017. **172**(4): p. 17.
11. Jackson, S.E., et al., *The application of laser ablation-inductively coupled plasma-mass spectrometry to in situ U–Pb zircon geochronology*. Chemical Geology, 2004. **211**(1–2): p. 47-69.
12. Fletcher, I.R., et al., *Improved calibration procedures and new standards for U–Pb and Th–Pb dating of Phanerozoic xenotime by ion microprobe*. Chemical Geology, 2004. **209**(3–4): p. 295-314.
13. Apukhtina, O.B., et al., *Early, deep magnetite-fluorapatite mineralization at the Olympic Dam Cu–U–Au–Ag deposit, South Australia*. Economic Geology, 2017. **112**(6): p. 1531-1542.
14. Chew, D.M., P.J. Sylvester, and M.N. Tubrett, *U–Pb and Th–Pb dating of apatite by LA-ICPMS*. Chemical Geology, 2011. **280**(1-2): p. 200-216.
15. Huang, Q., et al., *Neoproterozoic (ca. 820–830 Ma) mafic dykes at Olympic Dam, South Australia: Links with the Gairdner Large Igneous Province*. Precambrian Research, 2015. **271**: p. 160-172.
16. Berry, R., et al., *U–Th–Pb monazite dating and the timing of arc–continent collision in East Timor*. Australian Journal of Earth Sciences, 2016. **63**(4): p. 367-377.
17. Cheng, Y., et al., *Controls on cassiterite (SnO₂) crystallization: Evidence from cathodoluminescence, trace-element chemistry, and geochronology at the Gejiu Tin District*, in *American Mineralogist*. 2019. p. 118.
18. Becker, J.S., A. Matusch, and B. Wu, *Bioimaging mass spectrometry of trace elements – recent advance and applications of LA-ICP-MS: A review*. Analytica Chimica Acta, 2014. **835**: p. 1-18.
19. Hare, D., et al., *Elemental bio-imaging of trace elements in teeth using laser ablation-inductively coupled plasma-mass spectrometry*. Journal of Dentistry, 2011. **39**(5): p. 397-403.

20. Woodhead, J.D., et al., *Isotopic and elemental imaging of geological materials by laser ablation inductively coupled plasma-mass spectrometry*. Geostandards and Geoanalytical Research, 2007. **31**(4): p. 331-343.
21. Russo, R.E., et al., *Influence of wavelength on fractionation in laser ablation ICP-MS*. Journal of Analytical Atomic Spectrometry, 2000. **15**(9): p. 1115-1120.
22. Guillon, M., I. Horn, and D. Günther, *A comparison of 266 nm, 213 nm and 193 nm produced from a single solid state Nd:YAG laser for laser ablation ICP-MS*. Journal of Analytical Atomic Spectrometry, 2003. **18**(10): p. 1224.
23. Poitrasson, F., et al., *Comparison of ultraviolet femtosecond and nanosecond laser ablation inductively coupled plasma mass spectrometry analysis in glass, monazite, and zircon*. Analytical Chemistry, 2003. **75**(22): p. 6184-6190.
24. Russo, R.E., et al., *Femtosecond laser ablation ICP-MS*. Journal of Analytical Atomic Spectrometry, 2002. **17**(9): p. 1072-1075.
25. Diwakar, P.K., et al., *The influence of laser pulse duration and energy on ICP-MS signal intensity, elemental fractionation, and particle size distribution in NIR fs-LA-ICP-MS*. Journal of Analytical Atomic Spectrometry, 2013. **28**(9): p. 1420-1429.
26. Fryer, B.J., S.E. Jackson, and H.P. Longerich, *The design, operation and role of the laser-ablation microprobe coupled with an inductively coupled plasma; mass spectrometer (LAM-ICP-MS) in the earth sciences*. The Canadian Mineralogist, 1995. **33**(2): p. 303-312.
27. J. G. Mank, A. and P. R. D. Mason, *A critical assessment of laser ablation ICP-MS as an analytical tool for depth analysis in silica-based glass samples*. Journal of Analytical Atomic Spectrometry, 1999. **14**(8): p. 1143-1153.
28. Semerok, A., et al., *Experimental investigations of laser ablation efficiency of pure metals with femto, pico and nanosecond pulses*. Applied Surface Science, 1999. **138-139**: p. 311-314.
29. Furusawa, K., et al., *Ablation characteristics of Au, Ag, and Cu metals using a femtosecond Ti:sapphire laser*. Applied Physics A, 1999. **69**(1): p. S359-S366.
30. Poitrasson, F. and F.-X. d'Abzac, *Femtosecond laser ablation inductively coupled plasma source mass spectrometry for elemental and isotopic analysis: are ultrafast lasers worthwhile?* Journal of Analytical Atomic Spectrometry, 2017. **32**(6): p. 1075-1091.
31. Eggins, S.M., L.P.J. Kinsley, and J.M.G. Shelley, *Deposition and element fractionation processes during atmospheric pressure laser sampling for analysis by ICP-MS*. Applied Surface Science, 1998. **127-129**: p. 278-286.
32. Bleiner, D. and J. Koch, *Computer modeling of laser ablation elemental microanalysis*. Laser ablation-ICP-MS in the earth sciences : current practices and outstanding issues, ed. P.J. Sylvester. Vol. 40. 2008, Québec, Québec: Mineralogical Association of Canada.
33. Loewen, M.W. and A.J.R. Kent, *Sources of elemental fractionation and uncertainty during the analysis of semi-volatile metals in silicate glasses using LA-ICP-MS*. Journal of Analytical Atomic Spectrometry, 2012. **27**(9): p. 1502-1508.
34. Jackson, S.E., *The application of laser ablation microprobe (LAM)-ICP-MS to in situ U-Pb zircon geochronology*. J. Conf. Abstract, 1996. **1**: p. 283.
35. Hu, Z., et al., *A "wire" signal smoothing device for laser ablation inductively coupled plasma mass spectrometry analysis*. Spectrochimica Acta Part B: Atomic Spectroscopy, 2012. **78**: p. 50-57.
36. Bleiner, D. and D. Günther, *Theoretical description and experimental observation of aerosol transport processes in laser ablation inductively coupled plasma mass spectrometry*. Journal of Analytical Atomic Spectrometry, 2001. **16**(5): p. 449-456.
37. Gurevich, E.L. and R. Hergenröder, *A simple laser ICP-MS ablation cell with wash-out time less than 100 ms*. Journal of Analytical Atomic Spectrometry, 2007. **22**(9): p. 1043-1050.

38. Muller, W., et al., *Initial performance metrics of a new custom-designed ArF excimer LA-ICPMS system coupled to a two-volume laser-ablation cell*. Journal of Analytical Atomic Spectrometry, 2009. **24**(2): p. 209-214.
39. Eland, K.L., et al., *Energy dependence of emission intensity and temperature in a LIBS Plasma using femtosecond excitation*. Applied Spectroscopy, 2001. **55**(3): p. 286-291.
40. Mao, X., et al., *Preferential vaporization and plasma shielding during nano-second laser ablation*. Applied Surface Science, 1996. **96-98**: p. 126-130.
41. Hahn, D.W. and N. Omenetto, *Laser-induced breakdown spectroscopy (LIBS), part I: Review of basic diagnostics and plasma-particle interactions: Still-challenging issues within the analytical plasma community*. Applied Spectroscopy, 2010. **64**(12): p. 335A-366A.
42. Hahn, D.W. and N. Omenetto, *Laser-induced breakdown spectroscopy (LIBS), part II: Review of instrumental and methodological approaches to material analysis and applications to different fields*. Applied Spectroscopy, 2012. **66**(4): p. 347-419.
43. Ullmann, M., S.K. Friedlander, and A. Schmidt-Ott, *Nanoparticle formation by laser ablation*. Journal of Nanoparticle Research, 2002. **4**(6): p. 499-509.
44. Guillon, M. and D. Gunther, *Effect of particle size distribution on ICP-induced elemental fractionation in laser ablation-inductively coupled plasma-mass spectrometry*. Journal of Analytical Atomic Spectrometry, 2002. **17**(8): p. 831-837.
45. Kuhn, H.-R. and D. Günther, *Laser ablation-ICP-MS: particle size dependent elemental composition studies on filter-collected and online measured aerosols from glass*. Journal of Analytical Atomic Spectrometry, 2004. **19**(9): p. 1158-1164.
46. Kosler, J., et al., *Chemical and phase composition of particles produced by laser ablation of silicate glass and zircon-implications for elemental fractionation during ICP-MS analysis*. Journal of Analytical Atomic Spectrometry, 2005. **20**(5): p. 402-409.
47. Jochum, K.P., et al., *Determination of reference values for NIST SRM 610–617 glasses following ISO guidelines*. Geostandards and Geoanalytical Research, 2011. **35**(4): p. 397-429.
48. Kosler, J., et al., *Effect of oxygen in sample carrier gas on laser-induced elemental fractionation in U-Th-Pb zircon dating by laser ablation ICP-MS*. Journal of Analytical Atomic Spectrometry, 2014. **29**(5): p. 832-840.
49. Hirata, T., *Chemically assisted laser ablation ICP mass spectrometry*. Analytical Chemistry, 2003. **75**(2): p. 228-233.
50. Luo, T., et al., *Further investigation into ICP-induced elemental fractionation in LA-ICP-MS using a local aerosol extraction strategy*. Journal of Analytical Atomic Spectrometry, 2015. **30**(4): p. 941-949.
51. Tanner, M. and D. Günther, *In torch laser ablation sampling for inductively coupled plasma time of flight mass spectrometry*. Journal of Analytical Atomic Spectrometry, 2006. **21**(9): p. 941-947.
52. Fietzke, J. and M. Frische, *Experimental evaluation of elemental behavior during LA-ICP-MS: influences of plasma conditions and limits of plasma robustness*. Journal of Analytical Atomic Spectrometry, 2016. **31**(1): p. 234-244.
53. Liu, S., et al., *Signal enhancement in laser ablation inductively coupled plasma-mass spectrometry using water and/or ethanol vapor in combination with a shielded torch*. Journal of Analytical Atomic Spectrometry, 2014. **29**(3): p. 536-544.
54. Luo, T., et al., *Water vapor-assisted “universal” nonmatrix-matched analytical method for the in situ U–Pb dating of zircon, monazite, titanite, and xenotime by laser ablation-inductively coupled plasma mass spectrometry*. Analytical Chemistry, 2018. **90**(15): p. 9016-9024.
55. Kimura, J.-I., et al., *An improved U-Pb age dating method for zircon and monazite using 200/266 nm femtosecond laser ablation and enhanced sensitivity multiple-Faraday collector inductively coupled plasma mass spectrometry*. Journal of Analytical Atomic Spectrometry, 2015. **30**(2): p. 494-505.

56. Wohlgemuth-Ueberwasser, C.C., et al., *Matrix dependency of baddeleyite U–Pb geochronology by femtosecond-LA-ICP-MS and comparison with nanosecond-LA-ICP-MS*. Journal of Analytical Atomic Spectrometry, 2018. **33**(6): p. 967-974.
57. Pin, C. and B. Le Fèvre, *Isotope dilution with matrix element removal: A key for high-precision, high-accuracy trace analysis of geological samples using inductively coupled plasma-mass spectrometry*. Geostandards Newsletter, 2002. **26**(2): p. 135-148.
58. Longerich, H.P., S.E. Jackson, and D. Gunther, *Inter-laboratory note. Laser ablation inductively coupled plasma mass spectrometric transient signal data acquisition and analyte concentration calculation*. Journal of Analytical Atomic Spectrometry, 1996. **11**(9): p. 899-904.
59. Guillon, M., et al., *Preliminary Characterisation of new glass reference materials (GSA-1G, GSC-1G, GSD-1G and GSE-1G) by laser ablation-inductively coupled plasma-mass spectrometry using 193 nm, 213 nm and 266 nm wavelengths*. Geostandards and Geoanalytical Research, 2005. **29**(3): p. 315-331.
60. Koenig, A., *Personal Communication*. 2008.
61. Liu, Y., et al., *In situ analysis of major and trace elements of anhydrous minerals by LA-ICP-MS without applying an internal standard*. Chemical Geology, 2008. **257**(1): p. 34-43.
62. Kuhn, B.K., et al., *Fundamental studies on the ablation behaviour of Pb/U in NIST 610 and zircon 91500 using laser ablation inductively coupled plasma mass spectrometry with respect to geochronology*. Journal of Analytical Atomic Spectrometry, 2010. **25**(1): p. 21-27.
63. Danyushevsky, L.V., et al. *Application of small-volume low-dispersion sample cells for characterisation of heterogeneous materials by LA-ICPMS*. in *14th European Workshop on Laser Ablation*. 2018. Pau, France.
64. Greenfield, S., I.L. Jones, and C.T. Berry, *High-pressure plasmas as spectroscopic emission sources*. Analyst, 1964. **89**(1064): p. 713-720.
65. Wendt, R.H. and V.A. Fassel, *Induction-coupled plasma spectrometric excitation source*. Analytical Chemistry, 1965. **37**(7): p. 920-922.
66. Scott, R.H., et al., *Inductively coupled plasma-optical emission analytical spectrometry*. Analytical Chemistry, 1974. **46**(1): p. 75-80.
67. Vaughan, M.-A., G. Horlick, and S.H. Tan, *Effect of operating parameters on analyte signals in inductively coupled plasma mass spectrometry*. Journal of Analytical Atomic Spectrometry, 1987. **2**(8): p. 765-772.
68. Vanhaecke, F., R. Dams, and C. Vandecasteele, *'Zone model' as an explanation for signal behaviour and non-spectral interferences in inductively coupled plasma mass spectrometry*. Journal of Analytical Atomic Spectrometry, 1993. **8**(3): p. 433-438.
69. Houk, R.S., et al., *Inductively coupled argon plasma as an ion source for mass spectrometric determination of trace elements*. Analytical Chemistry, 1980. **52**(14): p. 2283-2289.
70. Hongsen Niu, R.S.H., *Fundamental aspects of ion extraction in inductively coupled plasma mass spectrometry*. Spectrochimica Acta Part B: Atomic Spectroscopy, 1996.
71. Hayhurst, A.N., D.B. Kittelson, and N.R. Telford, *Mass spectrometric sampling of ions from atmospheric pressure flames—II: Aerodynamic disturbance of a flame by the sampling system*. Combustion and Flame, 1977. **28**: p. 123-135.
72. Koirtyohann, S.R., J.S. Jones, and D.A. Yates, *Nomenclature system for the low-power argon inductively coupled plasma*. Analytical Chemistry, 1980. **52**(12): p. 1965-1966.
73. Witte, T.M. and R.S. Houk, *Origins of polyatomic ions in laser ablation-inductively coupled plasma-mass spectrometry: An examination of metal oxide ions and effects of nitrogen and helium in the aerosol gas flow*. Spectrochimica Acta Part B: Atomic Spectroscopy, 2012. **69**: p. 9-19.
74. Gilbert, S., et al., *Matrix dependency for oxide production rates by LA-ICP-MS*. Journal of Analytical Atomic Spectrometry, 2017.

75. Tanner, S.D., *Plasma temperature from ion kinetic energies and implications for the source of diatomic oxide ions in inductively coupled plasma mass spectrometry*. Journal of Analytical Atomic Spectrometry, 1993. **8**(6): p. 891-897.
76. Durrant, S., *Feasibility of improvement in analytical performance in laser ablation inductively coupled plasma-mass spectrometry (LA-ICP-MS) by addition of nitrogen to the argon plasma*. Fresenius' Journal of Analytical Chemistry, 1994. **349**(10-11): p. 768-771.
77. Sesi, N.N., et al., *Fundamental studies of mixed-gas inductively coupled plasmas*. Spectrochimica Acta Part B: Atomic Spectroscopy, 1994. **49**(12-14): p. 1259-1282.
78. Guillong, M. and C.A. Heinrich, *Sensitivity enhancement in laser ablation ICP-MS using small amounts of hydrogen in the carrier gas*. Journal of Analytical Atomic Spectrometry, 2007. **22**(12): p. 1488-1494.
79. Hu, Z., et al., *Signal enhancement in laser ablation ICP-MS by addition of nitrogen in the central channel gas*. Journal of Analytical Atomic Spectrometry, 2008. **23**(8): p. 1093-1101.
80. Gray, A.L. and A.R. Date, *Inductively coupled plasma source mass spectrometry using continuum flow ion extraction*. Analyst, 1983. **108**(1290): p. 1033-1050.
81. Gray, A.L., R.S. Houk, and J.G. Williams, *Langmuir probe potential measurements in the plasma and their correlation with mass spectral characteristics in inductively coupled plasma mass spectrometry*. Journal of Analytical Atomic Spectrometry, 1987. **2**(1): p. 13-20.
82. Olivares, J.A. and R.S. Houk, *Ion sampling for inductively coupled plasma mass spectrometry*. Analytical Chemistry, 1985. **57**(13): p. 2674-2679.
83. Sakata, K.i. and K. Kawabata, *Reduction of fundamental polyatomic ions in inductively coupled plasma mass spectrometry*. Spectrochimica Acta Part B: Atomic Spectroscopy, 1994. **49**(10): p. 1027-1038.
84. Douglas, D.J. and J.B. French, *An improved interface for inductively coupled plasma-mass spectrometry (ICP-MS)*. Spectrochimica Acta Part B: Atomic Spectroscopy, 1986. **41**(3): p. 197-204.
85. Sakata, K.i., et al., *Optimizing plasma-interface parameters in ICP-MS*, in *The Pittsburg Conference 2000*. 2000: New Orleans, Louisiana.
86. Resano, M., K.S. McIntosh, and F. Vanhaecke, *Laser ablation-inductively coupled plasma-mass spectrometry using a double-focusing sector field mass spectrometer of Mattauch–Herzog geometry and an array detector for the determination of platinum group metals and gold in NiS buttons obtained by fire assay of platiniferous ores*. Journal of Analytical Atomic Spectrometry, 2012. **27**(1): p. 165-173.
87. Fryer, B.J., S.E. Jackson, and H.P. Longerich, *The application of laser ablation microprobe-inductively coupled plasma-mass spectrometry (LAM-ICP-MS) to in situ (U)–Pb geochronology*. Chemical Geology, 1993. **109**(1): p. 1-8.
88. Mattinson, J.M., *Zircon U–Pb chemical abrasion (“CA-TIMS”) method: Combined annealing and multi-step partial dissolution analysis for improved precision and accuracy of zircon ages*. Chemical Geology, 2005. **220**(1-2): p. 47-66.
89. Schoene, B., et al., *Reassessing the uranium decay constants for geochronology using ID-TIMS U–Pb data*. Geochimica et Cosmochimica Acta, 2006. **70**(2): p. 426-445.
90. Lodders, K., *Solar system abundances and condensation temperatures of the elements*. The Astrophysical Journal, 2003. **591**(2): p. 1220-1247.
91. Steiger, R. and E. Jaeger, *Subcommission on geochronology: convention of the use of decay constants in geochronology and cosmochronology. Contributions to the geologic time scale*. Studies in geology, 1978. **6**: p. 67-72.
92. Chang, Z., et al., *U–Pb dating of zircon by LA-ICP-MS*. Geochemistry, Geophysics, Geosystems, 2006. **7**(5): p. Q05009.

93. Gehrels, G.E., V.A. Valencia, and J. Ruiz, *Enhanced precision, accuracy, efficiency, and spatial resolution of U-Pb ages by laser ablation-multicollector-inductively coupled plasma-mass spectrometry*. Geochemistry Geophysics Geosystems, 2008. **9**.
94. Paton, C., et al., *Improved laser ablation U-Pb zircon geochronology through robust downhole fractionation correction*. Geochemistry, Geophysics, Geosystems, 2010. **11**(3): p. n/a-n/a.
95. Allen, C.M. and I.H. Campbell, *Identification and elimination of a matrix-induced systematic error in LA-ICP-MS 206Pb/238U dating of zircon*. Chemical Geology, 2012. **332–333**: p. 157-165.
96. Marillo-Sialer, E., et al., *The zircon 'matrix effect': evidence for an ablation rate control on the accuracy of U-Pb age determinations by LA-ICP-MS*. Journal of Analytical Atomic Spectrometry, 2014. **29**(6): p. 981-989.
97. Marillo-Sialer, E., et al., *An investigation of the laser-induced zircon 'matrix effect'*. Chemical Geology, 2016. **438**: p. 11-24.
98. Shaheen, M.E., J.E. Gagnon, and B.J. Fryer, *Femtosecond (fs) lasers coupled with modern ICP-MS instruments provide new and improved potential for in situ elemental and isotopic analyses in the geosciences*. Chemical Geology, 2012. **330–331**: p. 260-273.
99. Allen Jr, J.D., et al., *A new electron spectrometer design:II*. Journal of Electron Spectroscopy and Related Phenomena, 1976. **8**(5): p. 395-410.
100. Bradshaw, N., E.F.H. Hall, and N.E. Sanderson, *Communication. Inductively coupled plasma as an ion source for high-resolution mass spectrometry*. Journal of Analytical Atomic Spectrometry, 1989. **4**(8): p. 801-803.
101. Myers, D.P., et al., *An inductively coupled plasma-time-of-flight mass spectrometer for elemental analysis. Part I: Optimization and characteristics*. Journal of the American Society for Mass Spectrometry. **5**(11): p. 1008-1016.
102. Feldmann, I., N. Jakubowski, and D. Stuewer, *Application of a hexapole collision and reaction cell in ICP-MS Part I: Instrumental aspects and operational optimization*. Fresenius' Journal of Analytical Chemistry. **365**(5): p. 415-421.
103. Guillon, M., et al., *The effect of quadrupole ICPMS interface and ion lens design on argide formation. Implications for LA-ICPMS analysis of PGE's in geological samples*. Journal of Analytical Atomic Spectrometry, 2011. **26**(7): p. 1401-1407.
104. Danyushevsky, L., et al., *Routine quantitative multi-element analysis of sulphide minerals by laser ablation ICP-MS: Standard development and consideration of matrix effects*. Geochemistry: Exploration, Environment, Analysis, 2011. **11**(1): p. 51-60.
105. Olivares, J.A. and R.S. Houk, *Kinetic energy distributions of positive ions in an inductively coupled plasma mass spectrometer*. Applied Spectroscopy, 1985. **39**(6): p. 1070-1077.
106. Chambers, D.M. and G.M. Hieftje, *Fundamental studies of the sampling process in an inductively coupled plasma mass spectrometer-II: Ion kinetic energy measurements*. Spectrochimica Acta Part B: Atomic Spectroscopy, 1991. **46**(6–7): p. 761-784.
107. Houk, R.S., *Unpublished results*. 2016.
108. Jacobs, J.L., *Diagnostic studies of ion beam formation in inductively coupled plasma mass spectrometry with the collision reaction interface*. 2015: p. 136.
109. Fulford, J.E. and D.J. Douglas, *Ion kinetic energies in inductively coupled plasma/mass spectrometry (ICP-MS)*. Applied Spectroscopy, 1986. **40**(7): p. 971-974.
110. Douglas, D.J. and J.B. French, *Gas dynamics of the inductively coupled plasma mass spectrometry interface*. Journal of Analytical Atomic Spectrometry, 1988. **3**(6): p. 743-747.
111. Olsen, J.B., J.H. Macedone, and P.B. Farnsworth, *Source gas kinetic temperatures in an ICP-MS determined by measurements of the gas velocities in the first vacuum stage*. Journal of Analytical Atomic Spectrometry, 2006. **21**(9): p. 856.
112. Taylor, N. and P.B. Farnsworth, *Experimental characterization of the effect of skimmer cone design on shock formation and ion transmission efficiency in the vacuum interface of an*

- inductively coupled plasma mass spectrometer*. *Spectrochimica Acta Part B: Atomic Spectroscopy*, 2012. **69**: p. 2-8.
113. Lim, H.B., et al., *Some fundamental characteristics of a reduced-pressure plasma extracted from an inductively coupled plasma*. *Journal of Analytical Atomic Spectrometry*, 1989. **4**(4): p. 365-370.
 114. Hutton, R.C. and A.N. Eaton, *Role of aerosol water vapour loading in inductively coupled plasma mass spectrometry*. *Journal of Analytical Atomic Spectrometry*, 1987. **2**(6): p. 595-598.
 115. Niu, H. and R.S. Houk, *Langmuir probe measurements of the ion extraction process in inductively coupled plasma mass spectrometry-I. spatially resolved determination of electron density and electron temperature*. *Spectrochimica Acta Part B: Atomic Spectroscopy*, 1994. **49**(12-14): p. 1283-1303.
 116. Choot, E.H. and G. Horlic, *Vertical spatial emission profiles in Ar-N₂ mixed gas inductively coupled plasmas—I*. *Spectrochimica Acta Part B: Atomic Spectroscopy*, 1986. **41**(9): p. 889-906.
 117. Vaughan, M.A. and G. Horlick, *Effect of sampler and skimmer orifice size on analyte and analyte oxide signals in inductively coupled plasma-mass spectrometry*. *Spectrochimica Acta Part B: Atomic Spectroscopy*, 1990. **45**(12): p. 1289-1299.
 118. Ungerer, A.J.R.K.a.C.A.A., *Production of barium and light rare earth element oxides during LA-ICP-MS microanalysis*. *Journal of Analytical Atomic Spectrometry*, 2005(11).
 119. Peate, D.W., et al., *Melt Inclusions as a recorder of crustal assimilation processes*. *Geochimica Et Cosmochimica Acta*, 2008. **72**(12): p. A732.
 120. Alder, J.F., R.M. Bombelka, and G.F. Kirkbright, *Electronic excitation and ionization temperature measurements in a high frequency inductively coupled argon plasma source and the influence of water vapour on plasma parameters*. *Spectrochimica Acta Part B: Atomic Spectroscopy*, 1980. **35**(4): p. 163-175.
 121. Maessen, F.J.M.J., G. Kreuning, and J. Balke, *Experimental control of the solvent load of inductively coupled argon plasmas and effects of the chloroform plasma load on their analytical performance*. *Spectrochimica Acta Part B: Atomic Spectroscopy*, 1986. **41**(1): p. 3-25.
 122. Klötzli, U., et al., *Accuracy of laser ablation U-Pb zircon dating: Results from a test using five different reference zircons*. *Geostandards and Geoanalytical Research*, 2009. **33**(1): p. 5-15.
 123. Chang, Z., et al., *U-Pb dating of zircon by LA-ICP-MS*. *Geochemistry, Geophysics, Geosystems*, 2006. **7**(5): p. n/a-n/a.
 124. Kosler, J., M.N. Tubrett, and P.J. Sylvester, *Application of laser ablation ICP-MS to U-Th-Pb dating of monazite*. *Geostandards Newsletter*, 2001. **25**(2-3): p. 375-386.
 125. Zack, T., et al., *In situ U-Pb rutile dating by LA-ICP-MS: ²⁰⁸Pb correction and prospects for geological applications*. *Contributions to Mineralogy and Petrology*, 2011. **162**(3): p. 515-530.
 126. Storey, C.D., T.E. Jeffries, and M. Smith, *Common lead-corrected laser ablation ICP-MS U-Pb systematics and geochronology of titanite*. *Chemical Geology*, 2006. **227**(1-2): p. 37-52.
 127. Smye, A.J., et al., *Characterising the U-Th-Pb systematics of allanite by ID and LA-ICPMS: Implications for geochronology*. *Geochimica et Cosmochimica Acta*, 2014. **135**: p. 1-28.
 128. Frei, D. and A. Gerdes, *Precise and accurate in situ U-Pb dating of zircon with high sample throughput by automated LA-SF-ICP-MS*. *Chemical Geology*, 2009. **261**(3-4): p. 261-270.
 129. Black, L.P., et al., *Improved ²⁰⁶Pb/²³⁸U microprobe geochronology by the monitoring of a trace-element-related matrix effect; SHRIMP, ID-TIMS, ELA-ICP-MS and oxygen isotope documentation for a series of zircon standards*. *Chemical Geology*, 2004. **205**(1-2): p. 115-140.
 130. Hughes, J.M. and J.F. Rakovan, *Structurally robust, chemically diverse: Apatite and apatite supergroup minerals*. *Elements*, 2015. **11**: p. 165-170.

131. Cherniak, D.J., W.A. Lanford, and F.J. Ryerson, *Lead diffusion in apatite and zircon using ion implantation and Rutherford Backscattering techniques*. *Geochimica et Cosmochimica Acta*, 1991. **55**(6): p. 1663-1673.
132. Dahl, P.S., *A crystal-chemical basis for Pb retention and fission-track annealing systematics in U-bearing minerals, with implications for geochronology*. *Earth and Planetary Science Letters*, 1997. **150**(3–4): p. 277-290.
133. Chew, D.M. and R.A. Spikings, *Geochronology and thermochronology using apatite: Time and temperature, lower crust to surface*. *Elements*, 2015. **11**: p. 189-194.
134. Corfu, F. and D. Stone, *The significance of titanite and apatite U-Pb ages: constraints for the post-magmatic thermal-hydrothermal evolution of a batholithic complex, Berens River area, northwestern Superior Province, Canada*. *Geochimica et Cosmochimica Acta*, 1998. **62**(17): p. 2979-2995.
135. Barfod, G.H., et al., *Lu-Hf and PbSL geochronology of apatites from Proterozoic terranes: A first look at Lu-Hf isotopic closure in metamorphic apatite*. *Geochimica et Cosmochimica Acta*, 2005. **69**(7): p. 1847-1859.
136. Schoene, B. and S.A. Bowring, *U–Pb systematics of the McClure Mountain syenite: thermochronological constraints on the age of the 40Ar/39Ar standard MMhb*. *Contributions to Mineralogy and Petrology*, 2006. **151**(5): p. 615-630.
137. Amelin, Y. and A.N. Zaitsev, *Precise geochronology of phoscorites and carbonatites:: The critical role of U-series disequilibrium in age interpretations*. *Geochimica et Cosmochimica Acta*, 2002. **66**(13): p. 2399-2419.
138. Coulson, I.M., et al., *Time-scales of assembly and thermal history of a composite felsic pluton: constraints from the Emerald Lake area, northern Canadian Cordillera, Yukon*. *Journal of Volcanology and Geothermal Research*, 2002. **114**(3–4): p. 331-356.
139. McDowell, F.W., W.C. McIntosh, and K.A. Farley, *A precise 40Ar–39Ar reference age for the Durango apatite (U–Th)/He and fission-track dating standard*. *Chemical Geology*, 2005. **214**(3–4): p. 249-263.
140. Black, L.P., et al., *TEMORA 1: a new zircon standard for Phanerozoic U–Pb geochronology*. *Chemical Geology*, 2003. **200**(1–2): p. 155-170.
141. Sláma, J., et al., *Plešovice zircon — A new natural reference material for U–Pb and Hf isotopic microanalysis*. *Chemical Geology*, 2008. **249**(1–2): p. 1-35.
142. Chew, D.M., J.A. Petrus, and B.S. Kamber, *U–Pb LA–ICPMS dating using accessory mineral standards with variable common Pb*. *Chemical Geology*, 2014. **363**: p. 185-199.
143. Baker, J., et al., *Pb isotopic analysis of standards and samples using a 207Pb–204Pb double spike and thallium to correct for mass bias with a double-focusing MC-ICP-MS*. *Chemical Geology*, 2004. **211**(3–4): p. 275-303.
144. Horstwood, M.S.A., et al., *Community-Derived Standards for LA-ICP-MS U-(Th)-Pb Geochronology – Uncertainty Propagation, Age Interpretation and Data Reporting*. *Geostandards and Geoanalytical Research*, 2016: p. n/a-n/a.
145. Sniderman, J.M.K., et al., *Pliocene reversal of late Neogene aridification*. *Proceedings of the National Academy of Sciences*, 2016. **113**(8): p. 1999-2004.
146. Krogh, T.E., *A low-contamination method for hydrothermal decomposition of zircon and extraction of U and Pb for isotopic age determinations*. *Geochimica et Cosmochimica Acta*, 1973. **37**(3): p. 485-494.
147. Schmitz, M.D. and B. Schoene, *Derivation of isotope ratios, errors, and error correlations for U-Pb geochronology using 205Pb-235U-(233U)-spiked isotope dilution thermal ionization mass spectrometric data*. *Geochemistry, Geophysics, Geosystems*, 2007. **8**(8): p. n/a-n/a.
148. Stormer, J.C., M.L. Pierson, and R.C. Tacker, *Variation of F and Cl X-ray intensity due to anisotropic diffusion in apatite during electron microprobe analysis*. *American Mineralogist*, 1993. **78**(5-6): p. 641-648.

149. Trotter, J.A. and S.M. Eggins, *Chemical systematics of conodont apatite determined by laser ablation ICPMS*. Chemical Geology, 2006. **233**(3–4): p. 196-216.
150. Jarosewich, E., J.A. Nelen, and J.A. Norberg, *Reference samples for electron microprobe analysis**. Geostandards Newsletter, 1980. **4**(1): p. 43-47.
151. Stacey, J.S. and J.D. Kramers, *Approximation of terrestrial lead isotope evolution by a two-stage model*. Earth and Planetary Science Letters, 1975. **26**(2): p. 207-221.
152. Schärer, U., *The effect of initial ^{230}Th disequilibrium on young UPb ages: the Makalu case, Himalaya*. Earth and Planetary Science Letters, 1984. **67**(2): p. 191-204.
153. Guillon, M., et al., *LA-ICP-MS Pb-U dating of young zircons from the Kos-Nisyros volcanic centre, SE Aegean arc*. Journal of Analytical Atomic Spectrometry, 2014. **29**(6): p. 963-970.
154. Solari, L.A., C. Ortega-Obregón, and J.P. Bernal, *U–Pb zircon geochronology by LAICPMS combined with thermal annealing: Achievements in precision and accuracy on dating standard and unknown samples*. Chemical Geology, 2015. **414**: p. 109-123.
155. Wiedenbeck, M., et al., *Three natural zircon standards for U-Th-Pb, Lu-Hf, trace element and REE analysis*. Geostandards Newsletter, 1995. **19**(1): p. 1-23.
156. Tiepolo, M., *In situ Pb geochronology of zircon with laser ablation–inductively coupled plasma–sector field mass spectrometry*. Chemical Geology, 2003. **199**(1–2): p. 159-177.
157. Yuan, H., et al., *Accurate U-Pb age and trace element determinations of zircon by laser ablation-inductively coupled plasma-mass spectrometry*. Geostandards and Geoanalytical Research, 2004. **28**(3): p. 353-370.
158. Li, X.-H., et al., *Penglai zircon megacrysts: A potential new working reference material for microbeam determination of Hf–O isotopes and U–Pb age*. Geostandards and Geoanalytical Research, 2010. **34**(2): p. 117-134.
159. Solari, L.A., et al., *U-Pb zircon geochronology with an integrated LA-ICP-MS microanalytical workstation: Achievements in precision and accuracy*. Geostandards and Geoanalytical Research, 2010. **34**(1): p. 5-18.
160. Košler, J., et al., *U-Pb detrital zircon analysis – Results of an inter-laboratory comparison*. Geostandards and Geoanalytical Research, 2013. **37**(3): p. 243-259.
161. Horstwood, M.S.A., et al., *Community-derived standards for LA-ICP-MS U-(Th)-Pb geochronology – Uncertainty propagation, age interpretation and data reporting*. Geostandards and Geoanalytical Research, 2016.
162. Hiess, J., et al., *$^{238}\text{U}/^{235}\text{U}$ Systematics in terrestrial uranium-bearing minerals*. Science, 2012. **335**(6076): p. 1610-1614.
163. Paton, C., et al., *Improved laser ablation U-Pb zircon geochronology through robust downhole fractionation correction*. Geochemistry, Geophysics, Geosystems, 2010. **11**(3): p. Q0AA06.
164. Halpin, J.A., et al., *Authigenic monazite and detrital zircon dating from the Proterozoic Rocky Cape Group, Tasmania: Links to the Belt-Purcell Supergroup, North America*. Precambrian Research, 2014. **250**: p. 50-67.
165. Paces, J.B. and J.D. Miller, *Precise U-Pb ages of Duluth Complex and related mafic intrusions, northeastern Minnesota: geochronological insights to physical, petrogenetic, paleomagnetic, and tectonomagmatic processes associated with the 1.1 Ga Midcontinent Rift System*. Journal of Geophysical Research: Solid Earth, 1993. **98**(B8): p. 13997-14013.
166. Stern, R.A., et al., *Measurement of SIMS instrumental mass fractionation of Pb Isotopes during zircon dating*. Geostandards and Geoanalytical Research, 2009. **33**(2): p. 145-168.
167. Kennedy, A.K., et al., *Eocene zircon reference material for microanalysis of U-Th-Pb isotopes and trace elements*. The Canadian Mineralogist, 2014. **52**(3): p. 409-421.
168. Zartman, S., et al., *Proceedings of the 7th International Kimberlite Conference: (J.B. Dawson volume). Authors A-K*. International Kimberlite Conference. 1999: Red Roof Design.
169. Black, L.P. and B.L. Gulson, *The age of the Mud Tank carbonatite, Strangways Range, Northern Territory*. BMR Journal of Australian Geology & Geophysics, 1978. **3**(3): p. 227-232.

170. Li, X., et al., *Qinghu zircon: A working reference for microbeam analysis of U-Pb age and Hf and O isotopes*. Chinese Science Bulletin, 2013. **58**(36): p. 4647-4654.
171. Nasdala, L., et al., *Zircon M257 - a homogeneous natural reference material for the ion microprobe U-Pb analysis of zircon*. Geostandards and Geoanalytical Research, 2008. **32**(3): p. 247-265.
172. Svensen, H., et al., *Rapid magma emplacement in the Karoo Large Igneous Province*. Earth and Planetary Science Letters, 2012. **325–326**: p. 1-9.
173. Ivanov, A.V., et al., *Timing and genesis of the Karoo-Ferrar large igneous province: New high precision U-Pb data for Tasmania confirm short duration of the major magmatic pulse*. Chemical Geology.
174. Ludwig, K.R., *A User's Manual for Isoplot 3.6: A Geochronological Toolkit for Microsoft Excel (Revision of April 8, 2008)*. in Berkeley Geochronology Center Special Publication No. 4. 2008. p. 77.
175. Günther, D., et al., *Effect of sampler orifice diameter on dry plasma inductively coupled plasma mass spectrometry (ICP-MS) backgrounds, sensitivities, and limits of detection using laser ablation sample introduction*. Fresenius' Journal of Analytical Chemistry, 1996. **355**(7): p. 771-773.
176. Nasdala, L., et al., *Metamictisation of natural zircon: accumulation versus thermal annealing of radioactivity-induced damage*. Contributions to Mineralogy and Petrology, 2004. **141**(2): p. 125-144.
177. Nasdala, L., et al., *Metamictisation of natural zircon: accumulation versus thermal annealing of radioactivity-induced damage*. Contributions to Mineralogy and Petrology, 2001. **141**(2): p. 125-144.
178. von Quadt, A., et al., *U-Pb dating of CA/non-CA treated zircons obtained by LA-ICP-MS and CA-TIMS techniques: impact for their geological interpretation*. Journal of Analytical Atomic Spectrometry, 2014. **29**(9): p. 1618-1629.
179. Gilbert, S., et al., *A Comparative Study of Five Reference Materials and the Lombard Meteorite for the Determination of the Platinum-Group Elements and Gold by LA-ICP-MS*. Geostandards and Geoanalytical Research, 2013. **37**(1): p. 51-64.
180. Pettke, T., et al., *Quadrupole mass spectrometry and optical emission spectroscopy: detection capabilities and representative sampling of short transient signals from laser-ablation*. Journal of Analytical Atomic Spectrometry, 2000. **15**(9): p. 1149-1155.
181. Myers, D.P., et al., *An inductively coupled plasma—time-of-flight mass spectrometer for elemental analysis. Part I: optimization and characteristics*. Journal of the American Society for Mass Spectrometry, 1994. **5**(11): p. 1008-1016.
182. Willie, S., Z. Mester, and R.E. Sturgeon, *Isotope ratio precision with transient sample introduction using ICP orthogonal acceleration time-of-flight mass spectrometry*. Journal of Analytical Atomic Spectrometry, 2005. **20**(12): p. 1358-1364.
183. Barnes, J.H.t., et al., *Use of a novel array detector for the direct analysis of solid samples by laser ablation inductively coupled plasma sector-field mass spectrometry*. J Am Soc Mass Spectrom, 2004. **15**(6): p. 769-76.
184. Felton, J.A., et al., *Evaluation of a fourth-generation focal plane camera for use in plasma-source mass spectrometry*. Journal of Analytical Atomic Spectrometry, 2011. **26**(2): p. 300-304.
185. Pearce, N.J.G., et al., *Communication. Mineral microanalysis by laser ablation inductively coupled plasma mass spectrometry*. Journal of Analytical Atomic Spectrometry, 1992. **7**(1): p. 53-57.
186. Thompson, J.M., S. Meffre, and L. Danyushevsky, *Impact of air, laser pulse width and fluence on U-Pb dating of zircons by LA-ICPMS*. Journal of Analytical Atomic Spectrometry, 2018. **33**(2): p. 221-230.

187. Hendriks, L., et al., *Characterization of a new ICP-TOFMS instrument with continuous and discrete introduction of solutions*. Journal of Analytical Atomic Spectrometry, 2017. **32**(3): p. 548-561.
188. Santos, M.M., et al., *A New Appraisal of Sri Lankan BB Zircon as a Reference Material for LA-ICP-MS U-Pb Geochronology and Lu-Hf Isotope Tracing*. Geostandards and Geoanalytical Research, 2017. **41**(3): p. 335-358.
189. Horstwood, M.S.A., et al., *Community-Derived Standards for LA-ICP-MS U-(Th)-Pb Geochronology – Uncertainty Propagation, Age Interpretation and Data Reporting*. Geostandards and Geoanalytical Research, 2016. **40**(3): p. 311-332.
190. Norris, C.A. and L. Danyushevsky, *Towards estimating the complete uncertainty budget of quantified results measured by LA-ICP-MS*. Goldschmidt Abstracts, 2018.
191. Danyushevsky, L.V., et al. *Application of small-volume low-dispersion sample cells for characterisation of heterogeneous materials by LA-ICPMS in 14th European Workshop on Laser Ablation*. 2018. Pau, France.
192. Watson, E.B. and T.M. Harrison, *Zircon Thermometer Reveals Minimum Melting Conditions on Earliest Earth*. Science, 2005. **308**(5723): p. 841-844.
193. Ballard, J.R., M.J. Palin, and I.H. Campbell, *Relative oxidation states of magmas inferred from Ce(IV)/Ce(III) in zircon: application to porphyry copper deposits of northern Chile*. Contributions to Mineralogy and Petrology, 2002. **144**(3): p. 347-364.
194. Trail, D., E. Bruce Watson, and N.D. Tailby, *Ce and Eu anomalies in zircon as proxies for the oxidation state of magmas*. Geochimica et Cosmochimica Acta, 2012. **97**: p. 70-87.
195. Ronzani, A.-L., et al., *Capabilities of laser ablation – ICP-TOF-MS coupling for isotopic analysis of individual uranium micrometric particles*. Journal of Analytical Atomic Spectrometry, 2018. **33**(11): p. 1892-1902.
196. Emteborg, H., et al., *Isotope ratio and isotope dilution measurements using axial inductively coupled plasma time of flight mass spectrometry*. Journal of Analytical Atomic Spectrometry, 2000. **15**(3): p. 239-246.
197. Burger, M., et al., *Capabilities of laser ablation inductively coupled plasma time-of-flight mass spectrometry*. Journal of Analytical Atomic Spectrometry, 2017. **32**(10): p. 1946-1959.
198. Wiedenbeck, M., et al., *Further Characterisation of the 91500 Zircon Crystal*. Geostandards and Geoanalytical Research, 2004. **28**(1): p. 9-39.

Appendices

A.1 List of additional publications

A.1.1 Co-authored publications

Abersteiner, A., Kamenetsky, V. S., Goemann, K., Giuliani, A., Howarth, G. H., Castillo-Oliver, M., **Thompson, J.**, Kamenetsky, C., Cherry, A. (2019). Composition and emplacement of the Benfontein kimberlite sill complex (Kimberley, South Africa): Textural, petrographic and melt inclusion constraints. *Lithos*, 324-325, 297-314.

Apukhtina, O. B., Kamenetsky, V. S., Ehrig, K., Kamenetsky, M. B., Maas, R., **Thompson, J.**, McPhie, J., Ciobanu, C.L., Cook, N. J. (2017). Early, deep magnetite-fluorapatite mineralization at the Olympic Dam Cu-U-Au-Ag deposit, South Australia. *Economic Geology*, 112(6), 1531-1542.

Baker, M.J., Hollings, P., Thompson, J.A., **Thompson, J.M.**, Burge, C. (2016). Age and geochemistry of host rocks of the Cobre Panama porphyry Cu–Au deposit, central Panama: Implications for the Paleogene evolution of the Panamanian magmatic arc. *Lithos*, 248-251, 40-54.

Batanova, V.G., **Thompson, J.M.**, Danyushevsky, L.V., Portnyagin, M.V., Garbe-Schönberg, D., Hauri, E., Kimura, J., Chang, Q., Senda, R., Goemann, K., Chauvel, S., Campillo, S., Ionov, D.A., Sobolev, A.V. (2019). New Olivine Reference Material for In Situ Microanalysis. *Geostandards and Geoanalytical Research*, 43(3), 453-473.

Berry, R., **Thompson, J.**, Meffre, S., & Goemann, K. (2016). U–Th–Pb monazite dating and the timing of arc–continent collision in East Timor. *Australian Journal of Earth Sciences*, 63(4), 367-377.

Berry, R.F., Goemann, K., **Thompson, J.**, Meffre, S., Bottrill, R. (2019). Geochemistry and provenance of the Turquoise Bluff Slate, northeastern Tasmania: tectonic significance. *Australian Journal of Earth Sciences*, 66(2), 227-246.

Borabadi, R., Mazaheri, S.A., Karimpour, M.H., Meffre, S., **Thompson, J.**, Murphy, R.C., Entezariharsini, A. (2018). Zircon U-Pb geochronology, Hf isotopes and geochemistry of intrusive rocks in the Simorgh prospecting area, Lut Block, eastern Iran: petrogenesis and geological implications. *Geosciences Journal*, 22, 711-732.

Bowden, B., Fraser, G., Davidson, G.J., Meffre, S., Skirrow, R., Bull, S., **Thompson, J.** (2017). Age constraints on the hydrothermal history of the Prominent Hill iron oxide copper-gold deposit, South Australia. *Mineralium Deposita*, 52, 863-881.

Cave, B. J., Pitcairn, I. K., Craw, D., Large, R. R., **Thompson, J. M.**, & Johnson, S. C. (2016). A metamorphic mineral source for tungsten in the turbidite-hosted orogenic gold deposits of the Otago Schist, New Zealand. *Mineralium Deposita*, 52, 515-537.

Cherry, A. R., Kamenetsky, V. S., McPhie, J., **Thompson, J. M.**, Ehrig, K., Meffre, S., Kamenetsky, M.B., Krneta, S. (2018). Tectonothermal events in the Olympic IOCG Province constrained by apatite and REE-phosphate geochronology. *Australian Journal of Earth Sciences*, 1-17.

Gilbert, S., Olin, P., **Thompson, J.**, Lounejeva, E., Danyushevsky, L. (2017). Matrix dependency for oxide production rates by LA-ICP-MS. *Journal of Analytical Atomic Spectrometry*, 32, 638-646.

Harrison, R.L., Maryono, A., Norris, M.S., Rohrlach, B.D., Cooke, D.R., **Thompson, J.M.**, Creaser, R.A., Thiede, D. S. (2018). Geochronology of the Tumpangpitu Porphyry Au-Cu-Mo and High-Sulfidation Epithermal Au-Ag-Cu Deposit: Evidence for Pre- and Postmineralization Diatremes in the Tujuh Bukit District, Southeast Java, Indonesia. *Economic Geology*, 113(1), 163-192.

Hong, W., Cooke, D. R., Huston, D. L., Maas, R., Meffre, S., **Thompson, J.**, Zhang, L., Fox, N. (2017). Geochronological, geochemical and Pb isotopic compositions of Tasmanian granites (southeast Australia): Controls on petrogenesis, geodynamic evolution and tin mineralisation. *Gondwana Research*, 46, 124-140.

Hong, W., Cooke, D.R., Zhang, L., Fox, N., **Thompson, J.** (2017). Tourmaline-rich features in the Heemskirk and Pieman Heads granites from western Tasmania, Australia: Characteristics, origins, and implications for tin mineralization. *American Mineralogist*, 102(4), 876-899.

Hong, W., David, R.C., Zhang, L., Fox, N., **Thompson, J.** (2019). Cathodoluminescence features, trace elements, and oxygen isotopes of quartz in unidirectional solidification textures from the Sn-mineralized Heemskirk Granite, western Tasmania. *American Mineralogist*, 104(1), 100-117.

Ivanov, A.V., Meffre, S., **Thompson, J.**, Corfu, F., Kamenetsky, V.S., Kamenetsky, M.B., Demonterova, E.I. (2017). Timing and genesis of the Karoo-Ferrar large igneous province: New high precision U-Pb data for Tasmania confirm short duration of the major magmatic pulse. *Chemical Geology*, 455(Supplement C), 32-43.

Liu, Y., Fan, Y., Zhou, T., Xiao, X., White, N.C., **Thompson, J.**, Hong, H., Zhang, L. (2019). Geochemical characteristics of magnetite in Longqiao skarn iron deposit in the Middle-Lower Yangtze Metallogenic Belt, Eastern China. *Mineralium Deposita*, 54, 1229–1242.

Mulder, J.A., Halpin, J.A., Daczko, N.R., Orth, K., Meffre, S., **Thompson, J.M.**, Morrissey, L.J. (2019). A Multiproxy provenance approach to uncovering the assembly of East Gondwana in Antarctica. *Geology*, 47(7), 645-649.

Paul Mbih, K., Meffre, S., Yongue, R.F., Kanouo, N.S., **Thompson, J.** (2016). Chemistry and origin of the Mayo Kila sapphires, NW region Cameroon (Central Africa): Their possible relationship with the Cameroon volcanic line. *Journal of African Earth Sciences*, 118, 263-273

Potter, N.J., Ferguson, M. R.M., Kamenetsky, V.S., Chakhmouradian, A.R., Sharygin, V.V., **Thompson, J.M.**, & Goemann, K. (2018). Textural evolution of perovskite in the Afrikanda alkaline-ultramafic complex, Kola Peninsula, Russia. *Contributions to Mineralogy and Petrology*, 173(12), 100.

Smyk, E., Hollings, P., Baker, M.J., Cooke, D.R., Thompson, J.A., **Thompson, J.M.**, Creaser, R. (2018). Geochemistry and geochronology of the intrusive rocks of the central Wasatch Mountains igneous belt, Utah, USA. *Utah Geological Association*, 47, 305-325.

Su, S.-Q., Qin, K.-Z., Li, G.-M., Olin, P., **Thompson, J.** (2019). Cathodoluminescence and trace elements of scheelite: Constraints on ore-forming processes of the Dabaoshan porphyry Mo-W deposit, South China. *Ore Geology Reviews*, 115, 103183.

Sutherland, F. L., Zaw, K., Meffre, S., **Thompson, J.**, Goemann, K., Thu, K., Nu, T.T., Zin, M.M., Harris, S. J. (2019). Diversity in Ruby Geochemistry and Its Inclusions: Intra- and Inter-Continental Comparisons from Myanmar and Eastern Australia. *Minerals*, 9(1), 28.

Winn, K., Ngai, L., Wong, Y., Zaw, K., **Thompson, J.** (2018). The Ayer Chawan Facies, Jurong Formation, Singapore: Age and observation of syndepositional pyroclastic sedimentation process with possible peperite formation. *Bulletin of the Geological Society of Malaysia*, 66, 25-31.

A.1.2 First-authored conference abstracts

Thompson, J.M.; Danyushevsky, L.V.; Norris, C.A. (2018) Laser Ablation ICP-MS - From Craters to Calculations. European Microbeam Analysis Society (EMAS) – Microbeam Analysis in the Earth Sciences. Bristol, UK. (Invited Oral Presentation)

Thompson, J.M.; Danyushevsky, L.V.; (2018) Advantages of LA-TOF-ICP-MS for analysis of geological materials. Goldschmidt Conference. Boston, Massachusetts, USA. (Oral Presentation)

Thompson, J.M.; Danyushevsky, L.V.; Meffre, S.; Corfu, F. (2018) The Mud Tank zircon revisited: New ID-TIMS ages reveal complex crystallization history. GeoAnalysis 2018 Conference Abstract. Sydney, Australia. (Poster Presentation)

Thompson, J.M.; Danyushevsky, L.V.; Meffre, S. (2018) Impact of atmospheric air and laser fluence on accuracy of zircon U-Pb dating. GeoAnalysis 2018 Conference Abstract. Sydney, Australia. (Oral Presentation)

Thompson, J.M.; Rodemann, T.; Meffre, S.; Danyushevsky, L.V (2017) Raman Spectroscopic imaging of zircon as a useful tool for the characterization of zircon prior to LA-ICP-MS analysis. Themochronology And Noble Gas Geochemistry and Geochronology (TANG30) workshop. Canberra, Australia. (Oral Presentation)

Thompson, J.M.; Danyushevsky, L.V.; Meffre, S. (2017) Monazite and Xenotime Pb/U dating by LA-ICP-MS: Importance of Operating conditions for accurate analysis. North American Workshop on Laser Ablation (NAWLA). Austin, Texas, USA. (Poster Presentation)

Thompson, J.M.; Meffre, S.; Danyushevsky, L.V (2016) Minimising Fractionation effects in Pb/U LA-ICP-MS geochronology. American Geophysical Union (AGU) Fall meeting. San Francisco, California, USA. (Oral Presentation)

Thompson, J.M.; Meffre, S.; Danyushevsky, L.V (2016) LA-TOF-ICPMS Pb/U geochronology of zircon: Some advantages and limitations. Themochronology And Noble Gas Geochemistry and Geochronology (TANG30) workshop. Perth, Australia. (Oral Presentation)

Thompson, J.M.; Meffre, S.; Danyushevsky, L.V (2016) Investigation into Matrix Effects in Apatite Pb/U Geochronology. Winter Conference on Plasma Spectrochemistry. Tucson, Arizona, USA. (Awarded Best Poster Presentation in session)

A.2 Electronic appendices for Chapter 2

This Excel file contains all of the individual ion energy stopping curves, diatomic gas addition tests and interference tests conducted for Chapter 2.

A.3 Electronic appendices for Chapter 3

- A3.1 EMPA results for individual apatite analyses and isotope dilution results on the OD306 and 401 apatite samples.*
- A3.2 EMPA instrument conditions and setup used to acquire major element compositions and halogen contents of the apatite in Chapter 3.*

A.4 Electronic appendices for Chapter 4

- A.4.1 LA-ICP-MS instrumentation metadata including all instrument parameters and settings.*
- A.4.2 Individual zircon results for all analyses and tests done in Chapter 4.*

A.5 Electronic appendices for Chapter 5

Individual zircon analyses for Experiment 1 and Experiment 2 utilized in Chapter 5. Includes U-Pb isotopes, Pb-Pb isotopes, trace element compositions, and count rate data for each analysis.